Design for urban vertical-axis wind turbines: balancing performance and noise

Brandetti, L.

DOI

Publication date
2024

Document Version
Final published version

Citation (APA)

Important note

To cite this publication, please use the final published version (if applicable).
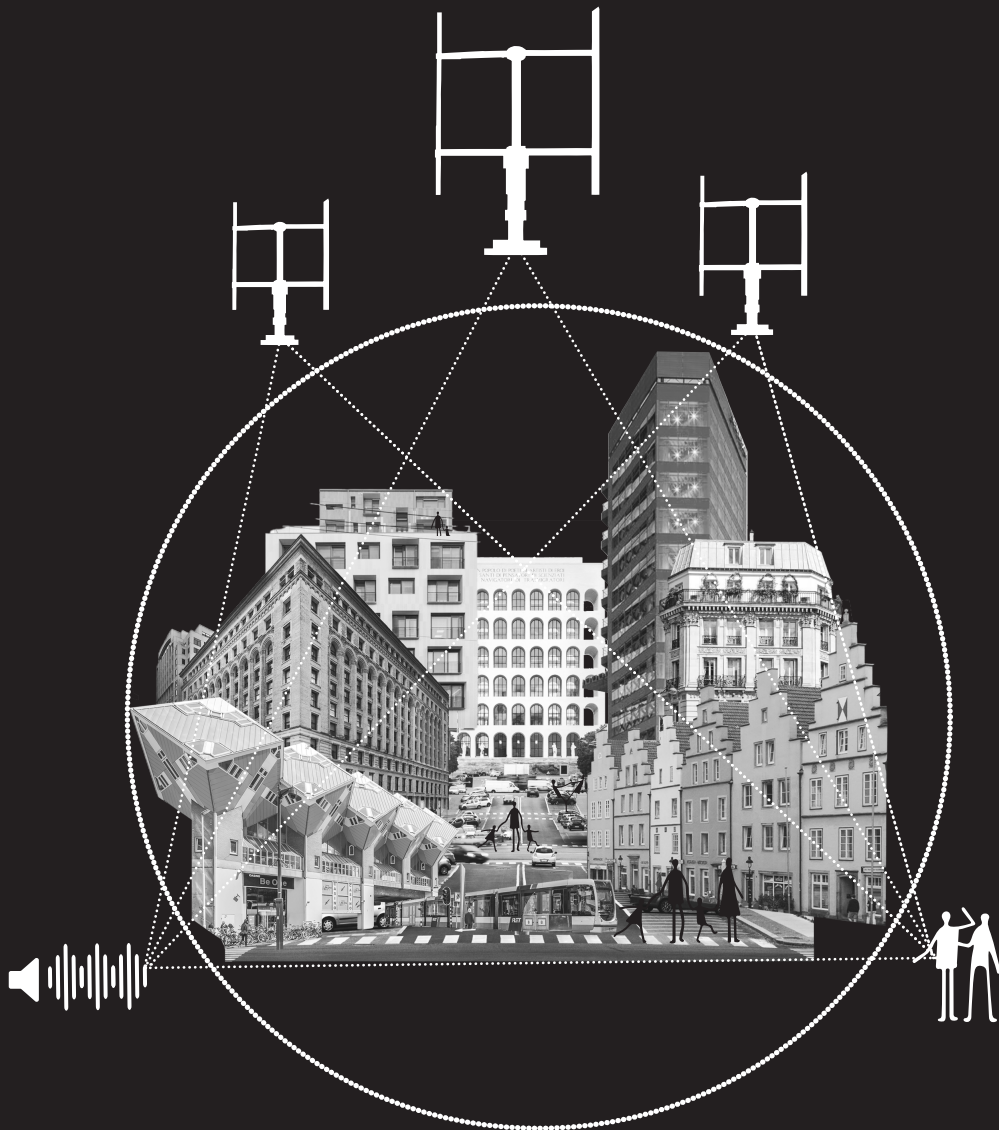Please check the document version above.

Design for urban vertical-axis wind turbines: balancing performance and noise

Livia Brandetti

DESIGN FOR URBAN VERTICAL-AXIS WIND TURBINES: BALANCING PERFORMANCE AND NOISE

DESIGN FOR URBAN VERTICAL-AXIS WIND TURBINES: BALANCING PERFORMANCE AND NOISE

Dissertation

for the purpose of obtaining the degree of doctor
at Delft University of Technology
by the authority of the Rector Magnificus, Prof. dr. ir. T.H.J.J. van der Hagen,
chair of the Board of Doctorates
to be defended publicly on Thursday 7 March 2024 at 12:30

by

Livia BRANDETTI

Master of Science in Sustainable Energy Technology,
Delft University of Technology, the Netherlands
born in Rome, Italy.

This dissertation has been approved by the candidate's promotors

promotor: prof. dr. ir. J.W. van Wingerden
promotor: prof. dr. S. J. Watson
copromotor: dr. ir. S. P. Mulders

Composition of the doctoral committee:

Rector Magnificus,	chairperson
Prof. dr. ir. J.W. van Wingerden,	Delft University of Technology
Prof. dr. S. J. Watson,	Delft University of Technology
Dr. ir. S. P. Mulders,	Delft University of Technology

Independent members:

Prof. dr. ir. A. C. Viré,	Delft University of Technology
Dr. ir. A. Bianchini,	Università degli Studi di Firenze, Italy
Prof. dr. ir. D. Schlipf,	Hochschule Flensburg, Germany
Prof. dr. ir. T. Oomen,	Delft University of Technology
Dr. ir. D. Ragni,	Delft University of Technology, reserve member

A mia madre e a mio zio | To my mother and my uncle
perché il tempo e lo spazio | because time and space
non ci separano mai. | never separate us.

ACKNOWLEDGEMENTS

Ciao, dear reader; I am pretty sure you jumped to this section when you received this printed copy or downloaded the PDF. Acknowledgements are, in fact, the most read part of a PhD thesis. I still do not know why, but I guess that, in the end, we are just curious to learn more about a PhD's personal side, which otherwise would be left out. Therefore, the first thanks go to you, reader, for being curious about me. Enjoy the reading!

In August 2019, I started my PhD, and saying it was a smooth and easy journey would be a lie. There were countless moments when I found myself questioning the decision I made, doubting my research capabilities—a journey not unlike Ulysses navigating his way to Ithaca. Hence, and because I am a huge fan of epic poems, you'll encounter references to the Odyssey within the pages of this thesis. Unlike Ulysses, however, I had the fortune of being surrounded by one of the best crews with whom I sailed through this sea of research.

First and foremost, thanks to my promotors, Jan-Willem and Simon, and my copro-motor, Sebastiaan, for guiding me and always encouraging me throughout the past years. To Jan-Willem, thank you for your enthusiasm in doing research and for believing in me since day one, even if I had no control background. Every meeting was an occasion to challenge myself, absorb your experience as much as possible, and convince you that black slides are the future! Thank you for making me feel so welcome in your group and fostering a collaborative and supportive atmosphere, proving that academia can thrive without unnecessary competition. To Simon, thank you for your advice and your constant guidance. I will always be grateful for empowering me to make my own choices and voice my perspective. All our discussions became an opportunity for personal and professional growth. Sebastiaan, working with you has been a privilege. Your passion for research has been a constant source of inspiration, elevating my enthusiasm and motivation to finish this PhD. You were always there if I needed to chat, whether they were intended to be 5 minutes and turned into an hour. Thank you for being not only one of the best officemates but also a supportive friend with whom I could share both my highs and lows. Your taste-testing of my cakes and shared passion for techno have added an extra layer of joy to this journey. See you sooooon!

Thank you, Axelle, Alessandro, David and Tom, for being part of this committee and for the valuable advice and contributions provided during our discussions and preparations for today.

Today, two paranymphs will accompany me to defend this PhD: Clara and Stefano. Even though your personalities are quite the opposite, you have the common trait of being my dearest friends. Clara, we immediately clicked the first day we met in the Filtering and System Identification course. I was so amazed by this German girl speaking Italian so fluently that you also feel a bit Italian in the end. Thank you for standing beside

me throughout this seemingly never-ending journey. Your daily infusion of spice and creativity into our work life made every moment more bearable. Whether it was our dance breaks or sharing scientific divulgating YouTube videos, these moments became my refuge during the challenges of Covid and stressful periods. Reflecting on the women we were four years ago, I can confidently say we have grown together. While the journey has often been arduous, the trajectory to reach the end has been less bitter with you. Stefano, our connection dates back to 2012, and even then, I already knew how smart you were. In fact, you remain one of the most brilliant minds I have ever met. Our discussions could jump from stupid topics, like TV trash, to more interesting topics, like gender diversity, without recognising it, all while possibly engaging in an entire night of Monopoly. Thank you for being so rational and even more pessimistic than me when I needed to face the reality of things. Thank you both for your support and for being integral parts of this significant chapter in my life.

During this journey, I had the luck to work in two different sections: the Wind Energy (WE) in the Faculty of Aerospace Engineering and the Delft Center of Systems and Control (DCSC) in the Faculty of Mechanical Engineering. Here, I had the opportunity to work and meet with people who significantly contributed to my well-being on this journey.

Thank you to Sylvia for not only being the cornerstone in the WE section but for being a true friend during my time at TU Delft. You were there not only to help me with the daily bureaucracies but to comfort me when I felt that I could not make it. I will miss our daily break, but I am sure we will continue to meet afterwards! I extend my gratitude to all the secretaries and support staff at DCSC—Francy, Bo, Anna, Martha, and Sandra—for organising our Christmas dinner and Pub quiz! This thesis has not included the experimental work I conducted during my PhD. However, it is essential to acknowledge the invaluable assistance of the technicians who made these experiments possible. Special thanks to Stefan, Emiel, Frits, Dennis, Peter and Wim. Thank you to my officemates at WE: Yanan, Sharif, Abhratej, Hafiz and Evert. The days working on my PhD would not have been the same without you. A heartfelt acknowledgement goes to Delphine, one of my officemates, a great wind energy scientist, but also such a good friend to me. Delphine has been a constant support, seeing us through the challenges of the Covid era and beyond. However, our connection goes beyond shared struggles; we have created lasting memories, from conference trips to celebrating each other's weddings. Delphine, your friendship has added richness to my professional and personal journey; thank you! A round of applause to Dani e Fra, the Ficarra e Picone of the Aeroacoustics. Your motivation and ambition stimulated my interest in continuing research after my Master's thesis. You taught me that the Devil is in the details (and sometimes even around us), and I am deeply grateful for the role you have played as both mentors and friends, shaping my professional and personal growth. Your availability and readiness to assist with any challenges, coupled with your invaluable advice and support, have significantly impacted my PhD journey. Grazie! A big thank you goes to Edoardo, the cyclist. Our paths first crossed during our Master's thesis, and from there, we started the PhD, unsure of the challenges that awaited us (and perhaps, we still do not fully grasp them). Countless evenings were spent making that Matlab code run or setting up that PowerFLOW simulation on the cluster. With the same proportional ratio, we went for

drinks or organised dinners based on your homemade pizze fritte. I will never forget the mozzarella delivery during Covid and your crazy timing for catching a flight. Beyond being there to answer all my questions and filling my gaps in aerodynamics and aeroacoustics, you were a constant listener capable of bringing my anxiety level back to zero and my Tremonti bank account to red. Thank you for being not just a colleague but a trustworthy fellow on this challenging journey.

Throughout my research, I had the opportunity to collaborate on projects with different people who shared with me their invaluable experiences.

A heartfelt appreciation goes to Yichao. As the first person I collaborated with in DCSC, supervising a Master's student and working on my PhD, your passion for science has inspired and motivated me. Aside from being interested in my professional development, your genuine concern for my personal well-being has left a lasting impact. I hope we will have other opportunities to work together in the future. Special thanks to Daniel for embarking on the QBlade adventure with me. Despite the inevitable challenges of debugging and deciphering the latest updates, our perseverance always triumphed, allowing us to explore new ideas and make significant progress. Our collective efforts culminated in a QBlade tutorial, crafted after a fantastic trip to Berlin, aimed at fostering the software's use. This tutorial not only shares a new interface but also offers practical dos and don'ts—wisdom we would have wished for during our PhD days. A big shout-out goes to Roberto, one of the coauthors of my last journal paper, for allowing me to dig into the World of psychoacoustic annoyance. I have always admired your enthusiasm and spirit in research, and I wish more academics would be like you. Appreciation extends to Atin for his constant support throughout my exploration of control topics. I am so happy that we are both finishing our PhDs around the same time. I am sure you will be a great researcher, and I look forward to further collaborating with you! A warm thank you goes to Guido, who, despite being a recent addition to the group, has already enriched my experience. Thanks for all the insightful discussions and for challenging me on wind turbine aerodynamics.

Thank you to the rest of the people who crossed my path in WE and DCSC, whether for a beer, a coffee or a chat, for whom I am grateful. You made my PhD time unforgettable!

Thank you, Federica (for being so rational when I needed it the most), Claudia (for sharing my book passion), Cristina (for always being there with a smile when I needed it), Federico (for being a vintage lover just like me), Nitish (for the endless paddle matches), Emanuel (our cakes will surely cross our paths!), Maarten and Jingna (for wrapping up the thesis together), Cooooooeeeen (the most Italian Dutch friend I have), David (go go go!!), Daan (I will never forget the bubbles and the cleaning!), Marcus (for being one of the hardest critics of design and plot colouring), the techno ravers/DJs (Mees, Jonas and Rogier), Amr (Habibi!!), the fantastic aeroacoustic group (Andrea, Leandro, Tercio, Frits, Christopher, Gabriel, Fernanda, Jatinder, Emanuele and Hugo), Marion (for your Lord of the Rings interest), Simone (for your crazy flight passion), Sebastiano (for teaching me the basis of Formula 1), Rishi (aaaaa Rishiiii!!), Mihir (for being one of the best dancers I have ever met), Adhyanth (for being one of the best dancer haters I have ever met), Ming (for all the discussions about VAWTs), Helena (for the amazing trip in Copenaghen and for making me discover the World behind environmental psychology), Jelle (for teaching

me about kites), Deepali (for the laughs and the bus talks), Guanqun (for boosting my confidence with your nice words), Methab, Mark, Likhitha, Abhyuday, Ricardo, Matteo, Oriol, Andre, David, Kiran, Shyam, Donatella, Roland, Michiel, Jenna, Tim, Unai, Uwe, Zhixin, Alex, Emilio, Eva, Frida, Jean, Jesse, Bert, Matteo, Sachin, Dimitris, Manon, Kim, Riccardo.

Outside academia, I had the opportunity to meet some incredible people who allowed me to not think (too much) about my PhD research.

Thank you to Raffaello, my roommate in Delft and the first to share the TU Delft experience with me. Thank you for being such a good friend, always there to support me in this journey, giving me advice for my future career, and laughing until crying. Thank you, my dear Svetlana, my experience in Delft would not have been the same without you! Thank you to La Comune for being my second family here in Delft. I will never forget all the adventures together, from the trip to Portugal and Spain to the beers at Bowpub, the dinners at Mienette straat and the afterparties at Steck or De Kurk. Eddy, you have been one of the best friends I could have asked for, from the surprise birthday celebration to the graphics for the wedding and the unforgettable weekend in Piacenza. You, Cinzia and il Dani will always have a special place in my heart. Thank you to Meme for being an honest friend with whom I have had some of the most profound discussions, and Lore for all your polemiche. I am sure you, my talented friends, will be famous one day. Moment of advertising: listen to "I fatti di cronaca" on Spotify! Thank you, Andrea, for your encyclopedic knowledge, especially about the most absurd things, and for printing my first 3D VAWT. Thank you to Paolino e Pietrone, gli apostoli for me, for sharing the same level of discretion and for never showing off, even though you are brilliant minds. Thank you to Le Sgallettate, Amina and Marghe for helping me make the cover of my thesis, but most importantly, for being such dear friends to me with our burraco games and cinema discussions. I know you will be there for me to talk about anything. Francesca, as part of Le Sgallettate, deserves special mention. Amica mia, words cannot fully express my gratitude for having you in my life since our Delft days. Our shared experiences, from sunsets to dance festivals, tears, and the right dose of anxiety, have created a bond that feels like a lifetime. "Con la consapevolezza di esserci sempre l'una per l'altra e la sensazione di conoscerci da una vita". Grazie, ti voglio bene! You and Silvia are part of what I call home. Two other people, Marco and Andrea, entered my Delft life in 2016, for whom I am grateful. The life spent together amounts to 100 years, as Marco used to say, filled with beautiful memories. Although we no longer share the same city, I know I can always count on your friendship. Thank you! Special thanks to Marianna, my fashion twin, for sharing a passion for vintage clothes and curating one of the most beautiful vintage shops in Rotterdam. Thank you for showing me we can be engineers, even with an inspiring fashion style. Thank you to Carolina for her understanding and support. Your brilliance is evident to all who know you, and I feel incredibly fortunate to have someone like you, whom I call a true friend. We navigated this PhD journey together, and your empathy for the challenges encountered is especially meaningful to me. Your encouragement has been the fuel that kept me going, and your advice has been a guiding light.

Thanks to my family and friends in Rome, a distance of 1.634 km is nothing for us!

To Francesca, or should I call you Vecchia Jane, for inspiring me with your creativity and making me feel so proud to be the cousin of such a great artist. We have shared many, maybe too many, beers in Delft while wondering if you could move to Galapagos (by the way, it is never too late!). That beautiful Dawson Creek day in Scheveningen, Cuchi, will forever hold a special place in my heart! To Fabby and Cri, for making me feel like the little genius of the family. Your mutual love and respect have consistently served as a guiding value for me to admire. To Leonardo, even though you may never read this (but your parents will), thank you for revealing a new side of myself. I have never considered myself a warm person, but I discovered my sweetest side with you. Thank you, patatone! A mia zia Tullia, grazie per avermi insegnato che una tavola apparecchiata con buon gusto dovrebbe essere un must anche per un pranzo veloce. Sei la Csaba che tutti vorrebbero! Grazie per aver condiviso con me uno dei momenti più magici della mia vita, la scelta del mio abito dei sogni. E anche se vuoi fare la dura, lo so che ti emozionerai a leggere queste parole. A Cinzia, grazie per aver sempre creduto in ogni mia decisione e per aver reso questi anni in Olanda più sopportabili a suon di lasagne e polpette. Le serate passate a riempire il freezer prima della tua partenza, mentre guardavamo Amici, sono tra i ricordi più dolci che conservo. Grazie di cuore! To Ludovica, your support during my toughest moments means the World to me. Thank you for your ability to understand me without a single word spoken. Your example has taught me the indispensable value of determination and hard work in shaping one's future. To my dear friends from high school: Lavinia, my romanista ultras and my apina, Conny, the suocera per eccellenza, and Giampaolo, the doctor. Even though we have decided to follow different paths, our friendship has only strengthened. I am so lucky to have you in my life and share many beautiful memories with you (soprattutto le ciotole rotte!). To Francesco, Emanuele and Damiano, our friendship has stood the test of time since our primary school days. I am grateful for the certainty that you will be right beside me no matter how many years pass. Thank you for the joy and support we share in each other's success and, yes, even the occasional failures. To Maria Luisa, my twin sister, for sharing with me the passion for dance. Since I moved to the Netherlands, I have always missed you and our time spent in the dance room at the barre. Witnessing the incredible woman you have become fills me with immense pride, especially in your role as a fantastic dance teacher. Doing lessons together after 7 years has been a dream coming true. Thank you for your unconditional love and understanding; your friendship means everything to me! To Irene, my adventurous friend, a heartfelt thank you for being a supportive companion who truly understands the challenges and joys of pursuing a PhD. Your presence and friendship have been a constant encouragement, even when physical distance kept us apart. To Sofia, one of my dearest friends, for being a constant in my growth since I was 13 years old. We have followed different trajectories in our lives and never lived in the same city. However, our reunions feel timeless, as if time has stood still. The depth of our conversations is inversely proportional to how many hours we sleep. Thank you for being there in every important step of my life!

Thanks to all the rest of my friends in Rome and around the World. You are simply amazing!

Last but certainly not least, heartfelt gratitude goes to the sunshine of my life—three

extraordinary individuals who not only believe in me more than I do but also unwaveringly support my decisions, filling me with pride.

To my sister, one of the most brilliant women in science I know, your passion and dedication to your work not only earned my deep admiration but have also fueled my scientific aspirations. You are my role model, showcasing strength even when the world seems to fall apart. Your resilience is my constant inspiration. Ti voglio bene. A mio papà, la persona più solare e incredibile che conosca, grazie per esserci sempre con il tuo sorriso contagioso e la tua instancabile voglia di fare. Mi hai insegnato il valore dell'amicizia e l'importanza di esplorare il mondo attraverso i viaggi, soprattutto se bisogna fare mille chilometri a piedi. Grazie a te ho imparato ad affrontare le sfide della vita con un coraggio sovraumano, senza mai abbattersi, e che solo avendo un animo buono e puro come il tuo si può rimanere per sempre nel cuore delle persone. Ti voglio bene. To Ale, my husband and life partner, who has been involved in this research journey since day one. Thank you for not just enduring but engaging with my countless presentations (at the point of knowing them by heart), for our escapes from our Dutch routine through travel, and for sharing in the joy of cooking and baking. Your constant presence has been my anchor through uncertain times, guiding me back to Earth when my mind was flying away with paranoids. You are the perfect circle in my otherwise square life. Ti amo.

Livia Brandetti
Delft, January 2024

TABLE OF CONTENTS

SUMMARY

Wind energy is crucial for addressing the escalating global energy demands and reducing greenhouse gas emissions. While offshore wind capacity is growing rapidly, onshore sites remain essential, accounting for three-quarters of wind turbine installations. In particular, urban areas are seeing a sustainable evolution for effectively integrating small-scale wind turbines.

Conventionally, horizontal-axis wind turbines (HAWTs) have dominated the urban wind energy market. However, their performance is often suboptimal when placed atop buildings or close to houses due to high turbulence levels and obstacles. Vertical-axis wind turbines (VAWTs) can exploit these wind conditions due to their inherent omnidirectionality, making them a suitable candidate for urban deployment.

Despite significant progress in urban VAWTs, extensive multidisciplinary research is needed to optimise their efficiency and use in such environments. This literature gap motivates the current research in developing analysis and design methods for urban VAWTs, trading-off energy capture, actuation effort and noise acceptance. To this end, this dissertation focuses on four aspects:

1. Developing a low-fidelity noise model based on state-of-the-art literature, allowing fast and acceptable accurate predictions for preliminary design stages of the main noise sources on an urban VAWT;

2. Designing a wind speed estimator and tip-speed ratio (WSE-TSR) tracking controller to maximise the power production of an urban VAWT in turbulent wind conditions, which turned out to be an ill-posed problem, impacting the turbine and controller performance in the presence of model uncertainty;

3. Presenting an approach that combines frequency-domain analysis and multi-objective optimisation, demonstrating its effectiveness in assessing and calibrating torque control strategies, thereby contradicting earlier assumptions and establishing new perspectives on performance optimisation for real-world wind turbines;

4. Deriving a decision-making framework capable of striking a balance between VAWT performance and noise acceptance, allowing for the first time to consider psychoacoustic annoyance as a metric.

The present dissertation identifies and tackles four challenges to fulfil this goal. First, the lack of a rigorous evaluation of aerodynamic and acoustic models for urban VAWT is solved by assessing the existing literature against high-fidelity simulations and experimental data on a two-bladed VAWT. In particular, the high-fidelity database allows for studying the complex relation between unsteady aerodynamics and far-field noise. It is confirmed that the choice of the aerodynamic polar and the occurrence of 3D effects, blade-blade interactions, flow separation and tower shadow affect the prediction of the angle of attack

and the blade-effective wind speed, and consequently of the aerodynamic performance. These limitations are reflected in the acoustic predictions. However, by coupling the Actuator Cylinder with semi-empirical noise models, the resulting low-fidelity model is shown to accurately estimate the aerodynamics and acoustics of a VAWT with a low computational time suitable for the preliminary design stages.

Based on the stringent requirements for maximising the power production of a VAWT when operating in urban conditions, this dissertation further explores the feasibility of applying a WSE-TSR tracking controller on an urban VAWT by means of a comprehensive study of its working mechanisms. The analysis demonstrates that the control scheme suffers from the ill-conditioning problem. Specifically, due to a lack of information in the controller, the wind speed cannot be uniquely estimated from the product with other model parameters in the power balance equation. By applying a frequency-domain framework, the ill-conditioning problem is shown to be exacerbated in the presence of model uncertainty, leading to biased wind speed estimates, erroneous tracking of the optimal aerodynamic performance, and, hence, reduced energy capture.

This discovery and the more complex performance requirements of present-day wind turbines have led to a review of previous studies, which claim an increased power production of 1 to 3% with the WSE-TSR tracking control scheme without providing an in-depth analysis of its dynamics. Therefore, a comparative investigation between the considered controller and the baseline $K\omega^2$ on a modern onshore wind turbine is undertaken with the proposed frequency-domain framework to evaluate the stability and performance characteristics of the controlled system. This framework is coupled with a multi-objective optimisation approach, as the direct correlation of actual turbine performance with the linear framework using traditional control theory is challenging, and there is currently no established systematic way for calibrating the considered controller. The resulting optimal solutions, balancing power and actuation effort objectives, are assessed in the frequency domain to relate control parameter insights to indicative performance metrics. Contrary to previous findings, the results demonstrate that the optimally calibrated WSE-TSR tracking control strategy does not enhance power capture but introduces a trade-off between torque control variance and power capture with control bandwidth.

Finally, these collective insights and the importance of considering residents in urban areas prompt the development of a multi-objective optimisation framework for an urban VAWT. This framework addresses the critical trade-off between operational performance and noise emissions from the perspective of controller calibration, aiming to foster community engagement and social acceptance while optimising VAWT performance in turbulent and fluctuating wind conditions. For the first time, noise annoyance is considered in the design and decision-making process, employing psychoacoustic annoyance as an indicator to satisfy the noise objective. This sound metric has proven to offer a more reliable estimate of the human perception of wind turbine noise. Leveraging the flexibility of the WSE-TSR tracking controller, the optimal set of controller calibration solutions is determined by solving a multi-objective optimisation problem based on Pareto front approximations. Employing a multi-criteria decision-making method (MCDM), the trade-off solutions that balance power, load, and psychoacoustic annoyance are identified and compared with the baseline $K\omega^2$ controller. Through the assessments of these MCDM results with a frequency-domain framework and mid-fidelity aero-servo-elastic simulations,

the performance benefits of using the WSE-TSR tracking controller for urban VAWTs are identified, providing guidelines for future designers for VAWTs in urban environments.

The combined contributions of this thesis drive advancements in comprehending the intricate dynamics of VAWTs, with a specific focus on the human acoustic perception in proximity to these turbines, thereby setting a foundation for integrating VAWTs into urban environments.

SAMENVATTING

Windenergie is van cruciaal belang voor het aanpakken van de escalerende mondiale vraag naar energie en het terugdringen van de uitstoot van broeikasgassen. Terwijl de capaciteit van wind op zee snel groeit, blijven locaties op land essentieel, omdat ze driekwart van de windturbine-installaties vertegenwoordigen. Met name stedelijke gebieden zien een duurzame ontwikkeling voor de effectieve integratie van kleinschalige windturbines.

Conventioneel hebben windturbines met horizontale as (HAWT's) de stedelijke windenergiemarkt gedomineerd. Hun prestaties zijn echter vaak niet optimaal wanneer ze bovenop gebouwen of dicht bij huizen worden geplaatst vanwege de hoge turbulentieniveaus en obstakels, wat leidt tot hoge energiekosten. Windturbines met verticale as (VAWT's) kunnen deze windomstandigheden benutten vanwege hun inherente omnidirectionaliteit, waardoor ze een geschikte kandidaat zijn voor stedelijke inzet.

Ondanks aanzienlijke vooruitgang bij stedelijke VAWT's is uitgebreid multidisciplinair onderzoek nodig om de efficiëntie en het gebruik ervan in dergelijke omgevingen te optimaliseren. Dit gat in de literatuur motiveert het huidige onderzoek naar de ontwikkeling van geïntegreerde analyse- en ontwerpmethoden voor stedelijke VAWT's om een balans te bereiken tussen energieafvang, turbinebelastingen en geluidsacceptatie. Om dit te bereiken richt dit proefschrift zich op vier aspecten:

1. Ontwikkeling van een low-fidelity geluidsmodel gebaseerd op de modernste literatuur, dat snelle en nauwkeurige voorspellingen mogelijk maakt van de belangrijkste geluidsbron op een stedelijke VAWT;

2. Formulering van het probleem van slechte conditionering voor de windsnelheidsschatter en tipsnelheidsratio (WSE-TSR) trackingcontroller, vaak toegepast om de energieproductie van windturbines in turbulente windomstandigheden te maximaliseren, waarbij de impact ervan op de prestaties van turbines en controllers wordt benadrukt in aanwezigheid van modelonzekerheid;

3. Het presenteren van een aanpak die frequentiedomeinanalyse en optimalisatie met meerdere doelstellingen combineert, waarbij de effectiviteit ervan wordt aangetoond bij het beoordelen en kalibreren van koppelcontrolestrategieën, waardoor eerdere aannames worden tegengesproken en een nieuw perspectief wordt gecreëerd op prestatie-optimalisatie voor echte windturbines;

4. Afleiding van een besluitvormingskader dat in staat is een evenwicht te vinden tussen VAWT-prestaties en geluidsacceptatie, waardoor psycho-akoestiche hinder voor het eerst als maatstaf kan worden beschouwd.

Het huidige proefschrift identificeert en pakt vier uitdagingen aan om dit doel te bereiken. Ten eerste wordt het gebrek aan een rigoureuze evaluatie van aerodynamische

en akoestische modellen voor stedelijke VAWT opgelost door de bestaande literatuur te vergelijken met high-fidelity simulaties en experimentele gegevens over een tweebladige VAWT. Met name de high-fidelity database maakt het mogelijk om de complexe relatie tussen tijdsafhankelijke aerodynamica en verre veldruis te bestuderen. Er wordt bevestigd dat de keuze van de aerodynamische polair en het optreden van 3D-effecten, blad-blad-interacties, stromingsscheiding en torenschaduw de voorspelling van de invalshoek en de blad-effectieve windsnelheid beïnvloeden, en bijgevolg van de aerodynamische prestaties. Deze beperkingen worden weerspiegeld in de akoestische voorspellingen. Door de actuatorcilinder echter te koppelen aan de semi-empirische geluidsmodellen, wordt aangetoond dat het resulterende low-fidelity-model de aerodynamica en akoestiek van een VAWT nauwkeurig schat met een lage rekentijd die geschikt is voor de voorlopige ontwerpfasen.

Gebaseerd op de strenge eisen voor het maximaliseren van de energieproductie van een VAWT bij gebruik in stedelijke omstandigheden, onderzoekt dit proefschrift verder de haalbaarheid van het toepassen van een WSE-TSR-trackingcontroller op een stedelijke VAWT door middel van een uitgebreide studie van de werkingsmechanismen ervan. De analyse toont aan dat het controleschema lijdt onder het probleem van slechte conditionering. Door een gebrek aan informatie in de controller kan de windsnelheid met name niet op unieke wijze worden geschat op basis van het product met andere modelparameters in de vermogensbalansvergelijking. Door een kader in het frequentiedomein toe te passen, wordt aangetoond dat het probleem van slechte conditionering wordt verergerd in de aanwezigheid van modelonzekerheid, wat leidt tot vertekende schattingen van de windsnelheid, het foutief volgen van de optimale aerodynamische prestaties en dus een verminderde energieopbrengst.

Deze ontdekking en de complexere prestatie-eisen van hedendaagse windturbines hebben geleid tot een overzicht van eerdere onderzoeken, die een verhoogde energieproductie van 1 tot 3% claimen met het WSE-TSR tracking control-schema zonder een diepgaande analyse te bieden. van zijn dynamiek. Daarom wordt een vergelijkend onderzoek uitgevoerd tussen de beschouwde controller en de $K\omega^2$ referentie op een moderne windturbine op land met het voorgestelde frequentiedomeinraamwerk om de stabiliteit en prestatiekenmerken van het aangestuurde systeem te evalueren. Dit raamwerk is gekoppeld aan een multi-objectieve optimalisatiebenadering, omdat de directe correlatie van de daadwerkelijke turbineprestaties met het lineaire kader met behulp van de traditionele regeltheorie een uitdaging is, en er momenteel geen gevestigde systematische manier is om de betreffende controller te kalibreren. De resulterende optimale oplossingen, het balanceren van het vermogen en de doelstellingen voor de activeringsinspanning, worden beoordeeld in het frequentiedomein om inzichten in controleparameters te relateren aan indicatieve prestatiestatistieken. In tegenstelling tot eerdere bevindingen tonen de resultaten aan dat de optimaal gekalibreerde WSE-TSR-trackingcontrolestrategie de vermogensopname niet verbetert, maar een compromis introduceert tussen koppelregelingsvariantie en vermogensopname met controlebandbreedte.

Ten slotte leiden deze collectieve inzichten en het belang van het rekening houden met bewoners in stedelijke gebieden tot de ontwikkeling van een optimalisatiekader met meerdere doelstellingen voor een stedelijke VAWT. Dit kader richt zich op de kritieke wisselwerking tussen operationele prestaties en geluidsemissies vanuit het perspectief

van kalibratie van de controller, met als doel de betrokkenheid van de gemeenschap en sociale acceptatie te bevorderen en tegelijkertijd de VAWT-prestaties in turbulente en fluctuerende windomstandigheden te optimaliseren. Voor het eerst wordt geluidshinder meegenomen in het ontwerp- en besluitvormingsproces, waarbij psycho-akoestische hinder als indicator wordt gebruikt om aan de geluidsdoelstelling te voldoen. Het is gebleken dat deze geluidsmetriek een betrouwbaardere schatting biedt van de menselijke perceptie van windturbinegeluid. Door gebruik te maken van de flexibiliteit van de WSE-TSR-trackingcontroller, wordt de optimale set controllerkalibratieoplossingen bepaald door het oplossen van een optimalisatieprobleem met meerdere doelstellingen op basis van Pareto-frontbenaderingen. Met behulp van een multi-criteria besluitvormingsmethode (MCDM) worden de afwegingsoplossingen die macht, belasting en psycho-akoestische hinder in evenwicht brengen, geïdentificeerd en vergeleken met de $K\omega^2$ referentiecontroller. Door de beoordelingen van deze MCDM-resultaten met een frequentiedomeinkader en mid-fidelity aero-servo-elastische simulaties worden de prestatievoordelen van het gebruik van de WSE-TSR-trackingcontroller voor stedelijke VAWT's geïdentificeerd, wat richtlijnen biedt voor toekomstige ontwerpers van VAWT's in stedelijke gebieden.

De gecombineerde bijdragen van dit proefschrift zorgen voor vooruitgang in het begrijpen van de ingewikkelde dynamiek van VAWTs, met een specifieke focus op de menselijke akoestische perceptie in de nabijheid van deze turbines, waardoor een basis wordt gelegd voor de integratie van VAWTs in stedelijke gebieden.

1

INTRODUCTION

Poh! disse Giove, incolperà l'uom dunque | Pshaw! said Jupiter, will man then always
sempre gli Dei? Quando a se stesso i mali | blame the gods? When he himself constructs
fabbrica, de' suoi mali a noi dà carco, | his own miseries, he burdens us with his woes,
e la stoltezza sua chiama destino | and his own foolishness he calls destiny

Odissea, libro I, versi 49-52 | Odyssey, book I, lines 49-52

This chapter presents the introduction to this dissertation, offering insights into the research
context, key challenges, objectives, and outline. It comprises five sections, each contributing
to a comprehensive understanding of the research's scope. The first section emphasises
the importance of onshore locations, mainly urban, for the future of wind energy. The
second section outlines the potential advantages of vertical-axis wind turbines (VAWTs) in
urban environments, supported by real-world case studies to illustrate their practicality
and effectiveness. Then, in the third section, the challenges of analysing VAWTs from an
aero-acoustic-servo-elastic point of view are discussed. Transitioning to the fourth section,
the overall thesis goal, delineated into sub-goals, is presented alongside the approach
employed for their realisation. Finally, the concluding section illustrates the thesis structure
through a summary outline of the contents of each chapter.

1.1. THE IMPORTANCE OF URBAN WIND ENERGY

The escalating global energy consumption and the urgency to mitigate greenhouse gas emissions have boosted the transition from a fossil fuel-dependent to a sustainable society. Among various renewable energy sources, wind energy has emerged as a pivotal player in meeting the rising demand for clean energy on a global scale [1]. The worldwide installed wind power capacity stands at 906 GW in 2023 and shows a consistent annual growth rate of 9% [2].

Notably, the offshore wind sector garners substantial attention due to its abundant wind resources, facilitating the deployment of large-scale wind turbines with capacities of approximately 8 MW [3]. Nevertheless, the role of onshore sites remains paramount for the spread of wind energy, as confirmed by the number of new wind turbine installations from 2017 to 2027, illustrated in Figure 1.1. Particularly noteworthy is that in 2022, onshore installations accounted for 16.7 GW of wind capacity, whereas offshore installations amounted to only 2.5 GW. Looking ahead to Europe's prospects for 2023-2027, the forecast entails 129 GW of newly installed wind turbines, with three-quarters of this capacity installed onshore [4].

Onshore wind energy sites can be categorised into rural and urban areas. Large-scale wind turbines are preferred for installations in open fields far from cities [5]. These turbines feature rotor diameters ranging from 20 m to 100 m and power generation capacities spanning 200 kW to 3 MW, with a clear trend towards an ongoing upscaling in both rated power and dimensions [6]. Spatial limitations generally constrain the feasibility of installing such large wind turbines within urban environments. An urban environment is defined as a densely built-up settlement compared to the surrounding area [7]. However, the potential for scaling down wind turbines exists, albeit with a consequential reduction in power generation [8]. Thus, small-scale wind turbines offer the opportunity to deploy wind energy within urban areas, facilitating direct energy production at the point of consumption [9]. Such installations contribute significantly to energy-efficient practices
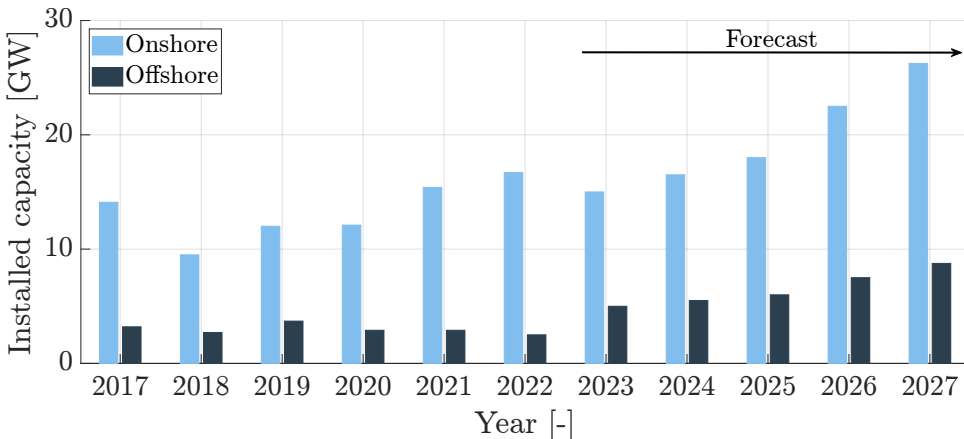

Figure 1.1: Overview of onshore and offshore wind turbine installations in Europe for the period between 2017 and 2027. This graph is reproduced from Ref. [4].

in the design of new buildings [10].

The exploration of urban wind energy has captured growing attention from urban planners, architects and engineers, all invested in fostering the sustainable evolution of urban landscapes and enhancing the well-being of urban inhabitants [5]. Extensive research is being conducted to identify suitable locations for effectively integrating small-scale wind turbines in urban environments [11]–[13]. Locating small rotors at the top of tall buildings enables the harnessing of higher wind speeds that are typically inaccessible to standard turbine towers [10]. Wind turbines are optimally positioned on the tallest structure, as far as possible from surrounding buildings, to mitigate unpredictable wind patterns [7].

1.2. THE CASE FOR VERTICAL-AXIS WIND TURBINES

While conventional horizontal-axis wind turbines (HAWTs) dominate building installations, their performance is influenced by the urban wind conditions [14], characterised by low speeds, high variability, elevated turbulence levels, and inclined or even reversed airflows [9]. Vertical-axis wind turbines (VAWTs) offer a promising alternative for urban installation owing to their inherent omnidirectionality that renders them less susceptible to changes in wind direction [1]. This advantage obviates the need for a yaw motor, a costly component for small wind turbines [15], [16]. As can be recognised from their name, the vertical rotational axis of VAWTs offers a larger design space than HAWTs, generating various cylindrical actuation surfaces that create a complex three-dimensional force field. This expanded swept area confers an advantage within urban locations, allowing greater freedom in energy extraction [17], [18] and, consequently, higher power densities than HAWTs [19], [20]. Moreover, siting the generator at ground level enhances accessibility and reduces maintenance costs for VAWTs [21]. Additionally, VAWTs are visually more appealing and emit less noise than HAWTs [22], [23], making them a favourable choice for urban wind energy applications.

VAWTs can be classified as either lift-driven or drag-driven. The latter has existed in various forms for centuries, such as the well-known Savonius design from 1922 [24]. They typically feature rounded paddles with a convex shape, creating a difference in drag between the upwind and downwind sides during rotation, resulting in a torque [25]. Although drag-driven turbines have limited efficiency (a power coefficient below 0.3), they offer advantages such as self-starting and high power output at low wind speeds [26]. On the other hand, lift-driven turbines rely on the aerodynamic lift created by the pressure difference due to the shape of the blade to generate torque and, as a result, are more efficient than drag machines [27].

Because of their higher power coefficients, Darrieus VAWTs are one of the most suitable turbines for rooftop integration [28]. Georges Darrieus invented the first lift-driven vertical-axis wind turbine in France during the 1920s [29]. The Darrieus patent covers two configurations: the Φ-shaped and H-shaped rotors. The first one has curved blades mounted directly to the vertical torque tube (i.e. the rotating shaft, which also serves as the support structure). This configuration ensures that the blades are constantly under tension, potentially improving structural performance and reducing blade weight. In contrast, the second one features straight or helical blades connected to the shaft by struts. A recent study of Darrieus wind turbines has shown good self-startup abilities, making

this turbine even more suitable for installation in urban areas [30].

Examples of vertical-axis wind turbines installed in urban areas are illustrated in Figure 1.2. The Lincoln Financial Field stadium in Philadelphia, United States, featured the installation of fourteen H-Darrieus VAWTs with helical blades situated on opposing walls and generating a combined power output of 3 MW along with 11,000 solar panels [31]. However, the specific power production data for these VAWTs remains undisclosed, and they were dismantled in 2019 after a service period since 2011. Notably, no information has been provided regarding their subsequent placement or official reasons for removal [5].

Further instances of VAWT applications mounted on top of buildings include the installation of five 100 W Savonius VAWTs, resembling tulips designed by Flower Turbines B.V. [32], and the 300 W Savonius Airturb [33], both located on distinct rooftops in Rotterdam, The Netherlands. The Delft University of Technology also designed an H-Darrieus VAWT with helical blades, namely the Turby, with a power capacity of 2.5 kW; however, this design failed to secure commercial utilisation [34].

Different use of VAWTs within urban environments is represented by the Hybrid Wind-Solar Power Generator CPH 200 W, developed by Cygnus Power [35]. This configuration combines two solar panels with an H-Darrieus VAWT with straight blades. Interestingly, this concept's commercial implementation has been predominantly observed along streets, exemplified by its installation in Tokyo, Japan. In the sphere of building-integrated wind turbines, there are two remarkable instances. Firstly, the Pearl River Tower in Guangzhou, China, features four Savonius VAWTs designed by SOM [36]. Secondly, the Newbery Tower in Glasgow, United Kingdom, showcases the incorporation of six CrossFlex Φ-Darrieus VAWTs[37], further underscoring the integration of wind turbines with architectural form.

1.3. Challenges in the aero-acoustic-servo-elastic analysis of VAWTs

Research on VAWTs in urban areas has grown in recent years [38]. Most research effort has focused on isolated aspects, such as blade aerodynamics [39]–[41] or structural design [42]–[44]. While these investigations provide valuable insights into specific aspects of VAWT performance, they fall short of offering a comprehensive understanding of the potential of this technology in urban settings. To fully unlock the advantages of VAWTs for the future of urban wind energy, it is imperative to undertake a holistic analysis that considers multiple facets of turbine operation, including aerodynamics, aeroacoustics, aeroelastics and controller strategies.

A comprehensive analysis encompassing these critical elements is essential for several reasons. Firstly, it enables a more accurate assessment of VAWT performance in real-world urban conditions, where challenges such as turbulence and variable wind direction play significant roles [12]. Secondly, it allows the development of advanced control strategies explicitly tailored to urban VAWT applications to find an ideal trade-off between energy capture, actuation effort, and noise emissions.

However, it is essential to acknowledge that challenges may arise when conducting such a comprehensive analysis. Addressing these challenges is pivotal to the widespread

1

Figure 1.2: Overview of vertical-axis wind turbines (VAWTs) in urban environments. Seven of the fourteen H-Darrieus VAWTs with helical blades installed on the Lincoln Financial Field stadium in Philadelphia (USA) [31], five 100 W Flower Turbines [32] installed on a rooftop in Rotterdam (NL) (Photo by M. van den Broek), the 300 W Airturb wind turbine designed by Airturb [33], the 2.5 kW Turby designed by Delft University of Technology [34], the Hybrid Wind-Solar Power Generator CPH 200 W [35] installed in the street of Tokyo (JP) (Photo by L. Brandetti), one of the four Savonius VAWTs installed in the Pearl River Tower in Guangzhou (CN) [36] and the six CrossFlex VAWTs installed on the Newbery Tower in Glasgow (UK) [37].

adoption of VAWTs in urban environments. This section illustrates the challenges encountered in the aero-acoustic-servo-elastic analysis of a VAWT that are addressed in this thesis. Each subsection presents the relevant literature and closes with the formulation of the thesis-driven challenges.

First, the lack of consensus on how noise generation mechanisms are modelled in these turbines is discussed. Then, the need for a controller capable of maximising power production while minimising the actuation effort when the VAWT operates in a turbulent environment is presented. Then, there follows an overview of methods for analysing and optimally calibrating the proposed wind turbine torque control strategy to assess potential advantages compared to a baseline control scheme. Finally, the focus shifts to the substantial obstacle of achieving community acceptance for urban VAWT integration. Emphasis is placed on the challenge of predicting the impact of wind turbine noise on nearby residents, stressing the importance of a controller capable of balancing turbine performance with noise acceptance metrics.

1.3.1. Modelling noise generation mechanisms of a VAWT

A major challenge when analysing a VAWT in an urban environment is correctly modelling its noise generation mechanisms [45]. Noise emitted by a wind turbine can be categorised into two primary sources: aerodynamic and mechanical. Mechanical noise arises from the dynamic response of the moving mechanical components within the turbine, whereas aerodynamic noise results from the interaction between the airflow and the turbine blades [46]–[49]. While the reduction of mechanical noise has seen significant effort, the focus of current research has shifted towards modelling and estimating aerodynamic noise [50].

Aerodynamic noise, further classified into Turbulence-Interaction (T-I) noise and airfoil-self noise, presents distinct challenges for accurate prediction. For estimating T-I noise generated when incoming turbulent flow interacts with the leading edge of the blade, an accurate characterisation of turbulent flow properties, including spectral energy content and the integral length scale of fluctuations, is needed [48], [51]. This aspect becomes particularly critical for a VAWT in an urban environment where the turbulent flow can be either induced by free-stream turbulence or self-generated, as seen in the wake-airfoil interactions [52]. Furthermore, T-I noise becomes dominant at high tip-speed ratios and high turbulence intensities due to the interaction between the turbulent near wake of one blade and the following one. However, the existing literature lacks an accurate model for T-I noise. Discrepancies between existing models and experimental data, such as the mismatch of up to 10 dB reported by Botha et al. [52] and Pearson [22] for the QR5 rotor, further underscore the need for improved noise prediction methodologies.

Conversely, for the airfoil-self noise generated by a blade in a smooth flow, only two of the five mechanisms are considered relevant for a VAWT in an urban environment: Turbulent Boundary Layer - Trailing Edge (TBL-TE) noise and Laminar Boundary Layer - Vortex Shedding (LBL-VS) [47]. At high Reynolds numbers ($Re > 5 \times 10^5$), TBL-TE noise is emitted due to the scattering of the turbulent pressure fluctuations convecting over the sharp trailing edge. LBL-VS noise is generated as tonal noise when the shear layer separates, creating coherent vortices. This noise source is expected to dominate in scenarios characterised by low Reynolds numbers ($Re \leq 5 \times 10^5$) and low tip-speed ratios,

further exacerbated by dynamic stall [22], [45].

Comparative evaluations of TBL-TE noise modelling, using both the Brooks, Pope, and Marcolini (BPM) approach [47] and the TNO model [53], [54] by Botha et al. [52], have underlined the need for a tailored low-fidelity model. The BPM model underestimates the sound pressure levels, whereas the TNO model marginally overpredicts. In addition, attempts to model LBL-VS noise with the BPM model have identified tonal peaks in the 1×10^3 Hz - 2×10^3 Hz frequency range for full-scale rotors [22]. However, these models fall short of replicating experimental observations, as evidenced by the findings of Dyne [55], mainly due to the assumption of steady incoming flow in the BPM model.

In light of these complex noise generation mechanisms in VAWTs in urban environments and the substantial discrepancies between existing models and experimental data, the following challenge is posed.

Challenge I: Assess the state-of-the-art low-fidelity noise models against high-fidelity simulations to solve the lack of a comprehensive and accurate noise prediction analysis model for a VAWT in an urban environment.

1.3.2. CONTROL STRATEGIES FOR VAWTS

Existing control strategies face limitations in optimising the energy production of a VAWT in an urban environment, primarily due to the intrinsic turbulent and fluctuating winds [1]. These varying flow conditions can give rise to dynamic stall, which reduces power production, hinders self-starting capabilities at low wind speeds and prevents overspeeding during high winds [56], [57]. One promising solution lies in active flow control, mainly through plasma actuators. Recent research by Jafari et al. [58] investigated the impact of dielectric barrier discharge plasma actuators on aerodynamic efficiency, revealing both potential benefits and negative aerodynamic effects. These effects are particularly evident in small-scale VAWTs designed for urban environments with small chord lengths and low Reynolds numbers. However, the high installation and maintenance costs associated with these blade surface flow actuators hamper their commercial deployment.

An alternative approach to maximise power production in VAWTs involves pitch control strategies, which can be categorised as active or passive. Active pitch entails optimising the blade pitch angle using actuators, while passive pitch control allows the blades to rotate freely or through a mechanical system that aligns them to the wind direction [59]. Passive pitch control faces challenges in generating the required torque, making it less practical in low-wind urban environments. On the other hand, active pitch control methods [60]–[62] have succeeded under specific wind conditions but have fallen short in terms of versatility in fluctuating wind conditions.

Many existing VAWT designs lack flexibility for blade modifications or implementing pitch control systems. Thus, developing advanced control systems is crucial to safeguard against mechanical and electrical damage. A study conducted by Andriollo et al. [63] compared various control strategies for a 12 kW VAWT, focusing on constant-mechanical-power and constant-torque controllers. Their findings favoured the constant-mechanical-power strategy for maximising power production but noted efficiency trade-offs, resulting in unstable rotor speeds during high winds. Conversely, the constant-torque strategy

faced overspeeding problems and failed to maximise power production.

In this context, the combined wind speed estimator and tip-speed ratio (WSE-TSR) tracking controller, originally designed for HAWTs by Bossanyi [64], emerges as a potential solution. The WSE-TSR tracking controller forces the turbine to operate at the maximum power coefficient corresponding to a specific tip-speed ratio and pitch angle [65]. To track the optimal operating point and extract the maximum power, the pitch angle is kept constant and the estimated rotor-effective wind speed (REWS) [66], [67] is used to estimate the desired rotor speed. This control scheme has shown promising results in optimising the power production for VAWTs in the urban environment, characterised by turbulent wind conditions.

Eriksson et al. [68] successfully applied the WSE-TSR tracking controller to an H-Darrieus VAWT using the generated power and rotational speed measurements, combined with an aerodynamic efficiency look-up table, to estimate the REWS and the desired operating point. Most importantly, this control strategy eliminates the need for direct wind speed measurements, using the VAWT as an anemometer, favouring a reduction of overall turbine costs. Furthermore, Bonaccorso et al. [69] modified the original formulation of the WSE-TSR tracking controller by employing an Extended Kalman Filter [67] to estimate REWS, eliminating the need for mechanical sensors measuring the rotational speed and consequently reducing turbine costs.

Overall, the WSE-TSR tracking controller has demonstrated good dynamic performance in tracking the optimal operating point, maximising the power production of a VAWT even in turbulent wind conditions. Despite its potential, a detailed study of the working mechanisms of the WSE-TSR tracking controller, especially in the context of VAWTs in urban environments, is absent in the existing literature. Of particular interest is investigating the controller performance when uncertainty occurs in the internal model parameters. These deviations from the actual aerodynamic properties of the wind turbine, further influenced by factors such as blade erosion or residue build-up [70], could lead to biased wind speed estimates, resulting in sub-optimal turbine operation by the WSE-TSR tracking controller. Therefore, the following challenge is formulated.

Challenge II: Explore the feasibility of implementing a WSE-TSR tracking controller through a comprehensive analysis of its working mechanisms to maximise power production on a VAWT in an urban environment. This analysis should consider scenarios for model uncertainty, acknowledging deviations that arise from real-world factors.

1.3.3. ANALYSING AND CALIBRATING WIND TURBINE CONTROLLERS

Modern wind turbines, particularly VAWTs in urban environments, exhibit complex and diverse design characteristics with a broad spectrum of performance requirements. The $K\omega^2$ controller, renowned for its simplicity and steady-state efficiency, has effectively been used to maximise energy capture of wind turbines in the partial load region [70], [71]. However, as wind turbine technology continues to advance, the need for a flexible control strategy capable of balancing power maximisation and actuation effort minimisation has become increasingly evident. Consequently, the combined WSE-TSR tracking controller has garnered attention in the wind industry [72] for its potential to address this demand and improve turbine performance even in turbulent wind conditions, making it the

1

perfect candidate for urban VAWTs.

One critical issue currently faced in wind turbine control is the lack of a systematic calibration method for the WSE-TSR tracking controller. The changing dynamics associated with the scaling up of modern wind turbines has introduced additional complexities in the calibration process, posing challenges when relying solely on traditional control theory. In light of this evolution, it is essential to revisit established methodologies to ensure their applicability to current wind turbines, especially VAWTs operating in urban areas. Existing conclusions may no longer fully capture the intricate turbine performance optimisation requirements.

Therefore, it is vital to evaluate whether previous findings regarding the advantages of the WSE-TSR tracking controller over the baseline $K\omega^2$ controller remain valid. Earlier research claimed energy capture benefits ranging from 1 to 3% with a manually calibrated WSE-TSR tracking controller compared to the baseline $K\omega^2$ [64]. Additionally, Boukhezzar and Siguerdidjane [73] noted a remarkable 10% improvement in power capture when using a Kalman filter estimator combined with rotor speed reference tracking in comparison to the $K\omega^2$ controller, albeit without providing an analytical demonstration of its dynamic behaviour. Another study by Abbas et al. [74] focused only on a time-domain analysis when comparing the combined estimator-feedback controller with the $K\omega^2$ control law. No effort has been undertaken to provide insights into the complex dynamics of the WSE-TSR tracking control scheme or to present a comprehensive comparison of the steady-state and dynamic characteristics between the baseline $K\omega^2$ and the considered controller.

In addition, when analysing and calibrating such controllers, addressing the increasing complexity of wind turbine technologies and the limitations of conventional control theory is crucial. Multi-objective optimisation techniques based on Pareto fronts have proven highly effective in calibrating wind turbine controllers. Odgaard et al. [75] showcased a systematic tuning approach based on a Pareto front, which optimises a model predictive controller by balancing the divergent objectives of power maximisation and actuation effort minimisation. Similarly, Lara et al. [76] proposed a Pareto optimisation approach using multi-objective optimisation to calibrate an adaptive pitch controller, integrating a range of objectives to minimise tower fore-aft displacements and generator speed deviations.

All these approaches recognise that achieving optimal turbine performance extends beyond mere power capture and encompasses a comprehensive range of objectives. The optimal solutions derived from this multi-objective optimisation define a balance between the conflicting objectives and influence the selection of a specific control bandwidth. Despite the shift towards a multi-objective optimisation framework, frequency-domain analysis remains an essential tool for assessing the stability and performance of closed-loop systems. As Leith and Leithead [77] demonstrated, analysing a controller in the frequency domain provides relevant insights into its performance.

Consequently, applying a frequency-domain framework to evaluate the optimal solutions derived from the multi-objective optimisation enables the connection of conflicting control objectives with the stability and performance of the closed-loop system. This combined approach offers a deeper understanding of the interplay between performance metrics and control dynamics, enabling WSE-TSR tracking control scheme users to make

well-informed decisions regarding its optimal calibration.

Given the predominance of research focused on HAWTs, selecting a reference turbine design used in the literature as a state-of-the-art benchmark for onshore locations becomes necessary when analysing and calibrating the WSE-TSR tracking controller. In this context, evaluating the potential benefits of the considered controller with respect to the $K\omega^2$ controller should be based on two performance metrics widely discussed in the literature: power maximisation and actuation effort minimisation [77], [78]. These findings can then be translated to VAWTs operating in urban environments. Based on these observations, the following challenge is posed.

Challenge III: Evaluate the potential benefits of employing a WSE-TSR tracking control strategy compared to a baseline controller in achieving a trade-off between power maximisation and actuation effort minimisation for a reference turbine design.

1.3.4. TAKING INTO ACCOUNT TURBINE NOISE ACCEPTANCE IN URBAN ENVIRONMENTS

While wind energy shows promise as a sustainable alternative to conventional fossil fuels, its practical implementation often encounters local resistance, particularly in densely populated urban areas [79]. This localised lack of acceptance remains a global challenge, hindering the progress of wind energy technology in urban environments [80].

Extensive research has been conducted to identify the factors contributing to local opposition against wind energy projects [81], [82]. Notably, concerns revolve around wind turbine noise annoyance. The noise generated by wind turbines can detrimentally affect the well-being of nearby residents [83]. Despite wind turbines typically exposing individuals to lower sound pressure levels than other community noise sources like aircraft, a higher proportion of people experience significant annoyance due to wind turbine noise, indicating a more pronounced relationship between noise exposure and annoyance [84]. Consequently, as the demand for wind energy continues to grow, noise regulations for wind turbines are becoming increasingly stringent, further exacerbating the challenge.

Although some studies suggest potential indirect health effects associated with wind turbine noise [85]–[87], this claim is not universally supported [88]. Nonetheless, it is imperative to acknowledge this concern during the decision-making process, as it may result in operational restrictions, such as nighttime turbine shutdowns, potentially reducing turbine power output and revenue generation [89], [90]. Bottasso et al. [91] have demonstrated that a power curve tracking controller can limit noise emissions without requiring turbine shutdown, albeit at the cost of reduced power generation. Thus, when considering the controller for a VAWT in an urban area, it should address the trade-off between power production and noise emissions.

Predicting the impact of wind turbine noise on nearby residents remains a complex task, influenced by factors such as wind speed, direction, distance from the observer, the number of turbines, and background noise [92]. Traditionally, the A-weighted sound pressure level has been applied as an indicator to describe sound exposure in a general and highly averaged way [50]. Nevertheless, this metric falls short of assessing wind turbine annoyance comprehensively. For instance, according to Persson Waye and Agge [93],

1

HAWT noise with tonal components and a dominant high-frequency component (frequency exceeding 1×10^3 Hz) was perceived as more annoying compared to those lacking tonal components and having a stronger low-frequency content, even when both had identical A-weighted sound pressure levels. Therefore, relying solely on conventional indicators may overlook critical aspects of noise perception.

Recent studies have proposed alternative approaches, such as logarithmic noise propagation functions and assessments based on the inverse square law, to estimate sound impact accurately [94], [95]. These methods consider distance from residences and sound pressure levels, offering a more comprehensive understanding of noise impact. However, these approaches still rely on the use of sound pressure levels, which quantify the purely physical magnitude of sound without accounting for the subjective perception of sound by human hearing [96].

A significant advancement in recent decades is the ability to auralize environmental acoustical scenarios, enabling the artificial recreation of audible situations from numerical data [97]. Auralization offers the potential to provide a more accurate representation of wind turbine noise and its impact on communities [98]. Several studies have successfully auralized wind turbine noise scenarios, creating realistic listening experiences. For example, Pieren et al. [99] reconstructed the audio signals of two HAWTs from their synthesised wind turbine noise, obtaining a close resemblance to the original turbine sound recordings. Merino-Martinez et al. [100] introduced a novel holistic approach for the perception-based evaluation of wind turbine noise and the efficacy of reduction measures, using synthetic sound auralization. The feasibility of the approach has been demonstrated using four state-of-the-art noise reduction trailing-edge add-ons applied synthetically to two 2 MW HAWTs at three observer locations.

While progress has been made in assessing the noise annoyance of HAWTs, a noticeable gap exists in evaluating the perception of VAWTs and developing control strategies that effectively balance the maximisation of turbine performance metrics with the minimisation of noise annoyance for residents. Consequently, the following challenge is posed.

Challenge IV: Analyse and optimally calibrate the WSE-TSR tracking controller for a VAWT, leveraging the insights obtained from the reference turbine design. The controller should find the optimal trade-off between the conflicting objectives of power capture, actuation effort and noise to facilitate the development of VAWTs in urban areas.

1.4. THESIS OBJECTIVE AND RESEARCH QUESTIONS

The previous section explained four key challenges, the resolution of which is the focus of this research. These challenges reveal an evident gap in how VAWTs are analysed in urban environments. To harness the full potential of these turbines, a multidisciplinary approach is needed to gain deeper insights into various aspects of turbine operation, encompassing aerodynamics, aeroacoustics, aeroelasticity, and controller strategies. This integrated analysis holds paramount importance for several reasons. Firstly, it allows for a more precise assessment of VAWT performance under real-world urban conditions, where factors like turbulence and variable wind directions exert significant influence. Secondly, it empowers the development of advanced control strategies finely tailored to

1

urban VAWT applications, optimising energy capture while minimising actuation effort and mitigating perceived noise annoyance.

Through this multifaceted exploration, this thesis seeks to uncover the feasibility and potential of VAWTs in urban environments, with a specific emphasis on achieving an optimal balance between turbine performance and noise acceptance metrics. In light of this discussion, the goal of this thesis is defined as follows:

Thesis goal: Develop an integrated analysis and design methods for urban vertical-axis wind turbines (VAWTs) incorporating advanced control, aerodynamic, aeroacoustic and aeroelastic models, trading off energy capture, actuation effort and noise acceptance.

Acknowledging the breadth and comprehensiveness of this thesis goal, the primary objective is subdivided into subgoals, each aligned with the earlier-discussed challenges. The corresponding text provides the necessary contextualisation and a strategic roadmap for achieving these objectives.

Given the potential installation of VAWTs in urban environments, where noise regulations impose constraints, applying low-fidelity modelling becomes essential to account for noise throughout the design phase. This approach allows for estimating noise generation mechanisms during VAWT operation while significantly reducing the computational time, a crucial factor during the design phase. However, the current body of literature lacks accurate noise modelling, leading to discrepancies between models and experimental data. Toward the development of a low-fidelity noise prediction analysis model for an urban VAWT, the following research question is formulated:

I: How can a low-fidelity noise prediction model be developed to advance the state-of-the-art in predicting noise emitted by VAWTs and achieve acceptable accuracy for the preliminary design stage?

The combined wind speed estimator and tip-speed ratio (WSE-TSR) tracking control scheme, initially designed for HAWTs, represents a promising solution to maximise the power production of VAWTs in urban environments, where turbulent and fluctuating winds challenge existing control strategies. In this framework, the measured generator torque and rotational speed of the wind turbine are used to estimate the rotor-effective wind speed (REWS) and calculate an estimate of the tip-speed ratio. This estimate is fed back to the controller, which, acting on the difference between the estimated and reference tip-speed ratio, ensures that the turbine operates at the rotor operating point for maximum power extraction efficiency. Several studies have applied and modified this controller to VAWTs, obtaining higher efficiency in power extraction and thus reducing the levelised cost of energy (LCoE).

However, despite its numerous advantages, an in-depth investigation of the operational mechanisms of the WSE-TSR tracking controller for urban VAWTs is lacking. Notably, an analysis of the controller performance in the presence of uncertainty in the internal model parameters holds significant interest, as these deviations from the actual aerodynamic properties of the turbine are further exacerbated over time. Inaccuracies in the power coefficient mapping could result in a biased estimation of the REWS, thereby

causing the real-world wind turbine to deviate from its optimal operating point. For this reason, the following research question is formulated:

> **II:** Can the WSE-TSR tracking control strategy offer a viable solution to balance power maximisation for an urban VAWT, even in the presence of model uncertainty?

The challenge in implementing the WSE-TSR tracking controller lies in the absence of a systematic optimal calibration method, complicated by the controller's nonlinearity and high reliance on prior model information. This shortcoming is becoming even more relevant as modern wind turbines evolve, introducing complexities in the analysis and calibration of torque control strategies and, in turn, raising questions about the applicability of traditional control theory. Therefore, it is essential to reevaluate established methodologies to ensure their suitability for contemporary wind turbines, especially VAWTs in urban areas. In particular, there is the need to assess previous claims regarding the advantages of the WSE-TSR tracking controller over the $K\omega^2$ controller, commonly employed as a baseline.

To this end, analysing a controller in the frequency domain allows the gathering of relevant insights into its performance. At the same time, multi-objective optimisation techniques have proven effective in calibrating wind turbine controllers, emphasising the required balance between complex optimisation objectives. These observations suggest that applying a frequency-domain framework to evaluate the optimal solutions derived from solving a multi-objective problem enables the connection between performance metrics and the stability and performance of the closed-loop system. This approach aims to address the following research question:

> **III:** What are the potential performance benefits of the WSE-TSR tracking controller compared to a baseline control scheme considering relevant power and actuation effort objectives on a reference turbine design?

Introducing wind turbines in urban areas often triggers local resistance, primarily due to noise annoyance concerns. This raises the importance of addressing noise-related complaints during decision-making, as they may result in operational restrictions and reduced power generation. Predicting the impact of wind turbine noise on residents is complex, influenced by various external factors, like wind conditions. Traditional sound pressure level indicators only provide a limited understanding of noise perception, often overlooking critical aspects of human hearing.

A significant advancement in the field is the ability to auralize wind turbine noise scenarios by artificially rendering an acoustical situation audible from numerical data. Auralization offers the potential for a more accurate representation of how local communities perceive wind turbine noise in urban environments. However, a gap exists in assessing the noise annoyance caused by VAWTs and developing control strategies to balance turbine performance and noise annoyance. Therefore, the following research question is posed:

1

> **IV:** How can the insights obtained from subquestions/challenges **I**, **II** and **III** be effectively leveraged to evaluate the feasibility of the WSE-TSR tracking controller for a VAWT in an urban environment in achieving an optimal trade-off between performance and noise acceptance metrics?

The six chapters encompassed within this thesis can be read independently since they are unrelated in a mathematical context. Each chapter establishes its own set of symbol definitions. An introductory section precedes each chapter, providing the context for readers to engage with the material effectively.

1.5. THESIS OUTLINE

This section presents the outline of this thesis, illustrated in Figure 1.3. Each paragraph summarises the content of each chapter.

Chapter 2 evaluates the state-of-the-art low-fidelity methods against high-fidelity simulations for a small-scale VAWT in an urban environment with available experimental data. Following this assessment, a novel low-fidelity noise model is developed, enabling accurate VAWT aerodynamics and acoustics prediction for preliminary design stages.

Chapter 3 introduces the wind turbine torque control strategy, specifically the combined wind speed estimator and tip-speed ratio (WSE-TSR) tracking controller. Its primary aim is to enhance power extraction efficiency on a small-scale VAWT in an urban area. The working mechanisms of the proposed controller are evaluated in-depth with a frequency-domain framework. The analysis reveals the inherent ill-conditioning problem within the control scheme. This problem is formalised, and simulation results confirm that inaccuracies in model parameters yield biased estimations of the actual turbine operating state, ultimately leading to sub-optimal turbine performance.

Chapter 4 explores, in the wake of the previous chapter, the potential benefits of the WSE-TSR tracking controller over a baseline control strategy. The analysis extends the previously described frequency-domain framework. The proposed controller is optimally calibrated, balancing power maximisation and actuation effort reduction objectives. The multi-objective optimisation is solved by approximating a Pareto front using the optimal solutions obtained through exploratory searches in the controller parameter space. Frequency and time domain evaluations of these optimal solutions are conducted on a reference turbine design that adheres to onshore large-scale standards. In particular, the frequency-domain analysis assesses the stability and performance characteristics of the controlled system using fundamental control theory and relates these insights to relevant performance metrics. This calibration framework facilitates the identification of WSE-TSR tracking controller design variables that effectively satisfy the power-actuation effort trade-off.

Chapter 5 aims to validate preceding findings on a small-scale VAWT, enhancing its efficiency and advancing its urban applicability. Considering potential community opposition to wind projects, noise annoyance, along with power maximisation and actuation

1

effort minimisation, serves as a new objective function for WSE-TSR tracking controller calibration. Noise annoyance is computed using a psychoacoustic annoyance model based on sound quality metrics coupled with the low-fidelity prediction tool from Chapter 2. The multi-objective optimisation framework allows Pareto fronts to be found, showcasing the trade-off between these control objectives and providing insights into turbine performance and its impact on noise acceptance metrics.

Chapter 6 serves as a comprehensive consolidation of the findings of this thesis, alongside providing recommendations for future work. The presentation of this summary aligns with the structure of the research questions posed earlier.
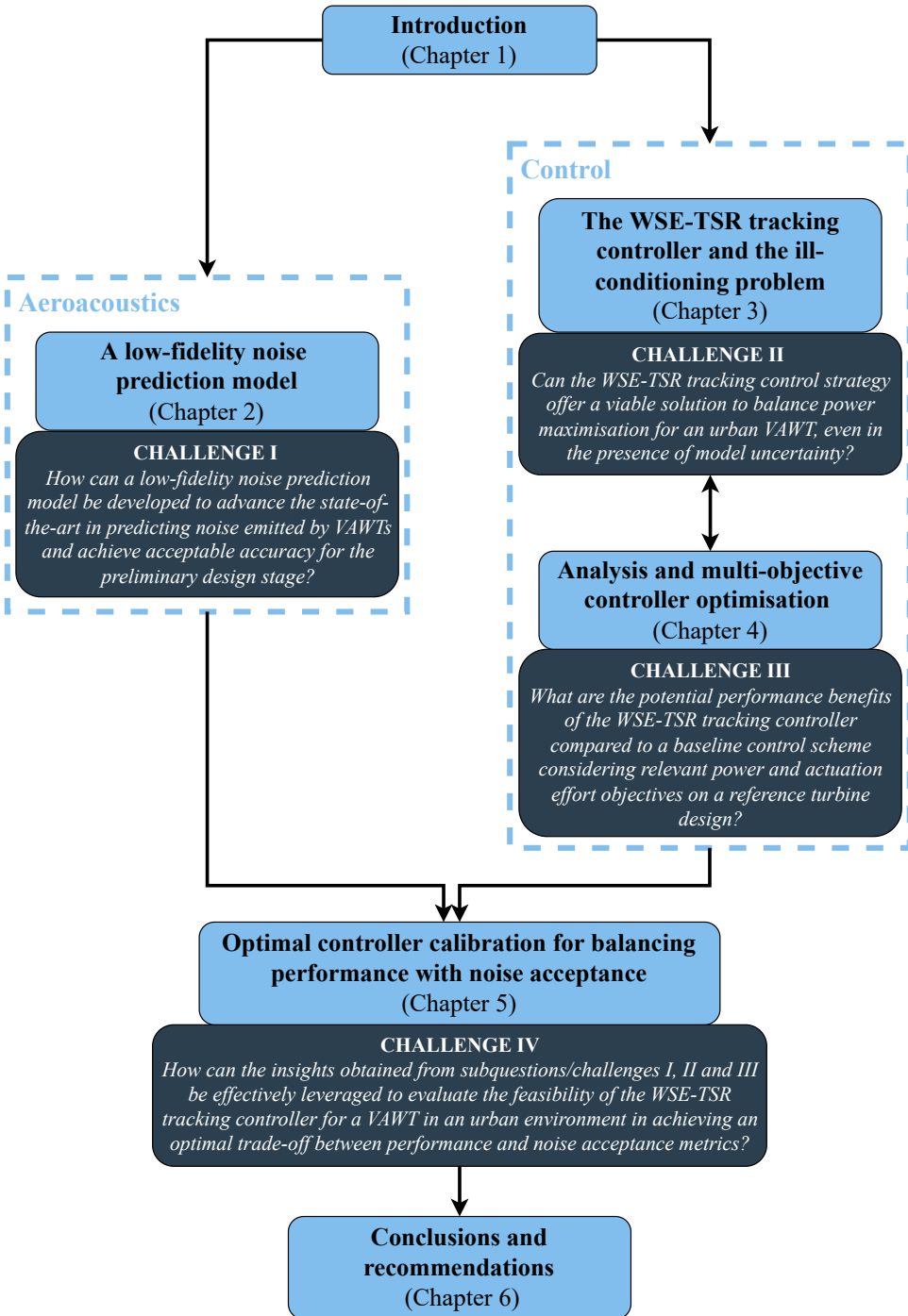
Introduction
(Chapter 1)

Aeroacoustics

A low-fidelity noise prediction model
(Chapter 2)

CHALLENGE I
How can a low-fidelity noise prediction model be developed to advance the state-of-the-art in predicting noise emitted by VAWTs and achieve acceptable accuracy for the preliminary design stage?

Control

The WSE-TSR tracking controller and the ill-conditioning problem
(Chapter 3)

CHALLENGE II
Can the WSE-TSR tracking control strategy offer a viable solution to balance power maximisation for an urban VAWT, even in the presence of model uncertainty?

Analysis and multi-objective controller optimisation
(Chapter 4)

CHALLENGE III
What are the potential performance benefits of the WSE-TSR tracking controller compared to a baseline control scheme considering relevant power and actuation effort objectives on a reference turbine design?

Optimal controller calibration for balancing performance with noise acceptance
(Chapter 5)

CHALLENGE IV
How can the insights obtained from subquestions/challenges I, II and III be effectively leveraged to evaluate the feasibility of the WSE-TSR tracking controller for a VAWT in an urban environment in achieving an optimal trade-off between performance and noise acceptance metrics?

Conclusions and recommendations
(Chapter 6)

Figure 1.3: Thesis outline

BIBLIOGRAPHY

[1] S. Watson, A. Moro, V. Reis, C. Baniotopoulos, S. Barth, G. Bartoli, F. Bauer, E. Boelman, D. Bosse, A. Cherubini, A. Croce, L. Fagiano, M. Fontana, A. Gambier, C. Gkoumas K.and Golightly, M. I. Latour, P. Jamieson, J. Kaldellis, A. Macdonald, J. Murphy, M. Muskulus, F. Petrini, L. Pigolotti, F. Rasmussen, P. Schild, R. Schmehl, N. Stavridou, J. Tande, N. Taylor, T. Telsnig, and R. Wiser, "Future emerging technologies in the wind power sector: A European perspective", *Renewable and Sustainable Energy Reviews*, vol. 113, 2019. DOI: 10.1016/j.rser.2019.109270. [Online]. Available: https://doi.org/10.1016/j.rser.2019.109270.

[2] M. Hutchinson and F. Zhao, "Global Wind Report 2023", Tech. Rep., 2023. [Online]. Available: https://gwec.net/wp-content/uploads/2023/03/GWR-2023_interactive_v2_compressed.pdf.

[3] L. Ramirez, "Offshore wind energy: 2023 statistics", Tech. Rep., 2023. [Online]. Available: https://windeurope.org/intelligence-platform/product/offshore-wind-in-europe-key-trends-and-statistics-2022/.

[4] G. Costanzo, G. Brindley, and P. Cole, "Wind energy in Europe: 2022 Statistics and the outlook for 2023-2027", Wind Europe, Tech. Rep., 2023. [Online]. Available: https://windeurope.org/intelligence-platform/product/wind-energy-in-europe-2022-statistics-and-the-outlook-for-2023-2027/#downloads.

[5] K. Kwok and G. Hu, "Wind energy system for buildings in an urban environment", *Journal of Wind Engineering and Industrial Aerodynamics*, vol. 234, 2023. DOI: 10.1016/j.jweia.2023.105349. [Online]. Available: https://www.sciencedirect.com/science/article/pii/S0167610523000521.

[6] P. Veers, K. Dykes, E. Lantz, S. Barth, C. L. Bottasso, O. Carlson, A. Clifton, J. Green, P. Green, H. Holttinen, D. Laird, V. Lehtomäki, J. K. Lundquist, J. Manwell, M. Marquis, C. Meneveau, P. Moriarty, X. Munduate, M. Muskulus, J. Naughton, L. Pao, J. Paquette, J. Peinke, A. Robertson, J. S. Rodrigo, A. M. Sempreviva, J. C. Smith, A. Tuohy, and R. Wiser, "Grand challenges in the science of wind energy", *Science*, vol. 366, no. 6464, 2019. DOI: 10.1126/science.aau2027. [Online]. Available: https://www.science.org/doi/10.1126/science.aau2027.

[7] T. Stathopoulos, H. Alrawashdeh, A. Al-Quraan, B. Blocken, A. Dilimulati, M. Paraschivoiu, and P. Pilay, "Urban wind energy: Some views on potential and challenges", *Journal of Wind Engineering and Industrial Aerodynamics*, vol. 179, pp. 146–157, 2018. DOI: 10.1016/j.jweia.2018.05.018. [Online]. Available: https://www.sciencedirect.com/science/article/pii/S0167610517304774.

1

[8]   P. Škvorc and H. Kozmar, "Wind energy harnessing on tall buildings in urban environments", *Renewable and Sustainable Energy Reviews*, vol. 152, 2021. DOI: 10.
1016/j.rser.2021.111662. [Online]. Available: https://www.sciencedirect.
com/science/article/pii/S1364032121009370.

[9]   A. Bianchini, G. Bangga, I. Baring-Gould, A. Croce, J. I. Cruz, R. Damiani, G. Erfort,
C. Simão Ferreira, D. Infield, C. N. Nayeri, G. Pechlivanoglou, M. Runacres, G.
Schepers, B. Summerville, D. Wood, and A. Orrell, "Current status and grand
challenges for small wind turbine technology", *Wind Energy Science*, vol. 7, no. 5,
pp. 2003–2037, 2022. DOI: 10.5194/wes-2022-34. [Online]. Available: https:
//wes.copernicus.org/articles/7/2003/2022/.

[10] F. Balduzzi, A. Bianchini, and L. Ferrari, "Microeolic turbines in the built environment: Influence of the installation site on the potential energy yield", *Renewable
Energy*, vol. 45, pp. 163–174, 2012. DOI: 10.1016/j.renene.2012.02.022. [Online]. Available: https://www.sciencedirect.com/science/article/pii/
S0960148112001619.

[11] F. Toja-Silva, A. Colmenar-Santos, and M. Castro-Gil, "Urban wind energy exploitation systems: Behaviour under multidirectional flow conditions—opportunities
and challenges", *Renewable and Sustainable Energy Reviews*, vol. 24, pp. 364–
378, 2013. DOI: 10.1016/j.rser.2013.03.052. [Online]. Available: https:
//www.sciencedirect.com/science/article/pii/S1364032113002116.

[12] A. Rezaeiha, H. Montazeri, and B. Blocken, "A framework for preliminary large-
scale urban wind energy potential assessment: Roof-mounted wind turbines",
Energy Conversion and Management, vol. 214, 2020. DOI: 10.1016/j.enconman.
2020.112770. [Online]. Available: https://www.sciencedirect.com/science/
article/pii/S0196890420303083.

[13] M. Anbarsooz and M. Amiri, "Towards enhancing the wind energy potential at the
built environment: Geometry effects of two adjacent buildings", *Energy*, vol. 239,
2022. DOI: 10.1016/j.energy.2021.122351. [Online]. Available: https://
www.sciencedirect.com/science/article/pii/S0360544221026001.

[14] N. Mithraratne, "Roof-top wind turbines for microgeneration in urban houses in
new zealand", *Energy and Buildings*, vol. 41, no. 10, pp. 1013–1018, 2009. DOI:
10.1016/j.enbuild.2009.05.003. [Online]. Available: https://www.
sciencedirect.com/science/article/pii/S037877880900098X.

[15] D. Song, X. Fan, J. Yang, A. Liu, S. Chen, and Y. Hoon Joo, "Power extraction efficiency optimization of horizontal-axis wind turbines through optimizing control
parameters of yaw control systems using an intelligent method", *Applied Energy*,
vol. 224, pp. 267–279, 2018. DOI: 10.1016/j.apenergy.2018.04.114. [Online]. Available: https://www.sciencedirect.com/science/article/pii/
S0306261918306755.

[16] D. Song, J. Yang, X. Fan, Y. Liu, A. Liu, G. Chen, and Y. Hoon Joo, "Maximum
power extraction for wind turbines through a novel yaw control solution using
predicted wind directions", *Energy Conversion and Management*, vol. 157, pp. 587–

599, 2018. DOI: 10.1016/j.enconman.2017.12.019. [Online]. Available: https://www.sciencedirect.com/science/article/pii/S0196890417311676.

[17] V. F.-C. Rolin and F. Porté-Agel, "Experimental investigation of vertical-axis wind-turbine wakes in boundary layer flow", *Renewable Energy*, vol. 118, pp. 1–13, 2018. DOI: 10.1016/j.renene.2017.10.105. [Online]. Available: https://www.sciencedirect.com/science/article/pii/S0960148117310753.

[18] S. H. Hezaveh, E. Bou-Zeid, J. Dabiri, M. Kinzel, G. Cortina, and L. Martinelli, "Increasing the power production of vertical-axis wind-turbine farms using synergistic clustering", *Boundary-Layer Meteorology*, vol. 169, pp. 1–22, 2018. DOI: 10.1007/s10546-018-0368-0. [Online]. Available: https://rdcu.be/dfU7q.

[19] J. O. Dabiri, "Potential order-of-magnitude enhancement of wind farm power density via counter-rotating vertical-axis wind turbine arrays", *Journal of Renewable and Sustainable Energy*, vol. 3, no. 4, 2011. DOI: 10.1063/1.3608170. [Online]. Available: https://doi.org/10.1063/1.3608170.

[20] L. C. Pagnini, M. Burlando, and M. P. Repetto, "Experimental power curve of small-size wind turbines in turbulent urban environment", *Applied Energy*, vol. 154, pp. 112–121, 2015. DOI: 10.1016/j.apenergy.2015.04.117. [Online]. Available: https://www.sciencedirect.com/science/article/pii/S0306261915005802.

[21] S. Eriksson, H. Bernhoff, and M. Leijon, "Evaluation of different turbine concepts for wind power", *Renewable and Sustainable Energy Reviews*, vol. 12, pp. 1419–1434, 2008. DOI: 10.1016/j.rser.2006.05.017. [Online]. Available: https://doi.org/10.1016/j.rser.2006.05.017.

[22] C. Pearson, "Vertical Axis Wind Turbine Acoustics", Ph.D. dissertation, Corpus Christi College Cambridge University, 2013. [Online]. Available: https://doi.org/10.17863/CAM.14070.

[23] E. Möllerström, F. Ottermo, J. Hylander, and H. Bernhoff, "Noise emission of a 200 kw vertical axis wind turbine", *Energies*, vol. 9, no. 1, 2016. DOI: 10.3390/en9010019. [Online]. Available: https://www.mdpi.com/1996-1073/9/1/19.

[24] B. N. Owen, *The Wind Power Story: A Century of Innovation that Reshaped the Global Energy Landscape*, J. W. Sons, Ed. 2019. DOI: 10.1002/9781118794289. [Online]. Available: https://onlinelibrary.wiley.com/doi/book/10.1002/9781118794289.

[25] V. J. Modi and M. S. U. K. Fernando, "On the performance of the savonius wind turbine", *Journal of Solar Energy Engineering*, vol. 111, no. 1, pp. 71–81, Feb. 1989. DOI: 10.1115/1.3268289. [Online]. Available: https://doi.org/10.1115/1.3268289.

[26] J. F. Manwell, J. Mcgowan, and A. L. Rogers, *Wind Energy Explained - Theory, Design and Application*, Second, Wiley, Ed. 2009, ISBN: 9780470015001.

1

1

[27] E. Möllerström, P. Gipe, J. Beurskens, and F. Ottermo, "A historical review of vertical axis wind turbines rated 100 kw and above", *Renewable and Sustainable Energy Reviews*, vol. 105, pp. 1–13, 2019. DOI: 10.1016/j.rser.2018.12.022. [Online]. Available: https://www.sciencedirect.com/science/article/pii/S1364032118308153.

[28] F. Balduzzi, A. Bianchini, E. A. Carnevale, L. Ferrari, and S. Magnani, "Feasibility analysis of a darrieus vertical-axis wind turbine installation in the rooftop of a building", *Applied Energy*, vol. 97, pp. 921–929, 2012. DOI: 10.1016/j.apenergy.2011.12.008. [Online]. Available: https://doi.org/10.1016/j.apenergy.2011.12.008.

[29] G. J. M. Darrieus, *Turbine having its rotating shaft transverse to the flow of the current*, 1931.

[30] N. Batista, R. Melício, V. M. F. Mendes, M. Calderón, and A. Ramiro, "On a self-start darrieus wind turbine: Blade design and field tests", *Renewable and Sustainable Energy Reviews*, vol. 52, pp. 508–522, 2015. DOI: 10.1016/j.rser.2015.07.147. [Online]. Available: https://www.sciencedirect.com/science/article/pii/S1364032115007947.

[31] S. E. Solution. "Lincoln financial field". (2019), [Online]. Available: http://www.sunoraenergy.com/ (visited on 08/14/2023).

[32] F. T. BV. "Flower turbine". (2019), [Online]. Available: https://www.flowerturbines.com/ (visited on 06/30/2023).

[33] A. B.V. "Airturb". (2018), [Online]. Available: https://airturb.com/ (visited on 06/30/2023).

[34] H. Polinder, G. van Bussel, and M. Dubois, "Design of a pm generator for the turby, a wind turbine for the built environment", Sep. 2004. [Online]. Available: https://www.researchgate.net/publication/262643110_Design_of_a_PM_generator_for_the_Turby_R_a_wind_turbine_for_the_built_environment.

[35] C. Power. "02 product types". (2008), [Online]. Available: http://cygnuspower.koreasme.com/business/producttype_02.html (visited on 08/14/2023).

[36] SOM. "Pearl river tower". (2013), [Online]. Available: https://www.som.com/projects/pearl-river-tower/ (visited on 08/14/2023).

[37] T. Sharpe and G. Proven, "Crossflex: Concept and early development of a true building integrated wind turbine", *Energy and Buildings*, vol. 42, no. 12, pp. 2365–2375, 2010. DOI: 10.1016/j.enbuild.2010.07.032. [Online]. Available: https://www.sciencedirect.com/science/article/pii/S0378778810002653.

[38] R. Kumar, K. Raahemifar, and A. S. Fung, "A critical review of vertical axis wind turbines for urban applications", *Renewable and Sustainable Energy Reviews*, vol. 89, pp. 281–291, 2018. DOI: 10.1016/j.rser.2018.03.033. [Online]. Available: https://www.sciencedirect.com/science/article/pii/S1364032118301254.

[39] C. Simão Ferreira, G. van Kuik, G. van Bussel, and F. Scarano, "Visualization by PIV of dynamic stall on a vertical axis wind turbine", *Experiments in Fluids*, no. 46, pp. 97–108, 2009. DOI: 10.1007/s00348-008-0543-z. [Online]. Available: https://doi.org/10.1007/s00348-008-0543-z.

[40] A. C. Molina, G. Bartoli, and T. de Troyer, "Wind tunnel testing of small vertical-axis wind turbines in turbulent flows", *Procedia Engineering*, vol. 199, pp. 3176–3181, 2017. DOI: 10.1016/j.proeng.2017.09.518. [Online]. Available: https://www.sciencedirect.com/science/article/pii/S1877705817340286.

[41] B. LeBlanc and C. Simão Ferreira, "Estimation of blade loads for a variable pitch Vertical Axis Wind Turbine with strain gage measurements", *Wind Energy*, pp. 1–16, 2022, ISSN: 10991824. DOI: 10.1002/we.2713. [Online]. Available: https://doi.org/10.1002/we.2713.

[42] C. Galinos, T. J. Larsen, H. A. Madsen, and U. S. Paulsen, "Vertical axis wind turbine design load cases investigation and comparison with horizontal axis wind turbine", *Energy Procedia*, vol. 94, pp. 319–328, 2016. DOI: 10.1016/j.egypro.2016.09.190. [Online]. Available: https://www.sciencedirect.com/science/article/pii/S1876610216308426.

[43] F. Ahsan, D. T. Griffith, and J. Gao, "Modal dynamics and flutter analysis of floating offshore vertical axis wind turbines", *Renewable Energy*, vol. 185, pp. 1284–1300, 2022. DOI: 10.1016/j.renene.2021.12.041. [Online]. Available: https://www.sciencedirect.com/science/article/pii/S0960148121017614.

[44] W. Deng, Y. Guo, L. Liu, Y. Li, Y. Jiang, and P. Xie, "Dynamic response analysis of a floating vertical axis wind turbine with helical blades based on the model test", *Ocean Engineering*, vol. 273, 2023. DOI: 10.1016/j.oceaneng.2023.113930. [Online]. Available: https://www.sciencedirect.com/science/article/pii/S0029801823003141.

[45] W. R. Graham and C. E. Pearson, "Noise from a Model-Scale Vertical-Axis Wind Turbine", *AIAA Journal*, vol. 60, no. 1, pp. 224–235, 2022. DOI: 10.2514/1.J060531. [Online]. Available: https://doi.org/10.2514/1.J060531.

[46] R. Paterson and R. Amiet, "Noise and surface pressure response of an airfoil to incident turbulence", *Journal of Aircraft*, vol. 14, no. 8, pp. 729–736, 1977. DOI: 10.2514/3.58845. [Online]. Available: https://doi.org/10.2514/3.58845.

[47] T. F. Brooks, S. Pope, and M. A. Marcolini, "Airfoil Self-Noise and Prediction", *NASA Reference Publication 1218*, pp. 1–142, 1989, ISSN: 14786095. DOI: 10.1080/09524622.2008.9753825. [Online]. Available: http://ntrs.nasa.gov/archive/nasa/casi.ntrs.nasa.gov/19890016302.pdf.

[48] A. L. Rogers, J. F. Manwell, and S. Wright, "Wind turbine acoustic noise", Tech. Rep., 2006. DOI: 10.1260/0957456042872777. [Online]. Available: https://docs.wind-watch.org/rogers-windturbinenoise_rev2006.pdf.

[49] S. Buck, S. Oerlemans, and S. Palo, "Experimental characterization of turbulent inflow noise on a full-scale wind turbine", *Journal of Sound and Vibration*, vol. 385, pp. 219–238, 2016. DOI: 10.1016/j.jsv.2016.09.010. [Online]. Available: https://doi.org/10.1016/j.jsv.2016.09.010.

[50] S. Wagner, R. Bareiss, and G. Guidati, *Wind Turbine Noise*. Springer Verlag, 1996, ISBN: 978-3-642-88710-9. DOI: 10.1007/978-3-642-88710-9_1. [Online]. Available: https://doi.org/10.1007/978-3-642-88710-9_1.

[51] J. W. Kim, S. Haeri, and P. F. Joseph, "On the reduction of aerofoil-turbulence interaction noise associated with wavy leading edges", *Journal of Fluid Mechanics*, vol. 792, pp. 526–552, 2016. DOI: 10.1017/jfm.2016.95. [Online]. Available: https://doi.org/10.1017/jfm.2016.95.

[52] J. D. M. Botha, A. Shahroki, and H. Rice, "An implementation of an aeroacoustic prediction model for broadband noise from a vertical axis wind turbine using a CFD informed methodology", *Journal of Sound and Vibration*, vol. 410, pp. 389–415, 2017, ISSN: 0022-460X. DOI: 10.1016/j.jsv.2017.08.038. [Online]. Available: http://dx.doi.org/10.1016/j.jsv.2017.08.038.

[53] W. K. Blake, *Mechanics of Flow-Induced Sound and Vibration, Volume 2*. 2017, p. 694, ISBN: 9780128122907. DOI: 10.1016/B978-0-12-809274-3.00006-4. [Online]. Available: https://doi.org/10.1016/B978-0-12-809274-3.00006-4.

[54] R. Parchen, "Progress report DRAW: A Prediction Scheme for Trailing-Edge Noise Based on Detailed Boundary-Layer Characteristics", TNO institute of Applied Physics, Tech. Rep., 1998. [Online]. Available: https://books.google.nl/books?id=t8LYtgAACAAJ.

[55] B. K. Dyne, "Wind turbine noise measurements", Tech. Rep., 2007.

[56] A.-J. Buchner, J. Soria, D. Honnery, and A. J. Smits, "Dynamic stall in vertical axis wind turbines: Scaling and topological considerations", *Journal of Fluid Mechanics*, vol. 841, pp. 746–766, 2018. DOI: 10.1017/jfm.2018.112. [Online]. Available: https://www.cambridge.org/core/journals/journal-of-fluid-mechanics/article/dynamic-stall-in-vertical-axis-wind-turbines-scaling-and-topological-considerations/1DC59C2F9D2D13666EEADB3144699282.

[57] S. Le Fouest, D. Fernex, and K. Mulleners, "Time scales of dynamic stall development on a vertical-axis wind turbine blade", *Flow*, vol. 3, 2023. DOI: 10.1017/flo.2023.5. [Online]. Available: https://www.cambridge.org/core/journals/flow/article/time-scales-of-dynamic-stall-development-on-a-verticalaxis-wind-turbine-blade/7999A5BBEBABBA738ECE090809E52F6F.

[58] M. Jafari, M. S. Sakib, D. T. Griffith, I. Brownstein, B. Strom, and J. Cooney, "Wind tunnel experiment to study aerodynamics and control of h-rotor vertical axis wind turbine", in *Journal of Physics: Conference Series*, vol. 2265, IOP Publishing, 2022. DOI: 10.1088/1742-6596/2265/2/022084. [Online]. Available: https://dx.doi.org/10.1088/1742-6596/2265/2/022084.

[59] J. F. Harmjanz, T. Westergaard, and D. Griffith, "Assessment of control methods for vertical axis wind turbines: Start-up, active flow control, and overspeed control", Jan. 2023. DOI: 10.2514/6.2023-0612. [Online]. Available: https://arc.aiaa.org/doi/pdf/10.2514/6.2023-0612.

[60] M. Elkhoury, T. Kiwata, and E. Aoun, "Experimental and numerical investigation of a three-dimensional vertical-axis wind turbine with variable-pitch", *Journal of Wind Engineering and Industrial Aerodynamics*, vol. 139, pp. 111–123, 2015. DOI: https://doi.org/10.1016/j.jweia.2015.01.004. [Online]. Available: https://www.sciencedirect.com/science/article/pii/S0167610515000136.

[61] P. Jain and A. Abhishek, "Performance prediction and fundamental understanding of small scale vertical axis wind turbine with variable amplitude blade pitching", *Renewable Energy*, vol. 97, pp. 97–113, 2016. DOI: https://doi.org/10.1016/j.renene.2016.05.056. [Online]. Available: https://www.sciencedirect.com/science/article/pii/S0960148116304669.

[62] A. Rezaeiha, H. Montazeri, and B. Blocken, "Towards optimal aerodynamic design of vertical axis wind turbines: Impact of solidity and number of blades", *Energy*, vol. 165, pp. 1129–1148, 2018. DOI: https://doi.org/10.1016/j.energy.2018.09.192. [Online]. Available: https://www.sciencedirect.com/science/article/pii/S0360544218319704.

[63] M. Andriollo, M. De Bortoli, G. Martinelli, A. Morini, and A. Tortella, "Control strategies for a vawt driven pm synchronous generator", in *2008 International Symposium on Power Electronics, Electrical Drives, Automation and Motion*, 2008, pp. 804–809. DOI: 10.1109/SPEEDHAM.2008.4581124. [Online]. Available: https://ieeexplore.ieee.org/document/4581124.

[64] E. A. Bossanyi, "The Design of closed loop controllers for wind turbines", *Wind Energy*, vol. 3, no. 3, pp. 149–163, 2000. DOI: 10.1002/we.34. [Online]. Available: https://doi-org.tudelft.idm.oclc.org/10.1002/we.34.

[65] T. Burton, N. Jenkings, D. Sharpe, and E. A. Bossanyi, *Wind Energy Handbook*, J. W. Sons, Ed. 2001. DOI: 10.1002/9781119992714. [Online]. Available: https://onlinelibrary.wiley.com/doi/book/10.1002/9781119992714.

[66] K. Z. Østergaard, P. Brath, and J. Stoustrup, "Estimation of effective wind speed", in *Journal of Physics: Conference Series*, 2007. DOI: 10.1088/1742-6596/75/1/012082. [Online]. Available: https://iopscience.iop.org/article/10.1088/1742-6596/75/1/012082.

[67] M. N. Soltani, T. Knudsen, M. Svenstrup, R. Wisniewski, P. Brath, R. Ortega, and K. Johnson, "Estimation of rotor effective wind speed: A comparison", *IEEE Transactions on Control Systems Technology*, vol. 21, no. 4, pp. 1155–1167, 2013. DOI: 10.1109/TCST.2013.2260751. [Online]. Available: https://ieeexplore.ieee.org/document/6524000.

[68] S. Eriksson, J. Kjellin, and H. Bernhoff, "Tip speed ratio control of a 200 kw vawt with synchronous generator and variable dc voltage", *Energy Science & Engineering*, vol. 1, no. 3, pp. 135–143, 2013. DOI: 10.1002/ese3.23. [Online]. Available: https://onlinelibrary.wiley.com/doi/10.1002/ese3.23.

1

[69]   F. Bonaccorso, G. Scelba, A. Consoli, and G. Muscato, "EKF - Based MPPT control for vertical axis wind turbines", in *IECON 2011 - 37th Annual Conference of the IEEE Industrial Electronics Society*, 2011, pp. 3614–3619. DOI: 10.1109/IECON.2011.6119896. [Online]. Available: https://ieeexplore-ieee-org.tudelft.idm.oclc.org/document/6119896.

[70]   K. E. Johnson, L. Pao, M. J. Balas, J. Lee, and L. J. Fingersh, "Control of Variable-Speed Wind Turbines: Standard and Adaptive Techniques for Maximizing Energy Capture", *IEEE Control Systems*, vol. 26, no. 3, pp. 70–81, 2006. DOI: 10.1109/MCS.2006.1636311. [Online]. Available: https://ieeexplore.ieee.org/document/1636311.

[71]   A. A. Ozdemir, P. Seilery, and G. J. Balas, "Benefits of preview wind information for region 2 wind turbine control", in *51st AIAA Aerospace Sciences Meeting including the New Horizons Forum and Aerospace Exposition 2013*, 2013, pp. 1–7. DOI: 10.2514/6.2013-317. [Online]. Available: https://arc.aiaa.org/doi/10.2514/6.2013-317.

[72]   S. P. Mulders, L. Brandetti, F. Spagnolo, Y. Liu, P. Brandt, and J. W. van Wingerden, "A learning algorithm to advanced wind turbine controllers for the calibration of internal model uncertainties: A wind speed measurement-free approach", ser. Proceedings of the 2023 American Control Conference (ACC 2023), Jun. 2023. DOI: 10.23919/ACC55779.2023.10156125. [Online]. Available: https://ieeexplore.ieee.org/document/10156125.

[73]   B. Boukhezzar and H. Siguerdidjane, "Nonlinear control of variable speed wind turbines without wind speed measurement", in *Proceedings of the 44th IEEE Conference on Decision and Control*, 2005, pp. 3456–3461. DOI: 10.1109/CDC.2005.1582697. [Online]. Available: https://ieeexplore.ieee.org/document/1582697.

[74]   N. J. Abbas, D. S. Zalkind, L. Pao, and A. Wright, "A reference open-source controller for fixed and floating offshore wind turbines", *Wind Energy Science*, vol. 7, no. 1, pp. 53–73, 2022. DOI: 10.5194/wes-7-53-2022. [Online]. Available: https://wes.copernicus.org/articles/7/53/2022/.

[75]   P. F. Odgaard, L. F. S. Larsen, R. Wisniewski, and T. G. Hovgaard, "On using pareto optimality to tune a linear model predictive controller for wind turbines", *Renewable Energy*, vol. 87, pp. 884–891, 2016. DOI: 10.1016/j.renene.2015.09.067. [Online]. Available: https://www.sciencedirect.com/science/article/pii/S0960148115303463.

[76]   M. Lara, J. Garrido, M. L. Ruz, and F. Vázquez, "Multi-objective optimization for simultaneously designing active control of tower vibrations and power control in wind turbines", *Energy Reports*, vol. 9, pp. 1637–1650, 2023. DOI: 10.1016/j.egyr.2022.12.141. [Online]. Available: https://www.sciencedirect.com/science/article/pii/S2352484722027421.

[77]   D. J. Leith and W. E. Leithead, "Implementation of wind turbine controllers", *International Journal of Control*, vol. 66, no. 3, pp. 349–380, 1997. DOI: 10.1080/002071797224621. [Online]. Available: https://doi.org/10.1080/002071797224621.

[78] W. E. Leithead and B. Connor, "Control of variable speed wind turbines: Design task", *International Journal of Control*, vol. 73, no. 13, pp. 1189–1212, 2000. DOI: 10.1080/002071700417849. [Online]. Available: https://doi.org/10.1080/002071700417849.

[79] P. Devine-Wright, "Beyond nimbyism: Towards an integrated framework for understanding public perceptions of wind energy", *Wind Energy*, vol. 8, no. 2, pp. 125–139, 2005. DOI: 10.1002/we.124. [Online]. Available: https://onlinelibrary.wiley.com/doi/abs/10.1002/we.124.

[80] J. R. Farkat Diógenes, J. Claro, J. Coelho Rodrigues, and M. Valentim Loureiro, "Barriers to onshore wind energy implementation: A systematic review", *Energy Research Social Science*, vol. 60, p. 101 337, 2020. DOI: https://doi.org/10.1016/j.erss.2019.101337. [Online]. Available: https://www.sciencedirect.com/science/article/pii/S2214629618311538.

[81] K. Langer, T. Decker, J. Roosen, and K. Menrad, "Factors influencing citizens' acceptance and non-acceptance of wind energy in germany", *Journal of Cleaner Production*, vol. 175, pp. 133–144, 2018. DOI: 10.1016/j.jclepro.2017.11.221. [Online]. Available: https://www.sciencedirect.com/science/article/pii/S0959652617328949.

[82] N. Dällenbach and R. Wüstenhagen, "How far do noise concerns travel? exploring how familiarity and justice shape noise expectations and social acceptance of planned wind energy projects", *Energy Research Social Science*, vol. 87, p. 102 300, 2022. DOI: 10.1016/j.erss.2021.102300. [Online]. Available: https://www.sciencedirect.com/science/article/pii/S2214629621003923.

[83] S. A. Jansse, H. Vos, A. R. Eisses, and E. Pedersen, "A comparison between exposure-response relationships for wind turbine annoyance and annoyance due to other noise sources", *The Journal of the Acoustical Society of America*, vol. 130, p. 3746, 2011. DOI: 10.1121/1.3653984. [Online]. Available: https://pubmed.ncbi.nlm.nih.gov/22225031/.

[84] E. Pedersen and K. Persson Waye, "Perception and annoyance due to wind turbine noise—a dose–response relationship", *The Journal of the Acoustical Society of America*, vol. 116, no. 6, pp. 3460–3470, 2004. DOI: 10.1121/1.1815091. [Online]. Available: https://doi.org/10.1121/1.1815091.

[85] R. H. Bakker, E. Pedersen, G. P. van den Berg, R. E. Stewart, W. Lok, and J. Bouma, "Impact of wind turbine sound on annoyance, self-reported sleep disturbance and psychological distress", *Science of The Total Environment*, vol. 425, pp. 42–51, 2012. DOI: 10.1016/j.scitotenv.2012.03.005. [Online]. Available: https://pubmed.ncbi.nlm.nih.gov/22481052/.

[86] L. D. Knopper and C. A. Ollson, "Health effects and wind turbines: A review of the literature", *Environmental Health*, vol. 10, p. 78, 2011. DOI: 10.1186/1476-069X-10-78. [Online]. Available: https://ehjournal.biomedcentral.com/articles/10.1186/1476-069X-10-78.

1

[87] L. D. Knopper, C. A. Ollson, L. C. McCallum, M. L. Whitfield Aslund, R. G. Berger, K. Souweine, and M. McDaniel, "Wind turbines and human health", *Frontiers in Public Health*, vol. 2, 2014. DOI: 10.3389/fpubh.2014.00063. [Online]. Available: https://pubmed.ncbi.nlm.nih.gov/24995266/.

[88] D. S. Michaud, K. Feder, S. E. Keith, S. A. Voicescu, L. Marro, J. Than, M. Guay, A. Denning, D. McGuire, T. Bower, E. Lavigne, B. J. Murray, S. K. Weiss, and F. van den Berg, "Exposure to wind turbine noise: Perceptual responses and reported health effects", *The Journal of the Acoustical Society of America*, vol. 139, p. 1443, 2016. DOI: 10.1121/1.4942391. [Online]. Available: https://pubmed.ncbi.nlm.nih.gov/27036283/.

[89] E. Peri, N. Becker, and A. Tal, "What really undermines public acceptance of wind turbines? a choice experiment analysis in israel", *Land Use Policy*, vol. 99, p. 105 113, 2020. DOI: 10.1016/j.landusepol.2020.105113. [Online]. Available: https://www.sciencedirect.com/science/article/pii/S0264837720309674.

[90] T. Höfer, Y. Sunak, H. Siddique, and R. Madlener, "Wind farm siting using a spatial analytic hierarchy process approach: A case study of the städteregion aachen", *Applied Energy*, vol. 163, pp. 222–243, 2016. DOI: 10.1016/j.apenergy.2015.10.138. [Online]. Available: https://www.sciencedirect.com/science/article/pii/S030626191501380X.

[91] C. L. Bottasso, A. Croce, Y. Nam, and C. E. D. Riboldi, "Power curve tracking in the presence of a tip speed constraint", *Renewable Energy*, vol. 40, no. 1, pp. 1–12, 2012. DOI: 10.1016/j.renene.2011.07.045. [Online]. Available: http://dx.doi.org/10.1016/j.renene.2011.07.045.

[92] A. H. Poulsen, O. Raaschou-Nielsen, A. Peña, A. N. Hahmann, R. B. Nordsborg, M. Ketzel, J. Brandt, and M. Sørensen, "Impact of long-term exposure to wind turbine noise on redemption of sleep medication and antidepressants: A nationwide cohort study", *Environmental Health Perspectives*, vol. 127, no. 3, p. 037 005, 2019. DOI: 10.1289/EHP3909. [Online]. Available: https://ehp.niehs.nih.gov/doi/10.1289/EHP3909.

[93] K. Persson Waye and A. Agge, "Experimental quantification of annoyance to unpleasant and pleasant wind turbine sounds", 2014. [Online]. Available: https://api.semanticscholar.org/CorpusID:204797198.

[94] E. Peri and A. Tal, "A sustainable way forward for wind power: Assessing turbines' environmental impacts using a holistic gis analysis", *Applied Energy*, vol. 279, p. 115 829, 2020. DOI: 10.1016/j.apenergy.2020.115829. [Online]. Available: https://www.sciencedirect.com/science/article/pii/S0306261920313076.

[95] C. W. Klok, A. F. Kirkels, and F. Alkemade, "Impacts, procedural processes, and local context: Rethinking the social acceptance of wind energy projects in the netherlands", *Energy Research Social Science*, vol. 99, p. 103 044, 2023. DOI: 10.1016/j.erss.2023.103044. [Online]. Available: https://www.sciencedirect.com/science/article/pii/S2214629623001044.

[96]   G. Q. Di, X. W. Chen, K. Song, B. Zhou, and C. M. Pei, "Improvement of zwicker's psychoacoustic annoyance model aiming at tonal noises", *Applied Acoustics*, vol. 105, pp. 164–170, 2016. DOI: 10.1016/j.apacoust.2015.12.006. [Online]. Available: https://www.sciencedirect.com/science/article/pii/S0003682X15003606.

[97]   R. Pieren, L. Bertsch, D. Lauper, and B. Schäffer, "Improving future low-noise aircraft technologies using experimental perception-based evaluation of synthetic flyovers", *Science of The Total Environment*, vol. 692, 2019. DOI: 10.1016/j.scitotenv.2019.07.253. [Online]. Available: https://www.sciencedirect.com/science/article/abs/pii/S0048969719333674.

[98]   M. Vorländer, *Auralization - Fundamentals of Acoustics, Modelling, Simulation, Algorithms and Acoustic Virtual Reality*. Springer, 2008, ISBN: 9781292022932.

[99]   R. Pieren, K. Heutschi, M. Müller, M. Manyoky, and K. Eggenschwiler, "Auralization of wind turbine noise: Emission synthesis", *Acta Acustica united with Acustica*, vol. 100, pp. 25–33, 2014. DOI: 10.3813/AAA.918683. [Online]. Available: https://www.ingentaconnect.com/content/dav/aaua/2014/00000100/00000001/art00007#Supp.

[100]   R. Merino-Martínez, R. Pieren, and B. Schäffer, "Holistic approach to wind turbine noise: From blade trailing-edge modifications to annoyance estimation", *Renewable and Sustainable Energy Reviews*, vol. 148, p. 111 285, 2021. DOI: 10.1016/j.rser.2021.111285. [Online]. Available: https://www.sciencedirect.com/science/article/pii/S1364032121005724.

1

2

A LOW-FIDELITY NOISE PREDICTION MODEL

Vertical-axis wind turbines (VAWTs) have the potential to be installed in nearby urban areas where noise regulations are a constraint. Accurate modelling of the far-field noise with low-fidelity methods is essential to account for noise early in the design phase. The challenge for the VAWT is the unsteady azimuthal variation of the flow over the blades, making the far-field noise prediction complex with low-fidelity methods. In this chapter, the state-of-the-art low-fidelity methods are assessed against scale-resolving high-fidelity numerical simulations of a realistic VAWT carried out with the lattice-Boltzmann very large eddy simulations method. High-fidelity numerical data are validated against experimental aerodynamics data of the same turbine. The low-fidelity method is based on the actuator cylinder model coupled with semi-empirical models for airfoil-self noise and turbulence-interaction noise. Results show a good agreement between the high-fidelity simulations and the low-fidelity model at low frequencies, where turbulence-interaction noise is the dominant noise source. At higher frequencies, the airfoil-self noise dominates, and existing methods, based on steady airfoils, do not correctly predict noise. Overall, the presented low-fidelity model predicts the aerodynamics and the aeroacoustics of the turbine with acceptable accuracy for a design stage.

2.1. INTRODUCTION

Depending on the orientation of the axis of rotation, wind turbines are classified as horizontal-axis wind turbines (HAWTs) and vertical-axis wind turbines (VAWTs). The advantages of the latter are, amongst others: omni-directionality, which makes them more suitable for installation in urban areas where wind direction variations are larger because of the presence of surrounding buildings, and lower maintenance cost because the generator is located on the ground [1].

When locating a wind energy system in urban areas, it is mandatory to account for noise regulations. Two major noise sources exist for operating wind turbines: mechanical and aerodynamic. The former is caused by the dynamic response of the moving mechanical components, while the latter is generated by the airflow interaction with the blade [2]–[5]. Nowadays, the primary focus is on aerodynamic noise, proving that mechanical noise has already been optimized [6].

Aerodynamic noise can be divided into Turbulence-Interaction (T-I) noise and airfoil-self noise. T-I noise occurs when incoming flow turbulence interacts with the blade leading edge [4], [7]. For this aerodynamic noise source, it is essential to carefully describe the turbulent flow in terms of spectral energy content and the integral length scale of the fluctuations. For a system like a VAWT, where the impinging turbulent flow can be self-generated (i.e. wake-airfoil interaction) or due to free-stream turbulence, characterization of the turbulent wake is essential. However, no accurate model has been reported in the literature yet. As a matter of fact, by comparing the analytical results of Botha et al. [8] and Pearson [9] on the QR5 rotor, a mismatch of up to 10 dB is found depending on the different correction factors applied. On the same line, Botha et al. [8] found that increasing the intensity of the turbulent fluctuations to 10-15% of the free-stream velocity increased the overall noise up to 5 dB.

Airfoil-self noise is the noise generated by a blade in a smooth flow [3]. Depending on the flow conditions, five airfoil-self noise mechanisms can be distinguished:

1. Laminar Boundary Layer – Vortex Shedding noise (LBL-VS);

2. Turbulent Boundary Layer – Trailing Edge noise (TBL-TE);

3. Separation-Stall noise (SS);

4. Trailing Edge Blunt – Vortex Shedding noise (TEB-VS);

5. Tip noise (TP).

For HAWTs, which usually operate at high Reynolds numbers Re (i.e. $Re \geq 5 \times 10^5$), TBL-TE noise is the most relevant noise source. TBL-TE is caused by the scattering of the turbulent pressure fluctuations convecting over the sharp trailing edge [3]. Conversely, for VAWTs, TBL-TE noise is not the primary noise source. Pearson [9] and Botha et al. [8] showed that, at low Tip-Speed Ratios (TSRs), the blades of a VAWT are subjected to dynamic stall. Under this condition, the shear layer separates, creating coherent vortices which generate tonal noise (LBL-VS) [3]. When the TSR increases, the dynamic stall is less relevant, and the major noise source is T-I noise, i.e. interaction between the turbulent near wake of a blade and the following one. Pearson [9] also demonstrated that

2

increasing the solidity of the rotor (σ) has a similar effect as increasing TSR because the induction factor is a function of both. If small VAWTs are considered, the operating Re numbers are relatively low (i.e. $Re \leq 5 \times 10^5$), and LBL-VS noise is expected to be the major source of noise. By modelling LBL-VS noise with the Brooks, Pope and Marcolini (BPM) approach [3], Pearson observed a tonal peak in the frequency range between 1×10^3 Hz $- 2 \times 10^3$ Hz for a full-scale rotor. However, this result does not match the experimental findings of Dyne [10] because of the assumption of steady incoming flow in the BPM model.

Based on the previous observations, a low-fidelity methodology to correctly predict noise for a VAWT operating at a low Re number is not available yet. An assessment of the noise sources is needed to pave the way towards a low-fidelity noise prediction tool. To this end, the current research investigates the aerodynamic and the aeroacoustic performance of a two-bladed H-Darrieus VAWT using a multi-fidelity numerical approach. First, Lattice-Boltzmann Very Large Eddy Simulations (LB-VLES) coupled with the Ffowcs Williams and Hawkings (FWH) integral solution are carried out. This is the first dataset presented in the literature where the aerodynamic and the acoustic fields are retrieved using the same tool, thus allowing the link of far-field noise with unsteady aerodynamics. Then, the high-fidelity numerical results are compared with the ones obtained from a low-fidelity model, used to predict the performance of a VAWT with very low computational time such that it can be used in preliminary design stages. The comparison will assess the limitations of the adopted models and provide relevant information for their improvement.

The chapter is structured as follows: Section 2.2 describes the geometry of the test case and the simulation settings. The adopted methodologies are discussed in Section 2.3. The computational set-up is validated in Section 2.4 by means of a grid convergence study and by comparison with experimental loading data in Section 2.5. Aerodynamic and acoustic results are discussed in Sections 2.5 and 2.6, respectively. The main findings are summarised in Section 2.7.

2.2. CASE STUDY

The two-bladed H-Darrieus PitchVAWT, shown in Figure 2.1 and experimentally investigated by LeBlanc and Simão Ferreira [11], [12], is used in this study. In order to minimize blade deflection, two horizontal struts are used for each blade and located at approximately 25% and 75% of the blade length. The blades have a NACA 0021 profile, and a chord c_b equals to 7.5×10^{-2} m, while the struts have a NACA 0018 profile with a chord c_s equals to 6×10^{-2} m. The diameter D of the VAWT is equal to 1.5 m, thus resulting in a rotor solidity σ of 0.1. The span s and the height H of the VAWT are equal to 1.5 m. For this study, the blade pitch angle, β, is constant and equals $0°$. More detailed information about the design of the PitchVAWT can be found in a previous work [13].

The coordinate system used in this study is shown in Figure 2.1. It is a Cartesian coordinate system with the origin at the turbine's centre.
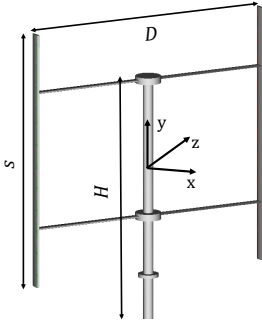
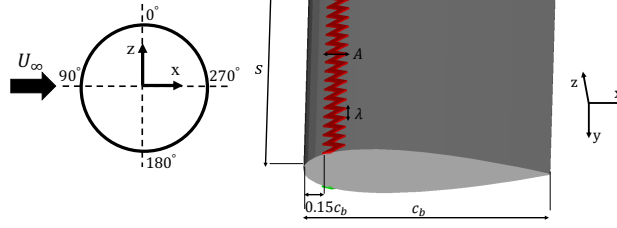Figure 2.1: PitchVAWT geometry, dimensions and coordinate system.

Figure 2.2: Blade airfoil NACA0021 and zig-zag strip.

Table 2.1: Flow condition and VAWT settings.

Parameter	Value
Free-stream velocity (U_∞)	4 m/s
Tip velocity (V_{tip})	16 m/s
Tip-Speed Ratio (TSR)	4
Free-stream Mach number (M)	1×10^{-2}
Free-stream Reynolds number (Re)	8.26×10^4
Free-stream turbulence intensity (I_t)	$1\%U_\infty$

To further help in the interpretation of the results, the blade orbit is divided into two regions:

- upwind or fore half: $0° \leq \theta < 180°$;

- downwind or aft half: $180° \leq \theta < 360°$;

with θ being the blade azimuthal position and $\theta = 90°$ and $270°$ being respectively the most upwind and downwind positions. θ is defined with respect to blade 1; therefore, blade 2 lags blade 1 by $180°$.

The free-stream velocity U_∞ is 4 m/s, corresponding to a Mach number M of 1×10^{-2} and a chord-based Reynolds number Re of 8.26×10^4. The free-stream turbulence intensity I_t is set to $1\%U_\infty$, similarly as in the wind tunnel experiment. The VAWT operates at a TSR of 4, corresponding to a tip velocity V_{tip} equals to 16 m/s. The flow conditions and the VAWT operation settings are summarized in Table 2.1.

Due to the low Re number, boundary-layer transition to turbulence, where possible, is controlled using a zig-zag strip on both airfoil sides at $15\%c_b$, as in the reference experiment. The tripping has a height h of 5×10^{-4} m, an amplitude A of 2×10^{-3} m and a wavelength λ of 5×10^{-3} m (Figure 2.2). The setup specifications are summarised in Table 2.2.

Table 2.2: PitchVAWT design specifications [12], [13].

Parameter	Value
Number of blades (N_b)	2
Span (s)	$1.5 \, \text{m}$
Height (H)	$1.5 \, \text{m}$
Diameter (D)	$1.5 \, \text{m}$
Solidity (σ)	0.1
Blade chord (c_b)	$7.5 \times 10^{-2} \, \text{m}$
Strut chord (c_s)	$6 \times 10^{-2} \, \text{m}$
Blade airfoil	NACA0021
Strut airfoil	NACA0018
Blade pitch angle (β)	$0°$
Trip location (x_t)	$15 \, \% \, c_b$
Trip height (h)	$5 \times 10^{-4} \, \text{m}$
Trip amplitude (A)	$2 \times 10^{-3} \, \text{m}$
Trip wavelength (λ)	$5 \times 10^{-3} \, \text{m}$

2.3. METHODOLOGY AND COMPUTATIONAL SETUP

2.3.1. HIGH-FIDELITY SIMULATIONS

The methodology and the computational setup used in the high-fidelity simulations are described in the following. The flow over the VAWT is computed by solving the explicit, transient, compressible LB equation, while the acoustic far field is obtained by means of the Ffowcs William and Hawkings (FWH) acoustic analogy [14].

FLOW SOLVER

The LB method is used to compute the flow field because it provides accurate and efficient aeroacoustic solutions for complex flow problems, as shown in previous studies in the wind energy field [15], [16]. The commercial software 3DS Simulia PowerFLOW 5.5b is employed. The software solves the discrete LB equation for a finite number of directions. A detailed description of the method is out of the scope of this manuscript, but the interested reader is referred to Succi [17], Shan et al. [18], and for a complete review to Chen and Doolen [19].

The LB method determines the macroscopic flow variables starting from the mesoscopic kinetic equation, i.e. the LB equation. The discretization used for this particular application consists of 19 discrete velocities in three dimensions (D3Q19), involving a third-order truncation of the Chapman-Enskog expansion. The distribution of particles is solved by means of the LB equation on a Cartesian mesh, known as a lattice. An explicit time integration and a collision model based on a unique Galilean invariant [20] are used. The equilibrium distribution function of Maxwell-Boltzmann, conventionally used for small Mach number flows, is adopted [21].

A Very Large Eddy Simulation (VLES) model is implemented to take into account the

effect of the sub-grid unresolved scales of turbulence. Following [22], a two-equation $k-\epsilon$ re-normalization group is used to compute a turbulent relaxation time that is added to the viscous relaxation time. In order to reduce the computational cost, a pressure-gradient extended wall model is used to approximate the no-slip boundary condition on solid walls [23], [24]. The model is based on the extension of the generalized law-of-the-wall model [25] to take into account the effect of the pressure gradient.

NOISE COMPUTATION

The compressible and time-dependent nature of the transient solution, together with the low dissipation and dispersion properties of the LB scheme [26] allow the extraction of the sound pressure field directly in the near field up to a cut-off frequency corresponding to approximately 15 voxels per acoustic wavelength. In the far field, noise is computed using the Ffowcs Williams & Hawkings [14] (FWH) equation. The formulation 1A, developed by Farassat and Succi [27] and extended to a convective wave equation, is used in this study [26]. The formulation is implemented in the time domain using a source-time dominant algorithm [28].

COMPUTATIONAL DOMAIN AND BOUNDARY CONDITIONS

The simulation domain is cubic with a length of 3.7×10^2 m centred at the origin of the wind turbine reference system. At the inlet, a velocity boundary condition with a velocity equal to U_∞ is set. At the outlet, the pressure is set to the ambient pressure 1.01×10^5 Pa. At the other edges of the domain, frictionless wall boundary conditions are set. No-slip boundary conditions are applied on the VAWT. A volume of revolution is generated containing the wind turbine in a cylinder with a radial clearance of 0.4 m.

Fifteen variable resolution (VR) regions are used. The resolution increases by a factor
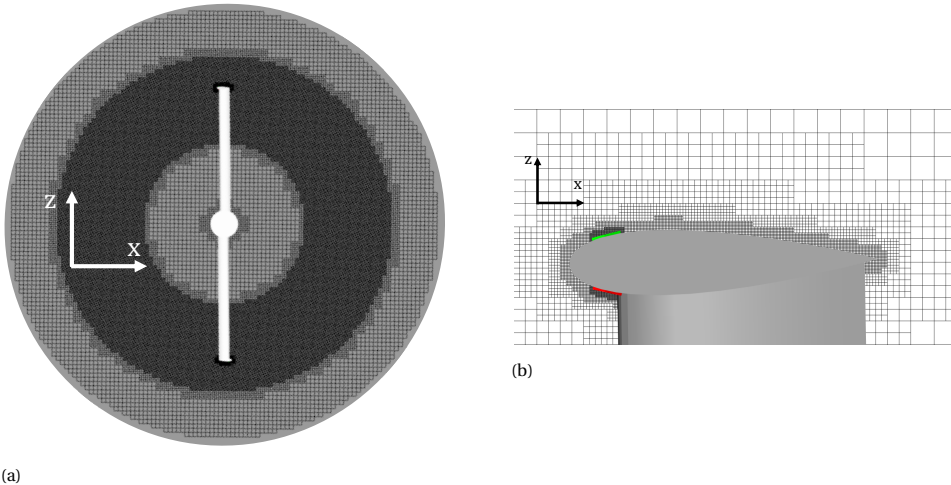
(a)

(b)

Figure 2.3: Distribution of the variable resolution (VR) regions in the near field: in the local rotating reference frame (Figure 2.3a) and around the blade, in the proximity of the tip, (Figure 2.3b). A darker colour means that the resolution is higher.

of two from one VR region to the next. Since the main focus is characterising the flow around the blades, the blade path region has a higher resolution than the tower region (Figure 2.3a). The finest resolution region (VR15) is defined by an offset of 1.06×10^{-3} m from the trip on both the suction side and the pressure side to capture the surface pressure fluctuations accurately. A resolution of 6×10^2 voxels along the blade chord c_b is used in VR15, resulting in the smallest voxel size of 1.25×10^{-4} m. The increase in resolution around the trip going from VR11 to VR15 can be observed in Figure 2.3b.

An acoustic sponge is implemented by exponentially varying the kinematic viscosity per unit temperature from 5×10^{-3} m^2/sK at 16 m up to 0.5 m^2/sK at 47 m. This is adopted to avoid spurious reflections from the edge of the domain contaminating the acoustic sampled data.

Simulations are seeded with the preceding simulation with a coarser grid. The flow simulation time is 2.94 s (i.e. 10 complete turbine revolutions), requiring 3.7×10^5 CPU hrs/revolution on a Linux Xeon E5-2690 2.9 GHz platform. The physical time step, corresponding to a Courant-Friedrichs-Lewy (CFL) number [29] of 1 in the finest mesh resolution level, is 2.06×10^{-7} s. The unsteady pressure on the surface of the VAWT is sampled with a frequency of 1×10^4 Hz for a physical time of 2.65 s (i.e. 9 complete turbine revolutions) after one transient revolution. Time convergence has been verified, as will be shown in Section 2.4.

2.3.2. LOW-FIDELITY MODEL

A low-fidelity model is implemented to predict the aerodynamics and the aeroacoustics of the VAWT.

The Actuator Cylinder (AC) model [30], corrected as described in Section 2.3.2, is used for the aerodynamics of the VAWT while the noise prediction methodology is based on the work of Botha et al. [8].

For the noise model, the angle of attack α and the velocity perceived by the blade V_{rel} are obtained, as described in Section 2.5, using three approaches: a geometric relation, the AC model and the AC model fed with blade loading data obtained from the high-fidelity simulations. These analytical models can be applied to calculate flow input parameters to be used in the low-fidelity prediction tool. This is considered acceptable for the preliminary design phase, where some inaccuracies can be tolerated. As it will be clarified in Sections 2.5 and 2.6, estimating α and V_{rel} from high-fidelity simulations is fundamental to obtaining more accurate aerodynamics and aeroacoustics predictions suitable for final design analysis.

The approach of Botha et al. [8] uses a blade element approach to discretize the blades of the wind turbine. Each blade element rotates in the azimuthal direction θ. For each blade element and azimuthal position, the airfoil-self noise is estimated with the BPM model [3], while the T-I noise is modelled following the approach of Buck et al. [5]. Notice that these models are applied in a rotating coordinate system under steady flow conditions. To account for the motion of the blades with respect to the stationary observer, the Doppler correction factor is computed [31], and the spectrum at the receiver location is obtained by applying the methodology of Brooks and Burley [32].
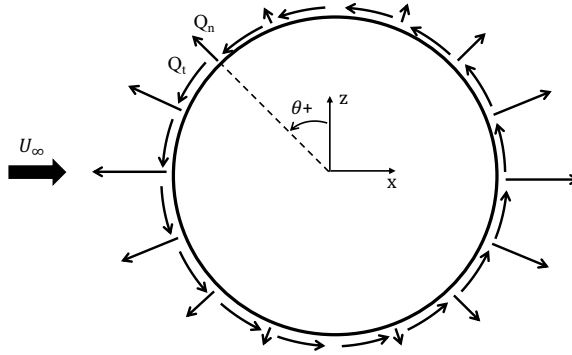
Figure 2.4: 2D representation of the Actuator Cylinder (AC) model and sign convention applied.

Aerodynamic model

The aerodynamic forces on the VAWT are computed using the AC model developed by Madsen [30] coupled with aerofoil aerodynamic data obtained from Xfoil [33]. This 2D model applies the actuator disk concept to the cylindrical actuation surface swept by the VAWT.

The reactions of the blade forces (F_n and F_t) are applied on the flow as distributed body forces (Q_n and Q_t) oriented perpendicular and tangential to the actuator surface [34]. The 2D, steady, incompressible Euler equations and the continuity equation are solved to determine the velocity field around the AC model [35]. The induced velocities are defined as the sum of a linear solution, which is a function of the volume forces, and a non-linear solution, which is a function of the induced forces. Since the solution of the non-linear part is computationally expensive, the Mod-Lin solution is adopted [34]. Here, only the linear version of the AC model is used, and a correction factor k_a is applied to account for the non-linear part. The factor k_a is calculated from the relation between the induction factor a and the thrust coefficient C_T of the whole rotor. This relation considers that $C_T = 4a(1-a)$ for $a < 0.5$, and includes the Glauert correction for $a > 0.5$ [30]. Figure 2.4 depicts the 2D AC model together with the sign convention employed in this research.

Once V_{rel} and α at each θ, the boundary layer integral parameters are computed with Xfoil.

Corrections applied to the aerodynamic model

Two unsteady effects characterize the VAWT's performance: dynamic stall and flow curvature. When the airfoil experiences rapid variations in the angle of attack, dynamic stall occurs. When the VAWT operates, each blade experiences a curvilinear inflow due to the rotation of the rotor. As a consequence of the fare known low curvature effect, V_{rel} and α vary along the chord [36]. To correctly assess the aerodynamics of the VAWT, these effects are modelled as follows:

- The Beddoes-Leishman (B-L) dynamic stall model [37] includes the effect of trailing-edge and leading-edge separation as well as the unsteady inviscid wake. The B-L model consists of four sub-models: non-linear attached flow, non-linear trailing

edge separation, dynamic stall onset, and vortex-induced air loads. The interested reader is referred to Leishman and Beddoes [37] and to Appendix A for further indications on the implementation and constants used.

- The flow curvature effect is taken into account by assuming that the evaluation point is at three-quarters of the chord [38].

In addition, k_a is modified in the AC model, due to the heavily loaded case study (i.e. high TSR), as follows [34]:

$$k_a = \begin{cases} \dfrac{1}{1-a}, & a \le 0.15 \\ \dfrac{1}{1-a}\left[0.65 + 0.35 \exp\left(-4.5(a-0.15)\right)\right], & a > 0.15 \end{cases}.$$ (2.1)

NOISE MODELS

To study the acoustics of the VAWT, the noise models for the LBL-VS noise source, the TBL-TE noise source and the T-I noise source are applied.

The implemented noise models present two important limitations:

- No blade-blade interaction is considered because the blades are modelled in isolation.

- Steady, free-stream conditions under a quasi-steady time dependence are assumed.

For simplicity, only the relevant equations will be reported. The interested reader is referred to Botha et al. [8] for further information about the noise models.

AIRFOIL-SELF NOISE

Airfoil-self noise is generated when a steady flow interacts with a blade [3].

At low Re numbers (i.e. $Re \le 5 \times 10^5$), Tollmien-Schlichting (T-S) waves can grow. They will generate vortex shedding, which causes tonal noise through a feedback loop. This noise generation mechanism is named LBL-VS noise and is modelled with the BPM approach [3] as follows:

$$\text{SPL}_{\text{LBL-VS}} = 10\log_{10}\left(\frac{\delta_p M^5 d\bar{D}_h}{r_e^2}\right) + G_1\left(\frac{St'}{St'_{\text{peak}}}\right) + G_2\left[\frac{Re}{(Re)_0}\right] + G_3(\alpha),$$ (2.2)

in which $\text{SPL}_{\text{LBL-VS}}$ is the Sound Pressure Level in $1/3^{\text{rd}}$ octave band, δ_p is the boundary layer thickness at the pressure side, d is the span-wise size of the blade element, $\bar{D}_h$ is the directivity function for the high-frequency limit, r_e is the absolute distance to the receiver and $(Re)_0$ is the chord-based Reynolds number at $\alpha = 0°$. For details on the Strouhal contributions, St' and St'_{peak}, and on the empirical functions, G_1, G_2 and G_3, the reader can refer to Brooks et al. [3].

At high Re number (i.e. $Re \ge 5 \times 10^5$), TBL develops over the airfoil. Because of the surface discontinuity at the trailing edge, the surface pressure fluctuations beneath the TBL are scattered as noise. This noise generation mechanism is named TBL-TE. The SPL in $1/3^{\text{rd}}$ octave band for the TBL-TE noise ($\text{SPL}_{\text{TBL-TE}}$) is obtained as the sum of

three contributions: one from the attached TBL at the pressure side (SPL_p), one from the attached TBL at the suction side (SPL_s) and one that accounts for the separated boundary layer at high α (SPL_α):

$$\text{SPL}_{\text{TBL}-\text{TE}} = 10\log_{10}\left(10^{\left(\frac{\text{SPL}p}{10}\right)} + 10^{\left(\frac{\text{SPL}s}{10}\right)} + 10^{\left(\frac{\text{SPL}\alpha}{10}\right)}\right). \quad (2.3)$$

For $\alpha \leq 12.5°$, the terms in Eq. (2.3) are:

$$\text{SPL}_p = 10\log_{10}\left(\frac{\delta_p^* M^5 d\bar{D}_h}{r_e^2}\right) + A\left(\frac{St_p}{St_1}\right) + (K_1 - 3) + \Delta K_1, \quad (2.4)$$

$$\text{SPL}_s = 10\log_{10}\left(\frac{\delta_s^* M^5 d\bar{D}_h}{r_e^2}\right) + A\left(\frac{St_s}{St_1}\right) + (K_1 - 3), \quad (2.5)$$

$$\text{SPL}_\alpha = 10\log_{10}\left(\frac{\delta_s^* M^5 d\bar{D}_h}{r_e^2}\right) + B\left(\frac{St_s}{St_2}\right) + (K_2), \quad (2.6)$$

while for $\alpha \geq 12.5°$

$$\text{SPL}_p = -\infty, \quad (2.7)$$

$$\text{SPL}_s = -\infty, \quad (2.8)$$

$$\text{SPL}_\alpha = 10\log_{10}\left(\frac{\delta_s^* M^5 d\bar{D}_l}{r_e^2}\right) + A'\left(\frac{St_s}{St_2}\right) + (K_2), \quad (2.9)$$

in which δ_p^* and δ_s^* are the boundary layer displacement thickness at the pressure side and at the suction side, respectively and $\bar{D}_l$ is the directivity function for the low-frequency limit. The Strouhal contributions, St_p, St_s, St_1 and St_2, the empirical functions, A, A' and B, and the amplitude correction factors, K_1, K_2 and ΔK_1, can be found in Brooks et al. [3].

Notice that the boundary layer parameters used in the BPM model are determined analytically. For the detailed equations, the interested reader is referred to Brooks et al. [3].

In the work of Botha et al. [8], the airfoil-self noise is also predicted with the iTNO model [39] (i.e. an improved version of the TNO model developed by Blake [40] and Parchen [41]). This model is found to provide accurate noise predictions for non-symmetric airfoils at high wind speeds. However, the separation-stall noise is not modelled. For this reason and for the fact that the PitchVAWT has symmetric airfoils and operates at low wind speeds, the iTNO model is not applied in the current study.

TURBULENCE-INTERACTION NOISE

T-I noise is produced when inflow turbulence impinges on the blade leading edge [4]. Different models have been proposed in the literature, such as the one of Paterson and Amiet [2] and the one of Buck et al. [5]. Both methodologies compute the SPL of the T-I noise ($\text{SPL}_{\text{inflow}}$) as the sum of the high-frequency and low-frequency components of the noise:

$$\text{SPL}_{\text{inflow}} = \text{SPL}_{\text{inflow}}^H + 10\log_{10}\left(\frac{\text{LFC}}{1 + \text{LFC}}\right), \quad (2.10)$$

in which LFC is the blending function introduced by Lowson and Ollerhead [42] and Moriarty and Migliore [43].

On the other hand, the high-frequency component, $\text{SPL}^H_{\text{inflow}}$, is different. For the model of Paterson and Amiet [2], the incoming turbulence is defined with the von Kármán spectrum, while for the one of Buck et al. [5] the turbulence length scale is substituted with the turbulence dissipation rate ε by applying the Kolmogorov spectrum [44]. The value of ε is estimated with the relationship from Taylor [45] as:

$$\varepsilon = c_\varepsilon \frac{k_t^{3/2}}{L_t}, \tag{2.11}$$

in which $c_\varepsilon = 5.5 \times 10^{-1}$ is a constant selected to match the high-frequency asymptote of the Buck model to that of the Paterson and Amiet model, k_t is the turbulent kinetic energy derived from the root mean square turbulent fluctuations as the product between the turbulence intensity at the inlet and the velocity perceived by the blade and $L_t = 7.5 \times 10^{-3}$ m is the integral length scale of turbulence at the airfoil inlet.

This modification leads to less complex calculations and to short measurement times. However, Botha et al. [8] demonstrate that the two models predict the same noise spectrum. Therefore, the model of Buck et al. [5] is preferred. The sound pressure level $\text{SPL}^H_{\text{inflow,B}}$ is:

$$\text{SPL}^H_{\text{inflow,B}} = 10 \log_{10} \left[\frac{\rho_\infty^2 c_0^2 d}{2 r_e^2} M^3 \varepsilon^{(2/3)} k^{-(5/3)} \bar{D}_{\text{LE}} \right] + 77.6, \tag{2.12}$$

where ρ_∞ is the free-stream density, c_0 is the sound speed, k is the wave-number ($k = (2\pi f)/V_{\text{rel}}$) and $\bar{D}_{\text{LE}}$ is the directivity function for the low-frequency limit computed at the leading edge.

2.4. ASSESSMENT OF THE HIGH-FIDELITY NUMERICAL SIMULATIONS

A grid resolution study is performed for high-fidelity numerical simulations to verify that the solution does not vary with the computational grid. High-fidelity numerical simulations with three grid resolutions are carried out with a refinement ratio of $\sqrt{2}$. For the three cases, the most refined region (i.e., around the blade) has 3×10^2 (coarse), 4.2×10^2 (medium) and 6×10^2 (fine) voxels per VAWT chord. This is achieved by proportionally increasing the resolution of each refinement region. The corresponding number of fine equivalent voxels N for the three configurations is 1.9×10^7, 3.6×10^7 and 6.9×10^7. A comprehensive overview of the simulation configurations employed in the grid independence study is presented in Table 2.3.

The time-averaged thrust coefficient C_T, defined as in Equation (2.13), the Power Spectral Density (PSD), expressed as dB/Hz, and the Overall Sound Pressure Level (OASPL) of far-field acoustic pressure, indicated in dB using a reference pressure of 2×10^{-5} Pa, are used as integral parameters for the convergence analysis.

$$C_T = \frac{T}{\frac{1}{2} \rho_\infty U_\infty^2 A_{\text{rot}}}, \tag{2.13}$$

Table 2.3: Domain statistics for the three simulation configurations employed in the grid independence study.

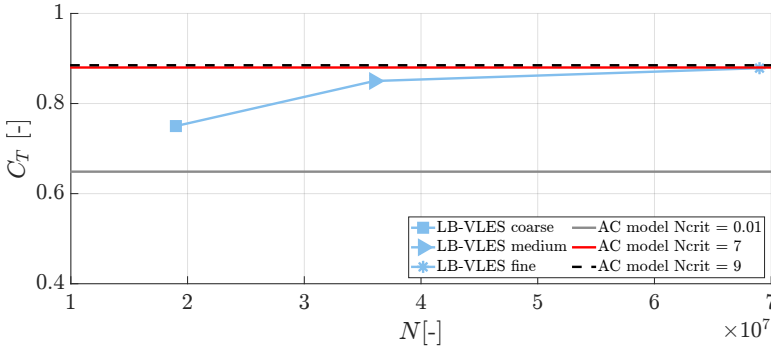| Type	Resolution	Fine equivalent voxels (N)
Coarse	3×10^2	1.9×10^7
Medium	4.2×10^2	3.6×10^7
Fine	6×10^2	6.9×10^7

Figure 2.5: The time-averaged thrust coefficient C_T versus the number of fine equivalent voxels N. The LB-VLES results are compared with results from the AC model with aerodynamic polars obtained using $Ncrit$ equal to 0.01, 7 and 9.

In Equation (2.13), T is the time-averaged thrust (i.e. the force along inflow direction, generated by the VAWT), and A_{rot} is the frontal rotor area, which is equal to $(D \times s)$.

The C_T is plotted in Figure 2.5 for the three grid resolutions, where N is the number of fine equivalent voxels. In the same figure, data from the AC models are reported as constant C_T values. Results from the AC model are plotted using polars obtained from Xfoil with $Ncrit$ equal to 0.01, 7 and 9 to stress the strong dependence of the results from the aerodynamic polars used as input. Details on the polars are given in Appendix B. Note that $Ncrit$ is used in the solver as Xfoil to determine the transition location. It is based on the e^N theory, which states that the transition occurs roughly when linear theory predicts that an initial disturbance has grown by a factor of e^N [33]. Using a range of polars with varying $Ncrit$ instead of only the polar with the zig-zag strip was motivated by the poor performance of Xfoil at low Reynolds numbers. Specifically, $Ncrit = 0.01$ represents the case of a fully turbulent flow, where the transition is amplified just after the linear instability begins. While $Ncrit = 9$ defines the default value in Xfoil, and $Ncrit = 7$ indicates that the disturbances in the boundary layer need to reach a moderate level of amplitude to induce the transition. Minor variations between the low-fidelity data with $Ncrit = 7$ and $Ncrit = 9$ can be observed in Figure 2.5. Results show convergence for the fine simulation case and very good agreement with the low-fidelity data with $Ncrit = 7$ (or $Ncrit = 9$). Time convergence for the LB-VLES simulation is also demonstrated with a time history of the normal force component on a single blade F_n in Figure 2.6. Simulation
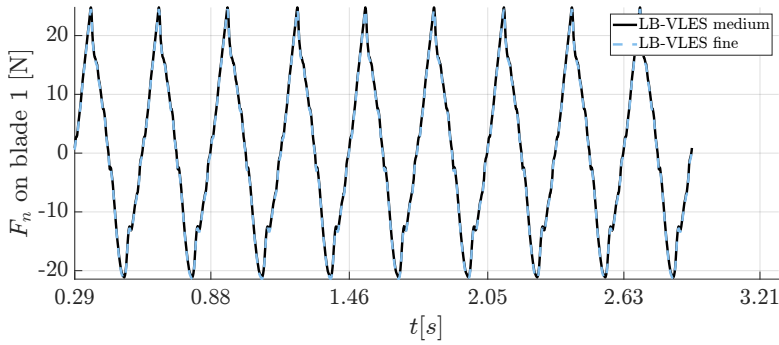
Figure 2.6: Time-history of the normal force component on a single blade F_n. The LB-VLES results with the medium resolution are compared with the LB-VLES results with fine resolution.

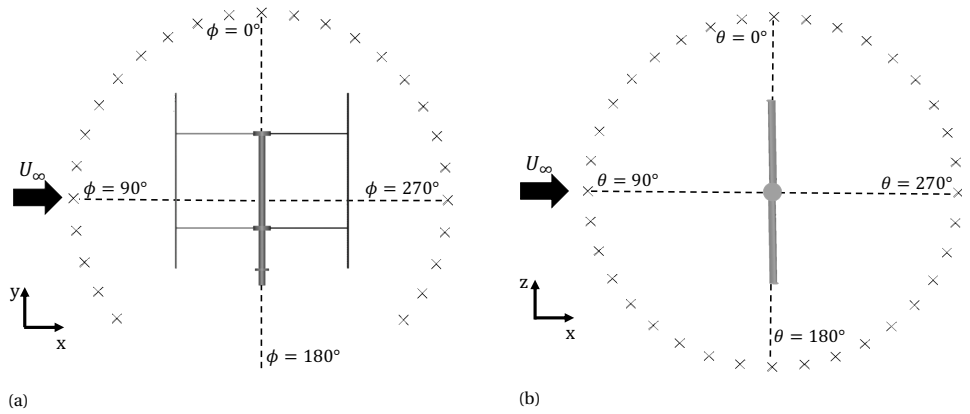(a)   (b)

Figure 2.7: Two circular arrays of equally spaced virtual microphones placed at $2.6D$ from the centre of the VAWT: array with 27 microphones in the x-y plane (Figure 2.7a) and array with 36 microphones in the x-z plane (Figure 2.7b).

results are plotted after one transient revolution and show a good agreement between the medium and the fine resolution.

Acoustic data are obtained on two circular arrays of equally spaced virtual microphones placed at $2.6D$ from the centre of the VAWT. The angular spacing between the microphones is $10°$. One array with 27 microphones is in the x-y plane (Figure 2.7a), while the other with 36 microphones is in the x-z plane (Figure 2.7b).

In Figures 2.8 and 2.9, the PSD as a function of frequency f and the OASPL directivity patterns are plotted to ensure that also far-field noise data converge. The far-field noise is computed using the FWH acoustic analogy described in Section 2.3.1. PSD is shown for two microphones at $\theta = 0°$ and at $\phi = 0°$, respectively. For the PSD, the maximum difference between the two finest grids is 2 dB/Hz for $\theta = 0°$. For the low grid resolution, an overestimation of the OASPL for angles in the range $100° < \phi < 300°$ and $135° < \theta < 315°$ is found and corresponds to 1.5 dB. Overall, results show a good agreement between the medium and fine resolutions, confirming that the fine simulation case has also reached
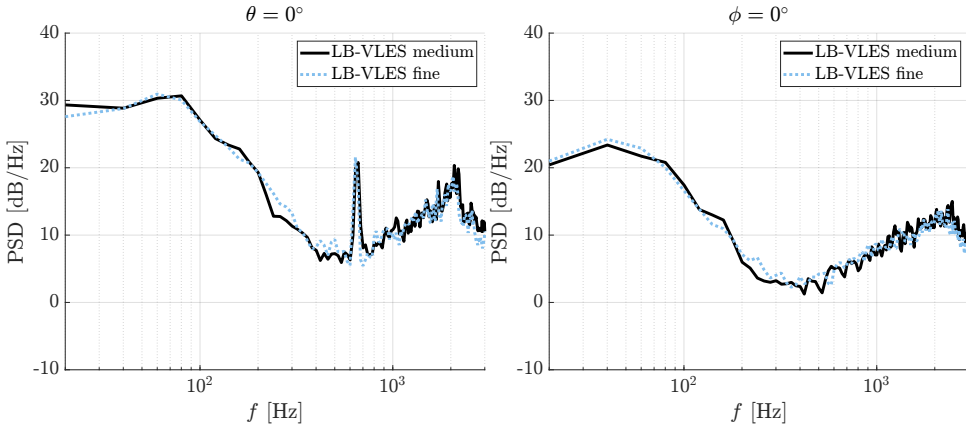
Figure 2.8: Power Spectral Density PSD versus frequency f for two microphones placed at $2.6D$ from the center of the VAWT: $\theta = 0°$ (left-side) and $\phi = 0°$ (right-side). The LB-VLES results with the medium resolution are compared with the LB-VLES results with fine resolution.
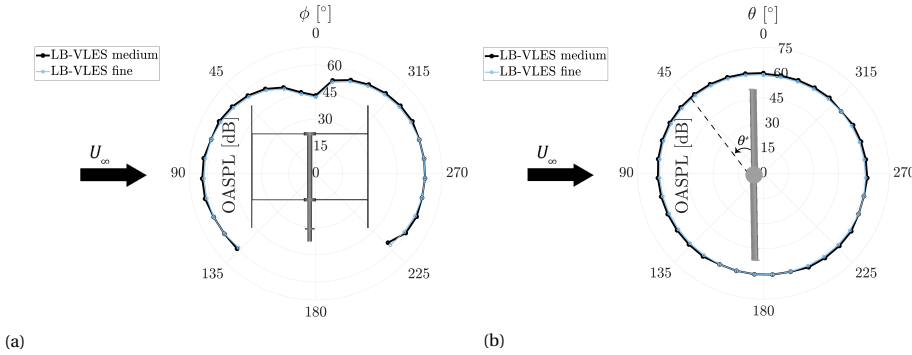
Figure 2.9: Directivity plots of the Overall Sound Pressure Level (OASPL) computed on: a circular array of 27 microphones in the x-y plane (Figure 2.9a) and on a circular array of 36 microphones in the x-z plane (Figure 2.9b). The LB-VLES results with the medium resolution are compared with the LB-VLES results with fine resolution.

convergence from an acoustic point of view. The fine simulation will be used in the following based on these results.

2.5. FLOW FIELD DESCRIPTION AND AERODYNAMIC PERFORMANCE

FLOW FIELD DESCRIPTION

A detailed analysis of the complex aerodynamic flow features is reported using data from high-fidelity simulations. This description is essential to understand the limitations of the low-fidelity methodology in predicting the VAWT's aerodynamic performance.

An instantaneous flow field at $\theta = 90°$ is shown in Figure 2.10 through iso-surfaces of the λ_2 criterion for vortex identification, colour-contoured with the non-dimensional velocity magnitude $\underline{V}/U_\infty$. The figure illustrates that most of the vortices in the near wake of each blade are generated at the tip and the struts. While at the tip, the vortices are coherent and have a large scale, in the proximity of the struts, they show a smaller scale already in the near wake.

Because of the presence of these structures, each blade is subjected to both Blade-Wake Interaction (BWI) and Blade-Vortex Interaction (BVI) [46]. These phenomena are better shown in Figure 2.11, where non-dimensional vorticity magnitude $\omega/(V_{\text{tip}}/c)$ is plotted at two planes: at the tip (sub-figures 1 and 2) and in correspondence of the upper struts (sub-figures 3 and 4). The blades are at two azimuthal positions for each plane, as annotated in the figures.

In the absence of the struts, the vorticity is mostly shed when the blade is located at $\theta = 0°$. This is expected because the derivative of the loading is the largest in this position. Conversely, where the struts are present, the vorticity is strongly shed at all the azimuthal positions. The interaction between the two blades is clearly visible in sub-figure 3, where the trailing edge shed vorticity of the blade in $\theta = 180°$ interacts with the leading edge of the blade in $\theta = 0°$. The vorticity is spread in the field and does not interact with the blade's leading edge in $\theta = 270°$.

Another important aspect that needs to be taken into account to properly model the aerodynamics of VAWTs with low-fidelity methods is the unsteady flow field to which each blade section is subjected during one rotation.

Flow separation is an inherent effect of this unsteadiness, which is investigated in Figure 2.12. Here, contours of the non-dimensional stream-wise velocity u/U_∞ at the mid plane are plotted for blade 1 at four θ: 50°, 90°, 220° and 270°. As can be observed, the contours look discrete because of the downsampling of the numerical results. At $\theta = 50°$, the flow is attached up to 50 % of the blade chord where separation starts. Conversely, for $\theta = 90°$, the most upwind location, separation starts at 20 % of the blade chord. At $\theta = 220°$, no flow separation is found in the high-fidelity simulations; separation is again visible at $\theta = 270°$. At this location, the blade passes through a region with velocity deficit caused by the downstream wake of the tower, which has a significant effect on the flow over the blade [47] and the acoustics of the turbine (Section 2.6). The qualitative description given from visual inspections of the figures is confirmed by the distributions of the pressure coefficient C_p over blade 1, which are not shown for the sake of conciseness.

2
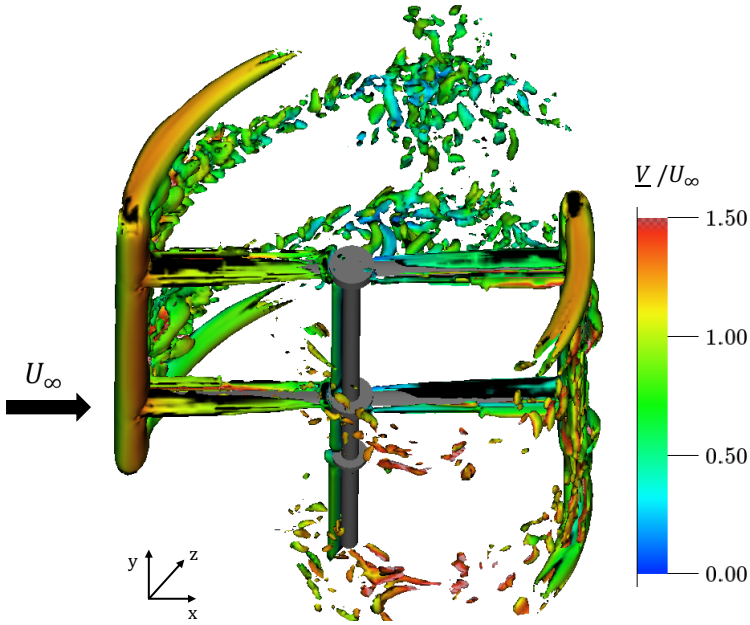
Figure 2.10: View of the instantaneous flow field at $\theta = 90°$ visualised through the λ_2 criterion for vortex visualisation colour contoured with the non-dimensional velocity magnitude $\underline{V}/U_\infty$.
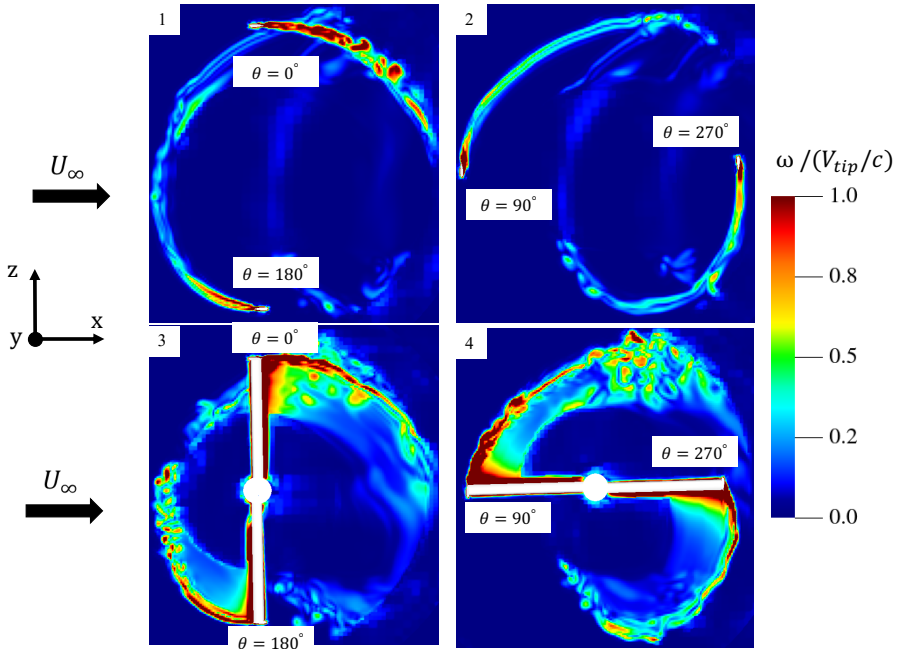
Figure 2.11: Instantaneous flow field visualized through the non-dimensional vorticity magnitude $\omega/(V_{\text{tip}}/c)$. Sub-figures 1 and 2: plane at the tip. Sub-figures 3 and 4: plane at the upper struts.

Figure 2.12: Instantaneous non-dimensional stream-wise velocity u/U_∞ at the mid plane for four azimuthal positions θ of blade 1: $50°$, $90°$, $220°$, $270°$. The rotating system of reference is used.

AERODYNAMIC PERFORMANCE

The phase-locked normal force component on a single blade F_n is shown in Figure 2.13. The LB-VLES forces are obtained from a phase-locked average over 9 rotations; the experimental f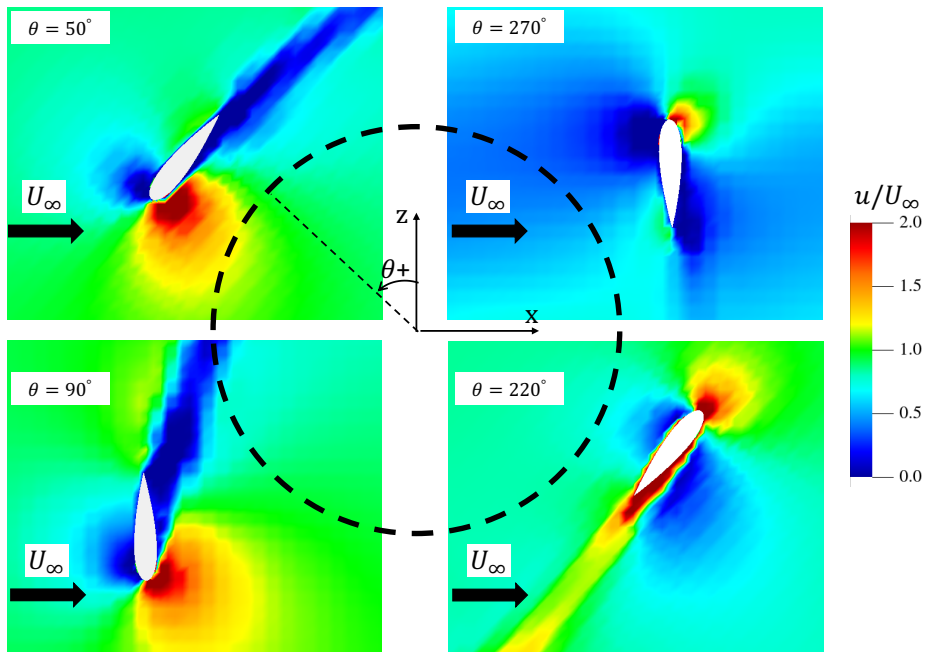orces are obtained from a phase-locked average of approximately 200 data points per azimuthal location. The experimental loading data presented for clean and tripped blades are measured using a set of strain gages on the top strut of blade 1. A full-bridge strain gage setup is utilised in an axial configuration to compensate for any vertical bending or temperature fluctuations which can occur while testing [12], [48]. Azimuthal locations are not plotted where experimental data have a poor signal-to-noise ratio. Results from the AC model are only presented for two extreme polars (i.e. $Ncrit = 0.01$ and $Ncrit = 7$) because results with $Ncrit = 9$ are very similar to those obtained with $Ncrit = 7$. It is important to mention that the loads from the LB-VLES simulation and the experiment are averaged over the rotor span, including 3D tip effects and vortex shedding. These 3D effects are not considered in the low-fidelity method due to its 2D formulation.

Overall, a good agreement between the methodologies is found both in terms of trends and absolute values. All methods correctly predict the F_n at $\theta = 0°$. For $15° < \theta < 48°$ and $200° < \theta < 220°$, the LB-VLES show good agreement with the two experimental datasets, while at $\theta = 90°$ and $\theta = 270°$ the LB-VLES results agree better with the clean experimental data. This is because the zig-zag strip used in the high-fidelity numerical simulation is not effective at those angles, as shown in the previous figures. Even if this can be solved by increasing the size of the zig-zag strip in the high-fidelity numerical simulation, this would result in additional unwanted noise sources and over-tripping in a range of angles of attack. The figure further shows that upwind for $0° < \theta < 180°$, the AC model results strongly depend on the polar used. Downwind, for $180° < \theta < 360°$, differences are mainly attributed to the inaccurate prediction of the induction and wake effects (3D) in the low-fidelity method.

A challenge for low-fidelity methods is to accurately predict the dynamic of α and V_{rel}, which vary with θ [49]. In the following, α and V_{rel} are obtained with three approaches: through a geometric relation, from the AC model and using the blade loads from the
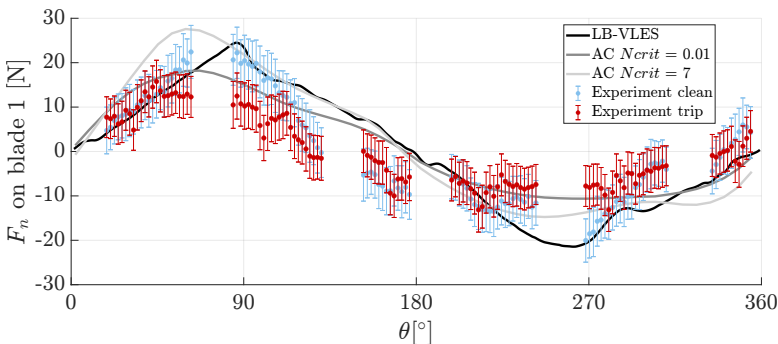

Figure 2.13: Phase-locked normal force on blade 1 F_n versus the azimuthal angle θ during one turbine rotation. The LB-VLES results are compared with experimental data and results from the AC model with two extreme polars ($Ncrit = 0.01$ and $Ncrit = 7$).
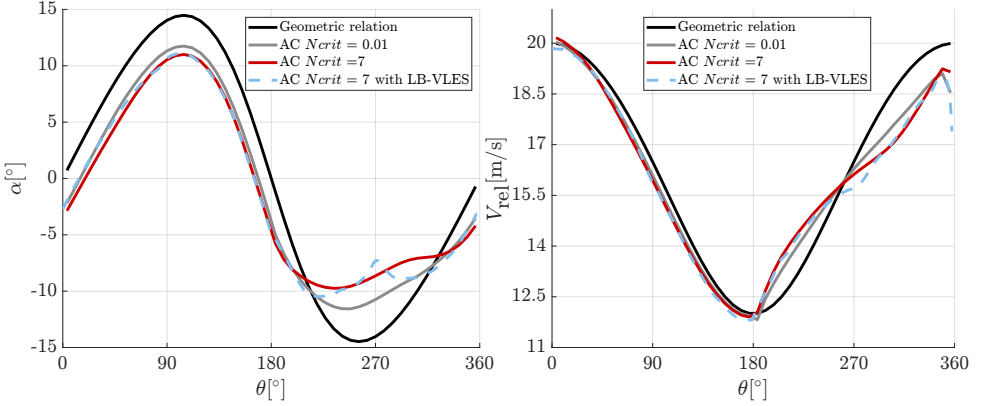
Figure 2.14: Angle of attack α (left-side) and perceived velocity V_{rel} (right-side) versus azimuthal angle θ during one turbine rotation. The geometric relation results are compared with the results from the AC model ($Ncrit$ = 0.01 and $Ncrit$ = 7) and AC model with $Ncrit$ = 7 feed with LB-VLES blade load data.

high-fidelity simulations as inputs for the AC model. The latter approach has been applied because there is no agreed formulation on how to extract α and V_{rel} from high-fidelity simulations [8], [50]. Details on the methodology to compute α and V_{rel} from high-fidelity normal blade loads are beyond the scope of the chapter, and the interested reader is referred to the literature [51]. No experimental data for α and V_{rel} are available.

The ones given by the geometric relation are shown in Equations (2.14) and (2.15), under the assumption of a constant V_{rot} and U_∞.

$$\alpha = \arctan\left(\frac{\sin(\theta)}{\cos(\theta) + \text{TSR}}\right) + p, \tag{2.14}$$

$$V_{\text{rel}} = U_\infty \sqrt{1 + 2\,\text{TSR}\cos(\theta) + \text{TSR}^2}, \tag{2.15}$$

where p is the fixed pitch angle of the airfoil.

For the AC model, α and V_{rel} are determined with Equations (2.16) and (2.17).

$$\alpha = \arctan\left(\frac{V_n}{V_t}\right) - p, \tag{2.16}$$

$$V_{\text{rel}} = \sqrt{V_n^2 + V_t^2}, \tag{2.17}$$

V_n and V_t are the normal and the tangential relative wind speed with respect to the AC, defined as:

$$V_n = V_x \sin\theta - V_z \cos\theta, \tag{2.18}$$

$$V_t = V_x \cos\theta + V_z \sin\theta + V_{\text{rot}}, \tag{2.19}$$

with $V_x = U_\infty(1 + w_x)$ and $V_z = U_\infty w_z$ the components in x- and z- directions of the velocity, respectively, w_x is the x-induction and w_z is the z-induction.

Both α and V_{rel}, computed with the three approaches, are plotted in Figure 2.14. Results obtained using the geometric relation show the most relevant differences between all the methodologies. This is because induction is not considered. For the other approaches, α has a sinusoidal shape in the turbine's fore half while a flat-shaped aft half. This is because the flow is significantly affected by the blade passage in the fore-aft [52]. The differences between the other approaches are smaller, and the minor impact of using high-fidelity blade load inputs in the AC model is evident.

2.6. ACOUSTICS

2.6.1. COMPARISON BETWEEN LOW-FIDELITY METHODOLOGIES

To demonstrate the effect of α and V_{rel} on the acoustic predictions, results from the noise model with α and V_{rel} predicted with the geometric relation and results from the noise model with α and V_{rel} predicted with the AC model for $Ncrit = 0.01$ and $Ncrit = 7$ are compared in Figures 2.15 and 2.16 as SPL versus frequency f. The SPL is expressed in dB and is evaluated at $2.6D$ from the centre of the VAWT in the x-z plane, specifically at $\theta = 90°$ and $\theta = 270°$. The methodology has been described in Section 2.3.2.

By looking at the different SPL spectra, it is clear that the most dominant noise sources are: T-I noise below 7×10^1 Hz, TBL-TE noise from 7×10^1 Hz to 3×10^2 Hz and LBL-VS noise from 3×10^2 Hz to 8×10^2 Hz.

For the T-I noise, a good agreement between the models is found in terms of trends and absolute values. This is because the Buck model only depends on V_{rel} (Equation (2.12)), which is very similar to the three models at $\theta = 90°$ (Fig. (Figure 2.14)).

For the TBL-TE noise, the geometric relation results show the most relevant differences between all the methods because of the largest difference in α (Figure 2.14).

The effect of a different α on the SPL is clearly visible in the LBL-VS noise spectra. This is because an α-dependent function is used to model the LBL-VS noise (Equation (2.2)).

Figure 2.15: Sound Pressure Level SPL versus frequency f. The noise model with geometric relation inputs results are compared with results from the noise model with AC data for two extreme polars ($Ncrit = 0.01$ and $Ncrit = 7$).
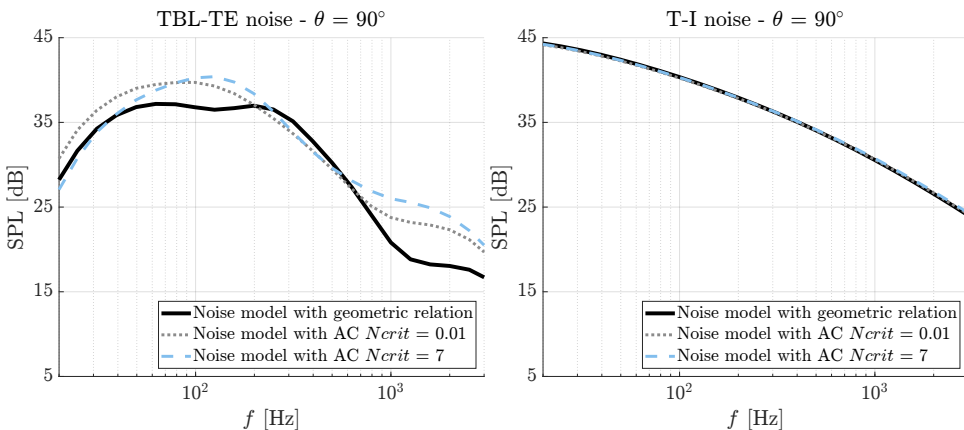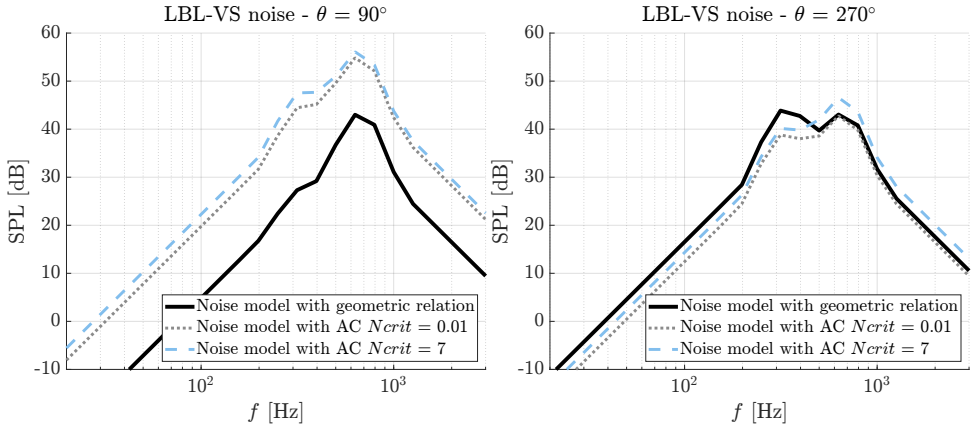
Figure 2.16: Sound Pressure Level SPL versus frequency f. The noise model with geometric relation inputs results are compared with results from the noise model with AC data for two extreme polars ($Ncrit = 0.01$ and $Ncrit = 7$).

2.6.2. COMPARISON BETWEEN LB-VLES AND NOISE MODEL WITH AERODYNAMIC DATA FROM THE AC MODEL

The comparison between LB-VLES data and low-fidelity data in Section 2.5 has shown the limitations of the low-fidelity methodologies in predicting the VAWT's aerodynamics. In the following, the effect of these limitations on the acoustic prediction will be investigated by comparing the LB-VLES results with the results from the noise model with aerodynamic inputs from the AC with $Ncrit = 7$. Aerodynamic inputs from the other low-fidelity models are not considered due to their inaccurate flow modelling. No experimental acoustic data is available for comparison.

Figure 2.17 illustrates the directivity plots of the OASPL on the two circular microphone arrays (Figure 2.7). The OASPL is expressed in dB with reference pressure equal to 2 ×

Figure 2.17: Directivity plots of the Overall Sound Pressure Level (OASPL) computed on: a circular array of 27 microphones in the x-y plane (Figure 2.17a) and on a circular array of 36 microphones in the x-z plane (Figure 2.17b). The LB-VLES results are compared with results from the noise model with AC data for $Ncrit = 7$.
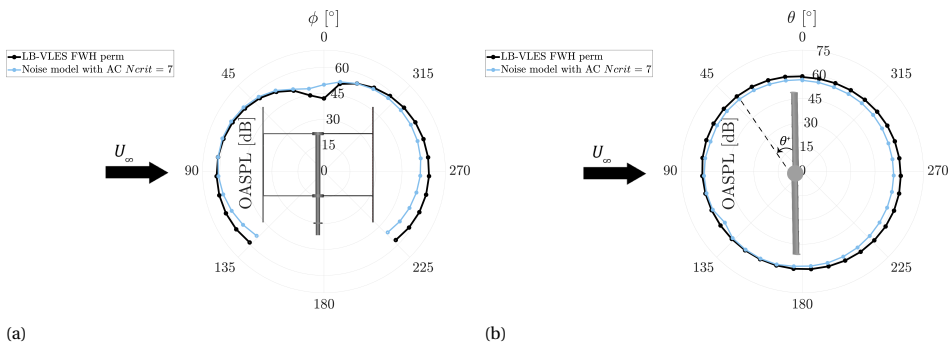
10^{-5} Pa. Data are integrated between one Blade Passing Frequency (BPF) and 20 BPF, where the BPF equals 6.8 Hz.

An overall good agreement between the methodologies is found in terms of trends. The resulting acoustic field is slightly asymmetric, as expected from the flow dynamics of the VAWT. The main differences in the absolute values are attributed, for the microphones located in the x-y plane, to the incoming wind speed and to 3D effects while, for the microphones located in the x-z plane, to the non-correct prediction of α and V_{rel}.

The previous observations are further supported by the SPL spectra in Figures 2.18 to 2.20. Two microphones in the x-y plane and four microphones in the x-z plane are used: $\phi = 20°$, $\phi = 270°$, $\theta = 50°$, $\theta = 90°$, $\theta = 220°$ and $\theta = 270°$.

The figures plotted results from the low-fidelity method for each noise generation mechanism. The tonal loading noise is not modelled because, for this case study, the rotational frequency is low and out of the audible range in real life.

At $\phi = 20°$, good agreement between LB-VLES and the results from the low-fidelity models is found. The two methods confirm the dominance of the T-I noise at low frequency and the dominance of the TBL-TE noise at medium frequency. The small differences in the tonal peak of the LBL-VS at 6×10^2 Hz are attributed to 3D vortex-shedding effects, which represent one of the limitations of the low-fidelity methodology.

At $\phi = 270°$, the acoustic predictions of the noise model are strongly affected by the presence of the struts and of the tower (Section 2.5).

At $\theta = 50°$, 90° and 220° and below 1×10^2 Hz, the differences between the LB-VLES and the noise model are small, and it is evident the relevance of T-I noise.

At $\theta = 270°$, the noise model predicts lower levels of T-I noise with respect to the LB-VLES. This is due to tower shadow, as illustrated in Figure 2.12. The consequent velocity deficit causes laminar flow over larger portions of the airfoil, which is reflected in the LBL-VS peak at 6×10^2 Hz [3]. At $\theta = 90°$, the increasing angle of attack caused by flow separation (Figure 2.12) leads to a decrease in the predicted LBL-VS peak by the
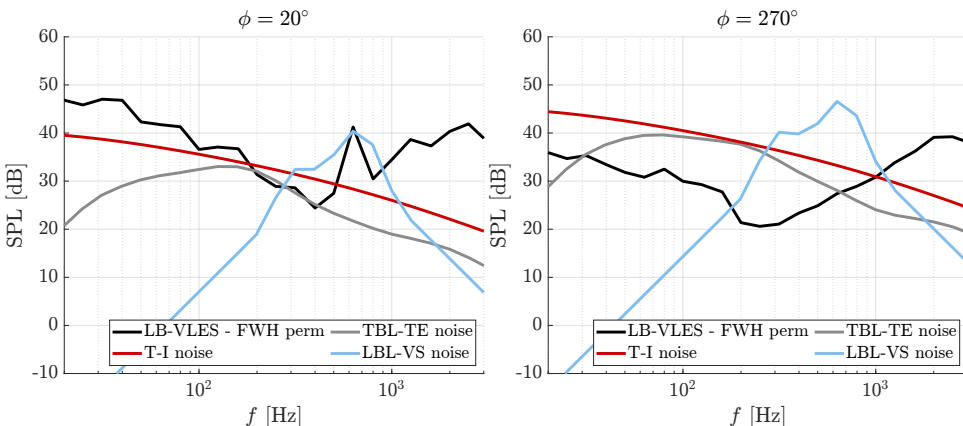
Figure 2.18: Sound Pressure Level SPL versus frequency f obtained from two microphones in the x-y plane: at $\phi = 20°$ (left-side) and at $\phi = 270°$ (right-side). The LB-VLES results are compared with results from the noise model with AC data for $Ncrit = 7$.
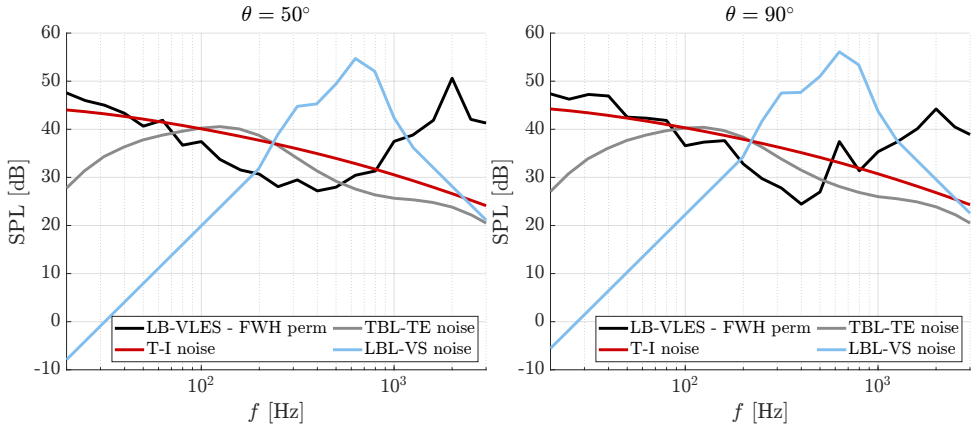
Figure 2.19: Sound Pressure Level SPL versus frequency f obtained from two microphones in the x-z plane: at $\theta = 50°$ (left-side) and at $\theta = 90°$ (right-side). The LB-VLES results are compared with results from the noise model with AC data for $Ncrit$ =7.
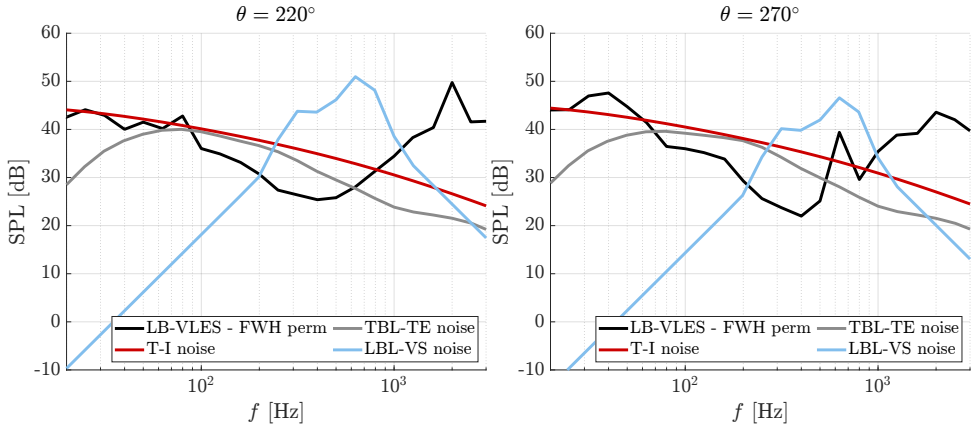
Figure 2.20: Sound Pressure Level SPL versus frequency f obtained from two microphones in the x-z plane: at $\theta = 220°$ (left-side) and at $\theta = 270°$ (right-side). The LB-VLES results are compared with results from the noise model with AC data for $Ncrit$ =7

.

LB-VLES [3]. The low-fidelity model does not capture this effect due to an inaccurate prediction of α and V_{rel}.

Overall, no agreement in the absolute value for the TBL-TE noise is found for two reasons. First, the low-fidelity model does not account for BVI and BWI because the blades are modelled as isolated [8]. Second, the model assumes steady flow conditions and the occurrence of flow separation only when $\alpha > 12.5°$ [9], [53]. This condition is demonstrated to be not true for the case under study (Section 2.5).

To further demonstrate the influence of the struts and the tower and the occurrence of 3D effects and blade-wake interactions, visualizations of the instantaneous noise

contribution from each solid surface at a given microphone location are computed with $Opty\partial B$-PFNOISESCAN [54]. The resulting unsteady surface field is Fourier transformed and then visualized in different integration bands as SPL/m^2.

Figures 2.21 to 2.23 illustrate the noise source maps computed by using three different microphones: $\phi = 270°$, $\theta = 50°$ and $\theta = 90°$. Since in the comparison of the SPL spectra, the noise models show to predict the TBL-TE noise and the LBL-VS noise inaccurately, the corresponding frequency ranges are used in the analysis: 2×10^2 Hz - 3×10^2 Hz and 5×10^2 Hz - 6×10^2 Hz.

At $\phi = 270°$, the struts and the tower are detected as the main noise sources, while the blades present lower noise contributions. This explains the trend observed in the SPL spectrum (Figure 2.18), where the low-fidelity model predicts higher noise levels for not modelling the struts and the tower.

The influence of 3D phenomena on the overall noise contribution is evident at $\theta = 50°$. Vortices are visible at the tip and the bottom of the blade, while 3D effects are generated from junction flows in the proximity of strut-blade connections. For this reason, the assumptions about the 2D flow and related radiated noise are not valid, resulting in lower noise levels of the LB-VLES with respect to the one predicted by the low-fidelity model between 2×10^2 Hz and 3×10^2 Hz (Figure 2.19).

At $\theta = 90°$, the noise source map reveals the dominance of the most upwind blade because it experiences higher flow velocity and angle of attack. As above-mentioned, from 5×10^2 Hz to 6×10^2 Hz, the increase in the angle of attack causes a decrease in the LBL-VS peak predicted by the LB-VLES (Figure 2.19). Another cause of the lower noise contribution of the most downwind blade is attributed to BVI and BWI, proving that the assumption of modelling blade as isolated is not valid for VAWT [53].
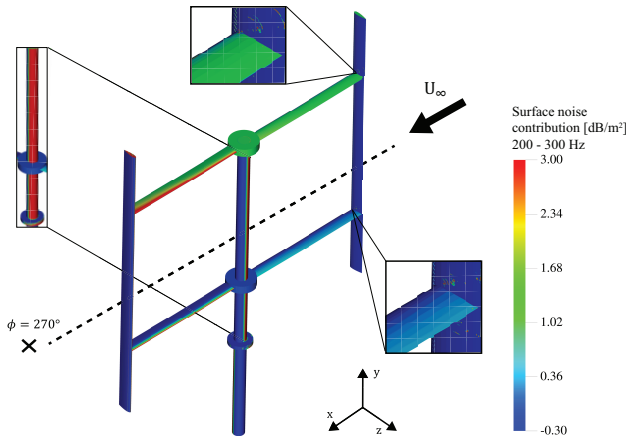
Figure 2.21: FWH integral contribution from a microphone in the x-y plane at $\phi = 270°$.
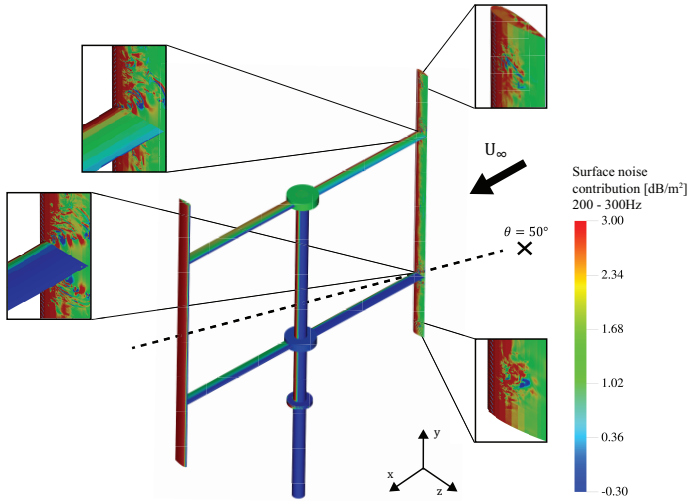
Figure 2.22: FWH integral contribution from a microphone in the x-z plane at $\theta = 50°$.
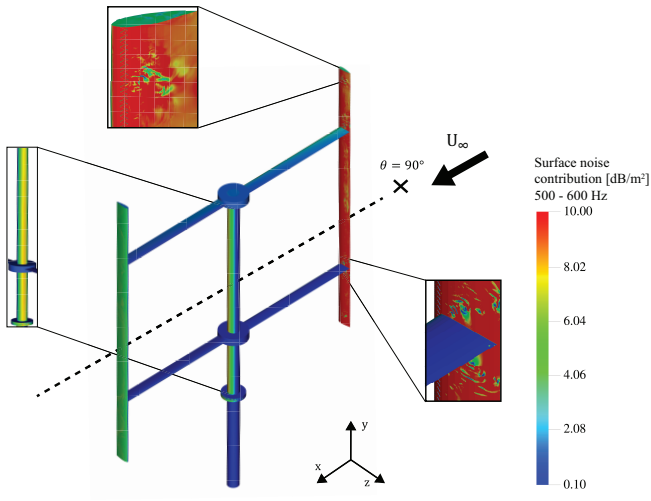
Figure 2.23: FWH integral contribution from a microphone in the x-z plane at $\theta = 90°$.

2.7. CONCLUSIONS

This study assesses the state-of-the-art low-fidelity noise prediction tool for a VAWT operating at a low *Re* number. The two-bladed H-Darrieus PitchVAWT geometry is used, for which experimental aerodynamic data are available. The limitations of the low-fidelity methodology are investigated through a comparison with high-fidelity data. This dataset allows studying the relation between the aerodynamics and the aeroacoustics of the VAWT.

Upwind, the results from the AC model strongly depend on the aerodynamic polars used as input because of the complex flow dynamic of airfoils at low *Re* number [55]. The influence of the polars confirms how a correct flow prediction is essential to correctly predict the VAWT's aerodynamics.

Downwind, differences in trend are found due to the inaccurate prediction of α and V_{rel}. These parameters cannot be correctly computed because the low-fidelity model does not include 3D effects, blade-blade interactions, flow separation, and tower shadow. The occurrence of 3D effects at the tip and the struts, as well as BVI and BWI, is demonstrated with three-dimensional flow visualization through the λ_2 criterion and contour of the instantaneous vorticity magnitude. Contours of the instantaneous stream-wise velocity component also demonstrate flow separation and tower shadow, which enhance the unsteady flow field.

These aerodynamic limitations are reflected in the directivity patterns and the SPLs. The Buck model is proven to accurately predict the T-I noise in the absence of tower shadow. Due to the inaccurate prediction of α and V_{rel} and the assumption of steady flow, the TBL-TE noise and the LBL-VS noise are not correctly modelled with the BPM approach. However, the applications of the model are reasonable since input parameters are varied in a quasi-steady way during the rotations. Overall, from the comparison between the low-fidelity prediction tool and the high-fidelity ones, it is found that they predict the aerodynamics and the aeroacoustics of a VAWT with acceptable accuracy for a preliminary design stage.

BIBLIOGRAPHY

[1] S. Eriksson, H. Bernhoff, and M. Leijon, "Evaluation of different turbine concepts for wind power", *Renewable and Sustainable Energy Reviews*, vol. 12, pp. 1419–1434, 2008. DOI: 10.1016/j.rser.2006.05.017. [Online]. Available: https://doi.org/10.1016/j.rser.2006.05.017.

[2] R. Paterson and R. Amiet, "Noise and surface pressure response of an airfoil to incident turbulence", *Journal of Aircraft*, vol. 14, no. 8, pp. 729–736, 1977. DOI: 10.2514/3.58845. [Online]. Available: https://doi.org/10.2514/3.58845.

[3] T. F. Brooks, S. Pope, and M. A. Marcolini, "Airfoil Self-Noise and Prediction", *NASA Reference Publication 1218*, pp. 1–142, 1989, ISSN: 14786095. DOI: 10.1080/09524622.2008.9753825. [Online]. Available: http://ntrs.nasa.gov/archive/nasa/casi.ntrs.nasa.gov/19890016302.pdf.

[4] A. L. Rogers, J. F. Manwell, and S. Wright, "Wind turbine acoustic noise", Tech. Rep., 2006. DOI: 10.1260/0957456042872777. [Online]. Available: https://docs.wind-watch.org/rogers-windturbinenoise_rev2006.pdf.

[5] S. Buck, S. Oerlemans, and S. Palo, "Experimental characterization of turbulent inflow noise on a full-scale wind turbine", *Journal of Sound and Vibration*, vol. 385, pp. 219–238, 2016. DOI: 10.1016/j.jsv.2016.09.010. [Online]. Available: https://doi.org/10.1016/j.jsv.2016.09.010.

[6] S. Wagner, R. Bareiss, and G. Guidati, *Wind Turbine Noise*. Springer Verlag, 1996, ISBN: 978-3-642-88710-9. DOI: 10.1007/978-3-642-88710-9_1. [Online]. Available: https://doi.org/10.1007/978-3-642-88710-9_1.

[7] J. W. Kim, S. Haeri, and P. F. Joseph, "On the reduction of aerofoil-turbulence interaction noise associated with wavy leading edges", *Journal of Fluid Mechanics*, vol. 792, pp. 526–552, 2016. DOI: 10.1017/jfm.2016.95. [Online]. Available: https://doi.org/10.1017/jfm.2016.95.

[8] J. D. M. Botha, A. Shahroki, and H. Rice, "An implementation of an aeroacoustic prediction model for broadband noise from a vertical axis wind turbine using a CFD informed methodology", *Journal of Sound and Vibration*, vol. 410, pp. 389–415, 2017, ISSN: 0022-460X. DOI: 10.1016/j.jsv.2017.08.038. [Online]. Available: http://dx.doi.org/10.1016/j.jsv.2017.08.038.

[9] C. Pearson, "Vertical Axis Wind Turbine Acoustics", Ph.D. dissertation, Corpus Christi College Cambridge University, 2013. [Online]. Available: https://doi.org/10.17863/CAM.14070.

[10] B. K. Dyne, "Wind turbine noise measurements", Tech. Rep., 2007.

[11]   B. LeBlanc and C. Simão Ferreira, "Experimental Determination of Thrust Loading of a 2-Bladed Vertical Axis Wind Turbine", 2, vol. 1037, 2018. DOI: 10.1088/1742-6596/1037/2/022043. [Online]. Available: https://dx.doi.org/10.1088/1742-6596/1037/2/022043.

[12]   B. LeBlanc and C. Simão Ferreira, "Estimation of blade loads for a variable pitch vertical axis wind turbine from particle image velocimetry", *Wind Energy*, pp. 1–20, 2021, ISSN: 10991824. DOI: 10.1002/we.2674. [Online]. Available: https://doi.org/10.1002/we.2674.

[13]   B. LeBlanc and C. Simão Ferreira, "Overview and Design of PitchVAWT : Vertical Axis Wind Turbine With Active Variable Pitch For Experimental and Numerical Comparison", Kissimmee, Florida, 2018, pp. 1–11, ISBN: 9781624105227. DOI: 10.2514/6.2018-1243. [Online]. Available: https://doi.org/10.2514/6.2018-1243.

[14]   J. E. Ffowcs Williams and D. L. Hawkings, "Sound generation by turbulence and surfaces in arbitray motion", *Philosophical Transactions of the Royal Society of London. Series A, Mathematical and Physical Sciences*, vol. 264, no. 1151, pp. 321–342, 1969. DOI: 10.1098/rsta.1969.0031. [Online]. Available: https://doi.org/10.1098/rsta.1969.0031.

[15]   F. Avallone, D. Ragni, and D. Casalino, "On the effect of the tip-clearance ratio on the aeroacoustics of a diffuser-augmented wind turbine", *Renewable Energy*, vol. 152, pp. 1317–1327, 2020, ISSN: 18790682. DOI: 10.1016/j.renene.2020.01.064. [Online]. Available: https://doi.org/10.1016/j.renene.2020.01.064.

[16]   V. Dighe, F. Avallone, and G. van Bussel, "Effects of yawed inflow on the aerodynamic and aeroacoustic performance of ducted wind turbines", *Journal of Wind Engineering and Industrial Aerodynamics*, vol. 201, p. 104 174, 2020, ISSN: 01676105. DOI: 10.1016/j.jweia.2020.104174. [Online]. Available: https://doi.org/10.1016/j.jweia.2020.104174.

[17]   S. Succi, *The Lattice Boltzmann Equation*, 1st editio. Claredon Press, Oxford, 2001.

[18]   X. Shan, X. F. Yuan, and H. Chen, "Kinetic theory representation of hydrodynamics: a way behond the Navier-Stokes equation", *Journal of Fluid Mechanics*, vol. 550, pp. 413–441, 2006. DOI: 10.1017/S0022112005008153. [Online]. Available: https://doi.org/10.1017/S0022112005008153.

[19]   S. Chen and G. D. Doolen, "Lattice Boltzmann Method for Fluid Flows", *Annual Review of Fluid Mechanics*, vol. 30, no. 1, pp. 329–364, 1998. DOI: 10.1146/annurev.fluid.30.1.329. [Online]. Available: https://doi.org/10.1146/annurev.fluid.30.1.329.

[20]   H. Chen, R. Zhang, and P. Gopalakrishnan, *Lattice Boltzmann Collision Operatos enforcing Isotropy and Galilean Invariance*, 2015. [Online]. Available: https://patents.google.com/patent/US9576087B2/en.

[21]   H. Chen, S. Chen, and W. H. Matthaeus, "Recovery of the Navier-Stokes equations using a lattice-gas Boltzmann method", *Physical Review A*, vol. 45, no. 8, pp. 5339–5342, 1992. DOI: 10.1103/PhysRevA.45.R5339. [Online]. Available: https://doi.org/10.1103/PhysRevA.45.R5339.

[22] S. A. Orszag and V. Yakhot, "Renormalization group analysis of turbulence. I. Basic theory", in *Journal of Scientific Computing*, 1986, pp. 3–51. DOI: 10.1007/BF01061452. [Online]. Available: https://doi.org/10.1007/BF01061452.

[23] C. M. Teixeria, "Incorporating turbulence models into the lattice-boltzmann method", *International Journal of Modern Physics C*, vol. 9, no. 8, pp. 1159–1175, 1998. DOI: 10.1142/S0129183198001060. [Online]. Available: https://doi.org/10.1142/S0129183198001060.

[24] D. Wilcox, *Turbulence Modeling for CFD* (Turbulence Modeling for CFD v. 1). DCW Industries, 2006, ISBN: 9781928729082. [Online]. Available: https://books.google.nl/books?id=q4ypAQAACAAJ.

[25] B. Launder and D. Spalding, "The Numerical Computation of Turbulent Flow Computer Methods", *Computer Methods in Applied Mechanics and Engineering*, vol. 3, pp. 269–289, 1974. DOI: 10.1016/0045-7825(74)90029-2. [Online]. Available: https://doi.org/10.1016/0045-7825(74)90029-2.

[26] G. A. Bres, F. Perot, and D. M. Freed, "Properties of the Lattice – Boltzmann Method for Acoustics", in *15th AIAA/CEAS Aeroacoustic Conference,*, 2009, pp. 2009–3711. DOI: 10.2514/6.2009-3395. [Online]. Available: https://doi.org/10.2514/6.2009-3395.

[27] F. Farassat and G. Succi, "A review of propeller discrete frequency noise prediction technology with emphasis on two current methods for time domain calculations", *Journal of Sound and Vibration*, vol. 71, no. 3, pp. 399–419, 1980. DOI: 10.1016/0022-460X(80)90422-8. [Online]. Available: https://doi.org/10.1016/0022-460X(80)90422-8.

[28] D. Casalino, "An advanced time approach for acoustic analogy predictions", *Journal of Sound and Vibration*, vol. 261, pp. 583–612, 2003. DOI: 10.1016/S0022-460X(02)00986-0. [Online]. Available: https://doi.org/10.1016/S0022-460X(02)00986-0.

[29] R. Courant, K. Friedrichs, and H. Lewy, "On the partial difference equations of mathematical physics", *IBM Journal of Research and Development*, vol. 11, no. 2, pp. 215–234, 1967. DOI: 10.1147/rd.112.0215. [Online]. Available: https://doi.org/10.1147/rd.112.0215.

[30] H. A. Madsen, "The Actuator Cylinder - A Flow Model for Vertical Axis Wind Turbines", Ph.D. dissertation, Aalborg University Centre, 1982. DOI: 10.13140/RG.2.1.2512.3040. [Online]. Available: https://doi.org/10.13140/RG.2.1.2512.3040.

[31] G. Ruijgrok, *Elements of Aviation Acoustics*. 1993, p. 309, ISBN: 90-6275-899-1. [Online]. Available: http://resolver.tudelft.nl/uuid:e4589b31-ffa3-4a5d-9400-1e2b446f60f3.

[32] T. F. Brooks and C. L. Burley, "Rotor broadband noise prediction with comparison to model data", *Journal of the American Helicopter Society*, vol. 49, no. 1, pp. 28–42, 2004. DOI: 10.4050/JAHS.49.28. [Online]. Available: https://doi.org/10.4050/JAHS.49.28.

2

[33]   M. Drela and M. B. Gilest, "Viscous-Inviscid Analysis of Transonic and Low Reynolds Number Airfoils", *AIAA Journal*, vol. 25, no. 10, pp. 1347–1355, 1987. DOI: 10.2514/3.9789. [Online]. Available: https://doi.org/10.2514/3.9789.

[34]   H. A. Madsen, T. J. Larsen, U. S. Paulsen, and L. Vita, "Implementation of the Actuator Cylinder Flow Model in the HAWC2 code for Aeroelastic Simulations on Vertical Axis Wind Turbines", in *51st AIAA Aerospace Sciences Meeting including the New Horizons Forum and Aerospace Exposition*, 2013, pp. 1–12. DOI: 10.2514/6.2013-913. [Online]. Available: https://doi.org/10.2514/6.2013-913.

[35]   J. Katz and A. Plotkin, *Low-Speed Aerodynamics*, 2nd Editio. Cambridge University Press, 2001, ISBN: 9780521665520. DOI: 10.1017/CBO9780511810329. [Online]. Available: https://doi.org/10.1017/CBO9780511810329.

[36]   P. Migliore, W. Wolfe, and J. Fanucci, "Flow curvature effects on darrieus turbine blade aerodynamics", *Journal of Energy*, vol. 4, no. 2, pp. 49–55, 1980. DOI: 10.2514/3.62459. [Online]. Available: https://doi.org/10.2514/3.62459.

[37]   J. Leishman and T. Beddoes, "A Semi-Empirical Model for Dynamic Stall", *Journal of the American Helicopter Society*, vol. 34, no. 3, pp. 3–17, 1989. DOI: 10.4050/JAHS.34.3.3. [Online]. Available: https://doi.org/10.4050/JAHS.34.3.3.

[38]   D. De Tavernier, "Aerodynamic advances in vertical-axis wind turbines", Ph.D. dissertation, 2021, ISBN: 9789055841745. [Online]. Available: https://doi.org/10.4233/uuid:7086f01f-28e7-4e1b-bf97-bb3e38dd22b9.

[39]   S. Lee, "Source Characterization of Turbulent Boundary Layer Trailing Edge Noise Using an Improved TNO Model", in *Aeroacoustics Conference*, American Institute of Aeroacoustics and Astronautics, 2016, pp. 1–28. DOI: 10.2514/6.2016-2812. [Online]. Available: https://doi.org/10.2514/6.2016-2812.

[40]   W. K. Blake, *Mechanics of Flow-Induced Sound and Vibration, Volume 2*. 2017, p. 694, ISBN: 9780128122907. DOI: 10.1016/B978-0-12-809274-3.00006-4. [Online]. Available: https://doi.org/10.1016/B978-0-12-809274-3.00006-4.

[41]   R. Parchen, "Progress report DRAW: A Prediction Scheme for Trailing-Edge Noise Based on Detailed Boundary-Layer Characteristics", TNO institute of Applied Physics, Tech. Rep., 1998. [Online]. Available: https://books.google.nl/books?id=t8LYtgAACAAJ.

[42]   M. V. Lowson and J. B. Ollerhead, "A theoretical study of helicopter noise", *Journal of Sound and Vibration*, vol. 9, no. 2, pp. 197–222, 1969. DOI: 10.1016/0022-460X(69)90028-5. [Online]. Available: https://doi.org/10.1016/0022-460X(69)90028-5.

[43]   P. Moriarty and P. Migliore, "Semi-Empirical Aeroacoustic Noise Prediction Code for Wind Turbines", National Renewable Energy Laboratory, Tech. Rep., 2003. DOI: 10.2172/15006098. [Online]. Available: https://doi.org/10.2172/15006098.

2

[44] P. A. Davidson, *Turbulence: An introduction for Scientists and Engineers (2nd edn)*. Oxford University Press, 2015. DOI: 10.1093/acprof:oso/9780198722588.001.0001. [Online]. Available: https://doi.org/10.1093/acprof:oso/9780198722588.001.0001.

[45] G. I. Taylor, "Statistical theory of turbulence", pp. 421–444, 1935, ISSN: 0080-4630. DOI: 10.1098/rspa.1935.0158. [Online]. Available: https://doi.org/10.1098/rspa.1935.0158.

[46] G. Tescione, "On the aerodynamics of a vertical axis wind turbine wake: An experimental and numerical study", Ph.D. dissertation, Delft University of Technology, 2016, ISBN: 9789462994621. DOI: 10.4233/uuid. [Online]. Available: https://doi.org/10.4233/uuid:86ac7352-46b8-4c2d-9014-817472d80174.

[47] C. Noyes, C. Qin, E. Loth, and S. Schreck, "Measurements and predictions of wind turbine tower shadow and fairing effects", *Journal of Wind Engineering and Industrial Aerodynamics*, vol. 179, pp. 297–307, 2018, ISSN: 0167-6105. DOI: https://doi.org/10.1016/j.jweia.2018.06.012. [Online]. Available: http://www.sciencedirect.com/science/article/pii/S0167610518301065.

[48] B. LeBlanc and C. Simão Ferreira, "Estimation of blade loads for a variable pitch Vertical Axis Wind Turbine with strain gage measurements", *Wind Energy*, pp. 1–16, 2022, ISSN: 10991824. DOI: 10.1002/we.2713. [Online]. Available: https://doi.org/10.1002/we.2713.

[49] C. Simão Ferreira, G. van Kuik, G. van Bussel, and F. Scarano, "Visualization by PIV of dynamic stall on a vertical axis wind turbine", *Experiments in Fluids*, no. 46, pp. 97–108, 2009. DOI: 10.1007/s00348-008-0543-z. [Online]. Available: https://doi.org/10.1007/s00348-008-0543-z.

[50] P. F. Melani, F. Balduzzi, L. Brandetti, C. Simão Ferreira, and A. Bianchini, "An experimental and numerical analysis of the dynamic variation of the angle of attack in a vertical-axis wind turbine", in *Journal of Physics: Conference Series*, vol. 1618, 2020. DOI: 10.1088/1742-6596/1618/5/052064. [Online]. Available: https://dx.doi.org/10.1088/1742-6596/1618/5/052064.

[51] P. F. Melani, F. Balduzzi, G. Ferrara, and A. Bianchini, "How to extract the angle attack on airfoils in cycloidal motion from a flow field solved with computational fluid dynamics? Development and verification of a robust computational procedure", *Energy Conversion and Management*, vol. 223, p. 113 284, 2020, ISSN: 01968904. DOI: 10.1016/j.enconman.2020.113284. [Online]. Available: https://doi.org/10.1016/j.enconman.2020.113284.

[52] A. Rezaeiha, H. Montazeri, and B. Blocken, "Characterization of aerodynamic performance of vertical axis wind turbines : Impact of operational parameters", *Energy Conversion and Management*, vol. 169, pp. 45–77, 2018, ISSN: 0196-8904. DOI: 10.1016/j.enconman.2018.05.042. [Online]. Available: https://doi.org/10.1016/j.enconman.2018.05.042.

[53] W. R. Graham and C. E. Pearson, "Noise from a Model-Scale Vertical-Axis Wind Turbine", *AIAA Journal*, vol. 60, no. 1, pp. 224–235, 2022. DOI: 10.2514/1.J060531. [Online]. Available: https://doi.org/10.2514/1.J060531.

2

[54] D. Casalino, E. Grande, G. Romani, D. Ragni, and F. Avallone, "Definition of a benchmark for low Reynolds number propeller aeroacoustics", *Aerospace Science and Technology*, vol. 113, p. 106 707, 2021, ISSN: 12709638. DOI: 10.1016/j.ast.2021.106707. [Online]. Available: https://doi.org/10.1016/j.ast.2021.106707.

[55] W. L. Traub, "Experimental investigation of the effect of trip strips at low Reynolds number", *Journal of Aircraft*, vol. 48, no. 5, pp. 1776–1784, 2011. DOI: 10.2514/1.C031375. [Online]. Available: https://doi.org/10.2514/1.C031375.

2

3

THE WSE-TSR TRACKING CONTROLLER AND THE ILL-CONDITIONING PROBLEM

In recent years, industrial controllers for modern wind turbines have been designed as a combined wind speed estimator and tip-speed ratio (WSE-TSR) tracking control scheme. In contrast to the conventional and widely used $K\omega^2$ torque control strategy, the WSE-TSR scheme provides flexibility in terms of controller responsiveness and potentially improves power extraction performance. However, both control schemes heavily rely on prior information about the aerodynamic properties of the turbine rotor. Using a control-oriented linear analysis framework, this chapter shows that the WSE-TSR scheme is inherently ill-conditioned. The ill-conditioning is defined as the inability of the scheme to uniquely determine the wind speed from the product with other model parameters in the power balance equation. Uncertainty of the power coefficient contribution in the latter-mentioned product inevitably leads to a biased effective wind speed estimate. As a consequence, in the presence of uncertainty, the real-world wind turbine deviates from the intended optimal operating point, while the controller believes that the turbine operates at the desired set-point. Simulation results confirm that inaccurate model parameters lead to biased estimates of the actual turbine operating point, causing sub-optimal power extraction efficiency.

3.1. INTRODUCTION

Wind energy plays a crucial role in the global energy mix as its installed power capacity continues to increase [1]. After the Glasgow climate summit, the net-zero emissions targets set for the middle of the century pose ambitious goals for the wind industry [2]. To efficiently achieve these goals, the sizes of wind turbines increase dramatically. Larger turbines together with a more flexible rotor assembly and support structure, result in a rising demand for optimization of wind turbine controllers [3].

Modern wind turbines usually employ a variable-speed variable-pitch (VS-VP) operating strategy and thereby use generator torque control to maximise energy capture in below-rated operating conditions [4], [5]. Until recently, the most common partial load wind turbine torque control strategy is the so-called $K\omega^2$ controller, being a fixed mapping as a function of the generator speed [6]. This control scheme has predefined control responsiveness and relies heavily on modeled aerodynamic rotor characteristics. As a partial solution, the current practice in industrial controllers for modern turbines is to use a combined wind-speed estimator and tip-speed ratio (WSE-TSR) tracking control scheme.

The TSR tracker aims to maximise and improve on power extraction by employing a dynamical controller implementation, allowing for an adaptable control responsiveness compared to the conventional $K\omega^2$ controller [4], [7]. The WSE-TSR tracking control scheme typically includes a wind speed estimator that, like the $K\omega^2$ controller, relies on information about aerodynamic rotor characteristics and other (environmental) properties. Inaccuracy in this information inevitably leads to biased wind speed estimates, resulting in sub-optimal turbine operation by the TSR tracking controller.

This chapter shows that the WSE-TSR tracking control scheme is still highly dependent on prior information about the wind turbine. More specifically, the TSR tracker lacks information when coupled with a wind speed estimator giving rise to the so-called ill-conditioning described in this chapter. This ill-conditioning prevents a unique estimation of the wind speed from the product with other model parameters in the power balance equation, and hinders the determination of the true turbine operating point. For the case under study, uncertainty in the power coefficient mapping results in a biased wind speed estimate from the actual effective wind speed. Because the estimated wind speed is subsequently used in the calculation of the feedback signal to the TSR tracker, this difference results in sub-optimal operational performance of the real-world turbine. In contrast, the controller believes to satisfy the desired optimal operating condition.

To the authors' knowledge, no detailed study of the WSE-TSR tracking control scheme is available in the literature. To this end, the current chapter outlines how the framework is generally implemented and thereby presents the following contributions:

- Formalising the problem of ill-conditioning, showing that this leads to steady-state biased wind speed (and thus tip-speed ratio) estimates and thus sub-optimal power tracking.

- Providing an analytical frequency-domain framework which gives an in-depth analysis of the working mechanisms of the controller, and which is used to analyse the problem of ill-conditioning.

The chapter is structured as follows: Section 3.2 gives a mathematical overview of the WSE-TSR tracking control scheme together with the assumptions made when analysing the scheme. The problem of ill-conditioning is formalised in Section 3.3. Section 3.4 presents the frequency-domain framework used to analyse the WSE-TSR scheme and the problem of ill-conditioning by deriving the most relevant transfer functions. Both a time-domain and a frequency-domain analysis of the framework is performed in Section 3.5 for different uncertainty in the modeled parameters. Finally, Section 3.6 summarises the main findings and recommendations for future work.

3.2. METHODOLOGY

While the exact implementation might differ between turbines, the general framework of the WSE-TSR control scheme is outlined in this section and is used for analysis throughout the chapter. As illustrated in Figure 3.1, the framework consists of the wind turbine, the rotor-effective wind speed estimator and the controller. The red box highlights the real wind turbine system with two inputs (the generator torque T_g, and the wind speed V), and with two outputs (the rotational speed ω_r, and the TSR λ). The measured T_g and ω_r are used to estimate the rotor-effective wind speed $\hat{V}$ and to calculate an estimate of the TSR $\hat{\lambda}$, in the estimator block. The estimated TSR is then fed back to the controller block to close the loop. By applying the TSR tracking control scheme, the turbine is ideally forced to operate at the optimal TSR λ^*, which corresponds to the rotor operating point for maximum power extraction efficiency C_p^*. In the following subsections, the wind turbine, the wind speed estimator and the controller are presented in detail, together with the assumptions made when analysing the framework.

3.2.1. ASSUMPTIONS

The first step in analysing the framework is the formulation of the assumptions under which the WSE-TSR tracking control scheme is operated.

Assumption 1. *The WSE-TSR tracking scheme is analysed in the below-rated region with a constant (fine-)pitch angle β, where the power coefficient $C_p(\cdot)$ is solely a function of the*
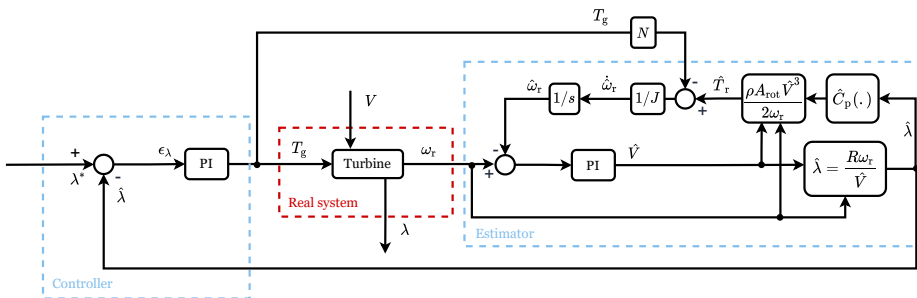
Figure 3.1: Block diagram of the WSE-TSR control framework: the wind turbine (*i.e.* the real system, **red** box), the tip-speed ratio (TSR) tracker (*i.e.* the controller) and the wind speed estimator (**cyan** boxes). The wind speed estimate $\hat{V}$, is used to calculate an estimation of tip-speed ratio $\hat{\lambda}$, which in turn is employed as a feedback signal to close the loop by the TSR tracking controller.

tip-speed ratio $\lambda := \omega_r R / V$, with R being the rotor radius, ω_r the measured rotor speed, and V the rotor-effective wind speed.

Assumption 2. *The generator torque T_g, and the rotational speed ω_r, are measured signals and the wind speed V, is an unknown positive signal.*

Assumption 3. *The equivalent inertia of the low-speed generator shaft J, the air density ρ, and the rotor swept area A_{rot}, are equal for the real wind turbine and for the estimator.*

Assumption 4. *The drive-train efficiency η, which is defined as the ratio between the generator power and the rotor power, is set to 1.*

3.2.2. WIND TURBINE

The dynamics of the wind turbine are given by

$$J\dot{\omega}_r = T_r - T_g N, \tag{3.1}$$

where J is obtained from the relation $J = J_g N^2 + J_r$. The inertias of the generator and rotor are J_g and J_r, respectively, and $N := \omega_g / \omega_r$ represents the gearbox ratio of the transmission with ω_g being the generator speed. According to Assumption 1, the aerodynamic rotor torque is given by

$$T_r := \frac{1}{2} \rho A_{rot} \frac{V^3}{\omega_r} C_p(\lambda). \tag{3.2}$$

3.2.3. ESTIMATOR

The rotor-effective wind speed is estimated based on the extended Immersion and Invariance (I&I) estimator with a Proportional and Integral (PI) correction term [8], [9], which is illustrated in Figure 3.2. Note that $\hat{V}$ indicates the estimated wind speed, while $\bar{V}$ corresponds to the steady-state wind speed. Given Assumption 2, the wind speed estimator can be formulated as follows

$$\begin{cases} J\dot{\hat{\omega}}_r = \hat{T}_r - T_g N \\ \epsilon_{\omega_r} = \omega_r - \hat{\omega}_r \\ \hat{V} = K_{p,w} \epsilon_{\omega_r} + K_{i,w} \int_0^t \epsilon_{\omega_r}(\tau) d\tau \end{cases}, \tag{3.3}$$

with t being the present time, τ the variable of integration, $K_{p,w}$ the proportional gain and $K_{i,w}$ the integral gain of the estimator. By adding the integrator, the extended formula given by Equation (3.3) forces the error ϵ_{ω_r} to converge to zero, providing consistent estimates of not only the wind speed, but also of the rotor speed $\hat{\omega}_r$ [8]. The estimated aerodynamic torque is defined as

$$\hat{T}_r := \frac{1}{2} \rho A_{rot} \frac{\hat{V}^3}{\omega_r} \hat{C}_p(\hat{\lambda}). \tag{3.4}$$

In this case, $\hat{C}_p$ is the estimated power coefficient and the nonlinear mapping $\hat{C}_p(\cdot)$ is a function of the estimated TSR $\hat{\lambda} := \omega_r R / \hat{V}$.
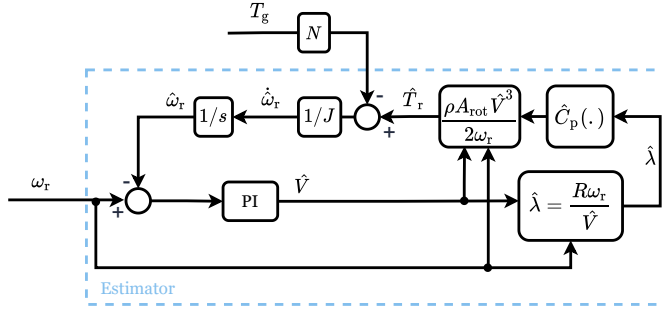
Figure 3.2: Block diagram of the extended I&I estimator with a Proportional and Integral (PI) correction term [8], [9]. The measured generator torque T_g, and rotational speed ω_r, are used to estimate the rotor-effective wind speed $\hat{V}$, and to calculate an estimate of TSR $\hat{\lambda}$.

3.2.4. CONTROL STRATEGY

A simple PI controller, acting on the TSR error, $\epsilon_\lambda := \lambda^* - \hat{\lambda}$, is used to calculate a generator torque demand to track λ^* as

$$T_g = K_{p,c}\epsilon_\lambda + K_{i,c}\int_0^t \epsilon_\lambda(\tau)\mathrm{d}\tau\,,\tag{3.5}$$

where $K_{p,c}$ and $K_{i,c}$ are the proportional and integral gains of the TSR tracking controller, respectively [4].

3.3. FORMULATION OF THE ILL-CONDITIONING

Upon closer inspection, the framework is found to be ill-conditioned. This section reveals the cause of the ill-conditioning and thus formulates the problem.

Ideally, in steady-state conditions and under Assumption 4, when the TSR tracker is applied, the actual aerodynamic rotor power P_r, equals the desired power P_d, that results as a set-point from the control scheme. This observation is mathematically formalised by:

$$P_r = P_d \quad \rightarrow \quad \frac{1}{2}\rho A_{rot}V^3 C_p(\lambda) = \frac{1}{2}\rho A_{rot}\hat{V}^3\hat{C}_p(\hat{\lambda})\,.\tag{3.6}$$

With Assumption 3, Equation (3.6) is simplified as:

$$V^3 C_p(\lambda) = \hat{V}^3\hat{C}_p(\hat{\lambda})\,.\tag{3.7}$$

Subject to a WSE-TSR tracking control scheme and in steady-state, Equation (3.7) should always be satisfied. Whilst the wind-speed-power-coefficient product is uniquely estimated, the individual values of the power coefficient and the wind speed cannot be uniquely estimated due to a lack of information in the framework, giving rise to the so-called ill-conditioning.

To further illustrate the effect of the ill-conditioning in the definition of the estimated quantities, the uncertainty in the model parameters is represented by:

$$\hat{V} := \frac{V}{\gamma^{1/3}}\,, \qquad \text{and} \qquad \hat{C}_p(\hat{\lambda}) := \gamma C_p(\lambda)\,,\tag{3.8}$$

with γ being a constant uncertainty factor. When $\hat{C}_\mathrm{p}(\hat{\lambda})$ differs from $C_\mathrm{p}(\lambda)$ then $\hat{V}$ will be biased to satisfy Equation (3.7). This is what defines the ill-conditioning problem when a WSE-TSR tracking control scheme is implemented. As will be shown in Sections 3.4 and 3.5, such ill-conditioning may introduce significant effects on the WSE-TSR tracking control scheme.

3.4. FREQUENCY-DOMAIN FRAMEWORK

This section provides the analytical frequency-domain framework used to describe the working mechanisms of the WSE-TSR tracking control scheme and to evaluate the problem of the ill-conditioning. To analyse the control scheme in the frequency domain, the dynamics of the nonlinear system are linearised at a specific operating point, defined by $(\bar{\omega}_\mathrm{r}, \bar{V})$. The relevant transfer functions are then derived and provided for the individual and combined subsystems in the subsequent sections. The resulting frequency-domain framework takes into account model uncertainty (Equation (3.8)) to study the problem of the ill-conditioning.

3.4.1. WIND TURBINE ROTOR DYNAMICS

By applying Equation (3.1) at the linearization point and in terms of the Laplace variable s, an expression for the dynamic response of the turbine rotor can be obtained

$$\omega_\mathrm{r}(s)s = D\omega_\mathrm{r}(s) + E T_\mathrm{g}(s) + B V(s), \tag{3.9}$$

where

$$D = \frac{1}{J}\frac{\partial T_\mathrm{r}}{\partial \omega_\mathrm{r}}\bigg|_{(\bar{\omega}_\mathrm{r}, \bar{V})} = \frac{1}{2J}\rho A_\mathrm{rot}\left(-\frac{\bar{V}^3}{\bar{\omega}_\mathrm{r}^2}C_\mathrm{p}(\bar{\omega}_\mathrm{r}, \bar{V}) + \frac{\bar{V}^2 R}{\bar{\omega}_\mathrm{r}}\frac{\partial C_\mathrm{p}(\omega_\mathrm{r}, V)}{\partial \lambda}\bigg|_{(\bar{\omega}_\mathrm{r}, \bar{V})}\right), \tag{3.10}$$

$$E = -\frac{1}{J}N, \tag{3.11}$$

$$B = \frac{1}{J}\frac{\partial T_\mathrm{r}}{\partial V}\bigg|_{(\bar{\omega}_\mathrm{r}, \bar{V})} = \frac{1}{2J}\rho A_\mathrm{rot}\left(\frac{3\bar{V}^2}{\bar{\omega}_\mathrm{r}}C_\mathrm{p}(\bar{\omega}_\mathrm{r}, \bar{V}) - \bar{V}R\frac{\partial C_\mathrm{p}(\omega_\mathrm{r}, V)}{\partial \lambda}\bigg|_{(\bar{\omega}_\mathrm{r}, \bar{V})}\right). \tag{3.12}$$

3.4.2. ESTIMATOR DYNAMICS

Similarly, the estimated rotor speed dynamics are formulated as

$$\hat{\omega}_\mathrm{r}(s)s = \hat{D}\omega_\mathrm{r}(s) + E T_\mathrm{g}(s) + \hat{B}\hat{V}(s), \tag{3.13}$$

where

$$\hat{D} = \frac{1}{J}\frac{\partial \hat{T}_\mathrm{r}}{\partial \omega_\mathrm{r}}\bigg|_{(\bar{\omega}_\mathrm{r}, \bar{V})} = \frac{1}{2J}\rho A_\mathrm{rot}\left(-\frac{\bar{V}^3}{\bar{\omega}_\mathrm{r}^2}\hat{C}_\mathrm{p}(\bar{\omega}_\mathrm{r}, \bar{V}) + \frac{\bar{V}^2 R}{\bar{\omega}_\mathrm{r}}\frac{\partial \hat{C}_\mathrm{p}(\omega_\mathrm{r}, V)}{\partial \lambda}\bigg|_{(\bar{\omega}_\mathrm{r}, \bar{V})}\right), \tag{3.14}$$

$$E = -\frac{1}{J}N, \tag{3.15}$$

$$\hat{B} = \frac{1}{J}\frac{\partial \hat{T}_\mathrm{r}}{\partial \hat{V}}\bigg|_{(\bar{\omega}_\mathrm{r}, \bar{V})} = \frac{1}{2J}\rho A_\mathrm{rot}\left(\frac{3\bar{V}^2}{\bar{\omega}_\mathrm{r}}\hat{C}_\mathrm{p}(\bar{\omega}_\mathrm{r}, \bar{V}) - \bar{V}R\frac{\partial \hat{C}_\mathrm{p}(\omega_\mathrm{r}, V)}{\partial \lambda}\bigg|_{(\bar{\omega}_\mathrm{r}, \bar{V})}\right). \tag{3.16}$$

Given Equation (3.3), the expression for $\hat{V}$ can also be written in the frequency domain as

$$\hat{V}(s) = \left(K_{p,w} + \frac{K_{i,w}}{s}\right)(\omega_r(s) - \hat{\omega}_r(s)). \tag{3.17}$$

3.4.3. COUPLED WIND TURBINE AND ESTIMATOR DYNAMICS

The next step in the analysis is to derive the transfer function of the coupled wind turbine and estimator dynamics, as sketched in Figure 3.3. By combining Equations (3.9), (3.13) and (3.17), it is possible to express the estimated TSR as a function of T_g and V

$$\hat{\lambda}(s) = \frac{R}{\bar{V}}\omega_r(s) - \frac{R\bar{\omega}_r}{\bar{V}^2}\hat{V}(s) \tag{3.18}$$

$$= L_1(s)T_g(s) + L_2(s)V(s) \tag{3.19}$$

$$= \hat{\lambda}_{T_g}(s) + \hat{\lambda}_V(s). \tag{3.20}$$

where $L_1(s)$ is the transfer function of $\hat{\lambda}$ to T_g

$$L_1(s) = \frac{\hat{\lambda}_{T_g}(s)}{T_g(s)} \tag{3.21}$$

$$= \frac{RE\left[s^2 + \left(\hat{B} - \frac{\bar{\omega}_r}{\bar{V}}(D - \hat{D})\right)K_{p,w}s + \left(\hat{B} - \frac{\bar{\omega}_r}{\bar{V}}(D - \hat{D})\right)K_{i,w}\right]}{\bar{V}(s - D)(s^2 + \hat{B}K_{p,w}s + \hat{B}K_{i,w})}, \tag{3.22}$$

and $L_2(s)$ is the transfer function of $\hat{\lambda}$ to V

$$L_2(s) = \frac{\hat{\lambda}_V(s)}{V(s)} \tag{3.23}$$

$$= \frac{RB\left(F_1s^2 + F_2 s + F_3\right)}{\bar{V}(s - D)(s^2 + \hat{B}K_{p,w}s + \hat{B}K_{i,w})}. \tag{3.24}$$

The terms $F_1 = (1 - (\bar{\omega}_r/\bar{V})K_{p,w})$, $F_2 = \left(\hat{B}K_{p,w} + (\bar{\omega}_r/\bar{V})\hat{D}K_{p,w} - (\bar{\omega}_r/\bar{V})K_{i,w}\right)$ and $F_3 = \left(\hat{B} - (\bar{\omega}_r/\bar{V})\hat{D}\right)K_{i,w}$ are used to make Equation (3.24) more compact.

By considering the effect of model uncertainty (Equation (3.8)), the wind speed estimator dynamics can be expressed as a function of the wind turbine dynamics as $\hat{D} = \gamma D$. According to the definition of ill-conditioning in Equation (3.7), the absence of model mismatch results in $\gamma = 1$, and $\hat{D} = D$. Thus, the transfer function $L_1(s)$ can be simplified as

$$L_1(s)\Big|_{\gamma=1} = \frac{RE}{\bar{V}(s - D)}. \tag{3.25}$$

On the other hand, if $\gamma \neq 1$, then $D - \hat{D} = D(1 - \gamma)$. It follows that

$$L_1(s)\Big|_{\gamma \neq 1} = \frac{RE\left[s^2 + \left(\hat{B} - \frac{\bar{\omega}_r}{\bar{V}}D(1 - \gamma)\right)K_{p,w}s + \left(\hat{B} - \frac{\bar{\omega}_r}{\bar{V}}D(1 - \gamma)\right)K_{i,w}\right]}{\bar{V}(s - D)(s^2 + \hat{B}K_{p,w}s + \hat{B}K_{i,w})}. \tag{3.26}$$

The following analysis employs the γ parameter to evaluate the effect of model uncertainty.
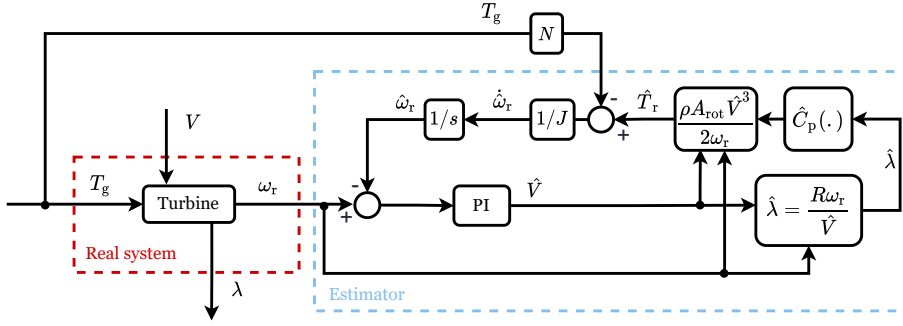
Figure 3.3: Block diagram of the coupled real system (**red** box) and the wind speed estimator (**cyan** box). The measured generator torque T_g, and rotational speed ω_r, from the wind turbine, are used to compute an estimate of the wind speed $\hat{V}$, and of the TSR $\hat{\lambda}$, in the estimator block.

3.4.4. COUPLED WIND TURBINE AND COMBINED ESTIMATOR-CONTROLLER SCHEME DYNAMICS

The closed-loop dynamics of the overall framework, illustrated in Figure 3.1, is obtained by coupling the wind turbine with the combined estimator-controller dynamics.

By applying both the definition of ϵ_λ and Equation (3.5), the estimated TSR can be expressed as a function of λ^* and V to obtain the closed-loop dynamics of the system

$$\hat{\lambda}(s) = L_3(s)\lambda^*(s) + L_4(s)V(s) \tag{3.27}$$

$$= \hat{\lambda}_{\lambda^*}(s) + \hat{\lambda}_V(s), \tag{3.28}$$

where $L_3(s)$ is the transfer function from $\hat{\lambda}$ to λ^*

$$L_3(s) = \frac{\hat{\lambda}_{\lambda^*}(s)}{\lambda^*(s)} \tag{3.29}$$

$$= \frac{F_4}{\bar{V}s(s-D)(s^2 + \hat{B}K_{p,w}s + \hat{B}K_{i,w}) + F_4}, \tag{3.30}$$

and $L_4(s)$ is the transfer function from $\hat{\lambda}$ to V

$$L_4(s) = \frac{\hat{\lambda}_V(s)}{V(s)} = \frac{RB(F_1 s^2 + F_2 s + F_3)s}{\bar{V}s(s-D)(s^2 + \hat{B}K_{p,w}s + \hat{B}K_{i,w}) + F_4}, \tag{3.31}$$

with $F_4 = RE\left[s^2 + \left(\hat{B} - (\bar{\omega}_r/\bar{V})D(1-\gamma)\right)K_{p,w}s + \left(\hat{B} - (\bar{\omega}_r/\bar{V})D(1-\gamma)\right)K_{i,w}\right](K_{p,c}s + K_{i,c})$.

In the absence of model uncertainty, $\gamma = 1$, $L_3(s)$ can be simplified as

$$L_3(s)\Big|_{\gamma=1} = \frac{RE(K_{p,c}s + K_{i,c})}{\bar{V}s^2 + (REK_{p,c} - \bar{V}D)s + REK_{i,c}}. \tag{3.32}$$

To analyse the ill-conditioning problem, it is also important to express the actual tip-speed ratio of the wind turbine λ, as a function of λ^* and V. By following the same derivation of Equations (3.18) and (3.27), this results in

$$\lambda(s) = L_5(s)\lambda^*(s) + L_6(s)V(s) \tag{3.33}$$

$$= \lambda_{\lambda^*}(s) + \lambda_{\mathrm{V}}(s), \tag{3.34}$$

where $L_5(s)$ is the transfer function from λ to λ^*

$$L_5(s) = \frac{\lambda_{\lambda^*}(s)}{\lambda^*(s)} \tag{3.35}$$

$$= \frac{RE\left(s^2 + \hat{B}K_{\mathrm{p,w}}s + \hat{B}K_{\mathrm{i,w}}\right)\left(K_{\mathrm{p,c}}s + K_{\mathrm{i,c}}\right)}{\bar{V}s(s-D)(s^2 + \hat{B}K_{\mathrm{p,w}}s + \hat{B}K_{\mathrm{i,w}}) + F_4}, \tag{3.36}$$

and $L_6(s)$ is the transfer function from λ to V

$$L_6(s) = \frac{\lambda_{\mathrm{V}}(s)}{V(s)} \tag{3.37}$$

$$= \frac{R\left[F_5 + F_6\left(\bar{V}s(s-D)(s^2 + \hat{B}K_{\mathrm{p,w}}s + \hat{B}K_{\mathrm{i,w}}) + F_4\right)\right]}{\bar{V}(s-D)\left(\bar{V}s(s-D)(s^2 + \hat{B}K_{\mathrm{p,w}}s + \hat{B}K_{\mathrm{i,w}}) + F_4\right)}. \tag{3.38}$$

with $F_5 = -REB\left(K_{\mathrm{p,c}}s + K_{\mathrm{i,c}}\right)\left(F_1 s^2 + F_2 s + F_3\right)$ and $F_6 = (\bar{\omega}_{\mathrm{r}}/\bar{V})s + (\bar{\omega}_{\mathrm{r}}/\bar{V})D + B$.

If there is no model mismatch, $\gamma = 1$, $L_5(s)$ can be simplified and results in the same expression as $L_3(s)$

$$L_5(s)\Big|_{\gamma=1} = \frac{RE(K_{\mathrm{p,c}}s + K_{\mathrm{i,c}})}{\bar{V}s^2 + (REK_{\mathrm{p,c}} - \bar{V}D)s + REK_{\mathrm{i,c}}}. \tag{3.39}$$

3.4.5. FRAMEWORK DYNAMICS
In summary, the transfer functions $L_3(s)$ and $L_5(s)$, characterise the closed-loop dynamics of the WSE-TSR tracking control scheme and will be used in the rest of the chapter to assess the ill-conditioning problem

$$L_3(s) = \frac{\hat{\lambda}_{\lambda^*}(s)}{\lambda^*(s)} = \frac{RE\left[s^2 + \left(\hat{B} - \frac{\bar{\omega}_{\mathrm{r}}}{\bar{V}}D(1-\gamma)\right)K_{\mathrm{p,w}}s + \left(\hat{B} - \frac{\bar{\omega}_{\mathrm{r}}}{\bar{V}}D(1-\gamma)\right)K_{\mathrm{i,w}}\right]\left(K_{\mathrm{p,c}}s + K_{\mathrm{i,c}}\right)}{\bar{V}s(s-D)(s^2 + \hat{B}K_{\mathrm{p,w}}s + \hat{B}K_{\mathrm{i,w}}) + F_4}, \tag{3.40}$$

$$L_5(s) = \frac{\lambda_{\lambda^*}(s)}{\lambda^*(s)} = \frac{RE\left(s^2 + \hat{B}K_{\mathrm{p,w}}s + \hat{B}K_{\mathrm{i,w}}\right)\left(K_{\mathrm{p,c}}s + K_{\mathrm{i,c}}\right)}{\bar{V}s(s-D)(s^2 + \hat{B}K_{\mathrm{p,w}}s + \hat{B}K_{\mathrm{i,w}}) + F_4}. \tag{3.41}$$

3.5. RESULTS
In this section, the WSE-TSR tracking control scheme is analysed both in the time domain and in the frequency domain. The effect of the ill-conditioning on the scheme is studied by simulating different uncertainty levels in the modelled parameters.
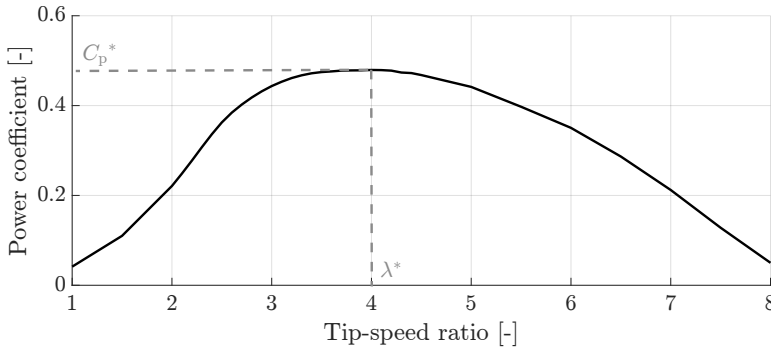
Figure 3.4: Power coefficient for the H-Darrieus VAWT for a pitch angle of $0°$ [10].

3.5.1. CASE STUDY

In this chapter, it is of interest to study a 1.5 m two-bladed H-Darrieus vertical-axis wind turbine (VAWT) [10] but the analysis can also be performed for a horizontal-axis wind turbine (HAWT). The $C_p(\lambda)$ curve of the studied VAWT is depicted in Figure 3.4 for $\beta = 0°$. The optimal TSR $\lambda^* = 4$ corresponds to $C_p^* = 0.47$.

3.5.2. EFFECT OF MODEL UNCERTAINTY

The effect of the uncertainty in the model parameters is investigated by simulating two extreme cases: $\gamma = 0.8$ and $\gamma = 1.2$. The I&I gains, $K_{p,w} = 20$ and $K_{i,w} = 50$, are selected and result in satisfactory estimator performance. The TSR tracker gains, $K_{p,c} = -10$ and $K_{i,c} = -0.5$, are tuned to achieve a balance between the performance and robustness of the PI controller [4].

Figure 3.5 summarises the steady-state results for two different wind speeds, *i.e.* $V = 4$ m/s and $V = 5$ m/s. When there is no model mismatch, T_g matches the optimal operating condition (*i.e.* the cross-point of the aerodynamic torque and the optimal steady-state trajectory). With an uncertainty in the modelled parameters, the system moves away from the optimal condition. According to Equation (3.8), when the magnitude of $\hat{C}_p$ is decreased ($\gamma = 0.8$), the wind speed is overestimated, resulting in a lower steady-state T_g from the TSR tracking controller. On the other hand, when $\hat{C}_p$ used by the wind speed estimator is increased ($\gamma = 1.2$), the wind speed is underestimated and the wind turbine operates at a lower λ in reality.

Figures 3.6 and 3.7 show how these trends propagate to the other variables in the framework. In this case, the wind turbine operates under a realistic turbulent wind field with a mean wind speed of 4 m/s and a turbulence intensity of 5% for 600 s. As can be observed, $\hat{V}$ is overestimated for $\gamma = 0.8$ while it is underestimated for $\gamma = 1.2$. Thus, the controller framework tracks λ^* using the estimated feedback quantity $\hat{\lambda}$, but in reality, the turbine's actual tip-speed ratio λ has a bias to the reference value. Since the wind turbine is not operating at its optimal operating point, the aerodynamic power extraction efficiency is suboptimal. Specifically, for $\gamma = 0.8$, a reduction in power of 1 % is obtained.

These observations are further supported by inspection of the frequency response of the system closed-loop transfer functions, $L_3(s)$ and $L_5(s)$ in Figure 3.8. The tuning of
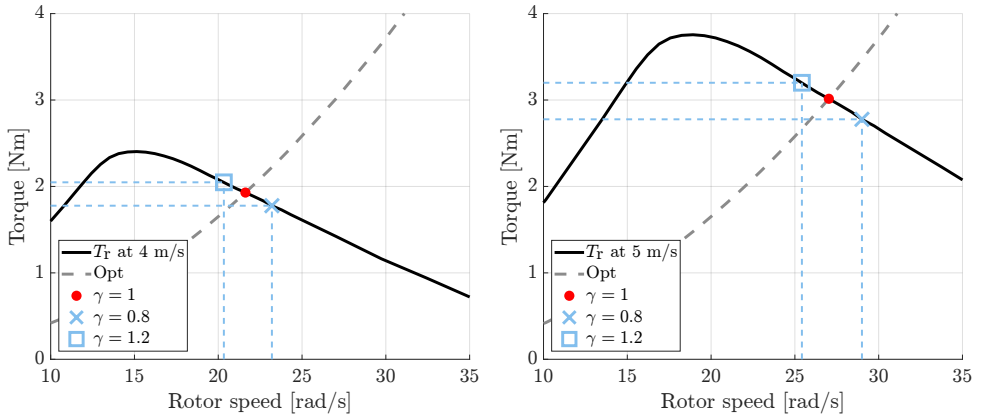
Figure 3.5: Torque-versus-speed response of the WSE-TSR tracking control scheme for two different wind speeds: 4 m/s (left-hand) and 5 m/s (right-hand)
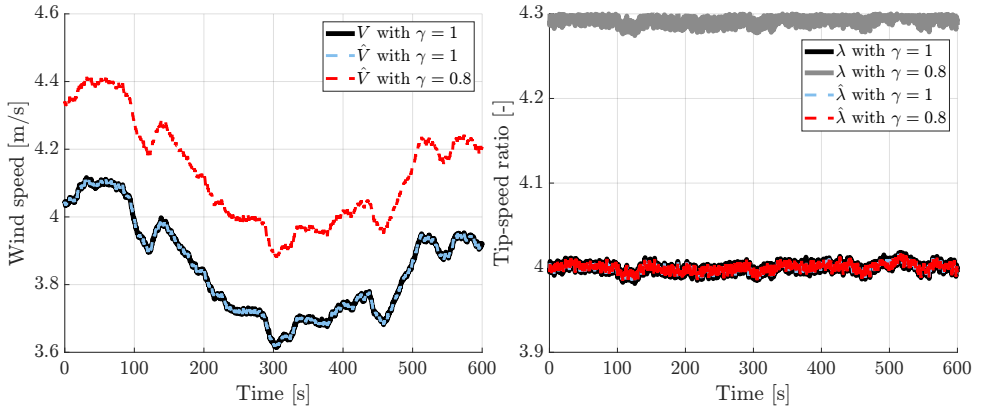
Figure 3.6: Simulation results showing the wind speed and the tip-speed ratio for an underestimation of C_p under a realistic turbulent wind profile.

the wind speed estimator gains is adapted to emphasise the effect of model uncertainty. Upon closer inspection, the frequency responses show differences in the static gains. Even with the presence of model uncertainty, the static gain of $L_3(s)$ will always be zero proving that the controller presumes to track the optimal condition (*i.e.* $\hat{\lambda} = \lambda^*$). However, in reality, the wind turbine will not operate at the point of maximum power extraction (*i.e.* $\lambda \neq \lambda^*$) as confirmed by the static gains of $L_5(s)$, which differ from zero in the presence of a model mismatch.

3.6. CONCLUSIONS

In this study, the WSE-TSR tracking controller scheme is studied in detail. Due to a lack of information in the scheme, the wind speed cannot be uniquely estimated from the product with other model parameters in the power balance equation. This results
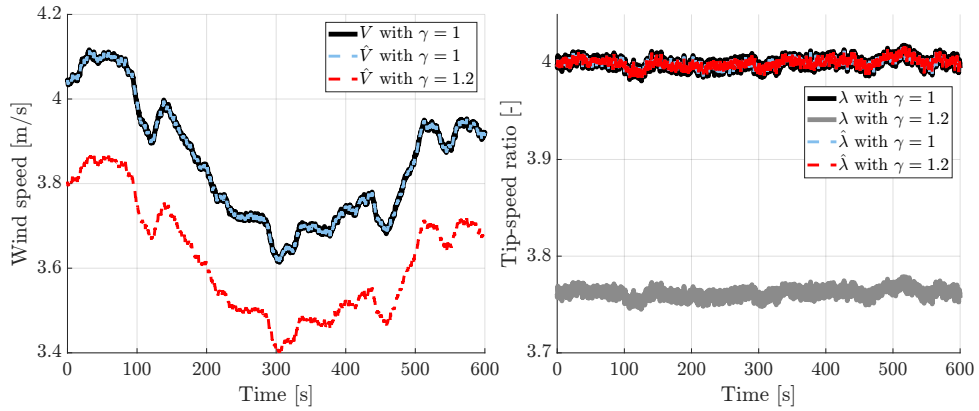
Figure 3.7: Simulation results showing the wind speed and the tip-speed ratio for an overestimation of C_{p} under a realistic turbulent wind profile.
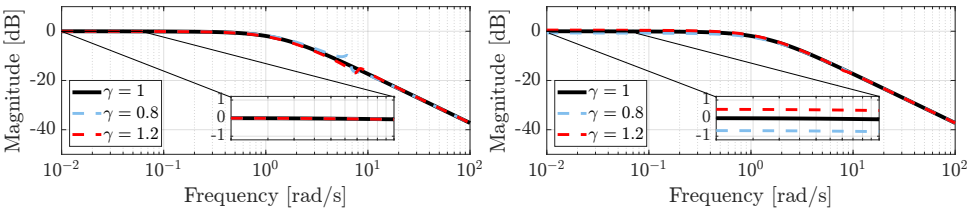
Figure 3.8: Frequency response of $L_3(s)$ and $L_5(s)$ under different model uncertainty and with an incorrect tuning of the wind speed estimator gains.

in the so-called ill-conditioning, leading to biased wind speed estimates and reduced energy capture under model uncertainty. A linear frequency-domain analysis has been performed by deriving transfer functions characterising the WSE-TSR tracking scheme, and are used to evaluate the problem of ill-conditioning. It is shown that uncertainty in modelled turbine parameters can lead to erroneous tracking of the optimal aerodynamic performance.

BIBLIOGRAPHY

[1]   A. Dalla Riva, J. Hethey, and A. Vitina, "IEA Wind TCP Task 26 - Impacts of Wind Turbine Technology on the System Value of Wind in Europe", Tech. Rep., 2017. [Online]. Available: https://www.nrel.gov/docs/fy18osti/70337.pdf.

[2]   *UN Climate change conference UK 2021*, 2021. [Online]. Available: https://ukcop26.org/cop26-goals/.

[3]   G. A. M. van Kuik, J. Peinke, R. Nijssen, D. Lekou, J. Mann, J. N. Sørensen, C. Simão Ferreira, J. W. van Wingerden, D. Schlipf, P. Gebraad, H. Polinder, A. Abrahamsen, G. J. W. van Bussel, J. D. Sørensen, P. Tavner, C. L. Bottasso, M. Muskulus, D. Matha, H. J. Lindeboom, S. Degraer, O. Kramer, S. Lehnhoff, M. Sonnenschein, P. E. Sørensen, R. W. Künneke, P. E. Morthorst, and K. Skytte, "Long-term research challenges in wind energy- A research agenda by the European Academy of Wind Energy", *Wind Energy Science*, vol. 1, no. 1, pp. 1–39, 2016. DOI: 10.5194/wes-1-1-2016. [Online]. Available: https://wes.copernicus.org/articles/1/1/2016/.

[4]   E. A. Bossanyi, "The Design of closed loop controllers for wind turbines", *Wind Energy*, vol. 3, no. 3, pp. 149–163, 2000. DOI: 10.1002/we.34. [Online]. Available: https://doi-org.tudelft.idm.oclc.org/10.1002/we.34.

[5]   S. P. Mulders, M. B. Zaaijer, R. Bos, and J. W. van Wingerden, "Wind turbine control: Open-source software for control education, standardization and compilation", in *Journal of Physics: Conference Series*, vol. 1452, 2020. DOI: 10.1088/1742-6596/1452/1/012010. [Online]. Available: https://iopscience-iop-org.tudelft.idm.oclc.org/article/10.1088/1742-6596/1452/1/012010.

[6]   L. Y. Pao and K. E. Johnson, "Control of wind turbines: Approaches, challenges, and recent developments", *IEEE Control Systems Magazine*, vol. 31, no. 2, pp. 44–62, 2011. DOI: 10.1109/MCS.2010.939962. [Online]. Available: https://ieeexplore-ieee-org.tudelft.idm.oclc.org/document/5730721.

[7]   F. Bonaccorso, G. Scelba, A. Consoli, and G. Muscato, "EKF - Based MPPT control for vertical axis wind turbines", in *IECON 2011 - 37th Annual Conference of the IEEE Industrial Electronics Society*, 2011, pp. 3614–3619. DOI: 10.1109/IECON.2011.6119896. [Online]. Available: https://ieeexplore-ieee-org.tudelft.idm.oclc.org/document/6119896.

[8]   Y. Liu, A. K. Pamososuryo, R. M. G. Ferrari, and J. W. van Wingerden, "The Immersion and Invariance Wind Speed Estimator Revisited and New Results", *IEEE Control Systems Letters*, vol. 6, pp. 361–366, 2022. DOI: 10.1109/LCSYS.2021.3076040. [Online]. Available: https://ieeexplore-ieee-org.tudelft.idm.oclc.org/document/9416566.

[9]   R. Ortega, F. Mancilla-David, and F. Jaramillo, "A globally convergent wind speed
      estimator for wind turbine systems", *International Journal of Adaptive Control and
      Signal Processing*, vol. 27, pp. 413–425, 2013. DOI: 10.1002/acs.2319. [Online].
      Available: https://doi-org.tudelft.idm.oclc.org/10.1002/acs.2319.

[10] B. LeBlanc and C. Simão Ferreira, "Experimental Determination of Thrust Loading
      of a 2-Bladed Vertical Axis Wind Turbine", 2, vol. 1037, 2018. DOI: 10.1088/1742-
      6596/1037/2/022043. [Online]. Available: https://dx.doi.org/10.1088/
      1742-6596/1037/2/022043.

3

4

ANALYSIS AND MULTI-OBJECTIVE CONTROLLER OPTIMISATION

The combined wind speed estimator and tip-speed ratio (WSE-TSR) tracking wind turbine control scheme has seen recent and increased traction from the wind industry. The modern control scheme provides a flexible trade-off between power and load objectives. On the other hand, the $K\omega^2$ controller is often used based on its simplicity and steady-state optimality and is taken as a baseline here. This chapter investigates the potential benefits of the WSE-TSR tracking controller compared to the baseline by analysis through a frequency-domain framework and by optimal calibration through a systematic procedure. A multi-objective optimisation problem is formulated for calibration with the conflicting objectives of power maximisation and torque fluctuations minimisation. The optimisation problem is solved by approximating the Pareto front based on the set of optimal solutions found by an explorative search. The Pareto fronts were obtained by mid-fidelity simulations with the NREL 5 MW turbine under turbulent wind conditions for calibration of the baseline and for increasing fidelities of the WSE-TSR tracking controller. Optimisation results show that the WSE-TSR tracking controller does not provide further benefits in energy capture compared to the baseline $K\omega^2$ controller. There is, however, a trade-off in torque control variance and power capture with control bandwidth. By lowering the bandwidth at the expense of generated power of 2%, the torque actuation effort reduces by 80% with respect to the optimal calibration corresponding to the highest control bandwidth.

4.1. INTRODUCTION

Of all the available renewable energy sources, wind energy is increasingly considered one of the most cost-effective and sustainable with regard to the global demand for clean energy [1]. The total present wind power capacity installed worldwide is now 837 GW, with year-on-year growth of 12% [2]. However, this growth rate must quadruple by the end of the decade to meet the net-zero emissions targets set after the Glasgow climate summit [3], [4]. To achieve these ambitious climate goals in an efficient manner, the industry is developing larger turbines with a more flexible rotor assembly and support structure to exploit higher wind speeds [5]. Increasingly advanced and optimised control technologies are needed to facilitate and enable the increased sizes of wind turbines [6].

Variable-speed turbines usually employ a generator torque control strategy to maximise the energy capture in partial load conditions [7], [8]. Maximum power is extracted by operating the turbine at the maximum power coefficient, corresponding to a specific tip-speed ratio and pitch angle [9]. The optimal tip-speed ratio is tracked by varying the generator torque resulting from a closed-loop controller, while the pitch angle is generally kept constant in the partial load region [6].

Nowadays, the $K\omega^2$ controller is still a commonly considered partial load region wind turbine torque control strategy due to its satisfactory performance, ease of derivation, and simple implementation by only requiring a measurement of the rotor or generator speed [10], [11]. Nevertheless, the $K\omega^2$ controller has shortcomings that can result in suboptimal power tracking performance [12]. First, the torque gain K is calculated from modelled wind turbine properties, often subject to assumptions and estimation errors [13]. Even if the gain K is initially accurate, the turbine properties can change over time due to, e.g. blade erosion and ice/dirt/bug buildup, thereby causing this initial value to be suboptimal [10], [12]. For instance, according to Fingersh and Carlin [14], a 5% error in the optimal tip-speed ratio can lead to inaccurate K and, consequently, to a cumulative captured energy loss of 1% - 3%. Second, suppose the wind turbine operates in turbulent wind conditions and that K is accurately determined. In that case, the large rotor inertia prevents fast acceleration and thus hinders the tracking of rapid changes in wind speed, leading to a lower operating power coefficient [7]. This problem is emphasised for heavy rotors and sharp power coefficient curves.

The torque gain K can be calibrated through an Extremum Seeking Control (ESC) acting on the rotor power to overcome the effect of time-varying wind turbine properties [15]. While providing an energy capture improvement of 8% - 12% when applied on the Controls Advanced Research Turbine (CART), this control scheme results in being sensitive to wind speed variations [16]. Therefore, Rotea [17] proposes a log-of-power feedback in the ESC algorithm (LP-ESC). Using high-fidelity large eddy simulations, Ciri et al. [18] demonstrate that this modification renders the controller independent from changes in the mean wind speed.

One way to increase the energy capture for higher turbulence intensity is by reducing the gain K below the nominal value. This choice allows the generator torque to decrease and the rotor to accelerate more quickly in response to a gust. For instance,in the study conducted by Johnson et al. [12], a reduction of 10% in the gain K for CART rotor's controller resulted in a measurable increase of 0.5% in captured power. his gain reduction strategy, aimed at enhancing energy capture, is not limited to the CART rotor alone; it

holds the potential for implementation on any existing wind turbine employing the $K\omega^2$ controller. It is important to note that there is no discernible linear correlation between the gain reduction factor and the specific site conditions. Consequently, it becomes evident that the extent of increased captured power is contingent upon the turbulent wind conditions and the characteristics of the particular turbine in use. Given this variability, selecting a constant value for the gain reduction factor is deemed impractical [12].

To provide better rotor acceleration and deceleration, Fingersh and Carlin [14] proposed the optimally tracking rotor (OTR) controller. This scheme augments the $K\omega^2$ controller with a second term. The additional term is a gain multiplied by the net torque, being the difference between the (estimated) aerodynamic torque and the generator torque contribution resulting from the $K\omega^2$ control law. Subtracting the new term from the original formulation will aid rotor acceleration or deceleration if the wind speed increases or decreases. With this approach applied to the CART, the controller bandwidth for tracking the actual optimal operating point is increased, thereby improving the energy capture by about 1.2% [14]. However, the OTR control scheme relies heavily on correct knowledge of the aerodynamic rotor properties. Incorrect information will inevitably lead to suboptimal operation in transient and steady-state conditions. Another more advanced turbine controller was developed by van der Hooft et al. [19] and includes pseudo-feedforward control based on an estimation of the rotor-effective wind speed (REWS) to realise an additional pitch control action in partial load. With this strategy, an energy yield increase of 0.9% was achieved at the expense of larger speed and load variations.

To cope with the described disadvantages of the $K\omega^2$ control scheme, combined wind speed estimator and tip-speed ratio (WSE-TSR) tracking control schemes have been recently considered [13]. The idea behind this scheme is to use the estimated REWS [20], [21] to calculate an estimate of the desired rotor speed, which in turn is employed as a feedback signal to close the loop by a PI controller. According to Bossanyi [7], this controller allows tracking the optimal tip-speed ratio even in turbulent wind, with a 1% power increase compared to the baseline $K\omega^2$, but at the expense of significant power variations.

In the work of Boukhezzar and Siguerdidjane [22], a Kalman filter estimator combined with a rotor speed reference tracking improves by 10% the power capture when compared with the $K\omega^2$ controller, but no analytical demonstration of its dynamic behaviour was provided. A similar study by Abbas et al. [13] focused only on a time-domain analysis when comparing the combined estimator-feedback controller with the $K\omega^2$ control law. Earlier work by the current authors [23] proved that an analytical frequency-domain framework could be a valuable tool for analysing the dynamics of the WSE-TSR tracking controller. However, neither the performance benefits of using such a control scheme over the baseline $K\omega^2$ controller nor the optimal calibration are discussed in [23].

Therefore, this chapter presents the steady-state equivalence and dynamic differences between these $K\omega^2$ and WSE-TSR tracking controllers and proposes a systematic procedure for optimal calibration. Calibration of the parameters in the WSE-TSR tracking control scheme is fundamental to optimising controller performance in terms of power maximisation, load minimisation and stability [7].

However, the use of classical analysis techniques to calibrate the proposed scheme is

complex due to the trade-off between conflicting control requirements, e.g. maximising power production and minimising the loads. Recent studies [24], [25] have demonstrated the effectiveness of multi-objective optimisation techniques based on Pareto fronts for tuning wind turbine controllers. For this reason, the calibration of the WSE-TSR tracking controller is formulated as a multi-objective optimisation problem. First, the parameter space of the considered control scheme is explored by a guided search procedure. Subsequently, the set of optimal solutions is found to construct the Pareto front in a trade-off between power maximisation and load minimisation. The solutions found are then assessed using the extended version of the frequency-domain framework, based on [23], for comparison with the baseline controller. As also shown by Leith and Leithead [26], analysing a controller in the frequency domain allows for gathering relevant insights into its performance. Therefore, applying a frequency-domain framework to evaluate the optimal solutions found by solving the multi-objective optimisation problem enables linking the conflicting control objectives with the stability and performance of the closed-loop system in terms of controller bandwidth.

In this context, the present research aims to illustrate the additional benefits of using the WSE-TSR tracking controller compared to the baseline $K\omega^2$ for partial load control when applied to realistic wind turbine sizes, in terms of two performance metrics widely discussed in the literature: power maximisation and load minimisation [26], [27]. Thereby, the following contributions are presented:

- Demonstrating the steady-state similarities and dynamic differences between the WSE-TSR tracking control scheme and the baseline $K\omega^2$ controller in the frequency domain by a universal linear analysis framework.

- Mapping the performance of the fixed-structure WSE-TSR tracking controller for sets of calibration parameters of increasing dimensionality by a guided exploratory search in their constrained parameter spaces.

- Formulating the optimal calibration as a multi-objective problem using Pareto front approximation techniques.

- Exploiting the frequency-domain framework in conjunction with mid-fidelity simulations under realistic environmental conditions to showcase and discover the characteristics of an *optimally* calibrated WSE-TSR tracking control scheme to the baseline strategy.

The chapter is structured as follows: the assumptions made for the implementation of the WSE-TSR tracking control scheme and baseline $K\omega^2$ controller are described in Section 4.2, while Section 4.3 gives their mathematical overview. Based on the nonlinear implementation, Section 4.4 provides a linear frequency-domain framework analysing the two controllers. Section 4.5 illustrates the exploration and multi-objective Pareto optimisation strategy for calibrating the WSE-TSR tracking control scheme. Section 4.6 evaluates the performance of the calibrated WSE-TSR tracking scheme compared to the baseline controller by leveraging the results from the frequency-domain analysis framework and the ones derived from realistic mid-fidelity time-domain simulations. Finally, Section 4.7 summarises the main findings and recommendations for future work.

4.2. PREREQUISITES

This section provides the prerequisites needed for the analysis of the controllers. Estimated quantities and time derivatives are indicated by $\hat{(\cdot)}$ and $\dot{(\cdot)}$, respectively. Values corresponding to a specific operating point are denoted by $\bar{(\cdot)}$, whereas values indicating the intended optimal parameters are presented with $(\cdot)_*$. The symbols ω_r, T_g, V and λ, represent the rotational speed, the generator torque, the wind speed and the tip-speed ratio signals in the time domain, while Ω_r, $\mathcal{T}_g$, $\mathcal{V}$ and Λ represent the corresponding signals in the frequency domain.

In addition, this work relies on a set of assumptions, which are formulated as follows:

Assumption 5. *The considered control schemes are analysed in the partial load region with a constant (fine-)pitch angle. For this reason, the power coefficient mapping is only taken as a function of the tip-speed ratio.*

Assumption 6. *The generator torque control input and the rotational speed of the turbine are measured signals. The rotor-effective wind speed is considered an unknown and positive disturbance input to the plant.*

Assumption 7. *The turbine model information included in the estimator and control framework represents the actual turbine characteristics. This assumption highlights the best-case performance benefits achievable with the WSE-TSR tracking control scheme over the baseline $K\omega^2$ control strategy without capturing the inherent uncertainties of real-world turbine dynamics.*

4.3. THEORY OF PARTIAL-LOAD CONTROL SCHEMES

The baseline $K\omega^2$ controller is a well-known, effective and commonly used torque control strategy for maximising energy capture in the partial load operating region [7]. Whereas the $K\omega^2$ strategy provides satisfactory performance, it is inflexible in providing a granular trade-off between power and load objectives for present-day wind turbines. Therefore, modern large-scale wind turbines are controlled by more advanced WSE-TSR tracking schemes [28], and wind turbine manufacturers are currently exploring the possibilities of applying model predictive control (MPC) to provide such flexibility [29], [30]. This work focuses on comparing the baseline strategy, with the first being the WSE-TSR tracking control scheme, which is also often referred to as a power coefficient C_p-tracking scheme in other works [7]. In this section, first, the $K\omega^2$ and the WSE-TSR tracking control schemes are derived in their full and nonlinear representations. To this end, the wind turbine system is considered, and the individual required component building blocks are obtained for completing the two schemes.

4.3.1. WIND TURBINE

The wind turbine system is represented by the first-order model

$$J\dot{\omega}_r = T_r - T_g N, \tag{4.1}$$

where ω_r represents the rotor speed, and J is the total drivetrain inertia at the low-speed shaft (LSS) side, obtained from the relation $J = J_g N^2 + J_r$, with J_g and J_r, respectively, representing the generator and rotor inertias. The gearbox ratio is defined as the transmission

ratio $N = \omega_g/\omega_r$, with ω_g representing the generator speed. The turbine is considered to be subject to a torque control input $T_g \in \mathbb{R}$, and, according to Assumption 5, the aerodynamic rotor torque is given by

$$T_r = \frac{1}{2}\rho A_{rot}\frac{V^3}{\omega_r}C_p(\lambda), \tag{4.2}$$

where ρ represents the air density, A_{rot} is the rotor-swept area, $V \in \mathbb{R}$ is the rotor-effective wind speed (REWS) and $C_p(\cdot)$ is the power coefficient, being a function of the tip-speed ratio

$$\lambda = \frac{\omega_r R}{V}, \tag{4.3}$$

with R being the rotor radius. The shape of the $C_p(\cdot)$ curve depends on the design of the turbine and can be computed either from numerical simulations or experimental data. For this study, the National Renewable Energy Laboratory (NREL) 5 MW wind turbine model [31] is used, for which the $C_p(\cdot)$ curve covering the operating region of interest is illustrated in Figure 4.1. The presented curve is obtained from steady-state wind turbine simulations for a wind profile with a uniform velocity of 9 m/s. It can be observed that a

Table 4.1: Main operational parameters for the National Renewable Energy Laboratory (NREL) 5 MW [31].

Description	Symbol	Value	Unit
Generator inertia	J_g	543.116	kg m^2
Rotor inertia	J_r	35.444×10^6	kg m^2
Total drive train inertia at the low-speed shaft	J	40.470×10^6	kg m^2
Gearbox ratio	N	97	-
Air density	ρ	1.225	kg m^{-3}
Fine pitch angle	β_0	0	rad
Rotor radius	R	63	m
Optimal tip-speed ratio	λ_*	7.2	-
Optimal power coefficient	C_p	0.4623	-
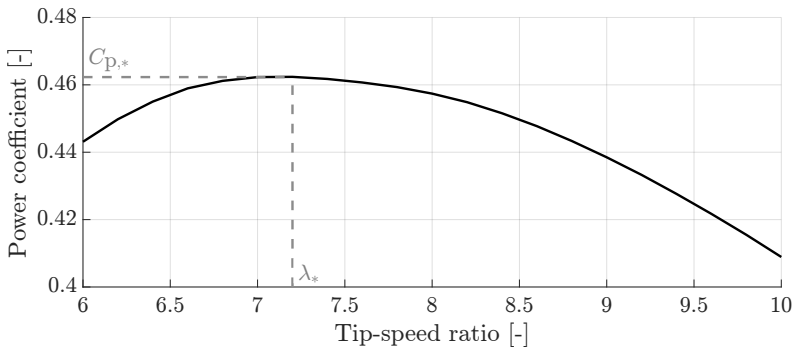
Figure 4.1: Power coefficient for the NREL 5 MW wind turbine model [31] under a uniform wind speed of 9 m/s. The maximum power extraction efficiency and the corresponding optimal tip-speed ratio are indicated as $C_{p,*}$ and λ_*, respectively.

constant λ_* exists, which corresponds to the rotor operating point for maximum power extraction efficiency $C_{p,*}(\lambda_*)$. In the remainder of this chapter, a distinction is made between the torque controller input variable for the two schemes, namely, $T_{g,K}$ and $T_{g,TSR}$, for the baseline $K\omega^2$ or WSE-TSR tracking controller, respectively.

4.3.2. BASELINE $K\omega^2$ CONTROLLER

The derivation of the baseline $K\omega^2$ control law is presented in this section. Figure 4.2 illustrates a block diagram of the controller, and as shown, the framework only consists of the wind turbine and the controller. The controller is a static (nonlinear) function without dynamics, providing the generator torque control signal based on the rotor speed:

$$T_{g,K} = K\frac{\omega_r^2}{N}, \tag{4.4}$$

in which the torque gain K [7] is defined at the LSS side of the drivetrain as

$$K = \frac{\rho A_{rot} R^3 C_{p,*}(\lambda_*)}{2\lambda_*^3}, \tag{4.5}$$

under Assumption 5.
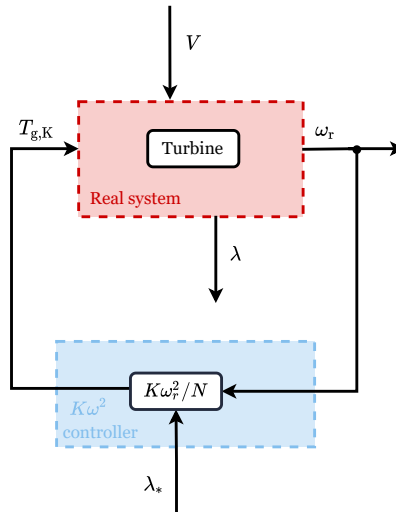
Figure 4.2: Block diagram of the $K\omega^2$ control framework. The **red** box highlights the wind turbine system with two inputs (the generator torque $T_{g,K}$, and the wind speed V), and with two outputs (the rotational speed, ω_r, and the TSR, λ). The measured ω_r and the optimal TSR, λ_*, are used as inputs of the controller (**cyan** box) to compute $T_{g,K}$.
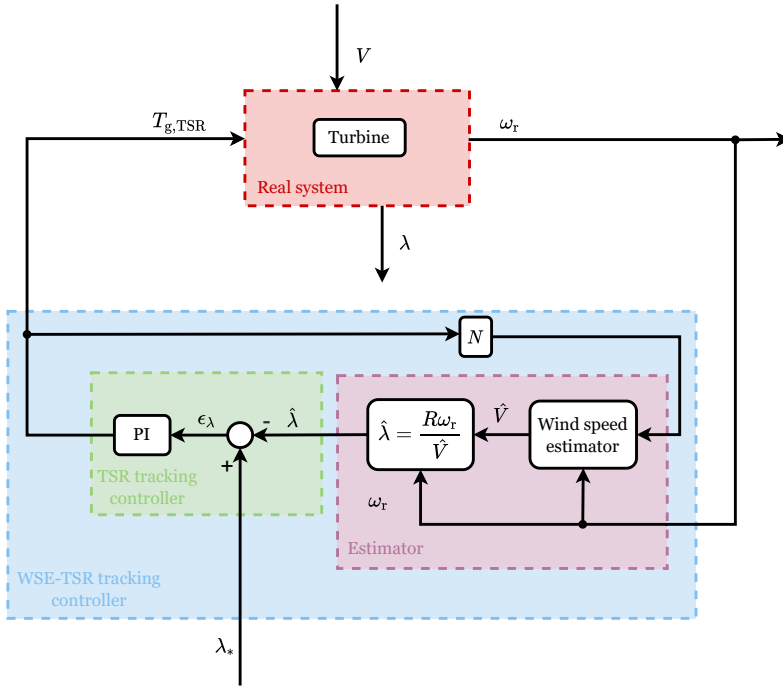
Figure 4.3: Block diagram of the WSE-TSR tracking control framework. The **red** box highlights the wind turbine system with two inputs (the generator torque $T_{g,TSR}$, and the wind speed V), and with two outputs (the rotational speed, ω_r, and the TSR, λ). The **cyan** box highlights the WSE-TSR tracking controller, which includes the estimator (**purple** box) and the TSR tracker controller (**green** box). The measured $T_{g,TSR}$ and ω_r are used to estimate the rotor-effective wind speed $\hat{V}$ and to calculate an estimate of TSR, $\hat{\lambda}$, in the estimator block. The controller acts on the difference between $\hat{\lambda}$ and the optimal TSR, λ_*, to calculate the torque control signal $T_{g,TSR}$.

4.3.3. WSE-TSR TRACKING CONTROLLER

The WSE-TSR tracking framework, outlined in Figure 4.3, combines an estimator and a tip-speed ratio tracking controller. The estimator provides the tip-speed ratio estimate $\hat{\lambda}$, which is used by the controller that acts on the difference between the estimate and the tip-speed ratio reference. This reference is usually taken as λ_*, corresponding to the rotor operating point for maximum power extraction efficiency C_p^*. The controller provides the torque control signal $T_{g,TSR}$ and forces the turbine to track the reference. The following section provides derivations of commonly used implementations for both elements in the WSE-TSR tracking framework.

WIND SPEED ESTIMATOR

The REWS is estimated based on the Immersion and Invariance (I&I) estimator[33] with an augmented integral correction term [32]. The estimator is illustrated in Figure 4.4 and uses the control signal, the measured system plant output and a nonlinear plant model to

estimate the REWS. Given Assumptions 6 and 7, the estimator is formulated as follows

$$
\begin{cases}
J\hat{\dot{\omega}}_\mathrm{r} = \hat{T}_\mathrm{r} - T_{\mathrm{g,TSR}}N \\
\epsilon_{\omega_\mathrm{r}} = \omega_\mathrm{r} - \hat{\omega}_\mathrm{r} \\
\hat{V} = K_{\mathrm{p,w}}\epsilon_{\omega_\mathrm{r}} + K_{\mathrm{i,w}}\int_0^t \epsilon_{\omega_\mathrm{r}}(\tau)\mathrm{d}\tau
\end{cases}, \tag{4.6}
$$

with $\hat{V}$ indicating the estimated REWS, $K_{\mathrm{p,w}}$ the proportional estimator gain, and $K_{\mathrm{i,w}}$ the integral estimator gain. Furthermore, t indicates the present time, and τ is the variable of integration. By adding integral action to the estimator, the error $\epsilon_{\omega_\mathrm{r}}$ is forced to converge to zero, providing consistent estimates of the rotor speed state $\hat{\omega}_\mathrm{r}$. Under Assumption 5, the estimated aerodynamic torque is defined as

$$
\hat{T}_\mathrm{r} = \frac{1}{2}\rho A_\mathrm{rot}\frac{\hat{V}^3}{\omega_\mathrm{r}}\hat{C}_\mathrm{p}(\hat{\lambda}), \tag{4.7}
$$

where $\hat{C}_\mathrm{p}(\cdot)$ is the estimated power coefficient, being a nonlinear function of the estimated tip-speed ratio $\hat{\lambda} = \omega_\mathrm{r}R/\hat{V}$.

TIP-SPEED RATIO TRACKING CONTROLLER

The proportional and integral (PI) controller in the WSE-TSR tracking scheme acts on the tip-speed ratio error, which is defined as

$$
\epsilon_\lambda = \lambda_* - \hat{\lambda}, \tag{4.8}
$$

being the difference between reference and estimated tip-speed ratio. This error is used to compute the generator torque demand

$$
T_{\mathrm{g,TSR}} = K_{\mathrm{p,c}}\epsilon_\lambda + K_{\mathrm{i,c}}\int_0^t \epsilon_\lambda(\tau)\mathrm{d}\tau, \tag{4.9}
$$

where $K_{\mathrm{p,c}}$ and $K_{\mathrm{i,c}}$ are the respective proportional and integral controller gains.
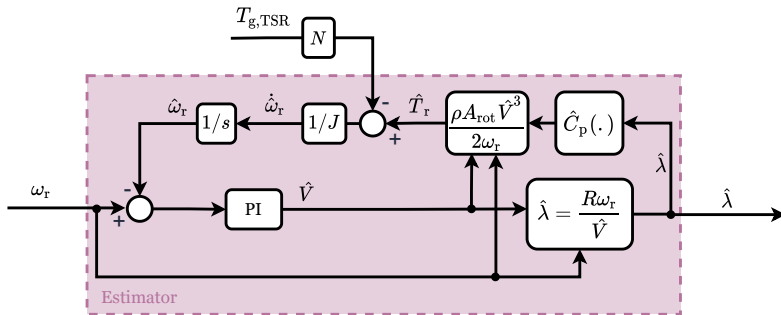

Figure 4.4: Block diagram of the estimator [32], [33]. The measured generator torque, $T_{\mathrm{g,TSR}}$, and rotational speed, ω_r, are used to estimate the REWS, $\hat{V}$, and to calculate an estimate of the TSR, $\hat{\lambda}$.

4.4. Frequency-domain framework

This section provides the linear frequency-domain framework for analysing the baseline $K\omega^2$ and the WSE-TSR tracking controllers, where the dynamics of the nonlinear system are linearised around a specific operating point. The subscripts $(\cdot)_K$ and $(\cdot)_{TSR}$ are employed to distinguish the transfer functions for the two schemes. Following the structure of Section 4.4 and in the subsequent subsections, the relevant transfer functions are first derived and provided for the wind turbine dynamics, followed by the individual and combined subsystems for the considered control schemes.

The presented framework has undergone rigorous verification procedures. Firstly, it was validated through linearisation of the fully-coupled and nonlinear system, using a numerical control system linearisation tool [34]. This initial step ensured the accuracy and reliability of our framework. Its correctness is further validated by comparison to the linearisation results for the same coupled system in related published work [28]. To ensure the applicability of the framework in real-world scenarios, extensive time-domain simulations of the nonlinear model were conducted using the mid-fidelity software OpenFAST [35]. These simulations provide empirical evidence of the effectiveness of the framework in capturing system dynamics. It is important to note that, in the interest of brevity and focus, the detailed verification process is not included in this chapter.

4.4.1. Wind turbine dynamics

This section considers the linearisation of the wind turbine dynamics. The differential equation in Equation (4.1) is first combined with the nonlinear expression for the aerodynamic rotor torque defined in Equation (4.2). Subsequently, the resulting expression is linearised with respect to the rotor speed state, generator torque control input, and wind speed disturbance input, resulting in

$$\dot{\omega}_r = G(V)\,\omega_r + E\,T_g + H(V)\,V. \tag{4.10}$$

For reasons of conciseness, the values perturbed around their operating points are defined using the same original variables. The introduced variables representing partial derivatives are defined as

$$G(V) = \frac{1}{J}\frac{\partial T_r}{\partial \omega_r}\bigg|_{(\bar{\omega}_r,\bar{V})} = \frac{1}{2J}\rho A_{rot}\left(-\frac{V^3}{\omega_r^2}C_p(\omega_r,V) + \frac{V^2 R}{\omega_r}\frac{\partial C_p(\omega_r,V)}{\partial \lambda}\right)\bigg|_{(\bar{\omega}_r,\bar{V})}, \quad E = -\frac{N}{J}, \tag{4.11}$$

$$H(V) = \frac{1}{J}\frac{\partial T_r}{\partial V}\bigg|_{(\bar{\omega}_r,\bar{V})} = \frac{1}{2J}\rho A_{rot}\left(\frac{3V^2}{\omega_r}C_p(\omega_r,V) - VR\frac{\partial C_p(\omega_r,V)}{\partial \lambda}\right)\bigg|_{(\bar{\omega}_r,\bar{V})}. \tag{4.12}$$

The argument V is included here to allow for the convenient definition of estimator-based expressions for G and H in a later section; however, the argument is omitted in expressions from this point onwards. Finally, the linearised expression is Laplace transformed to obtain the following

$$(s-G)\Omega_r(s) = E\mathcal{T}_g(s) + H\mathcal{V}(s),$$

where s represents the Laplace operator. The resulting equation is defined to give the rotor speed

$$\Omega_\mathrm{r}(s) = \frac{E}{s-G}\mathcal{T}_\mathrm{g}(s) + \frac{H}{s-G}\mathcal{V}(s), \qquad (4.13)$$

which depends on the transfer functions from the generator torque control and wind speed disturbance, respectively.

4.4.2. ANALYSIS FRAMEWORK

To compare the characteristics of the baseline $K\omega^2$ and WSE-TSR tracking control strategies, a universal analysis framework is defined in this section and is illustrated in Figure 4.5. Here, the controllers are generalised as a single block with two inputs and one output, being the reference tip-speed ratio, rotor speed and generator torque control signals, respectively. In the linear and frequency-domain formulation, the control scheme is formalised as

$$\mathcal{T}_\mathrm{g}(s) = K_{\Omega_\mathrm{r}\to\mathcal{T}_\mathrm{g}}(s)\Omega_\mathrm{r}(s) + K_{\Lambda_*\to\mathcal{T}_\mathrm{g}}(s)\Lambda_*(s). \qquad (4.14)$$

In the remainder of this section, the expressions $K_{\Omega_\mathrm{r}\to\mathcal{T}_\mathrm{g}}$ and $K_{\Lambda_*\to\mathcal{T}_\mathrm{g}}$ are derived and analysed for the different controllers, representing the feedback and the reference shaping terms, respectively. In particular, it will be shown that for the $K\omega^2$ controller, these elements are equivalent to a state feedback controller with reference shaping gain. Since
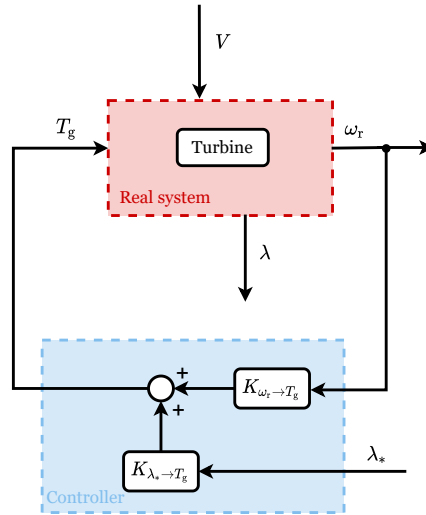
Figure 4.5: Block diagram of the universal framework used for the controller analysis. The **red** box highlights the wind turbine system with two inputs (the generator torque T_g, and the wind speed V), and two outputs (the rotational speed, ω_r, and the TSR, λ). The **cyan** box represents the controller with two inputs (ω_r and the TSR set point, λ_*), one output (T_g) and two terms used for the linear analysis framework (the feedback term, $K_{\omega_\mathrm{r}\to T_\mathrm{g}}$, and the reference shaping term $K_{\lambda_*\to T_\mathrm{g}}$).

both the WSE-TSR tracking controller and a state feedback controller aim to regulate the output of the wind turbine, ω_r, so that it tracks the reference input, λ_*, this equivalence represents the first step to comparing the baseline with the proposed controller.

By substituting Equation (4.14) into Equation (4.13), the following expression is obtained

$$\Omega_r(s) = \frac{EK_{\Omega_r \to \mathcal{T}_g}(s)}{s - G}\Omega_r(s) + \frac{EK_{\Lambda_* \to \mathcal{T}_g}(s)}{s - G}\Lambda_*(s) + \frac{H}{s - G}\mathcal{V}(s), \qquad (4.15)$$

and by further manipulation

$$\Omega_r(s) = \frac{EK_{\Lambda_* \to \mathcal{T}_g}(s)}{s - G - EK_{\Omega_r \to \mathcal{T}_g}(s)}\Lambda_*(s) + \frac{H}{s - G - EK_{\Omega_r \to \mathcal{T}_g}(s)}\mathcal{V}(s). \qquad (4.16)$$

In Equation (4.16), the closed-loop transfer functions are defined with the rotor speed as the output variable. As the scheme intends to regulate the tip-speed ratio to the TSR reference, this output should be converted to the actual tip-speed ratio λ of the turbine rotor. Therefore, the TSR expression defined in Equation (4.3) is linearised with respect to the rotor speed and wind speed, and the following expression is obtained

$$\Lambda(s) = \frac{R}{\bar{V}}\Omega_r(s) - \frac{R\bar{\omega}_r}{\bar{V}^2}\mathcal{V}(s). \qquad (4.17)$$

By combining Equation (4.17) with Equation (4.16)

$$\Lambda(s) = \underbrace{\frac{REK_{\Lambda_* \to \mathcal{T}_g}(s)}{\bar{V}\left(s - G - EK_{\Omega_r \to \mathcal{T}_g}(s)\right)}}_{T_{\Lambda_* \to \Lambda}(s)}\Lambda_*(s) + \underbrace{\frac{R\left(H - (\bar{\omega}_r/\bar{V})\left(s - G - EK_{\Omega_r \to \mathcal{T}_g}(s)\right)\right)}{\bar{V}\left(s - G - EK_{\Omega_r \to \mathcal{T}_g}(s)\right)}}_{T_{\mathcal{V} \to \Lambda}(s)}\mathcal{V}(s).$$

$$(4.18)$$

The two transfer function terms on the right-hand side of Equation (4.18) represent the closed-loop system reference tracking and disturbance attenuation capabilities, respectively. In particular, the term $T_{\Lambda_* \to \Lambda}(s)$ indicates if the controller is tracking the optimal condition (i.e. $\lambda = \lambda_*$), while $T_{\mathcal{V} \to \Lambda}(s)$ shows the controller's performance in reacting to external wind speed disturbances. Later in this chapter, these closed-loop transfer functions will be evaluated in terms of optimal controller calibration to further investigate the controller in the frequency domain.

4.4.3. BASELINE $K\omega^2$ CONTROL DYNAMICS
With the open-loop linearised wind turbine plant dynamics and analysis framework defined, this section derives the respective quantities in the universal controller framework for the baseline controller. The nonlinear representation of the $K\omega^2$ controller given by Equation (4.4) is linearised to obtain the quantities

$$K_{(\Omega_r \to \mathcal{T}_g),K} = \frac{\partial T_{g,K}}{\partial \omega_r}\bigg|_{(\bar{\omega}_r, \lambda_*)} = \frac{2K\bar{\omega}_r}{N} = \frac{\rho R^3 A_{rot}C_{p,*}(\lambda_*)}{N\lambda_*^3}\bar{\omega}_r, \qquad (4.19)$$

$$K_{(\Lambda_* \to \mathcal{T}_g),K} = \frac{\partial T_{g,K}}{\partial \lambda_*}\bigg|_{(\bar{\omega}_r, \lambda_*)} = \frac{\rho R^3 A_{rot}}{2N}\left(-\frac{3}{\lambda_*^4}C_{p,*}(\lambda_*) + \frac{1}{\lambda_*^3}\frac{\partial C_{p,*}(\lambda_*)}{\partial \lambda_*}\right)\bar{\omega}_r^2. \qquad (4.20)$$

These are equivalent to the state-feedback and reference shaping gain, respectively, as defined in state-feedback control theory. The interested reader is referred to Appendix C for the full derivation of this similarity.

4.4.4. WSE-TSR TRACKING CONTROL DYNAMICS

This section provides a derivation of the frequency-domain control dynamics of the WSE-TSR tracking controller. As shown in Figure 4.3, the control scheme consists of a combined estimator and tracking controller. For this reason, to obtain the dynamics of the full scheme, the linear frequency-domain representations of the individual estimator and controller are derived first. Then, the framework dynamics are achieved by coupling the estimator and the controller.

ESTIMATOR DYNAMICS

As illustrated in Figure 4.4, the estimator has the generator torque and the rotor speed as inputs and the estimated tip-speed ratio as output. Therefore, several steps must be taken to derive a frequency-domain representation for the estimator, which are briefly summarised here. First, the equations for the estimated rotor speed and REWS (Equation (4.6)) are combined and applied at the linearisation point in terms of the Laplace variable. As a result, the estimated REWS is defined as a function of the rotor speed and the generator torque. Then, by substituting this expression into the nonlinear function of the estimated tip-speed ratio, the following is obtained

$$\hat{\Lambda}(s) = X(s)\mathcal{T}_{\mathrm{g,TSR}}(s) + Y(s)\Omega_{\mathrm{r}}(s), \tag{4.21}$$

where

$$X(s) = \frac{\hat{\Lambda}_{\mathcal{T}_{\mathrm{g,TSR}}}(s)}{\mathcal{T}_{\mathrm{g,TSR}}(s)} = \frac{R\bar{\omega}_{\mathrm{r}}E\left(K_{\mathrm{p,w}}s + K_{\mathrm{i,w}}\right)}{\bar{V}^2\left(s^2 + \hat{H}K_{\mathrm{p,w}}s + \hat{H}K_{\mathrm{i,w}}\right)}, \tag{4.22}$$

and

$$Y(s) = \frac{\hat{\Lambda}_{\Omega_{\mathrm{r}}}(s)}{\Omega_{\mathrm{r}}(s)} \tag{4.23}$$

$$= \frac{R\left[\left(1 - (\bar{\omega}_{\mathrm{r}}/\bar{V})K_{\mathrm{p,w}}\right)s^2 + \left(\hat{H}K_{\mathrm{p,w}} - (\bar{\omega}_{\mathrm{r}}/\bar{V})\left(K_{\mathrm{i,w}} - \hat{G}K_{\mathrm{p,w}}\right)\right)s + \left(\hat{H} + (\bar{\omega}_{\mathrm{r}}/\bar{V})\hat{G}\right)K_{\mathrm{i,w}}\right]}{\bar{V}\left(s^2 + \hat{H}K_{\mathrm{p,w}}s + \hat{H}K_{\mathrm{i,w}}\right)}, \tag{4.24}$$

represent the transfer functions from the generator torque and rotational speed, respectively, to the estimated tip-speed ratio. According to Assumption 7, the variables $\hat{G} := G(\hat{V})$ and $\hat{H} := H(\hat{V})$ indicate the estimated partial derivatives defined in Equations (4.11) and (4.12).

TIP-SPEED RATIO TRACKING CONTROL DYNAMICS

According to Figure 4.3, the TSR tracking controller has two inputs, the tip-speed ratio estimate and set point, and one output, the generator torque. The TSR tracking control dynamics is derived in the frequency domain by combining Equation (4.9) with the

tracking error definition (Equation (4.8)) at the linearisation point in terms of the Laplace variable. Follows,

$$\mathcal{T}_{\text{g,TSR}}(s) = Z(s)\Lambda_*(s) + Q(s)\hat{\Lambda}(s),$$ (4.25)

with

$$Z(s) = \frac{\mathcal{T}_{\text{g,TSR}_{\Lambda_*}}(s)}{\Lambda_*(s)} = \frac{K_{\text{p,c}}s + K_{\text{i,c}}}{s},$$ (4.26)

and

$$Q(s) = \frac{\mathcal{T}_{\text{g,TSR}_{\hat{\Lambda}}}(s)}{\hat{\Lambda}(s)} = -\frac{K_{\text{p,c}}s + K_{\text{i,c}}}{s},$$ (4.27)

being the transfer functions from the reference and estimated tip-speed ratio, respectively, to the generator torque.

COMBINED SCHEME

The combined control scheme can now be formed using the individually derived elements. To this end, the linearised estimator and controller expressions Equations (4.21) and (4.25) are combined to comply with the desired form of Equation (4.14), resulting in the following expression:

$$\mathcal{T}_{\text{g,TSR}}(s) = Q(s)X(s)\mathcal{T}_{\text{g,TSR}}(s) + Q(s)Y(s)\Omega_{\text{r}}(s) + Z(s)\Lambda_*(s).$$ (4.28)

Following further manipulation

$$\mathcal{T}_{\text{g,TSR}}(s) = \underbrace{\frac{Q(s)Y(s)}{(1 - Q(s)X(s))}}_{K_{(\Omega_{\text{r}} \to \mathcal{T}_{\text{g}}),\text{TSR}}(s)} \Omega_{\text{r}}(s) + \underbrace{\frac{Z(s)}{(1 - Q(s)X(s))}}_{K_{(\Lambda_* \to \mathcal{T}_{\text{g}}),\text{TSR}}(s)} \Lambda_*(s),$$ (4.29)

with

$$K_{(\Omega_{\text{r}} \to \mathcal{T}_{\text{g}}),\text{TSR}}(s) = \frac{\mathcal{T}_{\text{g,TSR}_{\Omega_{\text{r}}}}(s)}{\Omega_{\text{r}}(s)} = \frac{R\left(K_{\text{p,c}}\,s + K_{\text{i,c}}\right)\left((\bar{\omega}_{\text{r}}K_{\text{p,w}} - \bar{V})\,s^2 + F_4\,s - (\bar{V}\hat{H} + \bar{\omega}_{\text{r}}\hat{G})K_{\text{i,w}}\right)}{\left(\bar{V}^2\,s^3 + F_1\,s^2 + F_2\,s + F_3\right)},$$ (4.30)

and

$$K_{(\Lambda_* \to \mathcal{T}_{\text{g}}),\text{TSR}}(s) = \frac{\mathcal{T}_{\text{g,TSR}_{\Lambda_*}}(s)}{\Lambda_*(s)} = \frac{\bar{V}^2\left(K_{\text{p,c}}\,s + K_{\text{i,c}}\right)\left(s^2 + \hat{H}K_{\text{p,w}}\,s + \hat{H}K_{\text{i,w}}\right)}{\left(\bar{V}^2\,s^3 + F_1\,s^2 + F_2\,s + F_3\right)},$$ (4.31)

representing the controller transfer functions from the rotational speed and tip-speed ratio reference, respectively, to the generator torque output. The unknown quantities in the above expressions are defined as

$$F_1 = \bar{V}^2\hat{H}K_{\text{p,w}} + R\bar{\omega}_{\text{r}}EK_{\text{p,c}}K_{\text{p,w}},$$
$$F_2 = \bar{V}^2\hat{H}K_{\text{i,w}} + R\bar{\omega}_{\text{r}}EK_{\text{p,c}}K_{\text{i,w}} + R\bar{\omega}_{\text{r}}EK_{\text{i,c}}K_{\text{p,w}},$$
$$F_3 = R\bar{\omega}_{\text{r}}EK_{\text{i,c}}K_{\text{i,w}},$$
$$F_4 = \bar{\omega}_{\text{r}}K_{\text{i,w}} - (\bar{V}\hat{H} + \bar{\omega}_{\text{r}}\hat{G})K_{\text{p,w}},$$

in order to simplify Equations (4.30) and (4.31).

4.4.5. COMPARISON BETWEEN CONTROLLERS

In the previous section, the controllers are expressed in a universal analysis framework to allow for comparison. Using the controller expression given by Equation (4.14), this section analyses the controller transfer functions $K_{\Omega_r \to \mathcal{T}_g}(s)$ and $K_{\Lambda_* \to \mathcal{T}_g}(s)$ of the baseline $K\omega^2$ and WSE-TSR tracking controllers to understand the similarities and differences between the two seemingly dissimilar controllers. Since the closed-loop dynamics is strictly dependent on the calibration chosen for the WSE-TSR tracking control scheme, the analysis of the corresponding transfer functions will be evaluated in a later section using the results from the multi-objective optimisation.

Equations (4.19) and (4.20) show that the controller transfer functions are merely frequency-independent static gains for the baseline controller. That is, the gain is constant over all frequencies. In contrast, the WSE-TSR tracking controller transfer functions possess dynamics (Equations (4.30) and (4.31)). For this reason, it is assumed that for the low-frequency region, the (DC-)gain of the latter controller equals the gain of the baseline controller, whereas, for higher frequencies, the frequency responses vary.

To examine the controller transfer functions, Equations (4.30) and (4.31) are symbolically evaluated $s = j\omega = 0$, with j being the imaginary unit number. By doing so, the steady-state responses of the WSE-TSR tracking controller transfer functions are computed, and after substitutions and simplifications, the following expressions are derived

$$K_{(\Omega_r \to \mathcal{T}_g),\mathrm{TSR}}(s=0) = -\frac{\left(\bar{V}\hat{H} + \bar{\omega}_r\hat{G}\right)}{\bar{\omega}_r E} = \frac{\bar{V}}{\bar{\omega}_r N}\left(\frac{\partial \hat{T}_r}{\partial \hat{V}}\right) + \frac{1}{N}\left(\frac{\partial \hat{T}_r}{\partial \omega_r}\right) \tag{4.32}$$

$$= \frac{\rho R^3 A_{\mathrm{rot}} C_{p,*}(\lambda_*)}{N\lambda_*^3}\bar{\omega}_r, \tag{4.33}$$

$$K_{(\Lambda_* \to \mathcal{T}_g),\mathrm{TSR}}(s=0) = \frac{\bar{V}^2\hat{H}}{R\bar{\omega}_r E} = -\frac{\bar{V}^2}{R\bar{\omega}_r N}\left(\frac{\partial \hat{T}_r}{\partial \hat{V}}\right) \tag{4.34}$$

$$= \frac{\rho R^3 A_{\mathrm{rot}}}{2N}\left(-\frac{3}{\lambda_*^4}C_{p,*}(\lambda_*) + \frac{1}{\lambda_*^3}\frac{\partial C_{p,*}(\lambda_*)}{\partial \lambda_*}\right)\bar{\omega}_r^2. \tag{4.35}$$

It is immediately evident that $K_{\mathrm{TSR}}(s=0) = K_K$ as defined earlier in Equations (4.19) and (4.20). This proves that the WSE-TSR tracking controller is equivalent to the $K\omega^2$ controller in steady-state. Thus, the two controllers will have the same static behaviour [36], operating at the same point of power extraction efficiency, $C_{p,*}(\lambda_*)$.

Similarities and differences between the two controllers are further illustrated in Figure 4.6 with Bode plots of the analysed controller transfer functions. The frequency responses are obtained using the NREL 5 MW reference turbine parameters [31] and a controller calibration that performs satisfactorily but is non-optimised. In the figure illustrating the Bode plot for $K_{\Omega_r \to \mathcal{T}_g}(s)$ of both controllers, it can be observed that the two controllers show the same characteristics for the low-frequency region (between 1×10^{-5} Hz and 1×10^{-2} Hz). However, for higher frequencies, the WSE-TSR tracking controller presents additional dynamics in the form of a resonance resulting from a complex left half-plane pole-pair and a double right half-plane zero. The explanation for these additional dynamics is the controller attaining a higher open-loop unity cross-over, resulting in an increased closed-loop control bandwidth. The right plot presents the frequency response for $K_{\Lambda_* \to \mathcal{T}_g}(s)$ and for the inverted transfer function of the wind turbine
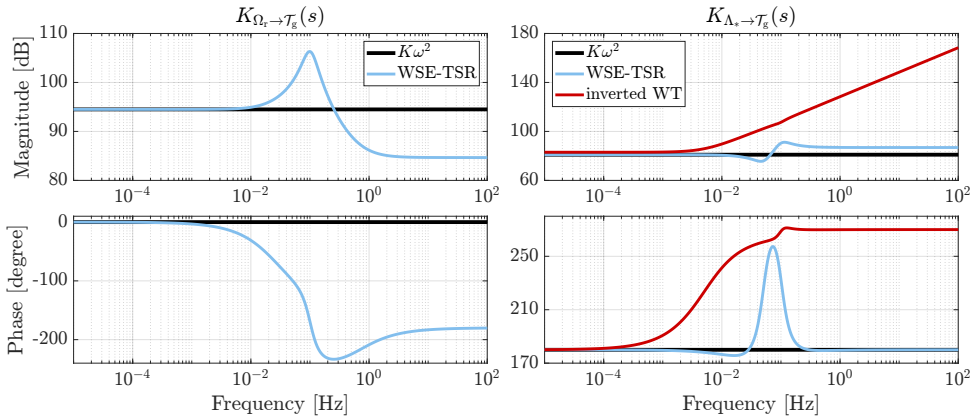
Figure 4.6: Bode plots of the controller transfer functions $K_{\Omega_r \to \mathcal{T}_g}(s)$ and $K_{\Lambda_* \to \mathcal{T}_g}(s)$ for the $K\omega^2$ controller (**black** line) and the WSE-TSR tracking controller (**cyan** line) without optimal calibration. For the baseline, both transfer functions are frequency-independent. For the combined scheme, in the low-frequency region, $K_{\Omega_r \to \mathcal{T}_g}(s)$ and $K_{\Lambda_* \to \mathcal{T}_g}(s)$ have gains equal to the baseline. In particular, for the right-hand plot, the controller gains match the inverted model of the wind turbine (**red** line), exhibiting a second-order lead-lag behaviour. By contrast, for higher frequencies, the response varies for both transfer functions for the combined scheme.

defined in Equation (4.13). It is clear that both controllers exhibit a second-order lead-lag behaviour related to the model inversion required for the reference shaping action [26].

4.5. CALIBRATION OF THE WSE-TSR TRACKING CONTROLLER

From the frequency-domain framework derived in the previous section, it is recognised that the WSE-TSR tracking controller presents a higher dimensional design space than the baseline $K\omega^2$. In particular, while the $K\omega^2$ controller has only the torque gain K to calibrate, the combined scheme has a total of five variables: $K_{p,w}$, $K_{i,w}$, $K_{p,c}$, $K_{i,c}$ and λ_*. This tight integration between a disturbance estimator and a tracking controller makes the mutual calibration of the design variables in the WSE-TSR tracking controller a complex and non-trivial task. Therefore, this section addresses the calibration of the controller by formulating a multi-objective optimisation problem. The approach to *solving* this multi-objective problem is by reconstructing (an approximation of) the true Pareto front, composed of a set of Pareto optimal solutions. To this end, first, the multi-objective optimisation problem is formalised in Section 4.5.1 and implemented in Section 4.5.2. An exploratory and guided search over the controller calibration variables examines the performance space formed by all objectives. The outcomes of this search are presented in Section 4.5.3 to construct approximations of the true Pareto front, which are related to the controller calibrations.

4.5.1. MULTI-OBJECTIVE OPTIMISATION

A multi-objective optimisation problem is considered over a set of continuous input variables $\mathcal{X} \subset \mathbb{R}^d$ called the design space [37]. The optimisation goal is to minimise the

vector of the objective functions defined as $\mathbf{f}(\mathbf{x}) = (f_1(\mathbf{x}), \cdots, f_m(\mathbf{x})))$ with $m \geq 2$, $\mathbf{x} \in \mathcal{X}$ the vector of input variables and $\mathbf{f}(\mathcal{X}) \subset \mathbb{R}^m$ the m-dimensional image representing the performance space.

The conflicting nature of the objective functions does not always allow the finding of a single best solution to the minimisation problem but rather a set of optimal solutions, referred to as Pareto set $\mathcal{P}_s \subseteq \mathcal{X}$ in the design space and as Pareto front $\mathcal{P}_f = \mathbf{f}(\mathcal{P}_s) \subset \mathbb{R}^m$ in the performance space [37]. In the following, the Pareto front is approximated by considering as Pareto optimal the point $\mathbf{x}_* \in \mathcal{P}_s$ for which there is no other point $\mathbf{x} \in \mathcal{X}$ such that $f_j(\mathbf{x}_*) \geq f_j(\mathbf{x})$ for all j and $f_j(\mathbf{x}_*) > f_j(\mathbf{x})$ for at least one j, with $j = \{1, \cdots, m\}$ [38].

4.5.2. IMPLEMENTATION OF THE OPTIMISATION FRAMEWORK

The methodology for calibrating the design variables of the WSE-TSR tracking control scheme is addressed as the multi-objective optimisation problem previously described. A two-dimensional vector of the objective functions is considered. The first objective is the variance of the torque control signal, representing the responsiveness of the controller (i.e. a measure of its response speed). This objective can also act as a measure of loads on the structural components of the turbine. The second objective is the mean generated power of the wind turbine. These two objectives are conflicting as a more responsive controller is expected to result in higher power production levels with increased loads and fast response time and vice-versa for milder controller calibration. Thereby, the objective function vector is given by:

$$\mathbf{f}(\Gamma_d) = [f_1(\Gamma_d), f_2(\Gamma_d)], \tag{4.36}$$

with the torque variance being defined as

$$f_1(\Gamma_d) = \frac{\sum_{i=1}^{n} (T_{g,i}(\Gamma_d) - T_{g,mean}(\Gamma_d))^2}{n},$$

and the mean power as

$$f_2(\Gamma_d) = -\frac{\sum_{i=1}^{n} P_{g,i}(\Gamma_d)}{n}.$$

In the above equations, n is the number of data points, $T_{g,mean}$ is the mean value of the generator torque, and $T_{g,i}$ and $P_{g,i}$ represent each value of generator torque and power in the dataset, respectively. As shown, the resulting signals T_g and P_g are a function of $\Gamma_d \in \mathcal{X}_d \subset \mathbb{R}^d$, which is the d-dimensional vector of input variables. In this study, the dimensionality of the input vectors is investigated to assess the performance of the controller for different levels of complexity as

$$\Gamma_5 = [K_{p,c}, K_{i,c}, K_{p,w}, K_{i,w}, \lambda_*] \in \mathcal{X}_5,$$
$$\Gamma_4 = [K_{p,c}, K_{i,c}, K_{p,w}, \lambda_*] \in \mathcal{X}_4,$$
$$\Gamma_3 = [K_{i,c}, K_{p,w}, \lambda_*] \in \mathcal{X}_3,$$
$$\Gamma_2 = [K_{i,c}, K_{p,w}] \in \mathcal{X}_2,$$
$$\Gamma_1 = [\lambda_*] \in \mathcal{X}_1,$$

where the subscript $(\cdot)_d$ represents the dimension of each design space and is used in the remainder of this Chapter to differentiate between the input vectors. Note that $d = 5$ refers

to the original formulation of the WSE-TSR tracking controller, for which the integral term in the estimator ($K_{i,w}$) was introduced recently in the work of Liu et al. [32]. The integral term ensures that the internal estimated rotor speed state is consistent with the actual rotor speed measurement. Furthermore, combining a proportional and integral term ($K_{p,w}$ and $K_{i,w}$) results in faster estimation convergence by rapidly reducing the estimation error. The input vectors $\Gamma_d \subset \Gamma_5$ for $d = \{2, 3, 4\}$, while, Γ_1 represents the one-dimensional design space of the $K\omega^2$ controller, in which the variation in λ_* leads to variation in the gain K according to Equation (4.5). Furthermore, as can be recognised from the defined input vectors Γ_d, the estimator and the controller are consistently and intricately calibrated in unison throughout the entire work.

Aero-servo-elastic simulations are performed with NREL's mid-fidelity wind turbine simulation software OpenFAST [35] to compute the objective function vector $\mathbf{f}(\Gamma_d)$. The NREL 5 MW reference wind turbine [31] is subject to a realistic turbulent wind profile with a mean wind speed of $\bar{V} = 9$ m/s at hub height and a turbulence intensity of TI = 15%. Under these operational conditions, the multi-objective optimisation is performed. For each simulation, the input vector is constrained for a guided search to find a set of optimal solutions $\mathcal{P}_s^d \subset \mathbb{R}^d$ to approximate the Pareto front $\mathcal{P}_f^d = \mathbf{f}(\mathcal{P}_s^d)$. Simulations are run in parallel by randomly varying the input vector inside the constrained design space. Each simulation has a length of 3600 s, of which the first 100 s are discarded to exclude the transient start-up effects from the results. The acquired time series is used to calculate the considered objectives $f_1(\Gamma_d)$ and $f_2(\Gamma_d)$

4.5.3. OPTIMISATION RESULTS

This section presents the results obtained with the described optimisation framework. The performance space is explored using the guided search for the five sets of calibration input variables. Subsequently, the results are used to approximate the corresponding Pareto fronts. Finally, the influence of the gains is assessed by analysing the different regions of the constrained design space.

EXPLORATORY SEARCH AND PARETO FRONT

Before constructing the Pareto front, the performance space is explored by means of a guided search of the input variables Γ_d. With an increasing dimension d of the design space, more data is collected to capture the performance space of interest effectively. The conventional $K\omega^2$ controller is used as a baseline comparison case.

With the exploration data at hand, the Pareto front is approximated by minimising a weighted linear combination of $f_1(\Gamma_d)$ and $f_2(\Gamma_d)$ on the complete data set and for a range of weights. As shown in Figure 4.7, Pareto fronts are approximated for different dimensionalities of the input vector Γ_d to compare the baseline to the performance of the WSE-TSR tracking controller. The optimal solutions based on each objective function $f_1(\Gamma_d)$ and $f_2(\Gamma_d)$ are indicated using circles ($\circ$) and crosses ($\times$), respectively.

From the figure, it is immediately apparent that the fronts of the higher-dimensional controllers $d = \{4, 5\}$ cover the widest area of the performance space; the remaining fronts are subsets of the original WSE-TSR tracking control scheme. Since the Pareto fronts for $d = \{4, 5\}$ overlap, it is concluded that adding an integral term to the estimator (i.e. $K_{i,w}$) leads to no (or marginal) benefits on the performance of the WSE-TSR tracking
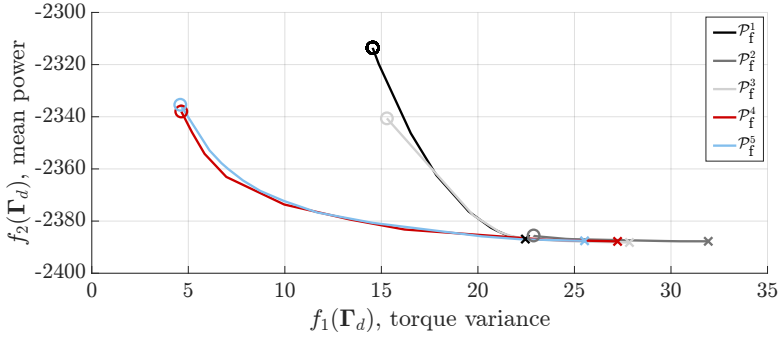
Figure 4.7: Pareto fronts obtained for the WSE-TSR tracking control scheme for different sets of estimator-controller design variables: $\Gamma_1, \Gamma_2, \Gamma_3, \Gamma_4$ and Γ_5. Simulations are performed with the NREL's mid-fidelity wind turbine simulation software OpenFAST [35] under realistic turbulent wind conditions. The objective functions $f_1(\Gamma_d)$, i.e. torque fluctuations minimisation, and $f_2(\Gamma_d)$, i.e. power maximisation, define the performance space for the controller. The optimal solutions for $f_1(\Gamma_d)$ and $f_2(\Gamma_d)$ are indicated using circles ($\circ$) and crosses ($\times$), respectively. Compared to the baseline controller represented by the Pareto front $\mathcal{P}_f^1$, the WSE-TSR tracking controller does not attain an enhancement in power maximisation but allows the minimisation of torque fluctuations with a small penalty in power extraction.

scheme. It follows that only by adding a proportional control gain (i.e. $K_{p,c}$) leads to more flexibility in reaching desired (Pareto) optimal solutions minimising torque fluctuations and corresponding (structural) loads, with a minimal impact on the power extraction performance. This shows the benefits of the more flexible structure of the WSE-TSR tracking scheme.

Another observation is that the baseline controller already attains a Pareto optimal solution minimising $f_2(\Gamma_d)$, i.e. maximising power production. It is clear that increasing the controller bandwidth and allowing for higher torque fluctuations $f_1(\Gamma_d)$ does not result in the enhancement of energy capture $f_2(\Gamma_d)$ compared to the baseline control strategy. A plausible explanation is that the higher inertia of large-scale wind turbines inherently provides resilience against deviations from the optimal operating point. Therefore, increasing the controller bandwidth, resulting in tighter tracking to the desired tip-speed ratio reference, might not directly result in additional benefits in terms of energy capture.

INFLUENCE OF THE CONTROLLER CALIBRATION VARIABLES

This section qualitatively assesses the influence and correlation of the gains to the performance of the WSE-TSR tracking controller. The analysis is presented in Figure 4.8, where two areas of interest are selected: the lowest value of $f_2(\Gamma_5)$ (power maximisation) and $f_1(\Gamma_5)$ (torque fluctuation minimisation). The analysis only draws conclusions relating the calibration of the scheme to the considered objectives; a more formal frequency- and time-domain analysis is described in the next section. Furthermore, only the five-dimensional input vector Γ_5 will be evaluated from this point onwards, as the current study focuses on providing calibration guidelines for the complete WSE-TSR tracking control scheme rather than for its subsets.

For the power maximisation case, λ_* should be taken between 7.1 and 7.3, which corresponds to the region of maximum power extraction for the NREL 5 MW (Figure 4.1).
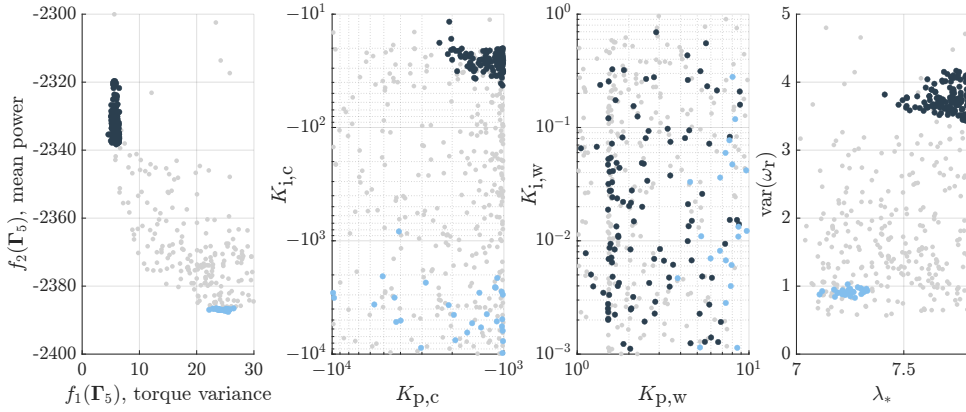
Figure 4.8: Results for the WSE-TSR tracking control scheme obtained with an exploratory search of its design variables (i.e. Γ_5). Different shades of cyan are used to highlight two areas of interest: the lowest values of $f_1(\Gamma_5)$ (torque fluctuation minimisation) and $f_2(\Gamma_5)$ (power maximisation). The two objectives and the rotor speed variance ($\text{var}(\omega_r)$) are plotted together with the controller gains ($K_{p,c}$ and $K_{i,c}$), the estimator gains ($K_{p,w}$ and $K_{i,w}$) and the reference tip-speed ratio (λ_*) to show how these calibration variables influence the scheme's performance. Clearly, neither $K_{i,w}$ nor $K_{p,c}$ correlates to the performance of the WSE-TSR tracking controller. While λ_* and $K_{p,w}$ follow an increasing trend proportional to the increase in torque variance, $K_{i,c}$ exhibits the opposite behaviour.

For the torque minimisation case, λ_* should be chosen higher than the power coefficient-maximising value, resulting in a power reduction and rotational speed variance increase. Furthermore, as observed from both cases, $K_{p,w}$ follows an increasing trend proportional to the increase in torque variance, while $K_{i,w}$ does not show a clear correlation to the controller performance.

Considering the controller gains, it is clear that the controller heavily relies on integral action to track the desired tip-speed ratio reference and therefore achieve power maximisation. The gain for the proportional action $K_{p,c}$ lies in the same area for the two regions of interest without directly influencing the performance.

4.6. ANALYSIS OF *optimally* CALIBRATED WSE-TSR TRACKING CONTROLLERS

Pareto fronts have been approximated in the previous section, representing a set of optimal solutions among the conflicting objectives. An analysis has been presented by directly relating the objectives to the input vectors of various dimensionalities. This section compares the characteristics of full-dimensional and *optimally* calibrated WSE-TSR tracking controllers to the baseline $K\omega^2$ strategy.

The initial step in this comparison involves a qualitative assessment of the impact of optimal calibrations on system parameters. Subsequently, to provide specific guidance for the optimal calibration of the controller, a sensitivity analysis examines the effect of each calibration variable on corresponding objectives and turbine loads. To conclude the study, the frequency domain framework outlined in Section 4.4 is applied alongside mid-fidelity time-domain simulations to replicate realistic turbulent wind conditions.
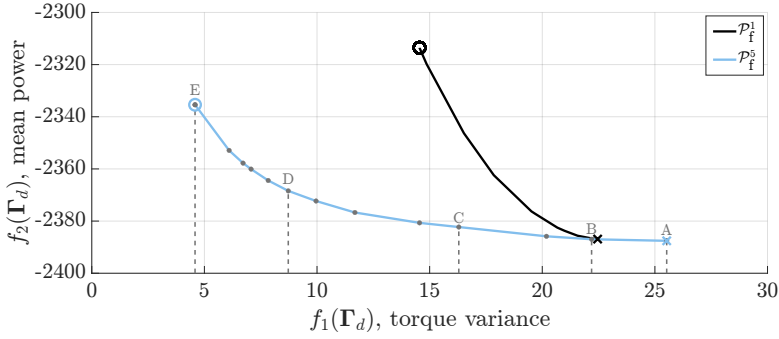
Figure 4.9: Pareto fronts $\mathcal{P}_\mathrm{f}^1$ and $\mathcal{P}_\mathrm{f}^5$ obtained for the baseline and WSE-TSR tracking control schemes and related to the Γ_1 and Γ_5 design variables. Simulations are performed with the NREL's mid-fidelity wind turbine simulation software OpenFAST [35] under realistic turbulent wind conditions. The case studies for the WSE-TSR tracking controller are marked on the $\mathcal{P}_\mathrm{f}^5$ front with letters ranging from A to E, respectively, corresponding to maximum power extraction and minimum generator torque fluctuations. Point B is closest to the optimal baseline controller calibration in terms of power extraction.

4.6.1. CASE STUDIES DEFINITION

The case studies analysed in this section are presented in Figure 4.9. The figure shows the approximated Pareto fronts $\mathcal{P}_\mathrm{f}^5$ and $\mathcal{P}_\mathrm{f}^1$, representing the WSE-TSR tracking and the baseline controllers, respectively. Along the $\mathcal{P}_\mathrm{f}^5$ front, five distinct optimal solutions are chosen, and the corresponding calibrations Γ_5 are considered for analysis in the following subsections. The selection considers the evaluation of different trade-off levels between the considered objectives from the point of maximum power extraction (A) to the point of minimum torque variance (E). Point B is closest to the maximum power extraction of the $K\omega^2$ controller and is selected to show similarities between these two schemes.

4.6.2. QUALITATIVE ASSESSMENTS OF OPTIMAL CONTROLLER SOLUTIONS

This section provides an overview of how optimal calibration points, as defined in Section 4.6.1, impact the system parameters, especially load components. The assessment is performed qualitatively as a first step in offering calibration guidelines for the WSE-TSR tracking controller. The analysis outcomes are summarised in Table 4.2, where symbols ○, ++, +, − and −− denote no influence, really positive influence, positive influence, negative influence and really negative influence on the performance metrics.

As points A and E have a positive effect on maximising power extraction, $f_2(\Gamma_5)$, and on minimising generator torque fluctuations, $f_1(\Gamma_5)$, respectively, it is confirmed that they represent the extremes of the Pareto front $\mathcal{P}_\mathrm{f}^5$. Point B emerges as the calibration point closest to the optimal $K\omega^2$ controller calibration in terms of power extraction. As the cases progress towards E, the primary aim of the controller is to minimise the generator torque variance, leading to a reduction in bandwidth. Consequently, these controllers positively affect the mean side-to-side tower moment (SSTM) and the edgewise blade 1 moment (EdgeBM). However, this improvement negatively influences the rotor speed variance and the mean/variance of both the fore-aft tower moment (FATM) and the flapwise blade 1 moment (FlapBM). Overall, the optimal controller calibrations under consideration do not

Table 4.2: Qualitative assessments of the $K\omega^2$ controller and the different WSE-TSR tracking controllers ranging from the maximum power extraction (A) to the minimum generator torque fluctuations (E) optimal calibrations. The following system quantities are used for the analysis: $f_1(\Gamma_d)$ (torque fluctuation minimisation), $f_2(\Gamma_d)$ (power maximisation), rotor speed variance, the fore-aft tower moment (FATM), the side-to-side tower moment (SSTM), the flapwise bending moment for blade 1 (FlapBM) and the edgewise bending moment for blade 1 (EdgeBM). For each tower and blade load, two values are presented corresponding to the mean and variance, respectively. No influence, really positive influence, positive influence, negative influence and really negative influence of the considered controllers are indicated with $\bigcirc$, ++, +, −, −−, respectively.

Case study	$f_1(\Gamma_d)$	$f_2(\Gamma_d)$	ω_r Variance
$K\omega^2$	−	+	++
A	−−	++	++
B	−	+	+
C	+	−	+
D	++	−−	−
E	++	−−	−−

Case study	FATM Mean	FATM Variance	SSTM Mean	SSTM Variance	FlapBM Mean	FlapBM Variance	EdgeBM Mean	EdgeBM Variance
$K\omega^2$	+	++	−	$\bigcirc$	+	++	−	$\bigcirc$
A	++	++	−−	$\bigcirc$	++	++	−−	$\bigcirc$
B	++	+	−−	$\bigcirc$	++	+	−−	$\bigcirc$
C	+	+	−	$\bigcirc$	+	+	−	$\bigcirc$
D	−	−	+	$\bigcirc$	−	−	+	$\bigcirc$
E	−−	−−	++	$\bigcirc$	−−	−−	++	$\bigcirc$

affect the variance of the side-to-side tower moment and the edgewise blade 1 moment. A coupling is evident between the fore-aft and the flapwise moments and between the side-to-side and the edgewise moments. This intricate interplay proves the complexity of calibrating the WSE-TSR tracking control scheme, as several system parameters are intertwined, and confirms the need for a multi-objective optimisation framework and a frequency-domain analysis to link controller insight with turbine performance metrics.

4.6.3. SENSITIVITY ANALYSIS OF OPTIMAL CALIBRATION VARIABLES

This section aims to comprehensively evaluate the effect of the optimal calibration variables on various system parameters. An optimally calibrated WSE-TSR tracking controller is selected from the case studies outlined in Section 4.6.1 for this sensitivity analysis. Specifically, controller C is chosen to represent a trade-off between minimising generator torque fluctuations and maximising power production. For this controller, the five calibration variables — $K_{p,c}$, $K_{i,c}$, $K_{p,w}$, $K_{i,w}$, and λ_* — are assessed in terms of their positive or negative influence on the turbine performance metrics. The gains are varied individually while keeping the others fixed to their optimal value. The analysis results are summarised in Table 4.3, where each row corresponds to the effect of increasing the absolute value of

Table 4.3: Sensitivity analysis of the optimal controller calibration C for the WSE-TSR tracking controller. For each row, the corresponding calibration variable is varied while the others are kept fixed to the optimal value. The following system quantities are used for the analysis: $f_1(\Gamma_d)$ (torque fluctuation minimisation), $f_2(\Gamma_d)$ (power maximisation), rotor speed variance, the fore-aft tower moment (FATM), the side-to-side tower moment (SSTM), the flapwise bending moment for blade 1 (FlapBM) and the edgewise bending moment for blade 1 (EdgeBM). For each tower and blade load, two values are presented corresponding to the mean and variance, respectively. No influence, positive influence and negative influence of the considered calibration variable is indicated with ○, + and −, respectively.

Calibration variables	$f_1(\Gamma_d)$	$f_2(\Gamma_d)$	ω_{r} Variance
$K_{\mathrm{p,c}}$	−	+	+
$K_{\mathrm{i,c}}$	−	+	+
$K_{\mathrm{p,w}}$	+	−	−
$K_{\mathrm{i,w}}$	+	−	−
λ_*	+	−	−

Calibration variables	FATM		SSTM		FlapBM		EdgeBM	
	Mean	Variance	Mean	Variance	Mean	Variance	Mean	Variance
$K_{\mathrm{p,c}}$	+	+	−	○	+	+	−	○
$K_{\mathrm{i,c}}$	+	+	−	○	+	+	−	○
$K_{\mathrm{p,w}}$	○	−	+	○	○	−	+	○
$K_{\mathrm{i,w}}$	+	−	○	○	+	−	○	○
λ_*	−	+	+	○	−	−	+	−

each calibration variable.

As observed, increasing $K_{\mathrm{p,c}}$ and $K_{\mathrm{i,c}}$, relative to their optimal value, positively affects $f_2(\Gamma_d)$, the rotor speed variance and the reduction of mean/variance of the fore-aft tower moment and flapwise bending moment for blade 1. This benefit, however, negatively impacts $f_1(\Gamma_d)$ and the mean of the side-to-side tower moment and edgewise bending moment for blade 1. No apparent influence is noted on the variance of the latter variables. These findings further confirm the coupling between the fore-aft and the flapwise moments and between the side-to-side and the edgewise moments. Conversely, an opposite trend for $f_1(\Gamma_d)$, $f_2(\Gamma_d)$ and the rotor speed variance is observed when increasing $K_{\mathrm{p,w}}$, $K_{\mathrm{i,w}}$ and λ_* beyond their optimal values. These observations confirm that optimal tuning of the calibration variables for the WSE-TSR tracking controller is needed to achieve a trade-off between power maximisation and torque minimisation.

4.6.4. FREQUENCY-DOMAIN RESULTS
This section compares the frequency domain characteristics for the defined cases using the linear analysis framework described in Section 4.4. First, the frequency responses for the controller transfer functions $K_{\Omega_{\mathrm{r}} \to \mathcal{T}_{\mathrm{g}}}(s)$ and $K_{\Lambda_* \to \mathcal{T}_{\mathrm{g}}}(s)$ are discussed, followed by the closed-loop transfer functions $T_{\Lambda_* \to \Lambda}(s)$ and $T_{\mathcal{V} \to \Lambda}(s)$.

CONTROLLER TRANSFER FUNCTIONS

The analysis strategy defined in Section 4.4.2 is employed to evaluate the characteristics of the controllers. The frequency responses of the transfer functions $K_{\Omega_r \to \mathcal{T}_g}(s)$ and $K_{\Lambda_* \to \mathcal{T}_g}(s)$ for the defined cases are presented in Figure 4.10. The results for the $K\omega^2$ controller are included as a baseline, being frequency independent with a constant gain over all frequencies.

For case E, the steady-state gain deviates from the baseline gain because the reference tip-speed ratio is calibrated at a higher and non-optimal set point of $\lambda_*^E = 7.71$. Furthermore, for the same case, it is seen that the controller cut-off frequencies are at the lowest frequency compared to the other cases, resulting in reduced torque variance responses. For increasing points towards case A, the controller cut-off frequency for both reference shaping and feedback-related transfer functions increases to higher frequencies, except for B. As shown in Figure 4.9, case B shows the closest resemblance in performance attained with the optimal baseline controller. A possible explanation is that the controller adheres to the $K\omega^2$-trajectory for the most extended frequency range. A notable observation is the resonance peaks for cases A and B, which enable a higher cut-off frequency of the loop gain, resulting in an increased closed-loop bandwidth to track the desired tip-speed ratio. In this context, it is essential to consider that while a slight increase in power performance is observed for case A, it is accompanied by elevated torque fluctuations. Therefore, having a controller with a bandwidth exceeding that of case A would not be advantageous, as it would likely be more aggressive, potentially leading to system instability and yielding no power gain at the expense of increased torque fluctuations. A further observation from the phase plots is the opposite sign of the controller transfer functions, which is understandable from a physical perspective. The generator torque increases for higher rotational speeds ($K_{\Omega_r \to \mathcal{T}_g}(s)$), whereas an inverse proportional relation exists between the desired tip-speed ratio and generator torque ($K_{\Lambda_* \to \mathcal{T}_g}(s)$).

CLOSED-LOOP TRANSFER FUNCTIONS

This section presents an analysis of the closed-loop controller characteristics. For the different cases, Figure 4.11 illustrates the frequency responses of the transfer functions $T_{\Lambda_* \to \Lambda}(s)$ and $T_{\mathcal{V} \to \Lambda}(s)$, representing the closed-loop system performance in terms of reference tracking (complementary sensitivity) and disturbance rejection (sensitivity), respectively. The results for these transfer functions confirm the observations in the open-loop analysis: increasing points toward point A exhibit an increased bandwidth and reference tracking performance. Furthermore, only points A and B show a resonance peak resulting in a higher closed-loop cut-off frequency. For the transfer function $T_{\mathcal{V} \to \Lambda}(s)$, it is concluded that cases C, D, and E are subpar in disturbance rejection performance compared to the baseline case. In addition, the effect of the Bode sensitivity integral is represented by the two remaining cases. That is, cases A and B show increased disturbance rejection performance for frequencies below the controller bandwidth, whereas, after this value, the characteristics worsen with respect to the baseline controller.

4.6.5. TIME-DOMAIN RESULTS

To further support the observations from the frequency-domain analysis, this section presents realistic time-domain simulation results. For clarity reasons, only two input
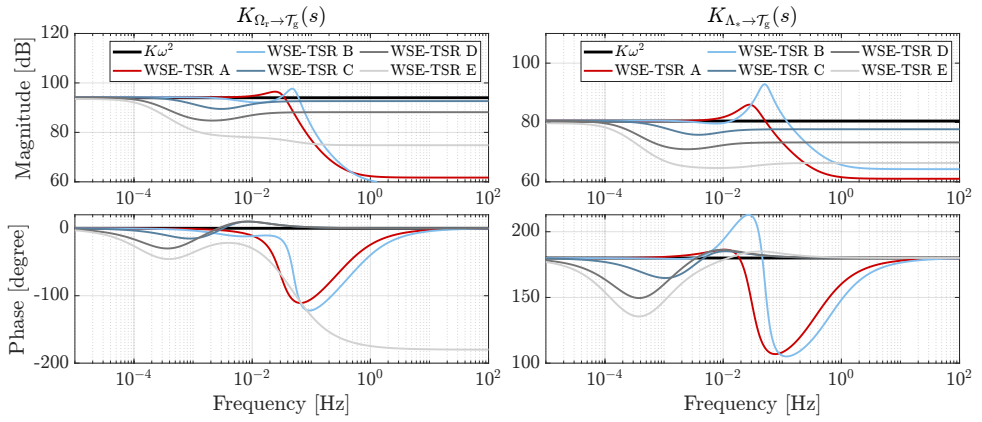
Figure 4.10: Bode plots of the controller transfer functions $K_{\Omega_r \to \mathcal{T}_g}(s)$ and $K_{\Lambda_* \to \mathcal{T}_g}(s)$ for the baseline $K\omega^2$ and the WSE-TSR tracking controller cases. While, for the baseline, $K_{(\Omega_r \to \mathcal{T}_g),K}$ and $K_{(\Lambda_* \to \mathcal{T}_g),K}$ show a constant gain over all frequencies, for the WSE-TSR tracking controllers, $K_{(\Omega_r \to \mathcal{T}_g),\text{TSR}}(s)$ and $K_{(\Lambda_* \to \mathcal{T}_g),\text{TSR}}(s)$ exhibit additional dynamics with an increasing cut-off frequency for increasing cases towards B. In particular, cases A and B present resonance peaks in their response to further improve the controller cut-off frequency.
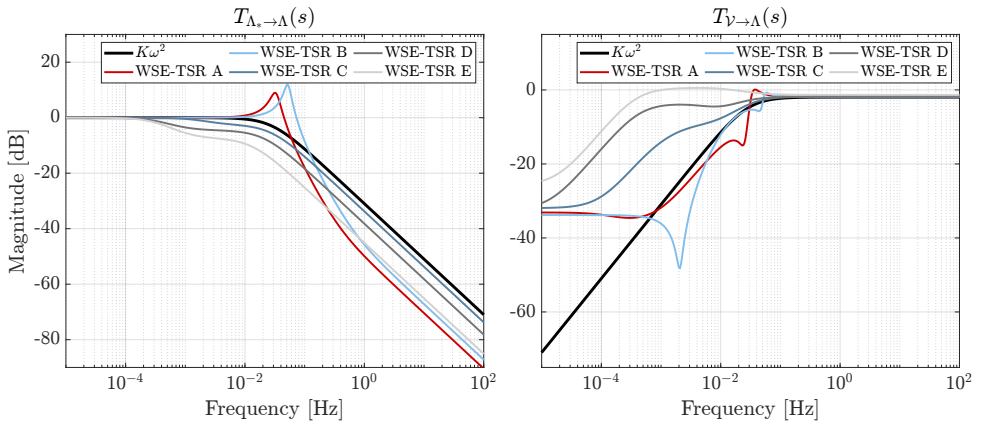
Figure 4.11: Bode plots of the closed-loop transfer functions $T_{\Lambda_* \to \Lambda}(s)$ and $T_{\mathcal{V} \to \Lambda}(s)$ for the baseline $K\omega^2$ and the WSE-TSR tracking controller cases. Regarding $T_{\Lambda_* \to \Lambda}(s)$, an increase in controller bandwidth with respect to the baseline can be observed when the calibration selected aims to maximise the power performance (i.e. A and B). On the other hand, for $T_{\mathcal{V} \to \Lambda}(s)$, this improvement is translated into a high-frequency sensitivity deterioration.

vectors Γ_5 corresponding to cases B and C are chosen. This selection aims to illustrate the characteristics of the WSE-TSR tracking controller for the optimal solution $f_2(\Gamma_d)$ and the trade-off between $f_1(\Gamma_d)$ and $f_2(\Gamma_d)$ compared to the baseline controller.

The mid-fidelity simulation is performed with OpenFAST using the NREL 5-MW reference turbine for a realistic turbulent wind profile, with a mean wind speed of $\bar{V} = 9\,\text{m/s}$ at hub height, a turbulence intensity of TI = 15%, and a total simulation time of 3600 s. Fig-

Figure 4.12: Simulation results for the $K\omega^2$ and the WSE-TSR tracking controllers subject to a realistic turbulent wind speed with a mean of 9 m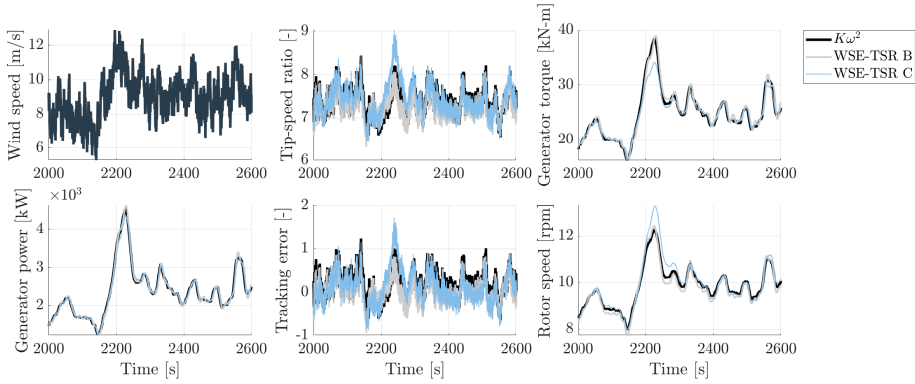/s and a turbulence intensity of 15%. Only results for cases B and C are presented. As expected from the location on the corresponding Pareto front $\mathcal{P}_f^5$, case B shows a similar performance to the baseline control strategy. On the other hand, case C represents a trade-off between the two objectives, minimising torque fluctuations with a minor impact on power production.

ure 4.12 shows the wind speed and the simulation results for the tip-speed ratio, tip-speed ratio tracking error, generator torque, rotor speed, and generator power. A smaller portion of the simulation is presented to emphasise the features in the time-domain results.

The WSE-TSR tracking controller, calibrated for case B, demonstrates performance comparable to the baseline controller without exhibiting superior power production. These observations align with the trends of the Pareto front illustrated in Figure 4.9. Simulation results obtained for case C show reduced torque fluctuations at the expense of increased oscillations in the rotor speed. This particular calibration results in a slower response of the WSE-TSR tracking controller, rendering the wind turbine more susceptible to variations in wind speed and, consequently, leading to higher fluctuations in rotor speed.

Upon closer examination, a notable instance occurs around 2200 s, wherein a change in wind speed from 8 m/s to 12 m/s prompts a corresponding change in rotor speed from 8 rpm to 13 rpm and an alteration in the tip-speed ratio from 7 to 9. During this transition period, the tip-speed ratio deviates from the reference λ_*, slightly increasing the tip-speed ratio tracking error (i.e. $\lambda - \lambda_*$). However, a minimal impact can be observed in power extraction from the wind, confirming that tuning C provides a good trade-off between power maximisation and load minimisation for the considered turbine.

4.7. CONCLUSIONS

This study presents a detailed analysis of the conventional $K\omega^2$ and the more advanced WSE-TSR tracking scheme, being a combined estimator-based tracking controller. A linear frequency-domain framework has been derived to evaluate the characteristics of both control schemes. A unified analysis strategy is proposed for a fair comparison of the controllers.

To explore the performance potential of both control schemes and, more specifically,

to discover whether the advanced controller provides benefits over the conventional one, a multi-objective optimisation problem is defined. The conflicting objectives are power maximisation and control signal variance minimisation. The approach to solving this optimisation problem is to explore the performance space using a constrained guided search for different dimensionalities of the design space. In other words, the controller calibration parameters have been categorised in input vectors of different dimensions, each subject to the multi-objective optimisation problem. The resulting Pareto front approximations represent the optimal solutions and controller calibrations, providing a trade-off between the defined objectives and dictating the selection of specific controller bandwidth. A set of Pareto optimal solutions has been evaluated in the frequency and time domains to provide more comprehensive insights into the balance between performance metrics and control dynamics, enabling users of the WSE-TSR tracking control scheme to make informed decisions on its optimal calibration.

Numerical simulations on the NREL 5 MW reference turbine show that an *optimally* calibrated WSE-TSR tracking control scheme can increase the controller bandwidth resulting in larger torque fluctuations. However, as opposed to claims about improved power capture in the literature, no power gains are attainable for present-day relevant turbine sizes compared to baseline control. On the other hand, the proposed calibration framework makes it possible to find a set of design variables for the WSE-TSR tracking control scheme that reduces torque fluctuations with a minor impact on the captured power.

Overall, the WSE-TSR tracking controller exhibits a more flexible control structure compared to the baseline $K\omega^2$ controller, providing a trade-off between power and load objectives that can facilitate the operation of large-scale modern wind turbines. Future work will focus on performing a similar analysis on smaller-scale wind turbines to confirm these benefits even for other commercial turbines.

BIBLIOGRAPHY

[1] S. Watson, A. Moro, V. Reis, C. Baniotopoulos, S. Barth, G. Bartoli, F. Bauer, E. Boelman, D. Bosse, A. Cherubini, A. Croce, L. Fagiano, M. Fontana, A. Gambier, C. Gkoumas K.and Golightly, M. I. Latour, P. Jamieson, J. Kaldellis, A. Macdonald, J. Murphy, M. Muskulus, F. Petrini, L. Pigolotti, F. Rasmussen, P. Schild, R. Schmehl, N. Stavridou, J. Tande, N. Taylor, T. Telsnig, and R. Wiser, "Future emerging technologies in the wind power sector: A European perspective", *Renewable and Sustainable Energy Reviews*, vol. 113, 2019. DOI: 10.1016/j.rser.2019.109270. [Online]. Available: https://doi.org/10.1016/j.rser.2019.109270.

[2] J. Lee and F. Zhao, "Global Wind Report 2022", Tech. Rep., 2022. [Online]. Available: https://gwec.net/global-wind-report-2022/.

[3] *UN Climate change conference UK 2021*, 2021. [Online]. Available: https://ukcop26.org/cop26-goals/.

[4] I. Komusanac, G. Brindley, D. Fraile, and L. Ramirez, "Wind energy in Europe - 2021 statistics and the outlook for 2022-2026", Tech. Rep., 2022. [Online]. Available: https://windeurope.org/intelligence-platform/product/wind-energy-in-europe-2021-statistics-and-the-outlook-for-2022-2026/.

[5] P. Veers, K. Dykes, E. Lantz, S. Barth, C. L. Bottasso, O. Carlson, A. Clifton, J. Green, P. Green, H. Holttinen, D. Laird, V. Lehtomäki, J. K. Lundquist, J. Manwell, M. Marquis, C. Meneveau, P. Moriarty, X. Munduate, M. Muskulus, J. Naughton, L. Pao, J. Paquette, J. Peinke, A. Robertson, J. S. Rodrigo, A. M. Sempreviva, J. C. Smith, A. Tuohy, and R. Wiser, "Grand challenges in the science of wind energy", *Science*, vol. 366, no. 6464, 2019. DOI: 10.1126/science.aau2027. [Online]. Available: https://www.science.org/doi/10.1126/science.aau2027.

[6] L. Y. Pao and K. E. Johnson, "Control of wind turbines: Approaches, challenges, and recent developments", *IEEE Control Systems Magazine*, vol. 31, no. 2, pp. 44–62, 2011. DOI: 10.1109/MCS.2010.939962. [Online]. Available: https://ieeexplore-ieee-org.tudelft.idm.oclc.org/document/5730721.

[7] E. A. Bossanyi, "The Design of closed loop controllers for wind turbines", *Wind Energy*, vol. 3, no. 3, pp. 149–163, 2000. DOI: 10.1002/we.34. [Online]. Available: https://doi-org.tudelft.idm.oclc.org/10.1002/we.34.

[8] T. Burton, N. Jenkings, D. Sharpe, and E. A. Bossanyi, *Wind Energy Handbook*, J. W. Sons, Ed. 2011. DOI: 10.1002/9781119992714. [Online]. Available: https://onlinelibrary.wiley.com/doi/book/10.1002/9781119992714.

[9]   C. L. Bottasso, A. Croce, Y. Nam, and C. E. D. Riboldi, "Power curve tracking in the presence of a tip speed constraint", *Renewable Energy*, vol. 40, no. 1, pp. 1–12, 2012. DOI: 10.1016/j.renene.2011.07.045. [Online]. Available: http://dx.doi.org/10.1016/j.renene.2011.07.045.

[10] K. E. Johnson, L. Pao, M. J. Balas, J. Lee, and L. J. Fingersh, "Control of Variable-Speed Wind Turbines: Standard and Adaptive Techniques for Maximizing Energy Capture", *IEEE Control Systems*, vol. 26, no. 3, pp. 70–81, 2006. DOI: 10.1109/MCS.2006.1636311. [Online]. Available: https://ieeexplore.ieee.org/document/1636311.

[11] A. A. Ozdemir, P. Seilery, and G. J. Balas, "Benefits of preview wind information for region 2 wind turbine control", in *51st AIAA Aerospace Sciences Meeting including the New Horizons Forum and Aerospace Exposition 2013*, 2013, pp. 1–7. DOI: 10.2514/6.2013-317. [Online]. Available: https://arc.aiaa.org/doi/10.2514/6.2013-317.

[12] K. E. Johnson, L. J. Fingersh, M. J. Balas, and L. Pao, "Methods for increasing region 2 power capture on a variable speed hawt", in *Collection of ASME Wind Energy Symposium Technical Papers AIAA Aerospace Sciences Meeting and Exhibit*, 2004, pp. 103–113. DOI: 10.2514/6.2004-350. [Online]. Available: https://arc.aiaa.org/doi/10.2514/6.2004-350.

[13] N. J. Abbas, D. S. Zalkind, L. Pao, and A. Wright, "A reference open-source controller for fixed and floating offshore wind turbines", *Wind Energy Science*, vol. 7, no. 1, pp. 53–73, 2022. DOI: 10.5194/wes-7-53-2022. [Online]. Available: https://wes.copernicus.org/articles/7/53/2022/.

[14] L. J. Fingersh and P. W. Carlin, "Results from the NREL variable-speed test bed", in *ASME 17th Wind Energy Symposium*, 1999, pp. 233–237. [Online]. Available: https://www.nrel.gov/docs/legosti/fy98/23811.pdf.

[15] J. Creaby, Y. Li, and J. E. Seem, "Maximizing Wind Turbine Energy Capture Using Multivariable Extremum Seeking Control", *Wind Engineering*, vol. 33, no. 4, pp. 361–387, 2009. DOI: 10.1260/030952409789685753. [Online]. Available: https://journals.sagepub.com/doi/abs/10.1260/030952409789685753.

[16] Y. Xiao, Y. Li, and M. A. Rotea, "Experimental evaluation of extremum seeking based region-2 controller for cart3 wind turbine", in *AIAA 2016 SciTech Wind Energy Symposium*, 2016. DOI: 10.2514/6.2016-1737. [Online]. Available: https://arc.aiaa.org/doi/10.2514/6.2016-1737.

[17] M. A. Rotea, "Logarithmic power feedback for extremum seeking control of wind turbines", in *IFAC-PapersOnLine*, vol. 50, 2017, pp. 4504–4509. DOI: 10.1016/j.ifacol.2017.08.381. [Online]. Available: https://www.sciencedirect.com/science/article/pii/S2405896317307255.

[18] U. Ciri, S. Leonardi, and M. A. Rotea, "Evaluation of log-of-power extremum seeking control for wind turbines using large eddy simulations", *Wind Energy*, vol. 22, pp. 992–1002, 2018. DOI: 10.1002/we.2336. [Online]. Available: https://doi.org/10.1002/we.2336.

[19] E. I. van der Hooft, P. Schaak, and T. G. van Engelen, "Wind turbine control algorithms", Tech. Rep., 2003. [Online]. Available: https://publications.tno.nl/publication/34628358/5H2cm6/c03111.pdf.

[20] K. Z. Østergaard, P. Brath, and J. Stoustrup, "Estimation of effective wind speed", in *Journal of Physics: Conference Series*, 2007. DOI: 10.1088/1742-6596/75/1/012082. [Online]. Available: https://iopscience.iop.org/article/10.1088/1742-6596/75/1/012082.

[21] M. N. Soltani, T. Knudsen, M. Svenstrup, R. Wisniewski, P. Brath, R. Ortega, and K. Johnson, "Estimation of rotor effective wind speed: A comparison", *IEEE Transactions on Control Systems Technology*, vol. 21, no. 4, pp. 1155–1167, 2013. DOI: 10.1109/TCST.2013.2260751. [Online]. Available: https://ieeexplore.ieee.org/document/6524000.

[22] B. Boukhezzar and H. Siguerdidjane, "Nonlinear control of variable speed wind turbines without wind speed measurement", in *Proceedings of the 44th IEEE Conference on Decision and Control*, 2005, pp. 3456–3461. DOI: 10.1109/CDC.2005.1582697. [Online]. Available: https://ieeexplore.ieee.org/document/1582697.

[23] L. Brandetti, Y. Liu, S. P. Mulders, C. Simão Ferreira, S. Watson, and J. W. van Wingerden, "On the ill-conditioning of the combined wind speed estimator and tip-speed ratio tracking control scheme", ser. Journal of Physics: Conference Series, 2022. DOI: 10.1088/1742-6596/2265/3/032085. [Online]. Available: https://iopscience.iop.org/article/10.1088/1742-6596/2265/3/032085.

[24] P. F. Odgaard, L. F. S. Larsen, R. Wisniewski, and T. G. Hovgaard, "On using pareto optimality to tune a linear model predictive controller for wind turbines", *Renewable Energy*, vol. 87, pp. 884–891, 2016. DOI: 10.1016/j.renene.2015.09.067. [Online]. Available: https://www.sciencedirect.com/science/article/pii/S0960148115303463.

[25] M. Lara, J. Garrido, M. L. Ruz, and F. Vázquez, "Multi-objective optimization for simultaneously designing active control of tower vibrations and power control in wind turbines", *Energy Reports*, vol. 9, pp. 1637–1650, 2023. DOI: 10.1016/j.egyr.2022.12.141. [Online]. Available: https://www.sciencedirect.com/science/article/pii/S2352484722027421.

[26] D. J. Leith and W. E. Leithead, "Implementation of wind turbine controllers", *International Journal of Control*, vol. 66, no. 3, pp. 349–380, 1997. DOI: 10.1080/002071797224621. [Online]. Available: https://doi.org/10.1080/002071797224621.

[27] W. E. Leithead and B. Connor, "Control of variable speed wind turbines: Design task", *International Journal of Control*, vol. 73, no. 13, pp. 1189–1212, 2000. DOI: 10.1080/002071700417849. [Online]. Available: https://doi.org/10.1080/002071700417849.

4

[28] S. P. Mulders, L. Brandetti, F. Spagnolo, Y. Liu, P. Brandt, and J. W. van Wingerden, "A learning algorithm to advanced wind turbine controllers for the calibration of internal model uncertainties: A wind speed measurement-free approach", ser. Proceedings of the 2023 American Control Conference (ACC 2023), Jun. 2023. DOI: 10.23919/ACC55779.2023.10156125. [Online]. Available: https://ieeexplore.ieee.org/document/10156125.

[29] T. G. Hovgaard, S. Boyd, and J. B. Jørgensen, "Model predictive control for wind power gradients", *Wind Energy*, vol. 18, no. 6, pp. 991–1006, 2015. DOI: 10.1002/we.1742. [Online]. Available: https://onlinelibrary.wiley.com/doi/abs/10.1002/we.1742.

[30] A. Pamososuryo, Y. Liu, T. Hovgaard, R. Ferrari, and J. W. van Wingerden, "Convex Economic Model Predictive Control for Blade Loads Mitigation on Wind Turbines", *Wind Energy*, 2023. [Online]. Available: https://d197for5662m48.cloudfront.net/documents/publicationstatus/129963/preprint_pdf/07a332bb16795d75c3c263d251738fb0.pdf.

[31] J. Jonkman, S. Butterfield, W. Musial, and G. Scott, "Definition of a 5-MW Reference Wind Turbine for Offshore System Development", Tech. Rep., 2009. DOI: NREL/TP-500-38060. [Online]. Available: https://www.nrel.gov/docs/fy09osti/38060.pdf.

[32] Y. Liu, A. K. Pamososuryo, R. M. G. Ferrari, and J. W. van Wingerden, "The Immersion and Invariance Wind Speed Estimator Revisited and New Results", *IEEE Control Systems Letters*, vol. 6, pp. 361–366, 2022. DOI: 10.1109/LCSYS.2021.3076040. [Online]. Available: https://ieeexplore-ieee-org.tudelft.idm.oclc.org/document/9416566.

[33] R. Ortega, F. Mancilla-David, and F. Jaramillo, "A globally convergent wind speed estimator for wind turbine systems", *International Journal of Adaptive Control and Signal Processing*, vol. 27, pp. 413–425, 2013. DOI: 10.1002/acs.2319. [Online]. Available: https://doi-org.tudelft.idm.oclc.org/10.1002/acs.2319.

[34] The MathWorks Inc., *Matlab version: 9.11.0 (r2021b)*, Natick, Massachusetts, United States, 2021. [Online]. Available: https://www.mathworks.com.

[35] NREL, "OpenFAST Documentation", National Renewable Energy Laboratory, Tech. Rep., 2021. [Online]. Available: https://openfast.readthedocs.io/en/main/.

[36] K. J. Aström and R. M. Murray, *Feedback systems: An Introduction for Scientists and Engineers*. 2010. DOI: 10.1086/596297. [Online]. Available: https://www.journals.uchicago.edu/doi/10.1086/596297.

[37] M. K. Lukovic, Y. Tian, and W. Matusik, "Diversity-guided multi-objective Bayesian optimization with batch evaluations", in *Advances in Neural Information Processing Systems*, vol. 33, 2020, pp. 17708–17720. [Online]. Available: https://proceedings.neurips.cc/paper_files/paper/2020/file/cd3109c63bf4323e6b987a Paper.pdf.

[38] K. Miettinen, *Nonlinear multiobjective optimization.* 1999. DOI: 10.1007/978-1-4615-5563-6. [Online]. Available: https://link.springer.com/book/10.1007/978-1-4615-5563-6.

4

5

OPTIMAL CONTROLLER CALIBRATION FOR BALANCING PERFORMANCE WITH NOISE ACCEPTANCE

Deploying VAWTs close to densely populated urban areas often triggers considerable local opposition to wind energy projects. Among the primary concerns raised by communities is the issue of noise emissions. Noise annoyance should be considered in the decision-making process to foster the social acceptance of VAWTs in urban areas. At the same time, maximising the operational efficiency of VAWTs in terms of power generation and actuation effort is equally important. This chapter balances noise and aero-servo-elastic performance by formulating and solving a multi-objective optimisation problem from a controller calibration perspective. Psychoacoustic annoyance is taken as a novel indicator for the noise objective by providing a more reliable estimate of the human perception of wind turbine noise than conventional sound metrics. The computation of the psychoacoustic annoyance metric is made feasible by integrating it with a low-fidelity noise prediction model. For optimisation, an advanced partial-load control scheme is considered, with the $K\omega^2$ controller as a baseline for comparison. Optimal solutions balancing the defined objectives are identified using the multi-criteria decision-making (MCDM) method and are subsequently assessed using a frequency-domain controller analysis framework and mid-fidelity time-domain aero-servo-elastic simulations. The MCDM results indicate that the optimally calibrated WSE-TSR tracking controller can effectively balance aero-servo-elastic performance with noise emissions, marking the first instance of integrating residential concerns into the decision-making process.

5.1. INTRODUCTION

The transition from fossil fuels to sustainable energy sources is motivated by the escalating demand for energy and the imperative to curtail greenhouse gas emissions. In this context, wind energy is vital, accounting for 906 GW of global installed capacity as of 2022, with an annual growth rate of 9% [1]. Projections for the next five years anticipate 680 GW of new installed capacity with an annual growth rate of 13%, considering both onshore and offshore locations. The offshore wind sector has garnered significant attention, primarily due to its abundant wind resources, which can be harnessed by large-scale wind turbines with an average rated output of around 8 MW connected to the grid [2]. However, it is worth noting that offshore wind installation is often associated with high costs both in construction and grid connection, hindering its rapid expansion compared to onshore wind projects [3].

Onshore wind sites remain critical for the exploitation of wind energy [4]. While most of this energy is generated from large-scale turbines [3], there is a growing interest in small-scale turbines due to their potential applications in urban environments [5]. Potential integration of small rotors on tall buildings might address local renewable energy demands, complementing the push for sustainable building design [6]. Moreover, the importance of small-scale wind turbines extends to future distributed energy networks, especially when effectively combined with energy storage systems [7].

In this context, vertical-axis wind turbines (VAWTs) present an attractive opportunity to harness urban wind conditions, characterised by low average wind speeds and high turbulence levels, because of their ability to receive wind from any direction without requiring a yaw mechanism [8], their simple blade design leading to cost-effective maintenance [9] and their reduced visual impact [10], [11] compared to the horizontal-axis wind turbines (HAWTs) dominating the urban wind energy market.

However, three main challenges remain for the urban deployment of small-scale VAWTs. The first revolves around the need to foster community engagement and social acceptance [4], [5]. Noise annoyance significantly contributes to the local opposition against urban wind energy projects [12]. Measures taken to mitigate such concerns result in reduced power capture efficiency, adversely impacting revenue generation, particularly if the turbines are required to cease operation during nighttime hours [13]. To reduce the impact of such measures on the VAWT performance, an accurate prediction of the wind turbine noise impact on nearby residents is essential. This task is complex due to the influence of various factors, such as wind speed, direction, distance, and background noise [14]. Commonly used time-averaged metrics, such as A-weighted sound pressure level or the day-evening-night level (L_{den}), may not fully capture the sound properties responsible for noise annoyance [15]. Therefore, recent efforts have focused on the auralization of environmental acoustic scenarios. Similar to its visual counterpart, this technique allows for the artificial reproduction of audible situations using numerical data [16]. A notable contribution to this topic comes from the work of Merino-Martínez et al. [13], who proposed a novel holistic approach based on synthetic sound auralization and psychoacoustic sound quality metrics to evaluate the annoyance caused by wind turbine noise.

Turning to the second and the third challenges, optimising the controller to ensure an optimal and reliable estimation of the performance of small-scale VAWTs in turbulent

and fluctuating wind conditions is paramount [4], [5], [17]. The combined wind speed estimator and tip-speed ratio (WSE-TSR) tracking controller [18] has been successfully applied to maximise the energy capture of VAWTs [19], [20], demonstrating good dynamic performance in tracking the optimal operating point in turbulent wind conditions and in predicting the turbine performance. This control scheme ensures that the wind turbine operates at the maximum power coefficient associated with a particular tip-speed ratio and pitch angle [21]. To track the optimal operating point and extract the maximum power, the estimated rotor-effective wind speed (REWS) [22], [23] is used to compute the desired rotor speed reference.

However, the optimal calibration of the WSE-TSR tracking controller is a crucial and nontrivial task due to the controller's nonlinearity and high dependence on a priori model information. The first effort in providing insights into the complex dynamic of the scheme is the derivation of a linear frequency-domain framework in [24]. The work also reveals that the system is ill-conditioned, meaning that the scheme is unable to uniquely provide a wind speed estimate from the product with other internal model parameters. While the frequency-domain framework provides insights for analysing turbine controllers in terms of bandwidth, relating the linear framework to practically meaningful performance metrics (e.g. energy capture and actuation effort) remains an intricate task.

To this end, a recent study by the same authors [25] focused on finding the optimal calibration of the WSE-TSR tracking controller in a multi-objective setting [26]–[28] with power maximisation and actuation effort minimisation as conflicting objectives. The set of Pareto optimal solutions is then evaluated with a frequency-domain framework to relate performance metrics to controller insights. Results obtained using the NREL 5 MW reference HAWT [29] under realistic turbulent wind conditions show that when compared to the baseline $K\omega^2$ controller, an optimally calibrated WSE-TSR tracking control strategy does not enhance power capture, however, does enable the reduction of torque actuation effort with a minor decrease in power production. This finding contradicts the expectations from the existing literature, which claimed energy capture benefits of 1% to 3% when applying a manually calibrated WSE-TSR tracking controller [18], [30]. It should be noted that these conclusions were made more than two decades back and based on the application of wind turbines much smaller than the NREL 5 MW turbine.

Hence, validating the above-mentioned hypothesis on a small-scale wind turbine, like an urban VAWT, holds a significant interest. In the existing body of literature, numerous studies have investigated the multi-faceted aspects of small-scale turbine optimisation, particularly concerning the trade-off between minimising noise emissions and maximising power performance on HAWTs [31]–[33]. Despite this interest, there is a distinct lack of corresponding studies addressing these aspects in the context of VAWTs. Therefore, this paper tackles the multi-objective optimisation problem from a control perspective by balancing aero-servo-elastic turbine performance (power capture and actuation effort) with noise (psychoacoustic annoyance) for an urban VAWT. Finding a balance between these objectives will further promote the application of VAWTs in urban environments.

The 1.5 m two-bladed H-Darrieus VAWT [34] is chosen as a case study in the current work. The selection of this specific turbine is motivated by the availability of experimental aerodynamic data and its suitability for rooftop integration [6]. The psychoacoustic annoyance value needed for the optimal controller calibration is computed by coupling the

perception-based approach proposed by Merino-Martínez et al. [13] and the low-fidelity noise prediction model developed and validated against high-fidelity simulations by Brandetti et al. [35]. As experimental acoustic VAWT data are unavailable, the aforementioned model is applied, providing the estimated noise spectra for the small-scale VAWT. These signals are subsequently auralized and assessed with psychoacoustic sound quality metrics to estimate the psychoacoustic noise annoyance.

The optimisation process explores the parameter space of the considered WSE-TSR tracking controller through a guided search procedure. A set of optimal solutions is found to construct the Pareto front in a trade-off between power maximisation, actuation effort minimisation, and psychoacoustic annoyance minimisation. These optimal results are then assessed by a linear frequency-domain system and controller analysis framework [25] for comparison to the baseline $K\omega^2$ controller. Therefore, the main contributions of this chapter are:

- Integrating perception-based psychoacoustic sound quality metrics with a low-fidelity noise prediction model to accurately predict and characterise the acoustic emissions of a small-scale VAWT in terms of psychoacoustic annoyance.

- Presenting an architecture for implementing torque control strategies in small-scale VAWTs with the mid-fidelity software QBlade [36] to conduct realistic aero-servo-elastic simulations of an urban VAWT.

- Formulating and solving a multi-objective optimisation problem for finding the optimal calibration of the WSE-TSR tracking controller as a trade-off between acoustic and aero-servo-elastic performance for an urban VAWT, for the first time taking into account residential concerns in the decision-making process.

The chapter is structured as follows: Section 5.3 derives the model for the wind turbine under study. Section 5.4 presents the two considered torque control strategies, namely the WSE-TSR tracking controller and the baseline $K\omega^2$ controller. Section 5.5 presents the combined noise prediction model and psychoacoustic annoyance model. The architecture for implementing the considered torque control strategies in QBlade and their calibration by means of multi-objective optimisation are provided in Section 5.6. The optimally calibrated WSE-TSR tracking control scheme is compared to the baseline for its performance in Section 5.7 using results from both the frequency-domain analysis and the realistic mid-fidelity, time-domain simulations. Section 5.8 provides an overview of the main findings and recommendations for future work.

5.2. PREREQUISITES

This section outlines the necessary prerequisites. The notations $\hat{(\cdot)}$ and $\dot{(\cdot)}$ indicate estimated quantities and time derivatives, respectively. The symbol $\bar{(\cdot)}$ represents values corresponding to a specific operating point but also a mean value, whereas $(\cdot)_*$ denotes values indicating the intended optimal or reference parameters.
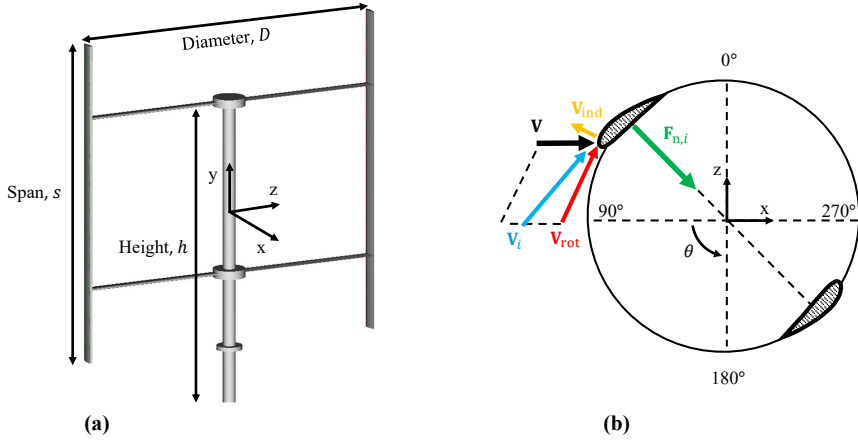
(a)   **(b)**

Figure 5.1: **(a)** Vertical-axis wind turbine (VAWT) geometry and dimensions. The turbine is a two-bladed H-Darrieus VAWT, with diameter D, span s and height h of dimensions equal to 1.5 m. **(b)** Coordinate system and definition of the rotor-effective wind speed (REWS) **V**, the blade-effective wind speed (BEWS) $\mathbf{V}_i$ and the normal load acting on the blade per unit span $F_{n,i}$ vectors adapted from [37]. The coordinate system is Cartesian, with the origin at the turbine centre. The blade azimuthal position θ is defined with respect to blade 1 and is considered positive in the counterclockwise direction. The vector of the BEWS $\mathbf{V}_i$ for the blade i results from the summation of three vector components: the REWS **V**, the rotational velocity $\mathbf{V}_{rot}$ of the turbine, and the induced velocity $\mathbf{V}_{ind}$. The normal force $\mathbf{F}_{n,i}$ per unit span has a positive sign when the vector points inwards.

5.3. VERTICAL-AXIS WIND TURBINE

In this section, the model for the VAWT is presented. Specifically, a two-bladed H-Darrieus turbine is considered, for which experimental aerodynamic data are available, as shown in Figure 5.1**(a)**. To minimise blade deflection, two horizontal struts are used for each blade, located at approximately 25% and 75% of the blade length. The blades have a NACA 0021 profile with a chord length $c_b = 0.075$ m, while the struts have a NACA 0018 profile with a chord length $c_s = 0.060$ m. The diameter of the VAWT is $D = 1.48$ m, with

Table 5.1: PitchVAWT design specifications [34].

Parameter	Value
Number of blades (N_b)	2
Span (s)	1.5 m
Height (h)	1.5 m
Diameter (D)	1.5 m
Blade chord (c_b)	7.5×10^{-2} m
Strut chord (c_s)	6×10^{-2} m
Rated power (P)	600 W
Generator efficiency (μ)	1
Gearbox ratio (N)	1
Rotor inertia (J)	1.5 kg m^2

a span s and a height h, both equal to 1.5 m. These specifications are summarised in Table 5.1, and more detailed information about the VAWT design can be found in previous work [34], where the turbine was experimentally investigated.

Figure 5.1(b) shows the turbine Cartesian coordinate system with the origin at the turbine centre. To aid in the interpretation of the results, the blade rotation is divided into two regions: the upwind region, where $0° \leq \theta < 180°$, and the downwind region, where $180° \leq \theta < 360°$. The blade azimuthal position θ is defined with respect to blade 1, and $\theta = 90°$ and $\theta = 270°$ represent the most upwind and downwind positions, respectively. Blade 2 lags behind blade 1 by $\theta = 180°$.

By examining the 2D blade element depicted in Figure 5.1(b), the vector of the blade-effective wind speed (BEWS) is defined for each blade as follows:

$$\mathbf{V}_i = \mathbf{V} + \mathbf{V}_{\text{rot}} + \mathbf{V}_{\text{ind}}, \tag{5.1}$$

where $i \in N_b = \{1, 2\}$ is the blade index for the VAWT under study, $\mathbf{V}$ denotes the vector for the REWS, $\mathbf{V}_{\text{rot}}$ represents the vector of the tangential velocity of the rotor, resulting from the cross product of the vectors of the rotational speed and the radius of the turbine, and $\mathbf{V}_{\text{ind}}$ is the vector of the induced velocity, caused by the force field that the turbine generates during the rotation. A detailed derivation of the BEWS can be found in [37] for interested readers. In the following, the italicised notations V and V_i denote the scalar representation for the REWS and BEWS vector quantities $\mathbf{V}$ and $\mathbf{V}_i$, respectively. The wind turbine rotor dynamics are given by

$$J\dot{\omega}_r = T_r - T_g N, \tag{5.2}$$

$$\dot{\theta} = \omega_r, \tag{5.3}$$

where J is the effective inertia at the low-speed shaft (LSS) and is obtained from the relation $J = J_g N^2 + J_r$, in which J_g and J_r are the inertia of the generator and rotor, respectively,
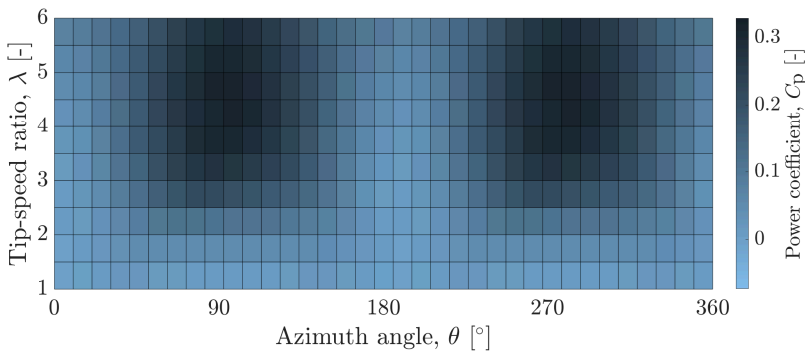
Figure 5.2: Power coefficient C_p, as a function of the tip-speed ratio λ and azimuth angle θ, for the two-bladed H-Darrieus VAWT. The maximum values for the C_p are observed at $\theta = 90°$ and at $\theta = 270°$, as they correspond to the most upwind locations for blade 1 and blade 2, respectively. Due to the presence of these two blades, the twice-per-revolution (2P) periodicity of C_p is evident, especially at high values of λ.
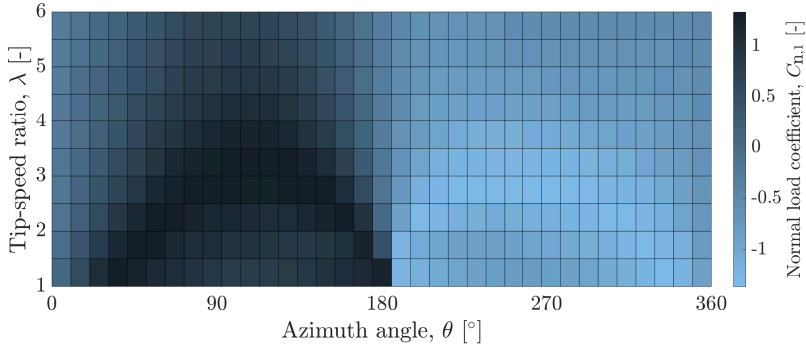
Figure 5.3: Normal load coefficient mapping $C_{n,1}$, as a function of the tip-speed ratio λ and azimuth angle θ, for blade 1 of the H-Darrieus VAWT. It is evident that the normal blade force varies over the rotation, being positive upwind ($0° \leq \theta < 180°$) and negative downwind ($180° \leq \theta < 360°$), with its maximum value at an azimuth angle $\theta = 90°$. This dynamics demonstrates the presence of a once-per-revolution periodicity (1P) on the $C_{n,1}$.

5

T_g is the generator torque, and $N := \omega_g/\omega_r$ represents the gearbox ratio of the transmission, with ω_g and ω_r being the generator and the rotor speed, respectively. Assuming a pitch angle β constant at an angle of $0°$, value that maximises the aerodynamic efficiency for the below-rated region, the aerodynamic rotor torque can be formulated as

$$T_r := \frac{1}{2} \rho A_{rot} \frac{V^3}{\omega_r} C_p(\lambda, \theta), \qquad (5.4)$$

with ρ and A_{rot} being the air density and the rotor area, respectively. In contrast to a HAWT, the power coefficient C_p for a VAWT is a non-linear mapping as a function of azimuth angle and the tip-speed ratio

$$\lambda := \frac{\omega_r R}{V}, \qquad (5.5)$$

where R represents the rotor radius. This dependency arises from the VAWT operation as the BEWS, and the angle of attack varies with the azimuth rotation angle, resulting in intrinsic three-dimensional aerodynamics [38]. These periodic and non-linear system characteristics are reflected in the dynamics of the VAWT, as illustrated in Equation (5.3) and Figure 5.2, where the C_p curves of the VAWT under study are plotted. The mapping is obtained from steady-state wind turbine simulations for a constant wind velocity of 4 m/s at various operating points. The power coefficient mapping exhibits a periodicity of twice-per-revolution (2P) due to the turbine having two blades [39].

For a VAWT, the normal load acting on the blade per unit span, shown in Figure 5.1, is defined as follows:

$$F_{n,i} = \frac{1}{2} \rho c_b V_i^2 C_{n,i}(\lambda, \theta_i), \qquad (5.6)$$

where V_i represents the magnitude of the BEWS for each blade. The normal load coefficient, denoted as $C_{n,i}$, is a nonlinear function that depends on the tip-speed ratio

and azimuthal position of blade i. It should be noted that $C_{n,i}$ also varies with the blade pitch angle β_i. However, β_i is considered constant throughout this study, maintaining a value of $0°$. Figure 5.3 illustrates the $C_{n,1}$ curve for the VAWT, obtained from wind turbine simulations conducted under steady-state conditions at a constant wind speed of 4 m/s. Notably, a maximum normal load occurs at approximately $\theta = 90°$, corresponding to blade 1 being upwind. Blade 2 exhibits similar behaviour, although with a $180°$ shift. The variations in load dynamics throughout the rotation demonstrate the presence of a once-per-revolution periodicity (1P) in $C_{n,i}$.

With the definition of the rotor and blade dynamics at hand, the wind turbine can be linearised around a specific operating point. Firstly, the non-linear expression for the aerodynamic rotor torque given in Equation (5.4) is combined with Equation (5.2). The resulting expression is then linearised with respect to the rotor speed state, generator torque control input, and wind speed disturbance input. The outcome is represented by

$$\dot{\omega}_r = G(V)\,\omega_r + E\,T_g + H(V)\,V. \tag{5.7}$$

The original variables express the values perturbed around their operating points to ensure conciseness, while $G(V), E$ and $H(V)$ represent partial derivatives defined as

$$G(V) = \frac{1}{J}\frac{\partial T_r}{\partial \omega_r}\bigg|_{(\bar{\omega}_r,\bar{V})} = \frac{1}{2J}\rho A_{\text{rot}}\left(-\frac{V^3}{\omega_r^2}C_p(\omega_r,V) + \frac{V^2 R}{\omega_r}\frac{\partial C_p(\omega_r,V)}{\partial\lambda}\right)\bigg|_{(\bar{\omega}_r,\bar{V})}, \quad E = -\frac{N}{J}, \tag{5.8}$$

$$H(V) = \frac{1}{J}\frac{\partial T_r}{\partial V}\bigg|_{(\bar{\omega}_r,\bar{V})} = \frac{1}{2J}\rho A_{\text{rot}}\left(\frac{3V^2}{\omega_r}C_p(\omega_r,V) - VR\frac{\partial C_p(\omega_r,V)}{\partial\lambda}\right)\bigg|_{(\bar{\omega}_r,\bar{V})}. \tag{5.9}$$

The argument V is included for the convenient definition of estimator-based expressions for G and H in a later section but is omitted in expressions from this point onwards.

The time domain form of Equation (5.7) is then Laplace transformed to give the transfer functions from generator torque and wind speed inputs to rotor speed as output

$$\Omega_r(s) = \frac{E}{s-G}\mathcal{T}_g(s) + \frac{H}{s-G}\mathcal{V}(s), \tag{5.10}$$

where s represents the Laplace operator. The variables $\Omega_r, \mathcal{T}_g,$ and $\mathcal{V}$ indicate the frequency-domain representation of the rotational speed, generator torque, and wind speed, respectively.

5.4. Theory and derivations of wind turbine controllers

The $K\omega^2$ controller is an effective and widely used approach for maximising energy capture in partial load operation. However, the control strategy is limited in balancing power and actuation effort objectives for large-scale wind turbines. To address this issue, the more advanced WSE-TSR tracking scheme offers greater control flexibility. The current study aims to evaluate these findings for small-scale wind turbines, particularly VAWTs, which are promising solutions for urban environments.

This section derives the complete and non-linear representations of both the WSE-TSR tracking controller and the baseline $K\omega^2$ used for comparison. This process involves
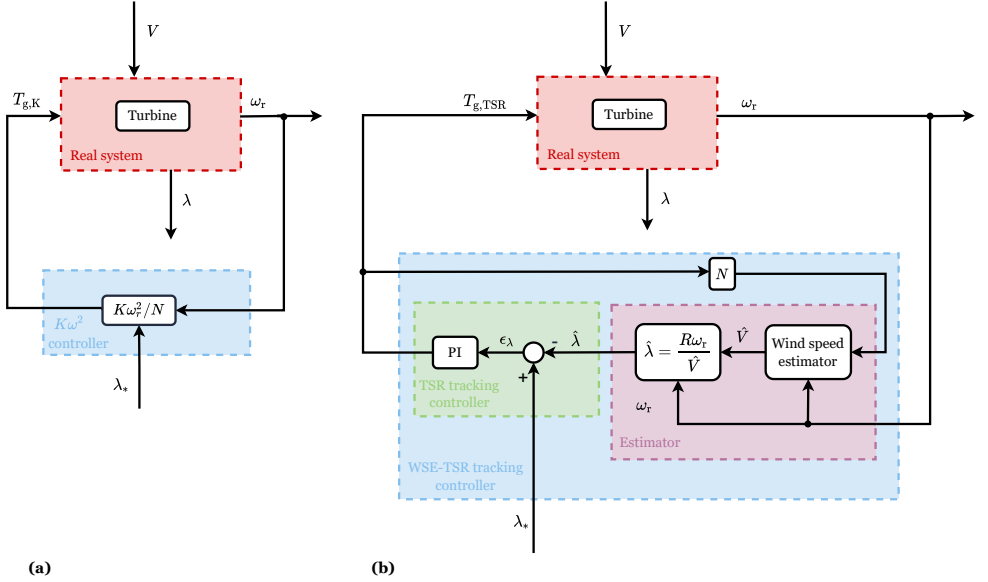
Figure 5.4: Block diagram of **(a)** the $K\omega^2$ and **(b)** the WSE-TSR tracking control frameworks. For both schemes, the **red** box highlights the wind turbine system with two inputs (the generator torque, $T_{g,K}$ and $T_{g,TSR}$ respectively, and the wind speed V), and with two outputs (the rotational speed, ω_r, and the TSR, λ). For **(a)** the $K\omega^2$ block diagram, the measured ω_r and the optimal TSR, λ_*, are used as inputs of the controller (**cyan** box) to compute $T_{g,K}$. On the other hand, for **(b)** the WSE-TSR tracking controller, the **cyan** box includes the estimator (**purple** box) and the TSR tracker controller (**green** box). The measured $T_{g,TSR}$ and ω_r are used to estimate the rotor-effective wind speed $\hat{V}$ and to calculate an estimate of TSR, $\hat{\lambda}$, in the estimator block. The controller acts on the difference between $\hat{\lambda}$ and the optimal TSR, λ_*, to calculate the torque control signal $T_{g,TSR}$.

identifying the essential component building blocks for each scheme. Subsequently, a linear frequency-domain framework is formulated to analyse the controllers and closed-loop systems. This framework was derived in [25], and the main results are given here; the interested reader is referred to the referenced work for a detailed derivation. The subscripts $(\cdot)_K$ and $(\cdot)_{TSR}$ differentiate between the transfer functions for the $K\omega^2$ and WSE-TSR control schemes, respectively.

The two torque control strategies applied to the VAWT are formalised in the following based on the defined wind turbine dynamics. First, the complete and non-linear formulation of the $K\omega^2$ controller is obtained, followed by the derivation of the WSE-TSR tracking controller. An overview of the control frameworks is provided in Figure 5.4 to facilitate the comparison between the two schemes. As can be observed, both controllers aim to maximise the power production of the urban VAWT by using the reference tip-speed ratio λ_* and the measured rotor speed ω_r as inputs. A more detailed description of each block diagram is given in the sub-sections below.

BASELINE $K\omega^2$ CONTROLLER

The $K\omega^2$ controller is widely used for the operation of a small-scale VAWT. As Haque et al. [40] demonstrated, this controller effectively maximises turbine power production by

measuring the rotor speed and determining the reference torque. However, no comparison with a more advanced controller is provided. This study employs the $K\omega^2$ control law as a baseline, deriving the equations characterising its performance. The block diagram of the controller, shown in Figure 5.4 **(a)**, includes the wind turbine and the controller. It becomes evident that the controller operates as a static non-linear function, generating the control signal for the generator torque based on the rotor speed. The control signal is given by

$$T_{\mathrm{g,K}} = K\frac{\omega_r^2}{N},$$ (5.11)

where the torque gain K [18] is defined at the LSS side of the drivetrain as

$$K = \frac{\rho A_{\mathrm{rot}} R^3 C_{\mathrm{p},*}(\lambda_*)}{2\lambda_*^3}.$$ (5.12)

The maximum power extraction efficiency and the corresponding optimal tip-speed ratio are indicated as $C_{\mathrm{p},*}$ and λ_*, respectively.

WSE-TSR TRACKING CONTROLLER

The WSE-TSR tracking scheme, illustrated in Figure 5.4 **(b)**, comprises an estimator and a tip-speed ratio tracking controller and has been shown to optimise the turbine performance of VAWTs in turbulent wind conditions [17], [20]. The estimator employs the control signal, measured system plant output and a non-linear plant model to estimate the REWS using the Immersion and Invariance (I&I) estimator [41] with an augmented integral correction term [42]. Assuming that the generator torque control input and the rotational speed of the turbine are measured signals and that the REWS is an unknown and positive disturbance input to the plant, the estimator is formulated as

$$\begin{cases} J\dot{\hat{\omega}}_{\mathrm{r}} = \hat{T}_{\mathrm{r}} - T_{\mathrm{g,TSR}}N \\ \epsilon_{\omega_{\mathrm{r}}} = \omega_{\mathrm{r}} - \hat{\omega}_{\mathrm{r}} \\ \hat{V} = K_{\mathrm{p,w}}\epsilon_{\omega_{\mathrm{r}}} + K_{\mathrm{i,w}}\int_0^t \epsilon_{\omega_{\mathrm{r}}}(\tau)\mathrm{d}\tau \end{cases},$$ (5.13)

where $\hat{V}$ represents the estimated REWS, $K_{\mathrm{p,w}}$ is the proportional estimator gain, $K_{\mathrm{i,w}}$ is the integral estimator gain, t denotes the present time, and τ is the variable of integration. The estimated aerodynamic torque is defined as

$$\hat{T}_{\mathrm{r}} = \frac{1}{2}\rho A_{\mathrm{rot}}\frac{\hat{V}^3}{\omega_{\mathrm{r}}}\hat{C}_{\mathrm{p}}(\hat{\lambda}),$$ (5.14)

where $\hat{C}_{\mathrm{p}}$ is the estimated power coefficient, being a nonlinear function of the estimated tip-speed ratio $\hat{\lambda} = \omega_{\mathrm{r}}R/\hat{V}$. Also, in this case, the pitch angle β is constant and equals $0°$.

Then, the proportional and integral (PI) controller in the WSE-TSR tracking scheme operates on the difference between the estimated and reference tip-speed ratio λ_*, corresponding to the rotor operating point for maximum power extraction efficiency C_{p}^*. This error is utilised to compute the generator torque demand $T_{\mathrm{g,TSR}}$, forcing the turbine to track the reference as

$$T_{\mathrm{g,TSR}} = K_{\mathrm{p,c}}\epsilon_\lambda + K_{\mathrm{i,c}}\int_0^t \epsilon_\lambda(\tau)\mathrm{d}\tau,$$ (5.15)

in which ϵ_λ is the tip-speed ratio error, $K_{\mathrm{p,c}}$ is the proportional controller gain and $K_{\mathrm{i,c}}$ is the integral controller gain.

5.4.1. ANALYSIS FRAMEWORK

The universal analysis framework proposed in [25] is used to evaluate the characteristics of the described control strategies and closed-loop systems. Only the main results are given in this section; the reader is referred to the referenced work for a more extensive derivation and explanation of the framework. The framework is illustrated in Figure 5.5, where the controllers are represented as a single block with two inputs and one output for the reference tip-speed ratio, rotor speed, and generator torque control signals. Each control scheme is formalised in the linear and frequency-domain formulation as

$$\mathcal{T}_g(s) = K_{\Omega_r \to \mathcal{T}_g}(s)\Omega_r(s) + K_{\Lambda_* \to \mathcal{T}_g}(s)\Lambda_*(s), \tag{5.16}$$

in which $K_{\Omega_r \to \mathcal{T}_g}$ and $K_{\Lambda_* \to \mathcal{T}_g}$ represent the feedback and the reference shaping terms, respectively, and Λ_* indicates the reference tip-speed ratio signal in the frequency domain.

Combining Equation (5.16) with Equation (5.10) and after manipulation, it is possible to derive the closed-loop transfer functions. As the scheme intends to regulate the tip-speed ratio to its reference value, the closed-loop transfer functions are expressed as a function of the actual tip-speed ratio λ of the turbine. It follows that the two transfer functions representing the closed-loop system reference tracking and disturbance attenuation
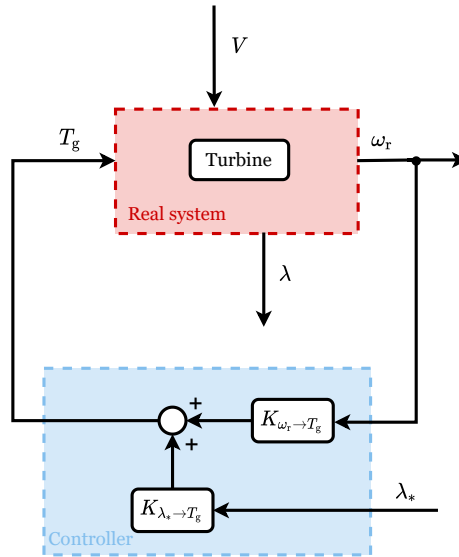
Figure 5.5: Block diagram of the universal framework used for the controller analysis. The **red** box highlights the wind turbine system with two inputs (the generator torque T_g, and the wind speed V), and two outputs (the rotational speed, ω_r, and the TSR, λ). The **cyan** box represents the controller with two inputs (ω_r and the TSR set point, λ_*), one output (T_g) and two terms used for the linear analysis framework (the feedback term, $K_{\omega_r \to T_g}$, and the reference shaping term $K_{\lambda_* \to T_g}$).

capabilities are defined as

$$
\Lambda(s) = \underbrace{\frac{REK_{\Lambda_* \to \mathcal{T}_g}(s)}{\bar{V}\left(s - G - EK_{\Omega_r \to \mathcal{T}_g}(s)\right)}}_{T_{\Lambda_* \to \Lambda}(s)} \Lambda_*(s) + \underbrace{\frac{R\left(H - (\bar{\omega}_r/\bar{V})\left(s - G - EK_{\Omega_r \to \mathcal{T}_g}(s)\right)\right)}{\bar{V}\left(s - G - EK_{\Omega_r \to \mathcal{T}_g}(s)\right)}}_{T_{\mathcal{V} \to \Lambda}(s)} \mathcal{V}(s).
$$

$$(5.17)$$

Specifically, the term $T_{\Lambda_* \to \Lambda}(s)$ is the complementary sensitivity function, indicating the controller performance in tracking the commanded reference (i.e. $\lambda = \lambda_*$); the sensitivity function $T_{\mathcal{V} \to \Lambda}(s)$ represents the controller performance in rejecting wind speed disturbances. In the analysis framework, the $(\bar{\cdot})$ represents values corresponding to a specific operating point.

BASELINE $K\omega^2$ CONTROLLER

To determine the $K\omega^2$ controller dynamics, Equation (5.11) can be linearised and combined with the open-loop linearised wind turbine plant dynamics (Equation (5.10)), obtaining the feedback and the reference shaping terms defined according to the universal controller framework as

$$
K_{(\Omega_r \to \mathcal{T}_g),K} = \left.\frac{\partial T_{g,K}}{\partial \omega_r}\right|_{(\bar{\omega}_r, \lambda_*)} = \frac{2K\bar{\omega}_r}{N} = \frac{\rho R^3 A_{rot} C_{p,*}(\lambda_*)}{N\lambda_*^3}\bar{\omega}_r,
$$

$$(5.18)$$

$$
K_{(\Lambda_* \to \mathcal{T}_g),K} = \left.\frac{\partial T_{g,K}}{\partial \lambda_*}\right|_{(\bar{\omega}_r, \lambda_*)} = \frac{\rho R^3 A_{rot}}{2N}\left(-\frac{3}{\lambda_*^4}C_{p,*}(\lambda_*) + \frac{1}{\lambda_*^3}\frac{\partial C_{p,*}(\lambda_*)}{\partial \lambda_*}\right)\bar{\omega}_r^2.
$$

$$(5.19)$$

It can be observed from Equations (5.18) and (5.19) that the transfer functions of the controller are frequency-independent gains for the baseline controller.

WSE-TSR TRACKING CONTROLLER

The dynamics of the WSE-TSR tracking controller are obtained by first deriving the linear frequency domain representations of the individual estimator and controller. Subsequently, coupling between the estimator and the controller is performed to achieve the dynamics of the overall scheme. The interested reader is referred to Brandetti et al. [25] for the complete derivation. For conciseness, only the controller transfer functions are here reported as

$$
K_{(\Omega_r \to \mathcal{T}_g),TSR}(s) = \frac{\mathcal{T}_{g,TSR_{\Omega_r}}(s)}{\Omega_r(s)} = \frac{R\left(K_{p,c}\,s + K_{i,c}\right)\left((\bar{\omega}_r K_{p,w} - \bar{V})\,s^2 + F_4\,s - (\bar{V}\hat{H} + \bar{\omega}_r\hat{G})K_{i,w}\right)}{\left(\bar{V}^2\,s^3 + F_1\,s^2 + F_2\,s + F_3\right)},
$$

$$(5.20)$$

and

$$
K_{(\Lambda_* \to \mathcal{T}_g),TSR}(s) = \frac{\mathcal{T}_{g,TSR_{\Lambda_*}}(s)}{\Lambda_*(s)} = \frac{\bar{V}^2\left(K_{p,c}\,s + K_{i,c}\right)\left(s^2 + \hat{H}K_{p,w}\,s + \hat{H}K_{i,w}\right)}{\left(\bar{V}^2\,s^3 + F_1\,s^2 + F_2\,s + F_3\right)},
$$

$$(5.21)$$

representing the transfer functions from the rotational speed and tip-speed ratio reference, respectively, to the generator torque output. To simplify Equations (5.20) and (5.21), the unknown quantities in the above expressions are defined as

$$F_1 = \bar{V}^2 \hat{H} K_{p,w} + R\bar{\omega}_r E K_{p,c} K_{p,w},$$
$$F_2 = \bar{V}^2 \hat{H} K_{i,w} + R\bar{\omega}_r E K_{p,c} K_{i,w} + R\bar{\omega}_r E K_{i,c} K_{p,w},$$
$$F_3 = R\bar{\omega}_r E K_{i,c} K_{i,w},$$
$$F_4 = \bar{\omega}_r K_{i,w} - (\bar{V}\hat{H} + \bar{\omega}_r \hat{G}) K_{p,w}.$$

As the considered WSE-TSR tracking control scheme incorporates turbine model information that accurately reflects the characteristics of the wind turbine system without explicitly addressing inherent uncertainties present in real-world turbine dynamics, the variables $\hat{G} := G(\hat{V})$ and $\hat{H} := H(\hat{V})$ indicate the estimated partial derivatives defined in Equations (5.8) and (5.9).

5.5. METHODOLOGY TO ASSESS THE NOISE LEVELS AND PSYCHOACOUSTIC ANNOYANCE ON A VAWT

This section outlines the methodology for estimating the noise generated by the VAWT under investigation and assessing the subsequent expected psychoacoustic annoyance. Figure 5.6 shows the subsequent steps required to determine the psychoacoustic annoyance metric. First, the acoustic emissions of the VAWT are modelled using the noise prediction method, which was introduced and validated against high-fidelity simulations in Brandetti et al. [35]. The estimated wind turbine noise spectra over time are then auralized to make the signal audible and then evaluated with a perception-based approach [13] to determine the expected psychoacoustic annoyance.

5.5.1. NOISE PREDICTION MODEL

This section provides an overview of the model used to estimate the aeroacoustics performance of the VAWT. Interested readers are referred to Brandetti et al. [35] for more comprehensive details. The noise model exclusively accounts for aerodynamic sources, excluding any influence from mechanical or electrical components, as aerodynamic noise is deemed dominant for these turbines. The model evaluates three distinct aerodynamic noise generation mechanisms that are considered dominant for the two-bladed 1.5 m H-Darrieus VAWT:
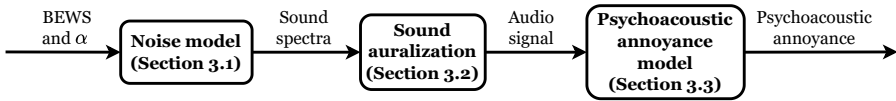
Figure 5.6: Block diagram illustrating the integrated low-fidelity noise model and the psychoacoustic annoyance model based on perception-based psychoacoustic sound quality metrics. The first step is loading the blade-effective wind speed (BEWS) and the angle of attack (α), retrieved from the aero-servo-elastic simulations of the VAWT in QBlade [36], into the noise model. Then, the estimated sound spectra are auralized, generating realistic audio signals. These audio files are then evaluated using psychoacoustic sound quality metrics to estimate the psychoacoustic annoyance.

1. Laminar Boundary Layer-Vortex Shedding (LBL-VS) noise;

2. Turbulent Boundary Layer-Trailing Edge (TBL-TE) noise;

3. Turbulence-Interaction (T-I) noise.

Among these sources, LBL-VS and TBL-TE are self-generated by the airfoil interacting
with a steady flow [43], whereas the T-I noise occurs from the interaction between the
blade leading edge and inflow turbulence [44], [45]. Note that the noise prediction model
does not consider blade-blade interaction, as the blades are treated as isolated entities,
and it assumes steady, free-stream conditions with quasi-steady time dependence.

The estimation of these noise sources involves several steps. Firstly, each blade is
discretised in a three-dimensional space, dividing it into sequential strips. These strips
possess identical airfoil chords and finite spans. Then, the computational domain is
discretised in time, enabling the blade to progress along its rotational trajectory for a
complete revolution [46]. Consequently, for each blade element and azimuthal position,
the airfoil-self noise and T-I noise are estimated using the methodologies presented by
Brooks et al. [43] and Buck et al. [47], respectively. The relevant equations to implement
these models are explained in the following and rely on flow input parameters, including
the angle of attack α and the BEWS. In the work conducted by Brandetti et al. [35], these
parameters were estimated with the two-dimensional Actuator Cylinder model [48]. This
study aims to enhance the accuracy of acoustic predictions by solving the flow over the
blade using three-dimensional lifting line-free vortex wake simulations performed in the
aero-servo-elastic software QBlade [36]. After determining the sound pressure levels from
these semi-empirical models, a Doppler correction factor is computed for the considered
noise sources to account for the relative motion between the blade and the stationary
observer [49]. The total noise emissions along the blades and throughout a single rotation
are finally calculated employing the approach Brooks and Burley [50] developed.

The resulting sound pressure levels for the three noise sources are then used as inputs
to perform the sound auralization to make the signals audible and assessable with the
perception-based approach to determine the corresponding psychoacoustic annoyance.

AIRFOIL-SELF NOISE MODEL

Only two of five airfoil-self noise mechanisms are considered relevant for a VAWT in an
urban environment: the LBL-VS noise and the TBL-TE noise. These noise sources are
modelled with the Brooks Pope and Marcolini (BPM) approach [43] and distinguished
according to the flow conditions.

LBL-VS noise is dominant at low Reynolds numbers (i.e. $Re \leq 5 \times 10^5$) when Tollmien-
Schlichting (T-S) waves develop, leading to the generation of vortex shedding and, con-
sequently, tonal noise through a feedback loop [43]. The Sound Pressure Level in $1/3^{\mathrm{rd}}$
octave bands for this noise generation mechanism (SPL$_{\mathrm{LBL-VS}}$) is calculated as:

$$\mathrm{SPL_{LBL-VS}} = 10\log_{10}\left(\frac{\delta_{\mathrm{p}} M^5 d \bar{D}_{\mathrm{h}}}{r_{\mathrm{e}}^2}\right) + Q_1\left(\frac{St'}{St'_{\mathrm{peak}}}\right) + Q_2\left[\frac{Re}{(Re)_0}\right] + Q_3(\alpha), \qquad (5.22)$$

where δ_{p} is the boundary layer thickness at the pressure side, d is the span-wise size of
the blade element, $\bar{D}_{\mathrm{h}}$ is the directivity function for the high-frequency limit, r_{e} is the

absolute distance to the receiver, and $(Re)_0$ is the chord-based Reynolds number at $\alpha = 0°$. A detailed description of the Strouhal contributions, St' and St'_{peak}, and the empirical functions, Q_1, Q_2 and Q_3 can be found in Brooks et al. [43].

The boundary layer developing over the airfoil for higher Reynolds numbers (i.e. $Re \geq 5 \times 10^5$) becomes turbulent. These turbulent pressure fluctuations are scattered as TBL-TE noise when convecting over the sharp trailing edge. For estimating the SPL of this noise source, three contributions are taken into account in the BPM model: one from the attached TBL on the pressure side (SPL_p), one from the attached TBL on the suction side (SPL_s), and a third component accounting for separation-stall at high angles of attack (SPL_α). The SPL in $1/3^{rd}$ octave bands for the TBL-TE noise (SPL_{TBL-TE}) is defined as:

$$SPL_{TBL-TE} = 10\log_{10}\left(10^{\left(\frac{SPL_p}{10}\right)} + 10^{\left(\frac{SPL_s}{10}\right)} + 10^{\left(\frac{SPL_\alpha}{10}\right)}\right). \tag{5.23}$$

$$SPL_p = \begin{cases} 10\log_{10}\left(\dfrac{\delta_p^* M^5 d\bar{D}_h}{r_e^2}\right) + L\left(\dfrac{St_p}{St_1}\right) + (Z_1 - 3) + \Delta Z_1, & \text{for } \alpha \leq 12.5°, \\ -\infty, & \text{for } \alpha \geq 12.5°, \end{cases} \tag{5.24}$$

$$SPL_s = \begin{cases} 10\log_{10}\left(\dfrac{\delta_s^* M^5 d\bar{D}_h}{r_e^2}\right) + L\left(\dfrac{St_s}{St_1}\right) + (Z_1 - 3), & \text{for } \alpha \leq 12.5°, \\ -\infty, & \text{for } \alpha \geq 12.5°, \end{cases} \tag{5.25}$$

$$SPL_\alpha = \begin{cases} 10\log_{10}\left(\dfrac{\delta_s^* M^5 d\bar{D}_h}{r_e^2}\right) + U\left(\dfrac{St_s}{St_2}\right) + Z_2, & \text{for } \alpha \leq 12.5°, \\ 10\log_{10}\left(\dfrac{\delta_s^* M^5 d\bar{D}_l}{r_e^2}\right) + L'\left(\dfrac{St_s}{St_2}\right) + Z_2, & \text{for } \alpha \geq 12.5°, \end{cases} \tag{5.26}$$

with δ_p^* and δ_s^* being the boundary layer displacement thickness at the pressure side and at the suction side, respectively, $\bar{D}_l$ being the directivity function for the low-frequency limit and M being the free-stream Mach number. For details on the Strouhal contributions, St_p, St_s, St_1 and St_2, the empirical functions, L, L' and U, and the amplitude correction factors, Z_1, Z_2 and ΔZ_1, the reader can refer to Brooks et al. [43].

Turbulence-Interaction noise model

Aerodynamic noise caused by the interaction between the incoming turbulent inflow and the leading edge of the blades is commonly referred to as T-I noise [44]. In the noise prediction model, this source is modelled with the approach of Buck et al. [47]. The SPL of the T-I noise (SPL_{T-I}) is computed in $1/3^{rd}$ octave bands as the sum of the high-frequency and low-frequency components of the noise

$$SPL_{T-I} = SPL_{T-I}^H + 10\log_{10}\left(\frac{LFC}{1 + LFC}\right). \tag{5.27}$$

In the above expression, LFC is the blending function introduced by Lowson and Oller-head [51] and Moriarty and Migliore [52], and SPL_{T-I}^H is the high-frequency component defined as

$$SPL_{T-I}^H = 10\log_{10}\left[\frac{\rho^2 c_0^2 d}{2r_e^2} M^3 \varepsilon^{(2/3)} k^{-(5/3)} \bar{D}_{LE}\right] + 77.6, \tag{5.28}$$
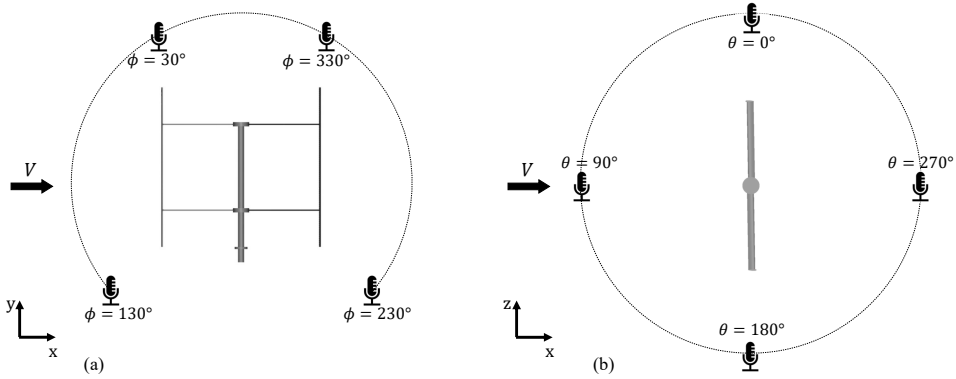
Figure 5.7: Two circular arrays of virtual microphones are positioned at a distance of $2.6D$ from the centre of the VAWT. Array (a) comprises 4 microphones located in the x-y plane, while array (b) consists of 4 microphones positioned in the x-z plane. These locations are considered relevant for characterising the psychoacoustic annoyance of the sound source.

where c_0 is the sound speed, k is the wave-number ($k = (2\pi f)/V_i$), and $\bar{D}_{LE}$ is the directivity function accounting for the motion between the leading edge and the stationary observer.

OBSERVER LOCATION

In the proposed low-fidelity noise model, 8 virtual microphones are considered. As shown in Figure 5.7, two circular arrays in the x-y and x-z planes, respectively, consisting of 4 virtual microphones, each positioned at $2.6D$ from the centre of the VAWT. This setup is chosen to cover the three-dimensional sound field of the turbine. The noise model is able to estimate the sound spectra at each of these observer locations. For every case study, a single observer location is chosen in the next section describing the sound auralization procedure.

5.5.2. SOUND AURALIZATION

The propagated sound spectra estimated in Section 5.5.1 are then auralized to obtain the audio signal in the time domain that a virtual observer at a specific location would perceive. Auralization is a technique that enables artificially making an acoustic situation audible from numerical (simulated, measured, or synthesised) data [16]. It can be considered the acoustic counterpart to visualisation.

To achieve more realistic auralized audio waves, each propagated $1/3^{rd}$-octave band spectrum per time step was interpolated to obtain an equivalent narrow-band spectrum with a frequency step of 1 Hz while maintaining the same sound pressure level per $1/3^{rd}$-octave band. This practice is common when auralizing the output of noise prediction models, which typically provide outputs as $1/3^{rd}$-octave band spectra [15], [53]. The narrow-band spectrum corresponding to each time block is then converted to the time domain using an inverse short-time Fourier transform, following the guidelines explained in [13], [16]. Each time block was windowed using a Hanning weighting function with 50% data overlap. A similar approach has been recently applied to the auralization of HAWT

noise [53], [54]. The interested reader is referred to the aforementioned publications for a more detailed explanation.

The resulting audio files were then fed into the psychoacoustic annoyance model (see section Section 5.5.3) to estimate the psychoacoustic annoyance of each sound, which is described in the next section.

5.5.3. Psychoacoustic annoyance model

This section introduces the psychoacoustic annoyance model employed for estimating the perceived annoyance due to the noise emitted by a VAWT in an urban environment. The audio files determined with the auralization of the sound spectra in Section 5.5.2 are assessed using a combination of perception-based Sound Quality Metrics (SQMs) [55], [56] to estimate the psychoacoustic annoyance.

Unlike the SPL metric, which quantifies the purely physical magnitude of sound based on the measured acoustic pressure, Sound Quality Metrics (SQMs) describe the subjective perception of sound by human hearing. Therefore, these metrics have been shown to better capture the auditory behaviour of the human ear compared to the conventional sound metrics typically employed in wind turbine noise assessments [13], [57]. The psychoacoustic annoyance model considers the five most common SQMs [58]:

- Loudness ($\mathcal{N}$): Subjective perception of sound magnitude corresponding to the overall sound intensity. The model proposed by International Organization for Standardization [59] and standardized in the ISO 532-1 norm was employed in this work. The unit of this metric is the sone (on a linear scale) or the phone (on a logarithmic scale).

- Tonality ($\mathcal{K}$): Measurement of the perceived strength of unmasked tonal energy within a complex sound following the model by Aures [60]. This metric is measured in tonality units (t.u.) and its values range from 0 (purely broadband) to 1 t.u. (purely tonal).

- Sharpness ($\mathcal{S}$): Representation of the high-frequency sound content (especially frequencies higher than 3000 Hz), as described by von Bismarck [61] and the German norm DIN 45692:2009. The unit of this metric is the acum.

- Roughness ($\mathcal{R}$): Hearing sensation caused by sounds with fast amplitude modulations with modulation frequencies frequencies between 15 Hz and 300 Hz. The model by Daniel and Webber [62] was considered in this study, and the unit of this metric is the asper.

- Fluctuation strength ($\mathcal{F}_s$): Assessment of slow fluctuations in loudness with modulation frequencies up to 20 Hz, with maximum sensitivity for modulation frequencies around 4 Hz. This work employs the model proposed by Osses Vecchi et al. [63]. The unit of this metric is the vacil.

All SQMs were computed using the open-source MATLAB toolbox SQAT (Sound Quality Analysis Toolbox) [64] and the 5% percentiles were considered, representing the threshold value of each SQMs that is exceeded for 5% of the total signal time. Following the

formulation of Di et al. [56], these SQMs can be combined to compute the psychoacoustic
annoyance (PA) as:

$$PA = \mathcal{N}\left(1 + \sqrt{v_{\mathcal{S}}(\mathcal{N},\mathcal{S})^2 + v_{\mathcal{FR}}(\mathcal{N},\mathcal{F}_s,\mathcal{R})^2 + v_{\mathcal{K}}(\mathcal{N},\mathcal{K})^2}\right). \qquad (5.29)$$

The variables $v_{\mathcal{S}}(\mathcal{N},\mathcal{S})$, $v_{\mathcal{K}}(\mathcal{N},\mathcal{K})$, and $v_{\mathcal{FR}}(\mathcal{N},\mathcal{F}_s,\mathcal{R})$ denote the contributions of the
sharpness, tonality, roughness, and fluctuation strength, respectively. As can be observed,
the loudness contribution is considered in all three terms as it exerts the strongest influ-
ence on psychoacoustic annoyance. For the sake of conciseness, the formulation for these
three terms is omitted, but the interested reader is referred to [55], [56] for additional
information on the field of psychoacoustic and to [58], [64] for the implementation of the
SQMs considered.

5.6. Multi-objective optimisation and implementation of the WSE-TSR tracking controller

This section presents an architecture for implementing and optimally calibrating torque
control strategies in small-scale VAWTs using the mid-fidelity wind turbine simulation
software QBlade [36].

In the following, Section 5.6.1 formally defines the multi-objective optimisation prob-
lem. Section 5.6.2 explains the multi-criteria decision-making method selected to find
the trade-off on the resulting Pareto front. Section 5.6.3 describes its implementation
as a systematic exploration and guided search of the controller calibration variables to
evaluate the performance space encompassing all objectives.

5.6.1. Multi-objective optimisation

The present study investigates a multi-objective optimisation problem characterised by a
set of continuous input variables $\mathcal{X} \subset \mathbb{R}^d$, referred to as the design space [65]. The objec-
tive is to minimise a vector of objective functions, denoted as $\mathbf{f}(\mathbf{x}) = (f_1(\mathbf{x}),\cdots,f_m(\mathbf{x}))$
where $m \geq 2$. In this context, $\mathbf{x} \in \mathcal{X}$ represents the vector of input variables, and $\mathbf{f}(\mathcal{X}) \subset \mathbb{R}^m$
denotes the m-dimensional image representing the performance space. Thus, the objec-
tive is to solve the following minimisation problem, subject to the operational conditions
governing the multi-objective optimisation process:

$$\min_{\mathbf{x}}(\mathbf{f}(\mathbf{x})). \qquad (5.30)$$

Since there is an inherent conflict among the objective functions, a single optimal
solution may not always exist. Instead, it is necessary to identify optimal solutions, known
as the Pareto set $\mathcal{P}_s \subseteq \mathcal{X}$ in the design space and the Pareto front $\mathcal{P}_f = \mathbf{f}(\mathcal{P}_s) \subset \mathbb{R}^m$ in the
performance space [65]. In this study, the Pareto front is approximated by considering a
point $\mathbf{x}_* \in \mathcal{P}_s$ as Pareto optimal if there is no other point $\mathbf{x} \in \mathcal{X}$ such that $f_j(\mathbf{x}_*) \geq f_j(\mathbf{x})$ for
all j and $f_j(\mathbf{x}_*) > f_j(\mathbf{x})$ for at least one j, where $j = \{1,\cdots,m\}$ [66].

5.6.2. Multi-criteria decision-making method

From the description of the multi-objective optimisation, it is clear that all points within
the Pareto front represent equally optimal solutions. No solution is better than others in

5

satisfying all conflicting objectives, as enhancing objective function inevitably compromises others [28], [67], [68]. Once the Pareto front is approximated, the decision-maker can assess various options and select the most favourable one. This collection of potential solutions underscores the adaptability of the design-making process, wherein the designer's role is to identify the optimal solution tailored to specific circumstances [69].

To facilitate the decision-making stage, this chapter aims to provide designers with a solution to the optimal calibration of the WSE-TSR tracking controller. Therefore, a multi-criteria decision-making (MCDM) method is proposed to select an appropriate trade-off of the considered objective functions. An MCDM method typically involves p alternatives $(A_1, A_2, \cdots, A_p)$ and q criteria $(C_1, C_2, \cdots, C_q)$, structured as a decision matrix $\mathbf{Y} = [y_{c,k}]_{p \times q}$ and weight vector $\mathbf{W} = [w_k]_q$, in which $y_{c,k}$ is the performance of the cth alternative with respect to the kth criterion and w_k is the weight of the kth criterion [70].

Simple Additive Weighting (SAW) is applied to each point along the Pareto front, as it is considered the most intuitive and straightforward MCDM approach [71], [72]. In the SAW method, the final score of a candidate solution is determined by summing the weighted values of its attributes, accomplished through three sequential steps [70]. Firstly, the decision matrix $\mathbf{Y}$ is normalised to enable fair comparison across the different criteria, using the Sum method as it is widely applied in the literature [73]. This normalisation yields the normalised decision matrix $\mathbf{R} = [r_{c,k}]_{p \times q}$. Subsequently, weight values are assigned to each criterion C_q within the weight vector $\mathbf{W}$ [70]. The next step involves the calculation of the ranking score S_c for each alternative as

$$S_c = \sum_{k=1}^{q} w_k r_{c,k}. \tag{5.31}$$

The alternative with the highest S_c value is considered the most satisfactory solution [28], and the associated calibration parameters are deemed the most effective trade-off settings for calibrating the WSE-TSR tracking controller.

5.6.3. Implementation of the controller and optimisation framework

In this section, first, the objective functions employed for the multi-objective optimisation of the WSE-TSR tracking controller are defined, followed by a detailed description of the simulation implementation.

Definition of the objective function

The methodology employed for calibrating the design variables of the WSE-TSR tracking control scheme aligns with the previously described multi-objective optimisation problem and MCDM method. In this case, a three-dimensional vector captures the objective functions and is expressed as follows:

$$\mathbf{f}(\Gamma_d) = [f_1(\Gamma_d), f_2(\Gamma_d), f_3(\Gamma_d)]. \tag{5.32}$$

The first objective, $f_1(\Gamma_d)$, relates to the variance of the torque control signal, representing the controller's responsiveness and serving as an indicator of the actuation effort

on the turbine. This is defined as:

$$f_1(\Gamma_d) = \frac{\sum_{l=1}^{L}(T_{g,l}(\Gamma_d) - \bar{T}_g(\Gamma_d))^2}{L}.$$

The second objective, $f_2(\Gamma_d)$, encompasses the mean generated power of the wind turbine and is defined as

$$f_2(\Gamma_d) = -\frac{\sum_{l=1}^{L} P_{g,l}(\Gamma_d)}{L}.$$

Note that the negative sign preceding the power term is inherent in the context of the minimisation problem defined in the multi-objective optimisation (Equation (5.30)).

The third objective $f_3(\Gamma_d)$ concerns psychoacoustic annoyance, quantifying the perceived noise emitted by the wind turbine as

$$f_3(\Gamma_d) = \mathrm{PA}(\Gamma_d).$$

These objectives are expected to be conflicting in the sense that a highly responsive controller tends to increase power generation, actuation effort, and noise annoyance. Conversely, a more conservative controller calibration would decrease power production while being beneficial regarding the actuation and noise objectives.

In the aforementioned equations, the variables are defined as follows: L denotes the total number of data points, $\bar{T}_g$ represents the mean value of the generator torque, $T_{g,l}$, and $P_{g,l}$ indicate individual values of generator torque, and power within the dataset, respectively, and PA is the psychoacoustic annoyance computed using α, and BEWS.

It is evident that the resulting signals T_g, P_g and PA are dependent on $\Gamma_d \in \mathcal{X}_d \subset \mathbb{R}^d$, which corresponds to the d-dimensional vector consisting of the input variables. This study investigates the dimensionality of input vectors to evaluate the controller performance under two levels of complexity. The considered input vectors are denoted as

$$\Gamma_4 = [K_{p,c}, K_{i,c}, K_{p,w}, \lambda_*] \in \mathcal{X}_4,$$
$$\Gamma_1 = [\lambda_*] \in \mathcal{X}_1,$$

where the subscript $(\cdot)_d$ represents the dimension of each design space and is used to differentiate between the input vectors throughout the chapter. It is important to note that $d = 5$ corresponds to the original formulation of the WSE-TSR tracking controller, denoted as $\Gamma_5 = [K_{p,c}, K_{i,c}, K_{p,w}, K_{i,w}, \lambda_*]$. The selection of a subset from the original formulation is based on the findings reported by [25], according to which adding an integral term to the estimator (i.e. $K_{i,w}$) provides little to no improvement in the performance of the WSE-TSR tracking control scheme. On the other hand, Γ_1 represents the one-dimensional design space of the $K\omega^2$ controller, where the variation in λ_* results in corresponding changes in the gain K, as described in Equation (5.12).

SIMULATION IMPLEMENTATION

Figure 5.8 provides an overview of the overall implementation and optimal controller calibration, which enables the execution of various simulations to explore the parameter space of the considered controllers through a guided search procedure. This process

yields a set of optimal solutions that form the Pareto fronts, representing a trade-off between $f_1(\Gamma_d)$, $f_2(\Gamma_d)$ and $f_3(\Gamma_d)$. The workflow consists of several steps. First, the input parameters, such as the turbine geometry, operating conditions, and torque control strategy, are defined. Then, mid-fidelity simulations are conducted employing the aero-servo-elastic software QBlade [36], loaded as a dynamic link library in MATLAB; the interested reader is referred to the tutorial by Brandetti and van den Berg [74] (summarised in Appendix D) for further details about this interface and to Appendix E for a detailed description of the QBlade turbine model. This interface allows the parallelisation of the original simulation case, referred to as ORIGIN in Figure 5.8, up to a specified index t = T, significantly reducing the computational time for the multi-objective controller optimisation. For each simulation, t, the controller settings are randomly varied and adhere to the constraints imposed by the design space. In this way, a range of optimal solutions $\mathcal{P}_s^d \subset \mathbb{R}^d$ is explored through a guided search within the constrained design space to approximate the Pareto front $\mathcal{P}_f^d = \mathbf{f}(\mathcal{P}_s^d)$.

The VAWT is subjected to a realistic turbulent wind profile characterised by a mean wind speed of $\bar{V} = 4$ m/s and a turbulence intensity of TI =15%. The simulation is set over a specific duration; however, for the analysis, only an average of 680 complete turbine revolutions is considered to eliminate any transient start-up effects from influencing the results. Subsequently, the obtained time series data are used to calculate $f_1(\Gamma_d)$ and $f_2(\Gamma_d)$.

For the computation of the third objective (noise annoyance), α and BEWS are extracted from these time series and employed as inputs for the noise prediction model (Section 5.5.1). The SPLs for the three noise generation mechanisms described in Section 5.5.1 are calculated for each time step within one full blade revolution period. Due to the different rotational speeds considered, the rotational period was different for different operational conditions. To consider the total noise emissions of the VAWT, the
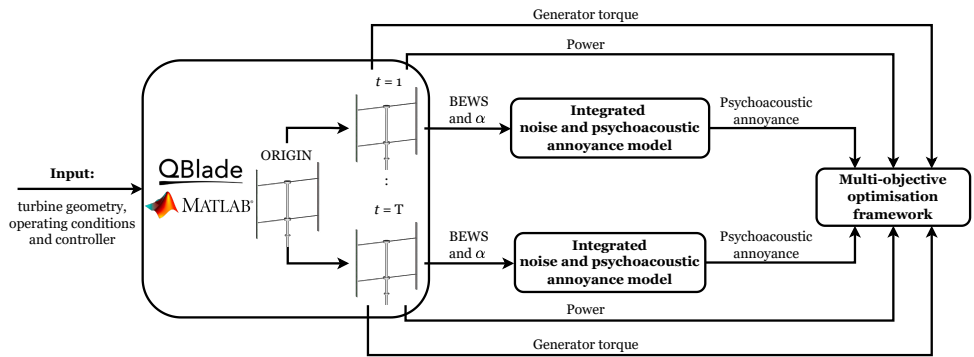

Figure 5.8: Block diagram illustrating the implementation and optimal calibration of controllers applied to the two-bladed 1.5 m H-Darrieus VAWT. The process involves: defining input parameters, parallelising the ORIGIN simulation case in t = 1,...,T cases, running simulation t with varied controller gains, extracting aero-servo-elastic information, loading the blade-effective wind speed (BEWS) and the angle of attack (α) into the integrated noise and psychoacoustic annoyance model to retrieve the corresponding psychoacoustic annoyance, and using the information within a multi-objective optimisation framework to determine the optimal calibration for the selected controller.

contributions of the three noise generation mechanisms (LBL-VS, TBL-TE, and T-I) were summed logarithmically for every time step and propagated to the selected observer position. The resulting sound spectra are then auralized, as explained in Section 5.5.2, to achieve realistic audio files, which are fed into the psychoacoustic annoyance model (Section 5.5.3), determining $f_3(\Gamma_d)$. Note that for the considered case study, it was found that $\mathcal{R}$ and $\mathcal{F}_s$ did not vary significantly. Therefore, a modified version of the PA model, employed in [57], is applied where these two metrics are not considered, equivalent to setting $v_{\mathcal{FR}} = 0$. In the following, $f_3(\Gamma_d)$ is defined as PA_{mod} to denote the modified version.

The last step is to use the computed objective functions $f_1(\Gamma_d)$, $f_2(\Gamma_d)$ and $f_3(\Gamma_d)$ within the multi-objective optimisation framework to determine the optimal calibration for the considered controller.

5.7. RESULTS

This section presents the multi-objective optimisation results. The exploration of the performance space is conducted through a guided search procedure for the sets of design variables Γ_1 and Γ_4, corresponding to the $K\omega^2$ controller and the WSE-TSR tracking controller, respectively. The approximation of the Pareto fronts is based on minimising a weighted linear combination of the objectives $f_1(\Gamma_d)$, $f_2(\Gamma_d)$ and $f_3(\Gamma_d)$, leveraging the data obtained during the exploration process.

The MCDM approach provides a trade-off between the considered objectives, leading to the optimal calibration for both the WSE-TSR tracking controller and the $K\omega^2$ controller. Subsequently, a comparative analysis of the resulting optimal controllers is conducted from two distinct perspectives: the wind turbine performance and the controller performance. Regarding the former perspective, time-domain results are used to evaluate the turbine from an aero-servo-elastic point of view. Additionally, the sound spectra averaged over a rotation are presented in the frequency domain to characterise the acoustic emissions of the VAWT in an urban environment. By extending the analysis beyond conventional performance metrics like power and torque, this study emphasises the critical importance of addressing the impact of noise emissions on psychoacoustic annoyance and its subsequent influence on public perception of VAWTs in urban environments. Lastly, the section uses the frequency-domain framework outlined in Section 5.4.1 to draw conclusions about controller bandwidth and disturbance rejection performance.

Notably, the analysis focused exclusively on the results obtained from the microphone at $\theta = 90°$, as Brandetti et al. [35] demonstrated the VAWT's almost-omnidirectional behaviour in terms of overall sound pressure level when averaging all noise sources.

5.7.1. PARETO FRONTS AND CASE STUDIES DEFINITION

The Pareto front construction begins with systematically exploring the performance space, guided by an investigation of the input variables Γ. Figure 5.9 visually presents the data points obtained from the mid-fidelity simulation scenario. For the higher-dimensional design space Γ_4, a more extensive dataset is collected to reconstruct the performance space of the WSE-TSR tracking controller. To facilitate comparative analysis, the $K\omega^2$ controller is used as a benchmark.

Significantly, within the Γ_1 set, data points demonstrate a clustering pattern with a convex configuration, revealing a distinct global minimum for the objective functions $f_1(\Gamma_d)$ and $f_2(\Gamma_d)$. However, when $f_1(\Gamma_d)$ and $f_3(\Gamma_d)$ are considered as objectives, a different pattern emerges. It becomes apparent that the psychoacoustic annoyance does not show a discernible trend with the torque variance, acting as a proxy for the controller actuation effort. Conversely, a clear correlation is observed between psychoacoustic annoyance and mean power production for both the Γ_1 and Γ_4 sets, indicating that higher power extraction levels do not necessarily lead to increased psychoacoustic annoyance.

From the available exploration data, the Pareto front is estimated. Figure 5.10 illustrates the derived Pareto fronts ($\mathcal{P}_f^1$ and $\mathcal{P}_f^4$) for two distinct dimensionalities of the input vector Γ_d, facilitating a comparative analysis between the baseline and the WSE-TSR tracking controller performance, respectively. The circles ($\bigcirc$), stars ($\stackrel{\star}{\star}$) and triangles ($\triangle$) in the plot represent the optimal solutions corresponding to each objective function, namely $f_1(\Gamma_d)$, $f_2(\Gamma_d)$, and $f_3(\Gamma_d)$, respectively. Based on the above-mentioned consideration, no Pareto front is constructed between $f_1(\Gamma_d)$ and $f_3(\Gamma_d)$ as the exploration points violate the Pareto optimality definition, described in Section 5.6.1. The trade-offs between $f_1(\Gamma_d)$ and $f_2(\Gamma_d)$ and $f_2(\Gamma_d)$ and $f_3(\Gamma_d)$ are computed applying the MCDM method defined in Section 5.6.2 and indicated with crosses ($\times$) and squares ($\square$), respectively.

The figure depicts that the higher-dimensional controller front ($d = 4$) covers the performance space most extensively, confirming the effectiveness of the WSE-TSR tracking control scheme in improving the Pareto optimal solutions. Specifically, the controller is capable of minimising psychoacoustic annoyance and torque fluctuations while having a minimal impact on power extraction performance. In addition, the application of the WSE-TSR tracking controller to small-scale wind turbines, such as VAWTs in urban environments, leads to attainable power gains. The role of wind turbine inertia in the controller performance is evident, as a higher parameter value enhances resilience

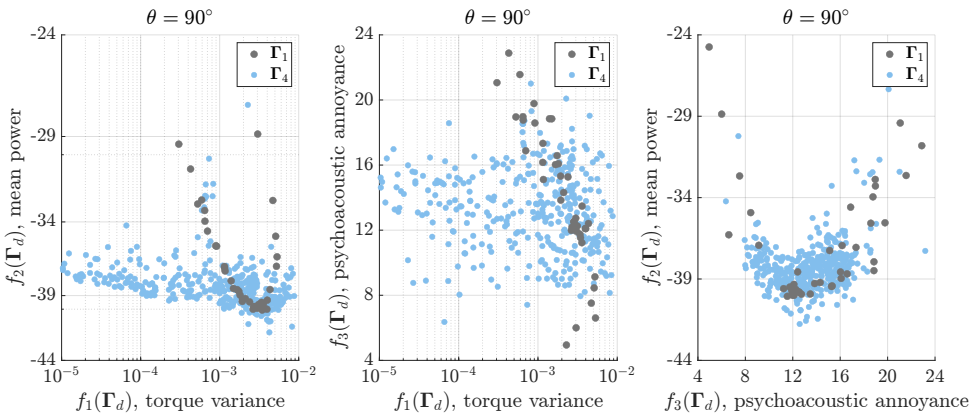Figure 5.9: Results for the WSE-TSR tracking control scheme under realistic turbulent wind conditions obtained with an exploratory search of two estimator-controller design variables: Γ_1 and Γ_4. The three objective functions $\mathbf{f}(\Gamma_d)$ define the performance space for the controller. For the calculation of the psychoacoustic annoyance, the microphone in the x-z plane at $\theta = 90°$ is selected.
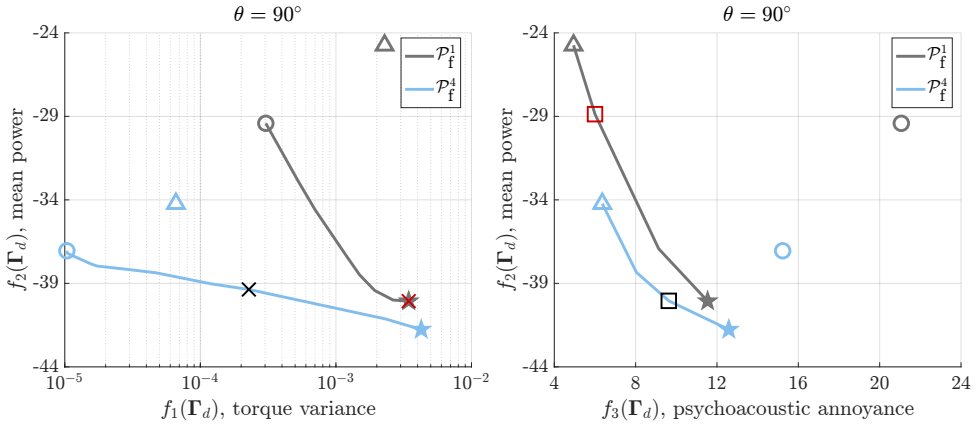
Figure 5.10: Pareto fronts $\mathcal{P}_f^1$ and $\mathcal{P}_f^4$ obtained for the $K\omega^2$ and the WSE-TSR tracking control schemes under realistic turbulent wind conditions, respectively. For the calculation of the psychoacoustic annoyance, the microphone $\theta = 90°$ is selected in the x-z plane. The optimal solutions for $f_1(\Gamma_d)$, $f_2(\Gamma_d)$ and $f_3(\Gamma_d)$ are indicated using circles ($\bigcirc$), stars ($\star$) and triangles ($\triangle$), respectively. The trade-off solutions for the two controllers are shown with a cross ($\times$) when $f_1(\Gamma_d)$ and $f_2(\Gamma_d)$ are considered as objectives, and with a square ($\square$) when $f_2(\Gamma_d)$ and $f_3(\Gamma_d)$ are considered. In contrast to the baseline controller, the WSE-TSR tracking controller achieves improved power maximisation while reducing torque fluctuations and psychoacoustic annoyance, albeit with a slight compromise in power extraction.

against deviations from the optimal operating point, causing no improvement in power production when applied to large-scale wind turbines [25]. However, the observed improved power production for the VAWT under study may result in a lower bandwidth than the baseline controller. This aspect will be investigated in the following by applying the frequency-domain framework described in Section 5.4.1.

The data derived from the Pareto front reveals key insights, as presented in Table 5.2. This table provides a comprehensive quantitative analysis of the impact of optimal calibration points on system parameters. Specifically, the percentage % increase is computed for each objective function, showcasing the change in the WSE-TSR tracking controller concerning the baseline $K\omega^2$. When comparing the optimal solutions $\bigcirc$, the WSE-TSR tracking controller demonstrates a remarkable reduction in actuation effort, up to 97%. This reduction corresponds to a power production increase of 26% and a psychoacoustic annoyance decrease of 28%. As observed, the optimal solution $\triangle$ also facilitates a reduction in torque fluctuations of up to 97%, accompanied by a 38% increase in mean power and a 28% increase in psychoacoustic annoyance compared to the baseline.

On the other hand, in the case of $\star$, the WSE-TSR tracking controller only marginally increases power production by 4%, with a significant increase of 26% in the torque variance and 9% in the psychoacoustic annoyance. A closer examination of the trade-off optimal solution $\times$ indicates that the WSE-TSR tracking controller reduces actuation effort by 25%, with a minor impact on power production (only a 2% decrease) and psychoacoustic annoyance (only a 6% increase). Conversely, for the case $\square$, the significant 39% increase in power production is offset by an increase in the psychoacoustic annoyance of 60% and an increase in torque fluctuations of 50%. The results for the trade-off solutions

highlight the complexities of the WSE-TSR tracking controller optimisation.

The following analysis only focuses on the trade-off results × and □ derived from the MCDM approach for the $K\omega^2$ and WSE-TSR tracking controllers. This selective approach aids the decision-making process by providing a clear representation of how these optimal solutions affect wind turbine and controller performance, offering calibration guidelines for the WSE-TSR tracking control scheme.

5.7.2. WIND TURBINE RESULTS

This section validates the insights obtained from the exploratory search and Pareto fronts by presenting the wind turbine performance results, focusing on aero-servo-elastic performance and acoustic emissions.

AERO-SERVO-ELASTIC PERFORMANCE

The mid-fidelity simulations are conducted in QBlade using the VAWT turbine, as outlined in Section 5.3, under realistic turbulent wind conditions for an urban environment, with a mean wind speed of $\bar{V}$ = 4 m/s, a turbulence intensity of TI = 15% and a total simulation

5

Table 5.2: Quantitative assessments of the $K\omega^2$ controller (Γ_1) and the WSE-TSR tracking controller (Γ_4) for different optimal solutions: ○, ☆, △, × and □. The % increase is computed for each objective function to show the percentage change of the WSE-TSR tracking controller with respect to the baseline $K\omega^2$. Optimal solutions, such as ○ and △, demonstrate a substantial reduction in actuation effort alongside increased power production and psychoacoustic changes. However, in some cases like ☆, the controller impact on $f_2(\Gamma_d)$ and $f_3(\Gamma_d)$ remains small. At the same time, trade-off solutions × and □ exhibit interplayed effects on various performance metrics, emphasising the multifaceted nature of controller optimisation.

Optimal solutions	$f_1(\Gamma_1)$	$f_1(\Gamma_4)$	% increase
○	3.04×10^{-4}	1.04×10^{-5}	-97
☆	3.4×10^{-3}	4.3×10^{-3}	26
△	2.3×10^{-3}	6.6×10^{-5}	-97
×	3.04×10^{-4}	2.28×10^{-4}	-25
□	3.0×10^{-3}	4.5×10^{-3}	50

Optimal solutions	$f_2(\Gamma_1)$	$f_2(\Gamma_4)$	% increase
○	-29.42	-37.05	26
☆	-40.06	-41.76	4
△	-24.74	-34.23	38
×	-40.06	-39.37	-2
□	-28.87	-40.05	39

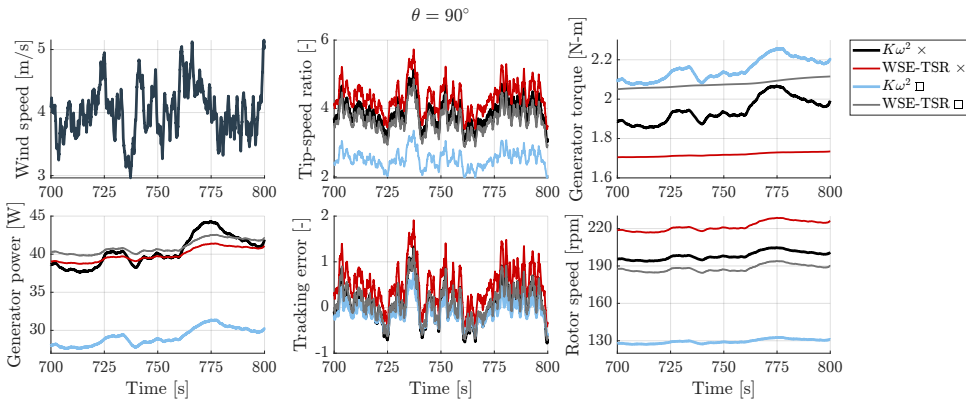| Optimal solutions	$f_3(\Gamma_1)$	$f_3(\Gamma_4)$	% increase
○	21.06	15.23	-28
☆	11.54	12.58	9
△	4.95	6.36	28
×	11.54	12.19	6
□	6.02	9.63	60

Figure 5.11: Simulation results for the $K\omega^2$ and the WSE-TSR tracking controllers subject to a realistic turbulent wind speed with a mean of 4 m/s and a turbulence intensity of 15%. The WSE-TSR tracking controller demonstrates smoother generator curves compared to the fluctuating behaviour of the $K\omega^2$ controller. The $K\omega^2$ trade-off □ case displays a 25% mean power reduction due to suboptimal operation at a reference tip-speed ratio $\lambda_* = 2.6$. Overall, the WSE-TSR tracking controller achieves an optimal balance between reducing psychoacoustic annoyance and maintaining a power output comparable to the maximum power extraction of the baseline control scheme.

duration of 800 s. Figure 5.11 provides a comprehensive representation of the wind speed and simulation results, encompassing the tip-speed ratio, tip-speed ratio tracking error, generator torque, rotor speed, and generator power. A condensed representation of the simulation results is included to highlight essential features in the time-domain analysis.

For both the selected trade-off case studies of the WSE-TSR tracking controller, the simulations reveal smoother generator torque curves, demonstrating remarkable stability even under turbulent wind conditions. Conversely, the $K\omega^2$ controller exhibits sporadic fluctuations in the generator torque, potentially causing elevated actuation effort and compromising the turbine integrity over prolonged periods of operation. In particular, the trade-off □ case for the $K\omega^2$ controller exhibits a lower mean power than the other three cases, indicating a reduction of over 25%. This difference arises from the controller operating at a non-optimal reference tip-speed ratio λ_* of 2.6 for the power production of the studied VAWT, as illustrated in the power curve of Figure 5.2. Consequently, the WSE-TSR tracking controller achieves a superior balance between minimising psychoacoustic annoyance and maximising mean production power, enabling comparable power output to the baseline calibrated for maximum power extraction while simultaneously reducing noise levels.

ACOUSTIC EMISSIONS

The following investigation outlines the different noise generation mechanisms characterising a VAWT in an urban environment by comparing the selected optimal trade-off solutions for the WSE-TSR tracking controller against the baseline control scheme. Given that the psychoacoustic annoyance yields a numerical output, the analysis of noise spectra averaged over a rotation aids in establishing a link between psychoacoustic annoyance and the conventional sound pressure level, thereby effectively characterising the acous-

tic emissions of a VAWT. In particular, the A-weighted Sound Pressure Level (SPL$_A$) is employed to account for the relative loudness perceived by human hearing, albeit acknowledging that the insights provided are general and highly averaged [13]. The SPL$_A$ is measured in dBA and computed with the noise model of Section 5.5.1 at a radial distance of 2.6D from the centre of the VAWT in the x-z plane, specifically at $\theta = 90°$.

By looking at the different SPL$_A$ spectra in Figure 5.12 for the considered trade-offs, it is clear that the most dominant noise source is the T-I noise. The SPL$_A$ spectra further support the previous observations derived from the exploratory search and the construction of the Pareto front. Specifically, for the case ×, the minimal difference in psychoacoustic annoyance is recognised in almost overlapping spectra. Conversely, in the case asterisk, the optimal WSE-TSR tracking controller shows higher psychoacoustic annoyance, reflected in higher SPL$_A$ levels across all three sources. For both cases, the differences between the controllers are most pronounced for the LBL-VS noise source. This is because the controllers lead to different trends in the angle of attack assumed by the wind turbine, which then leads to different alpha-dependent functions (Equation (5.22)) employed in the noise model to estimate this source.

5.7.3. ANALYSIS OF THE CONTROLLER PERFORMANCE

This section presents the frequency-domain characteristics of the designated cases, employing the linear analysis framework defined in Section 5.4.1. The analysis presents the frequency responses of the transfer functions $T_{\Lambda_* \to \Lambda}(s)$ and $T_{\mathcal{V} \to \Lambda}(s)$, representing the performance of the closed-loop system in terms of reference tracking (complementary sensitivity) and disturbance rejection (sensitivity), respectively. The results are illustrated in Figure 5.13 for the MCDM solutions.

In the case of the trade-off $K\omega^2$ ×, the steady-state gain diverges from the baseline gains due to the reference tip-speed ratio λ_* calibrated at a lower and non-optimal value of 2.6. On the other hand, the two optimally calibrated WSE-TSR tracking controllers
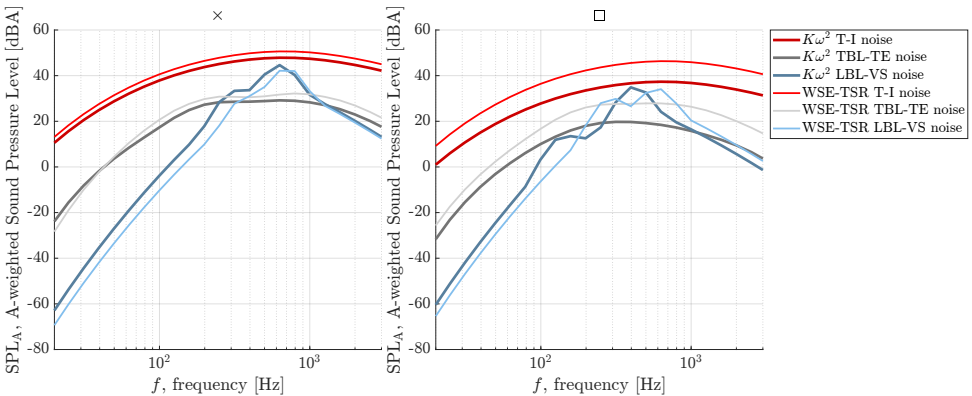
Figure 5.12: A-weighted Sound Pressure Level (SPL$_A$) versus frequency (f) obtained from a microphone in the x-z plane at $\theta = 90°$. The $K\omega^2$ controller and the WSE-TSR tracking controller are calibrated for obtaining a trade-off between mean power and torque variance, × (left), and a trade-off between mean power and psychoacoustic annoyance, □ (right). Overall, the most dominant noise source is the T-I noise.
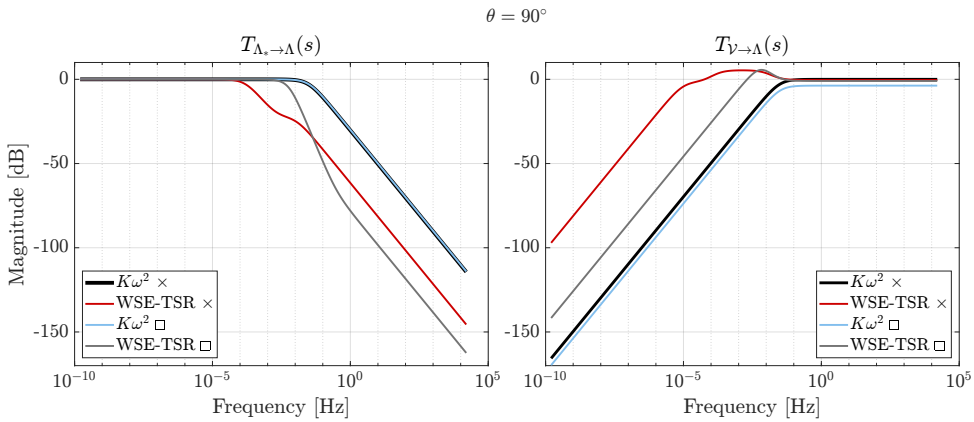
Figure 5.13: Bode plots of the closed-loop transfer functions $T_{\Lambda_* \to \Lambda}(s)$ and $T_{\mathcal{V} \to \Lambda}(s)$ for the baseline $K\omega^2$ and the WSE-TSR tracking controllers. The MCDM solutions for the WSE-TSR tracking controller reveal that the reference tip-speed ratio tracking and disturbance rejection capabilities have to be offset to achieve 39% increase in power production, for the case ×, and 25% reduction in actuation effort, at the cost of 2% power decrease and 6% increase in psychoacoustic annoyance, for the case □, compared to the $K\omega^2$ controller.

do not exhibit an improvement in control bandwidth but do demonstrate enhanced disturbance-rejection capabilities with respect to the baseline controller. This outcome aligns with the anticipated behaviour, as these optimal calibrations represent a balance between competing objectives, prioritising an integrated decision-making approach over mere power performance maximisation.

Furthermore, the results underscore the complex trade-offs inherent in the multi-objective calibration of the WSE-TSR tracking controller. As illustrated in Table 5.2, the improvements in reference tracking and disturbance rejection performance must be offset to achieve advancements in the considered performance metrics. For instance, the case □ demonstrates a remarkable 39% increase in power production, while the × solution allows a significant 25% reduction in torque actuation effort, albeit at the cost of a mere 2% power decrease and a 6% increase in psychoacoustic annoyance.

5.8. CONCLUSIONS

This study tackles crucial barriers to the acceptance of small-scale VAWTs in urban environments. Recognising the promising potential of VAWTs for urban wind energy generation, owing to their simple design, low maintenance costs, and reduced visual impact compared to HAWTs, the study emphasises the need to mitigate noise emissions to overcome local opposition. Specifically, the research explores the issue of noise annoyance, highlighting the need to incorporate psychoacoustic annoyance in the design and decision-making process to enhance community acceptance of VAWTs. Simultaneously, it underscores the importance of optimising VAWT torque control strategies to maximise the aero-servo-elastic performance of the turbine. By solving a multi-objective optimisation problem, an advanced control strategy is calibrated to achieve the trade-off between the considered operational performance and noise emissions.

In this study, the combined WSE-TSR tracking controller is employed, renowned for achieving flexible trade-offs in terms of power maximisation and load minimisation. This advanced controller is compared to the baseline $K\omega^2$ control strategy. By employing a multi-objective optimisation approach based on Pareto front approximation and a multi-criteria decision-making method, this chapter identifies optimal solutions for the WSE-TSR tracking controller to effectively address the trade-off between power extraction, actuation effort, and psychoacoustic annoyance. By analysing these optimal solutions using a frequency-domain framework and mid-fidelity time-domain simulations, the study reveals the significant potential of the optimally calibrated WSE-TSR tracking controller. The controller can decrease the actuation effort up to 25% at the expense of only a 2% decrease in power and a 6% increase in psychoacoustic annoyance in the small-scale urban VAWT under study compared to the baseline. Moreover, the findings underscore the flexible structure of the calibrated controller to balance the aero-servo-elastic performance with noise emissions effectively.

As regards the noise impact, the T-I noise source is shown to be the dominant noise source for a VAWT in an urban environment. Characterisation of the noise spectra enables a comprehensive understanding of the noise sources contributing to high levels of psychoacoustic annoyance, revealing that increased power extraction levels do not necessarily translate to increased psychoacoustic annoyance. While the current noise model focuses solely on aerodynamic sources, omitting consideration of mechanical and electrical noise, future iterations of this study hold the potential for extension to encompass these components. Such an expansion would facilitate a comprehensive controller calibration of urban VAWTs in addressing the broader spectrum of noise sources.

The findings demonstrate the potential of the proposed methodology, integrating a novel metric for psychoacoustic annoyance into a multi-objective controller optimisation. This comprehensive framework allows multifaceted challenges associated with VAWT deployment in urban environments to be addressed, thereby promoting their acceptance and effective implementation. Future research will be focused on further refining the estimation of psychoacoustic annoyance by performing listening experiments and experimental acoustic measurements on the turbine under study.

BIBLIOGRAPHY

[1] M. Hutchinson and F. Zhao, "Global Wind Report 2023", Tech. Rep., 2023. [Online]. Available: https://gwec.net/wp-content/uploads/2023/03/GWR-2023_interactive_v2_compressed.pdf.

[2] L. Ramirez, "Offshore wind energy: 2023 statistics", Tech. Rep., 2023. [Online]. Available: https://windeurope.org/intelligence-platform/product/offshore-wind-in-europe-key-trends-and-statistics-2022/.

[3] P. Veers, K. Dykes, E. Lantz, S. Barth, C. L. Bottasso, O. Carlson, A. Clifton, J. Green, P. Green, H. Holttinen, D. Laird, V. Lehtomäki, J. K. Lundquist, J. Manwell, M. Marquis, C. Meneveau, P. Moriarty, X. Munduate, M. Muskulus, J. Naughton, L. Pao, J. Paquette, J. Peinke, A. Robertson, J. S. Rodrigo, A. M. Sempreviva, J. C. Smith, A. Tuohy, and R. Wiser, "Grand challenges in the science of wind energy", *Science*, vol. 366, no. 6464, 2019. DOI: 10.1126/science.aau2027. [Online]. Available: https://www.science.org/doi/10.1126/science.aau2027.

[4] S. Watson, A. Moro, V. Reis, C. Baniotopoulos, S. Barth, G. Bartoli, F. Bauer, E. Boelman, D. Bosse, A. Cherubini, A. Croce, L. Fagiano, M. Fontana, A. Gambier, C. Gkoumas K.and Golightly, M. I. Latour, P. Jamieson, J. Kaldellis, A. Macdonald, J. Murphy, M. Muskulus, F. Petrini, L. Pigolotti, F. Rasmussen, P. Schild, R. Schmehl, N. Stavridou, J. Tande, N. Taylor, T. Telsnig, and R. Wiser, "Future emerging technologies in the wind power sector: A European perspective", *Renewable and Sustainable Energy Reviews*, vol. 113, 2019. DOI: 10.1016/j.rser.2019.109270. [Online]. Available: https://doi.org/10.1016/j.rser.2019.109270.

[5] A. Bianchini, G. Bangga, I. Baring-Gould, A. Croce, J. I. Cruz, R. Damiani, G. Erfort, C. Simão Ferreira, D. Infield, C. N. Nayeri, G. Pechlivanoglou, M. Runacres, G. Schepers, B. Summerville, D. Wood, and A. Orrell, "Current status and grand challenges for small wind turbine technology", *Wind Energy Science*, vol. 7, no. 5, pp. 2003–2037, 2022. DOI: 10.5194/wes-2022-34. [Online]. Available: https://wes.copernicus.org/articles/7/2003/2022/.

[6] F. Balduzzi, A. Bianchini, E. A. Carnevale, L. Ferrari, and S. Magnani, "Feasibility analysis of a darrieus vertical-axis wind turbine installation in the rooftop of a building", *Applied Energy*, vol. 97, pp. 921–929, 2012. DOI: 10.1016/j.apenergy.2011.12.008. [Online]. Available: https://doi.org/10.1016/j.apenergy.2011.12.008.

[7] F. Papi, A. Nocentini, G. Ferrara, and A. Bianchini, "On the Use of Modern Engineering Codes for Designing a Small Wind Turbine: An Annotated Case Study", *Energies*, vol. 14, 2021. DOI: 10.3390/en14041013. [Online]. Available: https://doi.org/10.3390/en14041013.

[8] S. Mertens, G. van Kuik, and G. van Bussel, "Performance of an h-darrieus in the skewed flow on a roof", *Journal of Solar Energy Engineering*, vol. 125, no. 4, pp. 433–440, 2003. DOI: 10.1115/1.1629309. [Online]. Available: https://asmedigitalcollection.asme.org/solarenergyengineering/article-abstract/125/4/433/464744/Performance-of-an-H-Darrieus-in-the-Skewed-Flow-on?redirectedFrom=fulltext.

[9] R. Howell, N. Qin, J. Edwards, and N. Durrani, "Wind tunnel and numerical study of a small vertical axis wind turbine", *Renewable Energy*, vol. 35, no. 2, pp. 412–422, 2010. DOI: 10.1016/j.renene.2009.07.025. [Online]. Available: https://www.sciencedirect.com/science/article/abs/pii/S0960148109003048.

[10] E. Dayan, "Wind energy in buildings: Power generation from wind in the urban environment - where it is needed most", *Refocus*, vol. 7, no. 2, pp. 33–38, 2006. DOI: 10.1016/S1471-0846(06)70545-5. [Online]. Available: https://www.sciencedirect.com/science/article/abs/pii/S1471084606705455.

[11] M. Khan, M. Alavi, N. Mohan, A. Azeez, A. Shanif, and B. Javed, "Wind turbine design and fabrication to power street lights", vol. 108, 2017. DOI: 10.1051/matecconf/201710808010. [Online]. Available: https://www.matec-conferences.org/articles/matecconf/abs/2017/22/matecconf_icmaa2017_08010/matecconf_icmaa2017_08010.html.

[12] C. W. Klok, A. F. Kirkels, and F. Alkemade, "Impacts, procedural processes, and local context: Rethinking the social acceptance of wind energy projects in the netherlands", *Energy Research Social Science*, vol. 99, p. 103 044, 2023. DOI: 10.1016/j.erss.2023.103044. [Online]. Available: https://www.sciencedirect.com/science/article/pii/S2214629623001044.

[13] R. Merino-Martínez, R. Pieren, and B. Schäffer, "Holistic approach to wind turbine noise: From blade trailing-edge modifications to annoyance estimation", *Renewable and Sustainable Energy Reviews*, vol. 148, p. 111 285, 2021. DOI: 10.1016/j.rser.2021.111285. [Online]. Available: https://www.sciencedirect.com/science/article/pii/S1364032121005724.

[14] A. H. Poulsen, O. Raaschou-Nielsen, A. Peña, A. N. Hahmann, R. B. Nordsborg, M. Ketzel, J. Brandt, and M. Sørensen, "Impact of long-term exposure to wind turbine noise on redemption of sleep medication and antidepressants: A nationwide cohort study", *Environmental Health Perspectives*, vol. 127, no. 3, p. 037 005, 2019. DOI: 10.1289/EHP3909. [Online]. Available: https://ehp.niehs.nih.gov/doi/10.1289/EHP3909.

[15] R. Pieren, L. Bertsch, D. Lauper, and B. Schäffer, "Improving future low-noise aircraft technologies using experimental perception-based evaluation of synthetic flyovers", *Science of The Total Environment*, vol. 692, 2019. DOI: 10.1016/j.scitotenv.2019.07.253. [Online]. Available: https://www.sciencedirect.com/science/article/abs/pii/S0048969719333674.

[16] M. Vorländer, *Auralization - Fundamentals of Acoustics, Modelling, Simulation, Algorithms and Acoustic Virtual Reality*. Springer, 2008, ISBN: 9781292022932.

5

[17] S. Eriksson, H. Bernhoff, and M. Leijon, "Evaluation of different turbine concepts for wind power", *Renewable and Sustainable Energy Reviews*, vol. 12, pp. 1419–1434, 2008. DOI: 10.1016/j.rser.2006.05.017. [Online]. Available: https://doi.org/10.1016/j.rser.2006.05.017.

[18] E. A. Bossanyi, "The Design of closed loop controllers for wind turbines", *Wind Energy*, vol. 3, no. 3, pp. 149–163, 2000. DOI: 10.1002/we.34. [Online]. Available: https://doi-org.tudelft.idm.oclc.org/10.1002/we.34.

[19] S. Eriksson, J. Kjellin, and H. Bernhoff, "Tip speed ratio control of a 200 kw vawt with synchronous generator and variable dc voltage", *Energy Science & Engineering*, vol. 1, no. 3, pp. 135–143, 2013. DOI: 10.1002/ese3.23. [Online]. Available: https://onlinelibrary.wiley.com/doi/10.1002/ese3.23.

[20] F. Bonaccorso, G. Scelba, A. Consoli, and G. Muscato, "EKF - Based MPPT control for vertical axis wind turbines", in *IECON 2011 - 37th Annual Conference of the IEEE Industrial Electronics Society*, 2011, pp. 3614–3619. DOI: 10.1109/IECON.2011.6119896. [Online]. Available: https://ieeexplore-ieee-org.tudelft.idm.oclc.org/document/6119896.

[21] T. Burton, N. Jenkings, D. Sharpe, and E. A. Bossanyi, *Wind Energy Handbook*, J. W. Sons, Ed. 2001. DOI: 10.1002/9781119992714. [Online]. Available: https://onlinelibrary.wiley.com/doi/book/10.1002/9781119992714.

[22] K. Z. Østergaard, P. Brath, and J. Stoustrup, "Estimation of effective wind speed", in *Journal of Physics: Conference Series*, 2007. DOI: 10.1088/1742-6596/75/1/012082. [Online]. Available: https://iopscience.iop.org/article/10.1088/1742-6596/75/1/012082.

[23] M. N. Soltani, T. Knudsen, M. Svenstrup, R. Wisniewski, P. Brath, R. Ortega, and K. Johnson, "Estimation of rotor effective wind speed: A comparison", *IEEE Transactions on Control Systems Technology*, vol. 21, no. 4, pp. 1155–1167, 2013. DOI: 10.1109/TCST.2013.2260751. [Online]. Available: https://ieeexplore.ieee.org/document/6524000.

[24] L. Brandetti, Y. Liu, S. P. Mulders, C. Simão Ferreira, S. Watson, and J. W. van Wingerden, "On the ill-conditioning of the combined wind speed estimator and tip-speed ratio tracking control scheme", ser. Journal of Physics: Conference Series, 2022. DOI: 10.1088/1742-6596/2265/3/032085. [Online]. Available: https://iopscience.iop.org/article/10.1088/1742-6596/2265/3/032085.

[25] L. Brandetti, S. P. Mulders, Y. Liu, S. Watson, and J. W. van Wingerden, "Analysis and multi-objective optimisation of wind turbine torque control strategies", *Wind Energy Science*, 2023. DOI: 10.5194/wes-2023-66. [Online]. Available: https://doi.org/10.5194/wes-2023-66.

[26] P. F. Odgaard, L. F. S. Larsen, R. Wisniewski, and T. G. Hovgaard, "On using pareto optimality to tune a linear model predictive controller for wind turbines", *Renewable Energy*, vol. 87, pp. 884–891, 2016. DOI: 10.1016/j.renene.2015.09.067. [Online]. Available: https://www.sciencedirect.com/science/article/pii/S0960148115303463.

5

[27]   N. Moustakis, S. P. Mulders, J. Kober, and J. W. van Wingerden, "A practical bayesian optimization approach for the optimal estimation of the rotor effective wind speed", in *2019 American Control Conference (ACC)*, 2019, pp. 4179–4185. DOI: 10.23919/ACC.2019.8814622. [Online]. Available: https://ieeexplore.ieee.org/abstract/document/8814622.

[28]   M. Lara, J. Garrido, M. L. Ruz, and F. Vázquez, "Multi-objective optimization for simultaneously designing active control of tower vibrations and power control in wind turbines", *Energy Reports*, vol. 9, pp. 1637–1650, 2023. DOI: 10.1016/j.egyr.2022.12.141. [Online]. Available: https://www.sciencedirect.com/science/article/pii/S2352484722027421.

[29]   J. Jonkman, S. Butterfield, W. Musial, and G. Scott, "Definition of a 5-MW Reference Wind Turbine for Offshore System Development", Tech. Rep., 2009. DOI: NREL/TP-500-38060. [Online]. Available: https://www.nrel.gov/docs/fy09osti/38060.pdf.

[30]   W. Holley, S. Rock, and K. Chaney, "Control of variable speed wind turbines below-rated wind speed", ser. Proceedings of the 3rd ASME/JSME Conference, ASME/JSME, 1999.

[31]   M. J. Clifton-Smith, "Aerodynamic Noise Reduction for Small Wind Turbine Rotors", *Wind Engineering*, vol. 34, 2010. DOI: 10.1260/0309-524X.3.4.403. [Online]. Available: https://journals.sagepub.com/doi/abs/10.1260/0309-524X.3.4.403?journalCode=wiea.

[32]   M. Sessarego and D. Wood, "Multi-dimensional optimization of small wind turbine blades", *Renewables: Wind, Water, and Solar*, vol. 9, 2015. DOI: 10.1186/s40807-015-0009-x. [Online]. Available: https://sustainenergyres.springeropen.com/articles/10.1186/s40807-015-0009-x#citeas.

[33]   A. Pourrajabian, S. Rahgozar, M. Dehghan, and D. Wood, "A comprehensive multi-objective optimization study for the aerodynamic noise mitigation of a small wind turbine", *Engineering Analysis with Boundary Elements*, vol. 155, pp. 553–564, 2023, ISSN: 0955-7997. DOI: https://doi.org/10.1016/j.enganabound.2023.06.035. [Online]. Available: https://www.sciencedirect.com/science/article/pii/S0955799723003521.

[34]   B. LeBlanc and C. Simão Ferreira, "Estimation of blade loads for a variable pitch vertical axis wind turbine from particle image velocimetry", *Wind Energy*, pp. 1–20, 2021, ISSN: 10991824. DOI: 10.1002/we.2674. [Online]. Available: https://doi.org/10.1002/we.2674.

[35]   L. Brandetti, F. Avallone, D. De Tavernier, B. LeBlanc, C. Simão Ferreira, and D. Casalino, "Assessment through high-fidelity simulations of a low-fidelity noise prediction tool for a vertical-axis wind turbine", *Journal of Sound and Vibration*, vol. 547, p. 117 486, 2023. DOI: 10.1016/j.jsv.2022.117486. [Online]. Available: https://www.sciencedirect.com/science/article/pii/S0022460X22006691.

[36]   D. Marten, "Qblade: A modern tool for the aeroelastic simulation of wind turbines", Ph.D. dissertation, 2020. DOI: 10.14279/depositonce-10646.

[37] D. M. A. De Tavernier, "Aerodynamic advances in vertical-axis wind turbines", Ph.D. dissertation, 2021, ISBN: 9789055841745.

[38] C. Simão Ferreira, G. van Kuik, G. van Bussel, and F. Scarano, "Visualization by PIV of dynamic stall on a vertical axis wind turbine", *Experiments in Fluids*, no. 46, pp. 97–108, 2009. DOI: 10.1007/s00348-008-0543-z. [Online]. Available: https://doi.org/10.1007/s00348-008-0543-z.

[39] Y. Lao, M. A. Rotea, J. P. Koeln, M. S. Sakib, and D. T. Griffith, "Economic Nonlinear Model Predictive Control of Offshore Vertical-Axis Wind Turbines", ser. 2022 American Control Conference (ACC), 2022, pp. 3518–3525. DOI: 10.23919/ACC53348.2022.9867846. [Online]. Available: https://ieeexplore.ieee.org/document/9867846.

[40] M. E. Haque, M. Negnevitsky, and K. M. Muttaqi, "A novel control strategy for a variable speed wind turbine with a permanent magnet synchronous generator", in *2008 IEEE Industry Applications Society Annual Meeting*, 2008, pp. 1–8. DOI: 10.1109/08IAS.2008.374. [Online]. Available: https://ieeexplore.ieee.org/document/4659162.

[41] R. Ortega, F. Mancilla-David, and F. Jaramillo, "A globally convergent wind speed estimator for wind turbine systems", *International Journal of Adaptive Control and Signal Processing*, vol. 27, pp. 413–425, 2013. DOI: 10.1002/acs.2319. [Online]. Available: https://doi-org.tudelft.idm.oclc.org/10.1002/acs.2319.

[42] Y. Liu, A. K. Pamososuryo, R. M. G. Ferrari, and J. W. van Wingerden, "The Immersion and Invariance Wind Speed Estimator Revisited and New Results", *IEEE Control Systems Letters*, vol. 6, pp. 361–366, 2022. DOI: 10.1109/LCSYS.2021.3076040. [Online]. Available: https://ieeexplore-ieee-org.tudelft.idm.oclc.org/document/9416566.

[43] T. F. Brooks, S. Pope, and M. A. Marcolini, "Airfoil Self-Noise and Prediction", *NASA Reference Publication 1218*, pp. 1–142, 1989, ISSN: 14786095. DOI: 10.1080/09524622.2008.9753825. [Online]. Available: http://ntrs.nasa.gov/archive/nasa/casi.ntrs.nasa.gov/19890016302.pdf.

[44] A. L. Rogers, J. F. Manwell, and S. Wright, "Wind turbine acoustic noise", Tech. Rep., 2006. DOI: 10.1260/0957456042872777. [Online]. Available: https://docs.wind-watch.org/rogers-windturbinenoise_rev2006.pdf.

[45] J. W. Kim, S. Haeri, and P. F. Joseph, "On the reduction of aerofoil-turbulence interaction noise associated with wavy leading edges", *Journal of Fluid Mechanics*, vol. 792, pp. 526–552, 2016. DOI: 10.1017/jfm.2016.95. [Online]. Available: https://doi.org/10.1017/jfm.2016.95.

[46] J. D. M. Botha, A. Shahroki, and H. Rice, "An implementation of an aeroacoustic prediction model for broadband noise from a vertical axis wind turbine using a CFD informed methodology", *Journal of Sound and Vibration*, vol. 410, pp. 389–415, 2017, ISSN: 0022-460X. DOI: 10.1016/j.jsv.2017.08.038. [Online]. Available: http://dx.doi.org/10.1016/j.jsv.2017.08.038.

5

[47] S. Buck, S. Oerlemans, and S. Palo, "Experimental characterization of turbulent inflow noise on a full-scale wind turbine", *Journal of Sound and Vibration*, vol. 385, pp. 219–238, 2016. DOI: 10.1016/j.jsv.2016.09.010. [Online]. Available: https://doi.org/10.1016/j.jsv.2016.09.010.

[48] H. A. Madsen, "The Actuator Cylinder - A Flow Model for Vertical Axis Wind Turbines", Ph.D. dissertation, Aalborg University Centre, 1982. DOI: 10.13140/RG.2.1.2512.3040. [Online]. Available: https://doi.org/10.13140/RG.2.1.2512.3040.

[49] G. Ruijgrok, *Elements of Aviation Acoustics*. 1993, p. 309, ISBN: 90-6275-899-1. [Online]. Available: http://resolver.tudelft.nl/uuid:e4589b31-ffa3-4a5d-9400-1e2b446f60f3.

[50] T. F. Brooks and C. L. Burley, "Rotor broadband noise prediction with comparison to model data", *Journal of the American Helicopter Society*, vol. 49, no. 1, pp. 28–42, 2004. DOI: 10.4050/JAHS.49.28. [Online]. Available: https://doi.org/10.4050/JAHS.49.28.

[51] M. V. Lowson and J. B. Ollerhead, "A theoretical study of helicopter noise", *Journal of Sound and Vibration*, vol. 9, no. 2, pp. 197–222, 1969. DOI: 10.1016/0022-460X(69)90028-5. [Online]. Available: https://doi.org/10.1016/0022-460X(69)90028-5.

[52] P. Moriarty and P. Migliore, "Semi-Empirical Aeroacoustic Noise Prediction Code for Wind Turbines", National Renewable Energy Laboratory, Tech. Rep., 2003. DOI: 10.2172/15006098. [Online]. Available: https://doi.org/10.2172/15006098.

[53] J. Maillard, A. P. C. Bresciani, and A. Finez, "Perceptual validation of wind turbine noise auralization", ser. Proceedings of the 10th Convention of the European Acoustics Association (Forum Acusticum) 2023, 2023.

[54] R. Pieren, K. Heutschi, M. Müller, M. Manyoky, and K. Eggenschwiler, "Auralization of wind turbine noise: Emission synthesis", *Acta Acustica united with Acustica*, vol. 100, pp. 25–33, 2014. DOI: 10.3813/AAA.918683. [Online]. Available: https://www.ingentaconnect.com/content/dav/aaua/2014/00000100/00000001/art00007#Supp.

[55] H. Fastl and E. Zwicker, *Psychoacoustics – Facts and models*. 2007, ISBN: 987–3–540–68888–4.

[56] G. Q. Di, X. W. Chen, K. Song, B. Zhou, and C. M. Pei, "Improvement of zwicker's psychoacoustic annoyance model aiming at tonal noises", *Applied Acoustics*, vol. 105, pp. 164–170, 2016. DOI: 10.1016/j.apacoust.2015.12.006. [Online]. Available: https://www.sciencedirect.com/science/article/pii/S0003682X15003606.

[57] R. Merino-Martínez, R. Pieren, B. Schäffer, and D. Simons, "Psychoacoustic model for predicting wind turbine noise annoyance", Oct. 2022. [Online]. Available: https://www.researchgate.net/publication/364996997_Psychoacoustic_model_for_predicting_wind_turbine_noise_annoyance.

[58] G. F. Greco, R. Merino-Martínez, and A. Osses, "SQAT: a MATLAB-based toolbox for quantitative sound quality analysis", ser. INTER-NOISE, 2023.

[59] International Organization for Standardization, "ISO norm 532–1 – Acoustics – Method for calculating loudness – Zwicker method", Tech. Rep., 2017. [Online]. Available: https://www.iso.org/standard/63077.html.

[60] W. Aures, "Procedure for calculating the sensory euphony of arbitrary sound signal. in german: Berechnungsverfahren für den sensorischen wohlklang beliebiger schallsignale", *Acustica*, vol. 59, pp. 130–41, 1985.

[61] G. von Bismarck, "Sharpness as an attribute of the timbre of steady sounds", *Acustica*, vol. 30, pp. 159–172, 1974. [Online]. Available: ingentaconnect.com/contentone/dav/aaua/1974/00000030/00000003/art00006.

[62] P. Daniel and R. Webber, "Psychoacoustical roughness: Implementation of an optimized model", *Acustica*, vol. 83, pp. 113–23, 1997. [Online]. Available: https://www.ingentaconnect.com/content/dav/aaua/1997/00000083/00000001/art00020?crawler=true.

[63] A. Osses Vecchi, G. R, and A. Kohlrausch, "Modelling the sensation of fluctuation strength", 1, vol. 28, Sep. 2016. DOI: 10.1121/2.0000410. [Online]. Available: https://doi.org/10.1121/2.0000410.

[64] G. F. Greco, R. Merino-Martínez, and A. Osses, *SQAT: a sound quality analysis toolbox for MATLAB*, 2023. DOI: 10.5281/zenodo.7934709.

[65] M. K. Lukovic, Y. Tian, and W. Matusik, "Diversity-guided multi-objective Bayesian optimization with batch evaluations", in *Advances in Neural Information Processing Systems*, vol. 33, 2020, pp. 17 708–17 720. [Online]. Available: https://proceedings.neurips.cc/paper_files/paper/2020/file/cd3109c63bf4323e6b987a5923 Paper.pdf.

[66] K. Miettinen, *Nonlinear multiobjective optimization*. 1999. DOI: 10.1007/978-1-4615-5563-6. [Online]. Available: https://link.springer.com/book/10.1007/978-1-4615-5563-6.

[67] A. Gambier, "Multiobjective optimal control of wind turbines: A survey on methods and recommendations for the implementation", *Energies*, vol. 15, p. 567, Jan. 2022. DOI: 10.3390/en15020567. [Online]. Available: https://www.mdpi.com/1996-1073/15/2/567.

[68] M. Lara, J. Garrido, J. W. van Wingerden, S. P. Mulders, and F. Vázquez, "Optimization with genetic algorithms of individual pitch control design with and without azimuth offset for wind turbines in the full load region", ser. 22nd IFAC World Congress, 2023, pp. 375–380.

[69] I. Santín, C. Pedret, and R. Vilanova, *Control and Decision Strategies in Wastewater Treatment Plants for Operation Improvement, Intelligent Systems*, S. Cham, Ed. 2017. DOI: 10.1007/978-3-319-46367-4. [Online]. Available: https://link.springer.com/book/10.1007/978-3-319-46367-4.

5

[70] P. Wang, Z. Zhu, and Y. Wang, "A novel hybrid mcdm model combining the saw, topsis and gra methods based on experimental design", *Information Sciences*, vol. 345, pp. 27–45, 2016. DOI: https://doi.org/10.1016/j.ins.2016.01.076. [Online]. Available: https://www.sciencedirect.com/science/article/pii/S0020025516300123.

[71] A. Afshari, M. Mojahed, and R. Yusuff, "Simple additive weighting approach to personnel selection problem.", *International Journal of Innovation, Management and Technology*, vol. 1, pp. 511–515, 2010. DOI: 10.7763/IJIMT.2010.V1.89. [Online]. Available: https://www.researchgate.net/publication/285828294_Simple_Additive_Weighting_Approach_to_Personnel_Selection_Problem.

[72] V. Bagočius, E. K. Zavadskas, and Z. Turskis, "Multi-person selection of the best wind turbine based on the multi-criteria integrated additive-multiplicative utility function", *Journal of Civil Engineering and Management*, vol. 20, no. 4, pp. 590–599, 2014. DOI: 10.3846/13923730.2014.932836. [Online]. Available: https://doi.org/10.3846/13923730.2014.932836.

[73] H.-C. Lee and C.-T. Chang, "Comparative analysis of mcdm methods for ranking renewable energy sources in taiwan", *Renewable and Sustainable Energy Reviews*, vol. 92, pp. 883–896, 2018. DOI: https://doi.org/10.1016/j.rser.2018.05.007. [Online]. Available: https://www.sciencedirect.com/science/article/pii/S1364032118303435.

[74] L. Brandetti and D. van den Berg, "QBlade 2.0.5.2 Matlab Tutorial", Tech. Rep., 2023. DOI: 10.4121/22134710.

6

CONCLUSIONS AND RECOMMENDATIONS

La mente degli uomini terreni si muta | The minds of earthly men change
come varia il giorno che manda | as the day varies, sent
su di loro il padre degli uomini e degli dèi | upon them by the father of men and gods

Odissea, libro XXVIII, versi 135-137 | Odissey, book XVIII, lines 135-137

6.1. SUMMARY OF FINDINGS

Vertical-axis wind turbines (VAWTs) are pivotal in advancing wind energy applications in urban environments. While prior research has investigated specific aspects of these turbines, a comprehensive interdisciplinary analysis encompassing turbine performance and the perceptions of neighbouring residents remains absent. This dissertation addresses the abovementioned research gap, as articulated in Chapter 1, with the following primary objective:

> **Thesis goal:** Develop an integrated analysis and design methods for urban VAWTs incorporating advanced control, aerodynamic, aeroacoustic and aeroelastic models, trading off energy capture, actuation effort and noise acceptance.

By exploring established aero-acoustic-servo-elastic models, this assessment brings the state-of-the-art noise predictions to the next level, enabling a low-fidelity noise model to estimate the noise sources on a VAWT in urban settings with acceptable accuracy for preliminary design phases. Furthermore, this study introduces an advanced controller to optimise the VAWT power production in turbulent conditions and proposes a frequency domain framework to examine its operational mechanisms comprehensively. This approach allows the formalisation of the ill-conditioning problem for the considered controller, shedding light on the cause of steady-state biased wind speed (and thus tip-speed ratio) estimates and sub-optimal power tracking in the presence of model uncertainty. Integrating a multi-objective optimisation technique within this frequency-domain framework marks a significant step towards addressing the limitations inherent in conventional control theories. These constraints primarily arise from the nonlinear and complex characteristics exhibited by turbine performance metrics, which do not readily align with linear control design techniques. By combining the multi-objective optimisation approach with the proposed methodology, this research establishes a connection between nonlinear turbine performance metrics and controller insights. Finally, these collective insights and the importance of considering urban residents in the decision-making have led to the development of a novel controller calibration approach combining aero-servo-elastic analysis with the assessment of the psychoacoustic annoyance of an urban VAWT. The combined contributions of this thesis drive advancements in comprehending the intricate dynamics of VAWTs, with a specific focus on achieving a balance between turbine performance and noise acceptance metrics, thereby setting a foundation for integrating VAWTs into urban environments.

In alignment with the subgoals outlined in Chapter 1, the following section presents the key conclusions drawn from each part of this thesis. This section is, therefore, organised into four distinct subsections, mirroring the thesis structure. Firstly, an evaluation of the low-fidelity prediction model is presented. Subsequently, comprehensive remarks on implementing the advanced controller in a small-scale VAWT and the ill-conditioning problem are provided. A detailed concluding analysis of the comparison between this advanced control scheme and a baseline control strategy on a reference turbine design follows. The last section presents how the insights obtained from the aero-acoustic-servo-elastic analysis allow the formulation of a control strategy for a VAWT capable of balancing turbine performance and noise acceptance metrics.

A LOW-FIDELITY NOISE PREDICTION MODEL

Vertical-axis wind turbines hold potential for deployment in urban areas, where wind turbine installation and operation require satisfying noise regulations. Accurate modelling of the far-field noise with low-order fidelity methods is essential to account for noise early in the design phase. The inherent challenge for VAWTs resides in the dynamic azimuthal flow variation along the blades, making far-field noise prediction complex when relying on low-fidelity methodologies. Given the absence of a consensus in existing literature regarding noise source modelling for VAWTs, the first research question posed in this thesis was:

> **I:** How can a low-fidelity noise prediction model be developed to advance the state-of-the-art in predicting noise emitted by VAWTs and achieve acceptable accuracy for the preliminary design stage?

To answer this research question, the state-of-the-art low-fidelity noise models for a VAWT operating at a low Reynolds number were investigated through a comparison with high-fidelity simulations and experimental data. This dataset establishes a novel link between far-field noise and the unsteady aerodynamics intrinsic to VAWTs. The low-fidelity aerodynamic approach is based on the actuator cylinder model with corrections to account for the dynamic stall, flow curvature effect, and the case of a heavily loaded rotor. Subsequently, low-fidelity far-field noise predictions are obtained using semi-empirical models for airfoil-self noise and turbulence-interaction (T-I) noise.

Regarding the AC model's accuracy, its dependence on precise aerodynamic polars is emphasised, highlighting the critical role of accurate flow prediction, particularly upwind. Conversely, discrepancies in trend predictions downwind are attributed to unaccounted-for phenomena in the low-fidelity noise approach, such as three-dimensional effects, blade-blade interactions, flow separation, and tower shadow, affecting the angle of attack and BEWS predictions.

These observed aerodynamic constraints are confirmed to affect the acoustic predictions. While the Buck model effectively predicts T-I noise, the BPM approach exhibits limitations in modelling airfoil-self noise due to the flow parameter prediction issues and the steady flow assumption. Despite these limitations, the proposed low-fidelity model yields fast and acceptable accuracy for assessing the VAWT's aeroacoustic performance in preliminary design phases.

A COMBINED WIND SPEED ESTIMATOR AND TIP-SPEED RATIO TRACKING CONTROL SCHEME AND THE ILL-CONDITIONING PROBLEM

One of the primary drawbacks inherent to VAWTs is rooted in their complex three-dimensional aerodynamics, which gives rise to variations in blade-effective wind speed and angle of attack in response to changes in azimuth angle. These periodic and nonlinear dynamics pose challenges in predicting the aerodynamic and acoustic VAWT performance and the wind acting on the rotor and blades. This challenge is particularly evident in turbulent urban environments with high turbulence levels and variable wind directions.

Enhancing the accuracy of wind speed estimation holds promising potential for advancing control algorithms, thereby enabling more effective actuation effort alleviation

and power regulation. Consequently, this thesis addresses the following research question:

> **II:** Can the WSE-TSR tracking control strategy offer a viable solution to balance power maximisation for an urban VAWT, even in the presence of model uncertainty?

Under ideal conditions, without model uncertainty, the proposed control mechanism successfully tracks the turbine's optimal operating condition, effectively maximising power production. Nevertheless, an in-depth analysis of the controller mechanisms revealed its high dependency on prior knowledge of the wind turbine, rendering it inherently ill-conditioned.

The lack of information in the scheme prevents accurate wind speed estimation based solely on the product of other model parameters within the power balance equation. As a result, using the estimated wind speed in calculating the feedback signal for the TSR tracker leads to deviations from the optimal real-world turbine performance. Conversely, the controller operates under the assumption of achieving the desired optimal operating point. An analytical approach was undertaken to formally address this issue, deriving the transfer functions characterising the WSE-TSR tracking controller via a linear frequency-domain analysis framework. This analysis aimed to evaluate the ill-conditioning problem thoroughly.

Time-domain and frequency-domain results demonstrate that uncertainties in the modelled turbine parameters, such as the power coefficient, introduce biases in the wind speed estimation. Subsequently, the accurate tracking of the turbine's optimal aerodynamic performance is hindered due to the inability to determine the actual turbine operating point.

ANALYSIS AND MULTI-OBJECTIVE OPTIMISATION OF WIND TURBINE CONTROLLERS

The frequency-domain analysis framework provides valuable insights into the bandwidth and stability margins of the modern and advanced WSE-TSR tracking controller. However, establishing a connection between this linear framework and practical performance metrics, such as power maximisation and actuation effort minimisation, presents a complex challenge. Furthermore, the feasibility of the WSE-TSR tracking controller should be assessed by applying the control scheme to a well-known and widely adopted reference turbine design before implementing it in the innovative VAWT concept. Considering these factors, the following research question is motivated:

> **III:** What are the potential performance benefits of the WSE-TSR tracking controller compared to a baseline control scheme considering relevant power and actuation effort objectives on a reference turbine design?

The investigation conducted in this thesis demonstrates that using a frequency-domain framework and an optimal calibration procedure enables an analysis of the potential benefits offered by the WSE-TSR tracking control scheme compared to the baseline $K\omega^2$ controller. Specifically, a multi-objective optimisation problem is formulated for calibration, considering the conflicting objectives of power maximisation and torque

fluctuations minimisation. The optimisation problem is solved by approximating the Pareto front using an exploratory search to identify optimal solutions.

The Pareto fronts reveal that applying the WSE-TSR tracking controller to contemporary turbine sizes does not yield any power gains, contradicting previous findings on improved power capture. However, the considered controller exhibits a more flexible control structure than the baseline, providing a trade-off between power and actuation effort objectives with a specific control bandwidth. In particular, reducing the control bandwidth leads to a 2% decrease in generated power and an 80% reduction in the torque actuation effort compared to the optimal calibration settings with the highest control bandwidth. This flexibility facilitates the operation of large-scale modern wind turbines and underscores the importance of an optimal calibration procedure.

Balancing the vertical-axis wind turbine performance with noise

Understanding how the intricate relationship between performance and noise acceptance metrics can be optimally balanced in the context of VAWTs presents a critical challenge in successfully deploying these turbines in urban areas. This concern gains further attention in light of the rising opposition from local communities due to noise emissions, thereby highlighting the need for a multi-disciplinary approach. Specifically, the design and decision-making process should consider noise annoyance as equally important as the imperative to maximise VAWT operational efficiency in turbulent and fluctuating urban wind conditions. In this context, employing the novel psychoacoustic annoyance metric could offer a more comprehensive understanding of the human perception of VAWT noise with respect to conventional sound metrics. Consequently, the last research question posed in this thesis is:

> **IV:** How can the insights obtained from subquestions/challenges **I**, **II** and **III** be effectively leveraged to evaluate the feasibility of the advanced controller for a VAWT in an urban environment in achieving an optimal trade-off between performance and noise acceptance metrics?

The problem of balancing aero-servo-elastic turbine performance with noise is tackled from a control calibration perspective. By taking advantage of the findings from subquestion **I**, the psychoacoustic annoyance value needed for the optimal controller calibration is computed by coupling the low-fidelity noise prediction model with a novel approach based on synthetic sound auralization and psychoacoustic sound quality metrics. Then, leveraging the insights from subquestions **II** and **III**, the WSE-TSR tracking controller is calibrated with a multi-objective optimisation technique based on Pareto fronts approximation. The optimal solutions are found as a trade-off for the considered objectives by applying a multi-criteria decision-making method.

Analysing these optimised solutions within a frequency-domain framework and mid-fidelity time-domain aero-servo-elastic simulations reveals the considerable potential of the optimally calibrated WSE-TSR tracking controller for small-scale urban VAWTs. The controller demonstrates the capacity to reduce actuation effort by up to 25%, with minimal impact on power, psychoacoustic annoyance, and lower controller bandwidth than the baseline. These results highlight the flexible structure of the WSE-TSR tracking

controller, emphasising its ability to balance aero-servo-elastic performance with noise acceptance effectively.

Furthermore, this interdisciplinary approach accurately predicts and characterises the acoustic emission of the VAWT in terms of psychoacoustic annoyance. The analysis of the noise spectra identifies T-I noise as the primary noise source for VAWTs in urban environments, contributing significantly to psychoacoustic annoyance levels. Importantly, the results indicate that increased power extraction levels do not necessarily lead to higher levels of psychoacoustic annoyance.

Overall, this interdisciplinary framework tackles the complex challenges of integrating VAWTs in urban environments, promoting their successful implementation and acceptance.

6.2. RECOMMENDATIONS FOR FUTURE WORK

This work has presented an advanced aero-acoustic-servo-elastic analysis for a VAWT in an urban environment, taking into account performance and noise acceptance metrics. In the course of the research, potential interesting opportunities for further investigation were identified. These recommendations are summarised in this section.

1. As demonstrated in this thesis, the accuracy of the noise prediction tool for the VAWT can be further improved by extracting BEWS from high-fidelity simulations. However, this improvement comes at the cost of increased computational time required for running such simulations. Therefore, a blade-effective wind speed estimator based on the Unscented Kalman Filter has already been developed for a VAWT, showing promising results for a first-order nonlinear model [1]. It would be interesting to explore its application in more complex implementations, such as the aero-servo-elastic software QBlade. Furthermore, since there is a direct correlation between the blade-effective wind speed and the blade loads, future work will take advantage of the knowledge of the estimated BEWS to develop strategies for reducing loads on VAWTs through Individual Pitch Control.

2. Enhance the design tool by including the aerodynamic and aeroacoustic estimation of the struts. For the aerodynamic estimation, it could be considered to replace the AC model, described in the corresponding chapter, with the Actuator-in-Actuator cylinder (ACsquared) model, as discussed by De Tavernier in [2] and applied to a rotor with inclined struts in Chapter 7 of De Tavernier [3]. Additionally, the approach introduced by Botha et al. [4] could be extended to account for the horizontal rotation of the struts in the aeroacoustic estimation. The resulting analysis of these structural components could lead to a more effective design tool with enhanced accuracy.

3. The presented WSE-TSR tracking control scheme is found inherently ill-conditioned when analysed with a control-oriented linear framework. This ill-conditioning leads to a biased estimation of the rotor-effective wind speed in the presence of model uncertainty. Thus, accurate wind speed estimation relies on precise internal model parameters that represent the actual properties of the wind turbine. However, these modelled parameters often deviate significantly from the true characteristics

initially and further vary over time due to factors like blade erosion and ice residue. Therefore, it is crucial to calibrate the internal model for enhanced accuracy to ensure reliable control performance. A novel learning algorithm has already been proposed to address this challenge [5]. This algorithm enables the calibration of turbine model parameters without relying on wind speed measurements. By leveraging the dynamic structure of the WSE-TSR tracking controller, the closed-loop system is excited, allowing real-time calibration of the internal model information. Preliminary results indicate that the algorithm can successfully detect and correct for a constant-factor power coefficient degradation case under ideal and turbulent wind conditions. An interesting opportunity would be to expand the algorithm's capabilities by relaxing constraints on the compensated degradation profile, enabling testing under even more realistic environmental conditions.

4. The multi-objective optimisation presented in the corresponding chapters allows for identifying optimal tuning for wind turbine torque controllers based on defined objective functions. However, the downside of this framework is that it requires a high computational time. Machine learning methods could be employed to solve the multi-objective optimisation problem, thereby enhancing the computational efficiency of the framework. For example, the combination of Bayesian optimisation with Gaussian processes has already demonstrated success in determining the optimal tuning for a Kalman filter-based wind speed estimator and individual pitch controller with minimal iterations.

5. The benefits of the WSE-TSR tracking control scheme over the baseline $K\omega^2$ controller have been evaluated under ideal conditions without considering the inherent uncertainties in real-world turbine dynamics. Therefore, a valuable avenue for future work would involve assessing the effects of model uncertainty on performance levels and control robustness.

6. Perform listening experiments to evaluate the real psychoacoustic annoyance experienced by human listeners. While the psychoacoustic annoyance model proposed in the corresponding chapter has been validated with high-fidelity simulations, it primarily provides an estimate of the noise annoyance generated by a VAWT in an urban environment. Hence, to enhance the approach, it would be beneficial to incorporate experiments and VR audio-visual simulations to evaluate these turbines' impact further.

7. Include the canyon effect in the psychoacoustic annoyance model to investigate the acoustic impact of VAWTs located on an urban rooftop or within urban cano-pies. Implementing a framework focused on Gaussian beam tracing (GBT) within an in-homogeneous atmospheric flow could solve this problem. Such a framework has already proven its capability to account for refraction effects resulting from wind velocity and air temperature variations in both vertical and horizontal directions.

8. Address the challenge posed by the rotor inertia, particularly in its impact on the VAWT responsiveness during startup and low rpm acceleration [6]. Building on the foundations of this work and leveraging Sessarego and Wood's multidimensional

blade design approach [7] for small-scale wind turbines, future investigations are recommended to include turbine inertia as a design variable within the proposed multi-objective optimisation framework. Additionally, considering resistive torque in the generator and drive train, mainly when using a gearbox, is recommended [8]. Although, in this study, a gearbox ratio of 1 was chosen to eliminate resistive torque for noise model simplification, future research should explore different ratios to understand their impact on rotor inertia and responsiveness, providing a comprehensive understanding of the mechanical-aerodynamic interplay in urban VAWTs.

6

BIBLIOGRAPHY

[1] L. Brandetti, Y. Liu, A. K. Pamososuryo, S. P. Mulders, S. Watson, and J. W. van Wingerden, "Unscented Kalman filter-based blade-effective wind speed estimation for a vertical-axis wind turbine", in *22nd IFAC World Congress Yokohama, Japan, July 9-14*, 2023, pp. 8393–8399. DOI: 10.1016/j.ifacol.2023.10.1033. [Online]. Available: https://www.sciencedirect.com/science/article/pii/S2405896323014167.

[2] D. De Tavernier and C. Simão Ferreira, "An extended actuator cylinder model : Actuator-in-actuator cylinder (AC-squared) model", *Wind Energy*, pp. 1–13, 2019. DOI: 10.1002/we.2340. [Online]. Available: https://doi.org/10.1002/we.2340.

[3] D. De Tavernier, "Aerodynamic advances in vertical-axis wind turbines", Ph.D. dissertation, 2021, ISBN: 9789055841745. [Online]. Available: https://doi.org/10.4233/uuid:7086f01f-28e7-4e1b-bf97-bb3e38dd22b9.

[4] J. D. M. Botha, A. Shahroki, and H. Rice, "An implementation of an aeroacoustic prediction model for broadband noise from a vertical axis wind turbine using a CFD informed methodology", *Journal of Sound and Vibration*, vol. 410, pp. 389–415, 2017, ISSN: 0022-460X. DOI: 10.1016/j.jsv.2017.08.038. [Online]. Available: http://dx.doi.org/10.1016/j.jsv.2017.08.038.

[5] S. P. Mulders, L. Brandetti, F. Spagnolo, Y. Liu, P. Brandt, and J. W. van Wingerden, "A learning algorithm to advanced wind turbine controllers for the calibration of internal model uncertainties: A wind speed measurement-free approach", ser. Proceedings of the 2023 American Control Conference (ACC 2023), Jun. 2023. DOI: 10.23919/ACC55779.2023.10156125. [Online]. Available: https://ieeexplore.ieee.org/document/10156125.

[6] Y. Celik, L. Ma, D. Ingham, and M. Pourkashanian, "Aerodynamic investigation of the start-up process of h-type vertical axis wind turbines using cfd", *Journal of Wind Engineering and Industrial Aerodynamics*, vol. 204, Jul. 2020. DOI: 10.1016/j.jweia.2020.104252. [Online]. Available: https://www.researchgate.net/publication/342822621_Aerodynamic_investigation_of_the_start-up_process_of_H-type_vertical_axis_wind_turbines_using_CFD.

[7] M. Sessarego and D. Wood, "Multi-dimensional optimization of small wind turbine blades", *Renewables: Wind, Water, and Solar*, vol. 9, 2015. DOI: 10.1186/s40807-015-0009-x. [Online]. Available: https://sustainenergyres.springeropen.com/articles/10.1186/s40807-015-0009-x#citeas.

[8]   J. R. P. Vaz, D. H. Wood, D. Bhattacharjee, and E. F. Lins, "Drivetrain resistance and starting performance of a small wind turbine", *Renewable Energy*, vol. 117, Oct. 2018. DOI: 10.1016/j.renene.2017.10.071. [Online]. Available: https://www.researchgate.net/publication/320761976_Drivetrain_resistance_and_starting_performance_of_a_small_wind_turbine.

6

A

BEDDOES-LEISHMAN DYNAMIC STALL MODEL

The Beddoes-Leishman (B-L) dynamic stall model [1] has been applied to address the impact of dynamic stall phenomena on the performance of the urban VAWT under study (Chapter 2). Acknowledged for its adaptability in dynamically modelling stall events, the B-L model requires only the lift and drag coefficients and the angle of attack as input parameters to characterise the equivalent dynamic loads on an airfoil. This model employs four indicial lift coefficients (A_1, A_2, b_1, b_2) and four time constants, defining the time delays inherent in aerodynamic loading:

- T_p, the peak pressure lag time constant, is dependent on Mach number but largely independent of airfoil shape, necessitating derivation from dynamic data [1].

- T_f, the boundary layer pressure lag time constant, is contingent upon both Mach number and airfoil shape.

Table A.1: Constants used in the Beddoes-Leishman (B-L) dynamic stall model [1], [2].

Parameter	Value
Indicial lift coefficient (A_1)	0.3
Indicial lift coefficient (A_2)	0.7
Indicial lift coefficient (b_1)	0.14
Indicial lift coefficient (b_2)	0.53
Peak pressure lag time constant (T_p)	1.5
Boundary layer pressure lag time constant (T_f)	5
Vortex decay time constant (T_v)	6
Vortex shedding time constant (T_{vl})	5

A

- T_{v}, the vortex decay time constant, shares a dependency on Mach number akin to Tp, with less sensitivity to airfoil shape [2].

- T_{vl}, the vortex shedding time constant, characterises the time for the leading edge vortex to shed over the airfoil. This coefficient, indicative of peak aerodynamic loading time, incorporates added vorticity [3].

The specific constants employed in the B-L dynamic stall model are briefly outlined in Table A.1. Notably, the refinement of precise time constants tailored for VAWTs is an active area of research beyond the scope of this thesis.

BIBLIOGRAPHY

[1] J. Leishman and T. Beddoes, "A Semi-Empirical Model for Dynamic Stall", *Journal of the American Helicopter Society*, vol. 34, no. 3, pp. 3–17, 1989. DOI: 10.4050/ JAHS.34.3.3. [Online]. Available: https://doi.org/10.4050/JAHS.34.3.3.

[2] R. Pereira, S. G, and P. M. D, "Validation of the Beddoes–Leishman dynamic stall model for horizontal axis wind turbines using MEXICO data", 2012. DOI: 10.1002/ we.541. [Online]. Available: https://doi.org/10.1002/we.541.

[3] M. Martinez, J. Boutet, X. Amanodlese, V. Terrapon, and G. Dimitriadis, "Computation of leishman-beddoes model parameters using a combination of experiments and simulations", Jan. 2019. DOI: 10.2514/6.2019-1854. [Online]. Available: https://www.researchgate.net/publication/330197526_Computation_ of_Leishman-Beddoes_model_parameters_using_a_combination_of_ experiments_and_simulations.

B

AIRFOIL POLARS DATABASE

The airfoil polars, used in Chapter 2 for the NACA0021, are calculated using Xfoil at an operating Reynolds number of 8.26×10^4. Three different $Ncrit$, equal to 0.01, 7 and 9, are selected to stress the strong dependence of the AC model from the polars used as input. The lift and the drag coefficients versus the experienced angle of attack are plotted in Figure B.1.
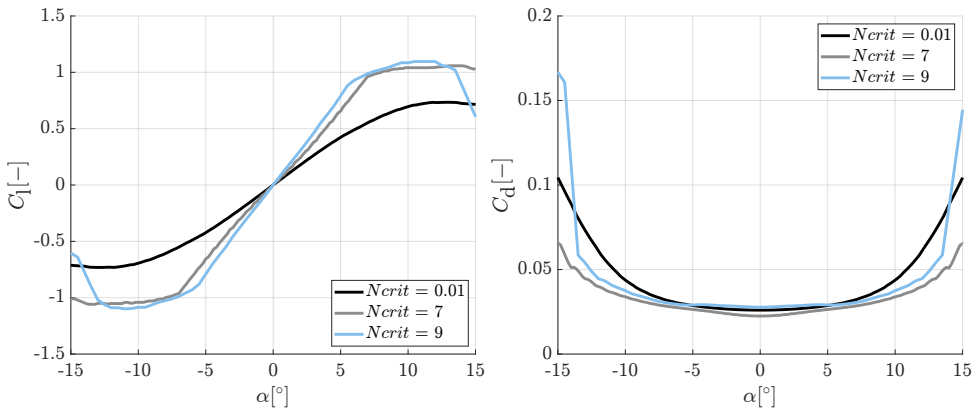

Figure B.1: Airfoil polars calculated with Xfoil for an operating Reynolds number of 8.26×10^4 and at three different $Ncrit$ equal to 0.01, 7 and 9. On the left side, the lift coefficient C_l is plotted versus the angle of attack α. On the right side, the drag coefficient C_d is plotted versus the angle of attack α.

C

SIMILARITY TO STATE FEEDBACK CONTROLLER DESIGN

This section proves that by following the state feedback control design theory, it is possible to end up with equal results to the analysis strategy proposed for the $K\omega^2$ controller, as illustrated in Figure C.1. First, the wind turbine to be controlled is assumed to be described by a linear state model with single input $T_{g,K}$, a single output ω_r and a single state ω_r [1]:

$$\dot{\omega}_r = A\omega_r + BT_{g,K}, \qquad \omega_r = C\omega_r + DT_{g,K}, \tag{C.1}$$

where $A = G(V)$, $B = E$, $C = 1$ and $D = 0$.

By applying Assumption 5, the model general time-invariant control law is a function of the state and the reference input:

$$T_{g,K} = \alpha\left(\omega_r, \lambda_*\right).$$

If the feedback is restricted to be linear, it can be written as

$$T_{g,K} = -K_f\omega_r + k_r\lambda_*, \tag{C.2}$$

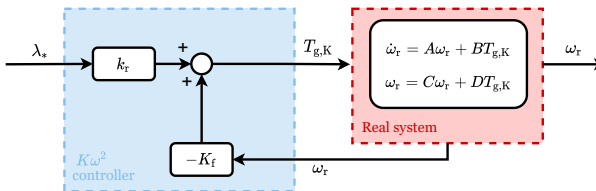Figure C.1: Block diagram of a state feedback controller with a reference shaping block, adapted for the $K\omega^2$ controller [1]. The full system consists of the real system dynamics (**red** box), here assumed to be linear, and the controller elements K_f and k_r. The controller (**cyan** box) uses the system state ω_r and the reference input λ_* to command the wind turbine through its input $T_{g,K}$.

in which K_f is the feedback gain, k_r is the reference shaping gain, and λ_* is assumed to be a constant reference signal. This representation illustrates the baseline controller with elements K_f and k_r in a similar form as the analysis strategy presented in Equation (4.14). Therefore, to prove that the $K\omega^2$ controller is equivalent to a state feedback controller with reference shaping, Equation (4.14) should match Equation (C.2), as

$$K_{1,K} = -K_f, \qquad \text{and} \qquad K_{2,K} = k_r. \tag{C.3}$$

Assuming that this equality is valid, it results in

$$K_f = -K_{(\Omega_r \to \mathcal{T}_g),K} = -\frac{\partial T_{g,K}}{\partial \omega_r}\bigg|_{(\bar{\omega}_r, \lambda_*)} = -\frac{\rho R^3 A_{rot} C_{p,*}(\lambda_*)}{N \lambda_*^3} \bar{\omega}_r. \tag{C.4}$$

When the feedback (Equation (C.2)) is applied to the wind turbine (Equation (C.1)), the closed-loop system is given by

$$\dot{\omega}_r = (A - B K_f) \omega_r + B k_r \lambda_*. \tag{C.5}$$

Follows the formulation of k_r as the controller aims to drive the output to the given reference

$$k_r = -\frac{1}{\left(C (A - B K_f)^{-1} B\right)} \frac{V}{R}, \tag{C.6}$$

in which the term V/R is added to the original formulation [1] to satisfy the goal of the controller:

$$\omega_r = \lambda_* \frac{V}{R}.$$

Substituting the expressions of A, B, C and D into the formulation of k_r (Equation (C.6)) yields

$$k_r = \frac{\rho R^3 A_{rot} C_{p,*}(\lambda_*)}{2N} \left(-\frac{3}{\lambda_*^4} C_{p,*}(\lambda_*) + \frac{1}{\lambda_*^3} \frac{\partial C_{p,*}(\lambda_*)}{\partial \lambda_*}\right) \bar{\omega}_r^2 = \frac{\partial T_{g,K}}{\partial \lambda_*}\bigg|_{(\bar{\omega}_r, \lambda_*)} = K_{(\Lambda_* \to \mathcal{T}_g),K}. \tag{C.7}$$

Since $K_{1,K}$ describes the feedback term and $K_{2,K}$ describes the reference shaping term, the equivalence between the $K\omega^2$ controller and state feedback controller with reference shaping is demonstrated.

BIBLIOGRAPHY

[1]   K. J. Aström and R. M. Murray, *Feedback systems: An Introduction for Scientists and Engineers.* 2010. DOI: 10.1086/596297. [Online]. Available: https://www.journals.uchicago.edu/doi/10.1086/596297.

D

QBLADE VERSION 2.0.5.2: MATLAB TUTORIAL

D.1. INTRODUCTION

QBlade is a highly advanced multi-physics code that covers the complete range of aspects required for the aero-servo-hydro-elastic design, prototyping, simulation, and certification of wind turbines. To use this interface, the QBlade code is loaded into the desired framework as a dynamic link library (.dll). In contrast, the scripting functions are exported through dedicated functions in an include.h header file.

Since, at present, only an example for using QBlade in Python is available, the main goal of this document is to provide a detailed explanation of how to use MATLAB to communicate with the QBlade Enterprise Edition (i.e. QBlade-EE) in a `.dll` format. However, since the EE version requires a license, the examples provided in this report have been adapted to work with the CE version. In both cases, the first step is to download the desired version (e.g. QBlade-CE or QBlade-EE) from the following website: `https://qblade.org/downloads/`. Then, by making use of the help function and the required syntax, the .dll interface is accessed in Matlab.

In the following, Appendix D.2 gives an overview of the motivation for using a .dll interface. A detailed description of every function included in the header file and the Matlab syntax required to build the interface are provided in Appendix D.3. Appendix D.4 illustrates several working examples together with their implementation in Matlab.

D.2. MOTIVATION FOR USING QBLADE AS DLL

This documentation will show how QBlade can be interfaced with Matlab by accessing it as a dynamic link library (.dll). The primary reason for this is to be able to run a number of different simulations, defined within Matlab, without having to set up a large number of simulations within QBlade. The desired workflow can be described as follows:

- Begin with a baseline simulation case.

175

- Make a copy of this simulation case and alter either controller or structural settings for this particular simulation.

- Initialize and run the simulation.

- Optional: Change wind/operating conditions during simulation.

- Optional: Read out structural and aerodynamic information during simulations.

- Optional: Apply control inputs.

- At the end of the simulation, save the project.

Figure D.1 shows a graphical representation of the desired workflow. The main idea depicted is that you begin with a baseline set-up (In this case a floating wind turbine) and copy that whilst altering some properties of the system. The Matlab code is only added for illustrative purposes. Appendix D.4 will have examples of working Matlab code for common wind turbine simulation cases.

Figure D.1: Graphical representation of the desired workflow using QBlade as .dll within Matlab. The Matlab code included is only for illustrative purposes.

This workflow reduces the number of interactions required with the GUI version of QBlade, reducing the number of potential mistakes when setting up a simulation and allowing for easier batch simulations.

D.3. INTERFACING QBLADE AND MATLAB

This section will give a brief overview of how one can use Matlab to interact with a .dll file. It will provide a short introduction to the commonly used Matlab commands and an overview of all the functions associated specifically with the QBlade .dll. The final section also introduces a Matlab help function that contains information on all the associated functions, including examples on how to interact with it using Matlab.

D.3.1. Matlab syntax

To build the interface in Matlab, the user needs to create a folder called **QBladeDLLInterface** in the example, containing the license file, QBladeEE.dll, QBladeDLLInclude.h (i.e. the header file for all the functions of the .dll), QBladeEE.exe and the following sub-folders:

1. **Source** contains the QBlade project in .sim format or .qpr format and the folder with the information on the simulation.

2. **MATLAB files** is where the Matlab interface will be built and where a sub-folder, called **Functions** in the example, can be created to include any Matlab functions needed in the simulations. For instance, in the example, one of these functions is used to write the parameters for the discon.in of the Delft Research Controller .dll.

After creating the required folders, the user should create a Matlab script and apply the following syntax:

- `loadlibrary` to load the .dll library.
  Example:
  `loadlibrary('<userpath> QBladeEE.dll',`
  `'QBladeDLLFunctions.h','alias','QBladeDLL')`

- `libfunctions` to store the functions in a cell.
  Example:
  `m = libfunctions('QBladeDLL')`

- `libfunctionsview` to display the signature of the function, i.e. what a function includes in terms of data and datatype;

- `calllib` to call the functions. It is important to check the type of data the functions need (Appendix D.3.2).
  Example:
  `calllib('QBladeDLL','initializeSimulation')`

- `unloadlibrary` to unload the library.

The order in which the commands are presented here should be the same order in which the commands are called in the Matlab code. The paths to load the library and the project should be set absolute. This is the reason why in the example, the <**userpath**> is used.

D.3.2. Help Function

Interacting with the .dll can be done by calling one of the 24 included functions. These functions are defined in C code and provided with the .dll. When loading the library using the `loadlibrary` command (see Appendix D.3.1) a so-called header file also needs to be provided. The header file and .dll need to be the same programming language, i.e., if the .dll is compiled in C, then the header should also be written in C. The full list of functions is given by:

1. loadProject

D

D

   2. loadSimDefinition

   3. storeProject

   4. setDebugInfo

   5. setLibraryPath

   6. createInstance

   7. closeInstance

   8. loadTurbulentWindBinary

   9. addTurbulentWind

10. initializeSimulation

11. setTimestepSize

12. setRPMPrescribeType_at_num

13. setRampupTime

14. getWindspeed

15. getCustomData_at_num

16. setInitialConditions_at_num

17. setTurbinePosition_at_num

18. setPowerLawWind

19. setControlVars_at_num

20. getTurbineOperation_at_num

21. advanceController_at_num

22. advanceTurbineSimulation

23. runFullSimulation

24. setLibraryPath

25. getTowerBottomLoads_at_num

A full description of each function, and how to interact with it using Matlab, can be found in [1]. All the descriptions there can also be had in Matlab directly as an output of a Matlab help function called `QBladeFunctionHelp`. This function is provided with the example files (Appendix D.4). To get information on one of the individual functions, call the help function with the name of the library call functions as a string. All these functions are called using the `calllib` function in Matlab, see Appendix D.3.1.

Example:
Call information on the 'getCustomData_at_num' library function:
QBladeFunctionHelp('getCustomData_at_num')

D.4. EXAMPLES

This section presents five different applications of the QBlade Matlab interface. First, a minimum working example, which can be used as a starting point, is described. Then, the conventional and most-used torque control strategy, i.e. the baseline $K\omega^2$ controller, is implemented in a turbine simulation. Example D.4.3 expands on the baseline $K\omega^2$ controller by also including a step in wind speed. This could be of interest to test controllers for a range of wind speeds. Example D.4.4 contains two examples of how to interact with the Delft Research Controller DLL. These examples are specific to the work carried out at the TU Delft. However, these examples also show how one can set-up batch simulations, output data for each simulation and interact with a project that contains a controller using the bladed interface. The final example D.4.5 is based on example D.4.2, but contains two turbines. The first turbine is modelled using the free-vortex wake, such that its wake interacts with the second turbine. This example shows how two turbines can be used using the Matlab interface and can only run for the QBlade–EE version.

D.4.1. MINIMUM WORKING EXAMPLE

A minimum working example of how to interface with QBlade in Matlab is presented by providing both the Matlab code and a detailed description of the steps that need to be performed. In this example, the NREL-5MW reference turbine bottom fixed [2] is simulated for ten-time steps and outputs the rotational speed in rpm. The QBlade project, called 'NREL5MW.qpr', was made available by the developers.

The following steps are performed in the example below:

1. load the .dll library with the `loadlibrary` command;

2. store the .dll functions in a cell with the `libfunctions` command. Note that if the cell is empty, it will mean that the library is not loaded correctly, and an error message is given as a warning;

3. set the library path with the following command
   `calllib('QBladeDLL','setLibraryPath','../../QBladeCE2.0.5.2.dll')`

4. create a new instance of QBlade with the `calllib` command;

5. define the project file that needs to be loaded, in this case, is the 'NREL5MW.qpr';

6. load the project with the `calllib` command;

7. initialize the simulation for a selected device, i.e. 1, and certain OpenCL parameters, i.e. 24, with the `calllib` command;

8. define the time length of the simulation, which equals the number of simulation steps times the time step with which the simulation has been set up. It is possible to check in the GUI under the simulation settings tab to avoid any mistakes;

9. define the variable that will be read and loaded during the simulation, i.e. the rotational speed. Note that the variable name should follow the label of the graphs in the GUI;

10. advance the structural part of the simulation and calculates all structural forces with the `calllib` command;

11. advance the aerodynamic part of the simulation and calculates all aerodynamic forces with the `calllib` command;

12. extract the rotational speed during the simulation with the `calllib` command;

13. end the simulation by closing the QBlade instance with the `calllib` command.

D

```matlab
1  addpath('..\..\');
2  % Establish connection
3
4  %this is setup using relative path and depends on the location of ...
       this file, if there are issues use absolute path to these files
5  loadlibrary('../../QBladeCE_2.0.5.2.dll',
6  '../QBladeDLLFunctions.h','alias','QBladeDLL')
7
8  m = libfunctions('QBladeDLL') ;
9
10 if isempty(m)
11     fprintf('Error')
12 end
13
14 %this is setup using relative path and depends on the location of ...
       this file, if there are issues use absolute path to these files
15 calllib('QBladeDLL','setLibraryPath','../../QBladeCE_2.0.5.2.dll')
16
17 calllib('QBladeDLL','createInstance',0,24)
18
19 %this is setup using relative path and depends on the location of ...
       this file, if there are issues use absolute path to these files
20 projectFile = '../../Source/NREL5MW.qpr';
21
22 calllib('QBladeDLL','loadProject',projectFile)
23 calllib('QBladeDLL','initializeSimulation')
24 simTime = 100; %in timestep, actual time is timestep*#timesteps
25 valuestr = 'Rotational Speed [rpm]';
26
27 f = waitbar(0,'Initializing Simulation') ;
28
29 for i = 1:1:simTime
30     calllib('QBladeDLL','advanceTurbineSimulation')
31     a = calllib('QBladeDLL','getCustomData_at_num',valuestr, 0, 0);
32     rpm(i,:) = a;
33
34     waitbar(i/simTime,f,'Simulation Running')
35
36 end
37
38 close(f);
39 %calllib('QBladeDLL','storeProject','check.qpr')
40 calllib('QBladeDLL','closeInstance')
```

D

D.4.2. BASELINE $K\omega^2$ CONTROLLER

This example builds on the minimum work example by also adding a $K\omega^2$ controller to the for-loop that runs the wind turbine simulation. In this example, the $K\omega^2$ controller is used because it is a commonly used control scheme in wind turbines. However, within this example, there is room to change the $K\omega^2$ controller for more complex control methods. Furthermore, this example only uses generator torque as a control action, however, the other four inputs constitute the turbine yaw angle and individual blade pitch angles. These can all be used for control simultaneously if needed.

For this example, we use the same project as with the minimum working example, a bottom-fixed NREL 5MW reference turbine. The gain K equals 2.24 for the NREL 5MW turbine and the gearbox ratio, needed to change rotor rpm to Low-Speed-Shaft (LSS) rpm, is $N = 97$. The controller is implemented in line 42 of the Matlab code. A conversion from rpm to rad/s is needed for it to function correctly.

D

```matlab
1  addpath('..\..\');
2
3  %this is setup using relative path and depends on the location of ...
       this file, if there are issues use absolute path to these files
4  loadlibrary('../../QBladeCE_2.0.5.2.dll',
5  '../QBladeDLLFunctions.h','alias','QBladeDLL')
6
7  m = libfunctions('QBladeDLL') ;
8
9  if isempty(m)
10     fprintf('Error')
11 end
12
13 %this is setup using relative path and depends on the location of ...
       this file, if there are issues use absolute path to these files
14 calllib('QBladeDLL','setLibraryPath','../../QBladeCE_2.0.5.2.dll')
15
16 calllib('QBladeDLL','createInstance',0,24)
17
18 %this is setup using relative path and depends on the location of ...
       this file, if there are issues use absolute path to these files
19 projectFile = '../../Source/NREL5MW.qpr';
20
21 calllib('QBladeDLL','loadProject',projectFile)
22 calllib('QBladeDLL','initializeSimulation')
23
24 simTime = 400; %in timestep, actual time is timestep*#timesteps
25 valuestr = 'Rotational Speed [rpm]';
26 valuestr2 = 'Gen. HSS Torque [Nm]';
27 % valuestr2 = 'Gen. Power (w.o. losses) [kW]';
28
29 K = 2.24;
30 N = 97;
31
32 f = waitbar(0,'Initializing Simulation') ;
33
34 for i = 1:1:simTime
35
36     calllib('QBladeDLL','advanceTurbineSimulation')
```

```matlab
37        omega = calllib('QBladeDLL','getCustomData_at_num',valuestr, ...
              0.5, 0);
38        genTorqueQB = ...
              calllib('QBladeDLL','getCustomData_at_num',valuestr2, 0, 0);
39        genTorqueQB_store(i,:) = genTorqueQB;
40
41        omega_g = omega*N;
42        genTorque = K.*(omega_g*(2*pi/60))^2;
43        genTorque_store(i,:) = genTorque ;
44
45        calllib('QBladeDLL','setControlVars_at_num',[genTorque 0 0 0 0],0)
46
47        waitbar(i/simTime,f,'Simulation Running')
48
49   end
50   close(f)
51
52   calllib('QBladeDLL','closeInstance')
53
54   figure;
55   plot(genTorqueQB_store)
56   hold on
57   plot(genTorque_store)
58   grid on
59   legend('QB HSS Torque','K omega^2')
```

D

Once run, without altering the code, the output should look as in Figure D.2. The blue line represents the generator torque that is being sent to QBlade using `setControlVars_at_num`. The red line shows the generator torque read out from QBlade using `getCustomData_at_num`. Notice how the data from QBlade is one step behind the calculated torque; this is because that data channel is read before applying the torque to the system (one step behind).
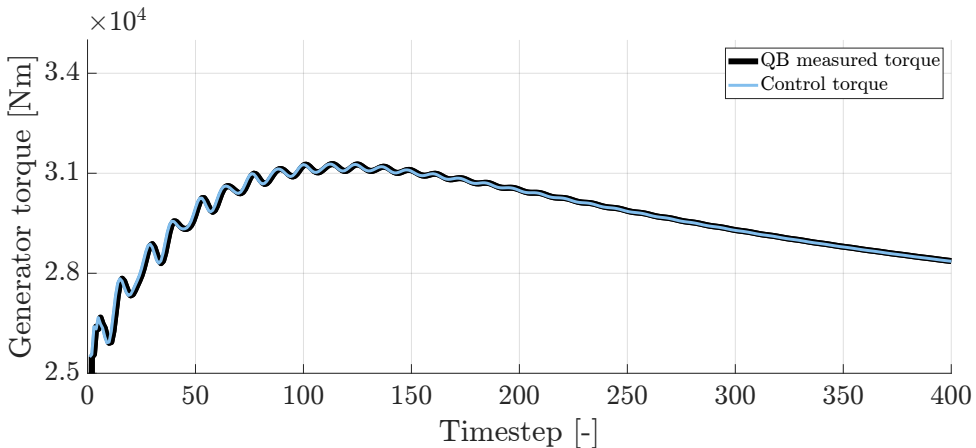

Figure D.2: Output of the example code running the $K\omega^2$ controller.

D.4.3. STEP IN WIND SIMULATION

In this example, we will expand on the $K\omega^2$ controller build in Appendix D.4.2. Specifically, during the simulation, we put a step on the wind speed of 1 m/s, raising it from 9 m/s to 10 m/s. Also included in the script is a measurement of the wind speed in x, y and z directions at hub height. An increase in wind speed also warrants a response from the $K\omega^2$ controller, hence its inclusion in this code.

D

```matlab
1   addpath('..\..\');
2
3   %this is setup using relative path and depends on the location of ...
        this file, if there are issues use absolute path to these files
4   loadlibrary('../../QBladeCE_2.0.5.2.dll',
5   '../QBladeDLLFunctions.h','alias','QBladeDLL')
6
7   m = libfunctions('QBladeDLL') ;
8
9   if isempty(m)
10      fprintf('Error')
11  end
12
13  %this is setup using relative path and depends on the location of ...
        this file, if there are issues use absolute path to these files
14  calllib('QBladeDLL','setLibraryPath','../../QBladeCE_2.0.5.2.dll')
15
16  calllib('QBladeDLL','createInstance',0,24)
17
18  %this is setup using relative path and depends on the location of ...
        this file, if there are issues use absolute path to these files
19  projectFile = '../../Source/NREL5MW.qpr';
20
21  calllib('QBladeDLL','loadProject',projectFile)
22  calllib('QBladeDLL','initializeSimulation')
23
24  simTime = 3000; %in timestep, actual time is timestep*#timesteps
25  valuestr = 'Rotational Speed [rpm]';
26  valuestr2 = 'Gen. HSS Torque [Nm]';
27  f = waitbar(0,'Initializing Simulation') ;
28
29
30  K = 2.24;
31  N = 97;
32  startWind = 1500;
33  for i = 1:1:simTime
34
35      calllib('QBladeDLL','advanceTurbineSimulation')
36      if i > startWind
37      calllib('QBladeDLL','setPowerLawWind', 10, 0, 0, 0, 87.6)
38      end
39      omega = calllib('QBladeDLL','getCustomData_at_num',valuestr, ...
            0.5, 0) ;
40      genTorqueQB = ...
            calllib('QBladeDLL','getCustomData_at_num',valuestr2, 0, 0) ;
41      genTorqueQB_store(i,:) = genTorqueQB;
42
```

```
43      omega_g = omega*N;
44      genTorque = K.*(omega_g*(2*pi/60))^2;
45      genTorque_store(i,:) = genTorque ;
46
47      calllib('QBladeDLL','setControlVars_at_num',[genTorque 0 0 0 0],0)
48      V_hub(i,:) = calllib('QBladeDLL','getWindspeed', -20, 0, 87.6, ...
            [0 0 0]);
49      waitbar(i/simTime,f,'Simulation Running')
50
51 end
52
53 close(f)
54 % calllib('QBladeDLL','storeProject','Test.qpr')
55 calllib('QBladeDLL','closeInstance')
56
57 figure;
58 subplot(2,1,1)
59 plot(genTorqueQB_store)
60 hold on
61 plot(genTorque_store)
62 grid on
63 legend('QB HSS Torque','K omega^2')
64
65 subplot(2,1,2)
66 plot(V_hub)
67 grid on
68 legend('Wind Speed [m/s]')
```

D.4.4. DELFT RESEARCH CONTROLLER

The Delft Research Controller (DRC) provides an open, modular and fully adaptable wind turbine controller [3]. New controller implementations can be added to the existing controller, allowing the assessment of new algorithms. The DRC is developed in Fortran and uses the Bladed-style DISCON controller interface. The compiled controller is configured by a single control settings parameter file, i.e. discon.in, and can work with any wind turbine model and simulation software using the DISCON interface. These variables are called UserVars and are communicated to the controller .dll through the SWAP array. The relative path to the file containing the UserVars is hard-coded into the compiled version of the DRC.

NREL recently acknowledged the potential of the DRC by adopting it as their baseline control solution of choice and dubbed it as the Reference OpenSource Controller (ROSCO) [4], [5]. To provide an easy and convenient way of controller development via a graphical interface, this controller design and compilation environment has been developed in Simulink and refer to SimulinkDRC [6]. These examples are primarily included for the people working in the Data-Driven Control group at the Delft University of Technology. These examples do show how QBlade can be used to run batch simulations and, at the same time, save data sets for post-processing.

WSE-TSR TRACKING CONTROLLER

This example uses a stripped-down version of the Delft Research Controller specifically designed for partial load torque control either with the most common $K\omega^2$ controller

or with the combined wind speed estimator and tip-speed ratio (WSE-TSR) tracking
controller [7]. In this example, the WSE-TSR tracking controller is enabled with two
different settings of gain. The controller and estimator gains are governed by an input
file called discon.in. The values in this file are passed to it through Matlab and the
`writeDisconWSETSR` function.

   Main:

```matlab
1  %%
2  % Writing DISCON loop.
3
4  %%
5  clear all
6  close all
7  clc
8
9  %% Define paths
10
11 %set the absolute path to your qblade directory here
12 UserPath = '<userpath>\QBladeCE_2.0.5.2\';
13 disconPath = UserPath ;
14 MatlabPath = [UserPath ...
       'MATLAB_Files\4p4_DRC_Cases\4p41_BaselineTorqueControl\'];
15 SourcePath = [UserPath 'Source'] ;
16 DllPath = [UserPath 'QBladeCE_2.0.5.2.dll'];
17 addpath('..\Functions');
18 addpath('..\..\..\');
19 %%
20
21 %this is setup using relative path and depends on the location of ...
       this file, if there are issues use absolute path to these files
22 loadlibrary(DllPath,'../../QBladeDLLFunctions.h','alias','QBladeDLL')
23
24 m = libfunctions('QBladeDLL') ;
25
26 if isempty(m)
27     fprintf('Error')
28 end
29
30 %% Defining Settings
31 Pitchb1 = 0;
32 Pitchb2 = 0;
33 Pitchb3 = 0;
34 KpTSR = [-1635.1714 -2079.5682];
35 KiTSR = [-6451.3008 -11.6565];
36 KpWSE = [8.0258 11.2468];
37 KiWSE = [0.2796 0.2775];
38 TSRref = [7.2385 7.7187];
39 K = [0.0000 0.0000];
40 Tg0 = [25000.0000 25000.0000];
41
42 SimNr = length(TSRref);
43 tic
44 for i_for1 = 1:1:SimNr
45
46     Sim_name_folder = ['Sim_', num2str(i_for1)] ;
```

```
47
48      copyfile([SourcePath],Sim_name_folder);
49
50      cd(disconPath)
51
52      writeDisconWSETSR(Pitchb1,Pitchb2,Pitchb3, ...
53          KpTSR(i_for1),KiTSR(i_for1),KpWSE(i_for1),KiWSE(i_for1), ...
54          TSRref(i_for1),K(i_for1),Tg0(i_for1))
55      cd(MatlabPath)
56
57      run Torque_Simulation.m
58
59      cd(Sim_name_folder)
60
61      save(['Output_',num2str(i_for1)],'DATA')
62      cd('..\..\..\..\')
63      delete('discon.in');
64      cd(MatlabPath)
65 end
66 %%
67 toc
68
69 figure();grid on;
70 subplot(1,4,1)
71 title('Generator Torque')
72 plot(DATA.time,DATA.Tg); hold on;
73 plot(DATA.time,DATA.TgSWAP);
74 subplot(1,4,2)
75 title('Rotational speed')
76 plot(DATA.time,DATA.Omega);
77 subplot(1,4,3)
78 title('Tip-speed ratio')
79 plot(DATA.time,DATA.TSR);
80 hold on;
81 plot(DATA.time,DATA.TSRest);
82 legend('Measured','Estimated');
83 subplot(1,4,4)
84 title('Rotor-effective wind speed')
85 plot(DATA.time,DATA.U);
86 hold on;
87 plot(DATA.time,DATA.Uest);
88 legend('Measured','Estimated');
```

Function:

```
1  simFile_loc = [MatlabPath Sim_name_folder '\'];
2
3  calllib('QBladeDLL','setLibraryPath',DllPath)
4  calllib('QBladeDLL','createInstance',1,24)
5  simName = 'NREL5MW_WSETSRK.sim';
6  calllib('QBladeDLL','loadSimDefinition',[simFile_loc simName])
7  calllib('QBladeDLL','initializeSimulation')
8
9  simTime = 4000; %in timestep, actual time is timestep*#timesteps %TO ...
       DO CHANGE
10 valuestr = 'Time [s]';
```

```
11  valuestr1 = 'Rotational Speed [rpm]';
12  valuestr2 = 'Gen. HSS Torque [Nm]';
13  valuestr3 = 'SWAP[46] [-]'; %Generator torque
14  valuestr4 = 'Abs Wind Vel. at Hub [m/s]';
15  valuestr5 = 'SWAP[84] [-]'; %Estimated wind speed
16  valuestr6 = 'Tip Speed Ratio [-]';
17  valuestr7 = 'SWAP[85] [-]'; %Estimated tip-speed ratio
18
19  for i_for2 = 1:1:simTime
20
21      calllib('QBladeDLL','advanceTurbineSimulation')
22      calllib('QBladeDLL','advanceController_at_num',[0 0 0 0 0],0)
23
24      Time = calllib('QBladeDLL','getCustomData_at_num',valuestr, 0, 0);
25      Rpm = calllib('QBladeDLL','getCustomData_at_num',valuestr1, 0, 0);
26      GenTg = calllib('QBladeDLL','getCustomData_at_num',valuestr2, 0, 0);
27      GenTgSWAP = ...
            calllib('QBladeDLL','getCustomData_at_num',valuestr3, 0, 0);
28      U = calllib('QBladeDLL','getCustomData_at_num',valuestr4, 0, 0);
29      Uest = calllib('QBladeDLL','getCustomData_at_num',valuestr5, 0, 0);
30      TSR = calllib('QBladeDLL','getCustomData_at_num',valuestr6, 0, 0);
31      TSRest = calllib('QBladeDLL','getCustomData_at_num',valuestr7, ...
            0, 0);
32
33      DATA.time(i_for2,:) = Time;
34      DATA.Omega(i_for2,:) = Rpm;
35      DATA.Tg(i_for2,:) = GenTg;
36      DATA.TgSWAP(i_for2,:) = GenTgSWAP;
37      DATA.U(i_for2,:) = U;
38      DATA.Uest(i_for2,:) = Uest;
39      DATA.TSR(i_for2,:) = TSR;
40      DATA.TSRest(i_for2,:) = TSRest;
41
42  end
43
44  calllib('QBladeDLL','closeInstance')
```

INDIVIDUAL PITCH CONTROL

This example uses a stripped-down version of the Delft Research Controller specifically designed for dynamic induction control (Pulse [8]) or dynamic individual pitch control (Helix [9]). In this example, the Helix is enabled with an amplitude of degrees and at two different frequencies. The excitation frequency and technique are governed by an input file called discon.in. The values in this file are passed to it through Matlab and the `writeDisconIPC` function.

Main:

```
1  %%
2  % Writing DISCON loop.
3
4  %%
5  clear all
6  close all
```

```matlab
 7  clc
 8
 9  %% Define paths
10  %set the absolute path to your qblade directory here
11  UserPath = '<userpath>\QBladeCE_2.0.5.2\';
12  disconPath = UserPath ;
13  MatlabPath = [UserPath ...
        'MATLAB_Files\4p4_DRC_Cases\4p42_IndividualPitchControl\'];
14  SourcePath = [UserPath 'Source'] ;
15  DllPath = [UserPath 'QBladeCE_2.0.5.2.dll'];
16  addpath('..\Functions');
17  addpath('..\..\..\');
18  %%
19
20  %this is setup using relative path and depends on the location of ...
        this file, if there are issues use absolute path to these files
21  loadlibrary(DllPath,'../../QBladeDLLFunctions.h','alias','QBladeDLL')
22
23  m = libfunctions('QBladeDLL') ;
24
25  if isempty(m)
26      fprintf('Error')
27  end
28
29  %% Defining Settings
30  Str = [0.25 0.5];
31
32  IPC = 0;
33  Pulse = 0/57.3;
34  Helix_CM2 = 4/57.3;
35  Helix_CM3 = 4/57.3;
36  Freq = Str*9/126*2*pi ;
37  Pitch_off = 0/57.3;
38  uservar7 = 0;
39  uservar8 = 0;
40  uservar9 = 0;
41  uservar10 = 0;
42
43  SimNr = length(Freq);
44  tic
45  for i_for1 = 1:1:SimNr
46
47      Sim_name_folder = ['Sim_', num2str(i_for1)] ;
48
49      copyfile([SourcePath],Sim_name_folder);
50
51      cd(disconPath)
52
53      writeDisconIPC(IPC,Pulse,Helix_CM2,Helix_CM3,Freq(i_for1),Pitch_off)
54      cd(MatlabPath)
55
56      run IPC_Simulation.m
57
58      cd(Sim_name_folder)
59
60      save(['Output_',num2str(i_for1)],'PitchAngles')
61
```

D

```matlab
62      cd('..\..\..\..\')
63      delete('discon.in');
64      cd(MatlabPath)
65 end
66 %%
67 toc
68
69 figure;
70 plot(PitchAngles(:,1))
71 hold on
72 plot(PitchAngles(:,2))
73 plot(PitchAngles(:,3))
74 grid on
75 legend('Blade 1','Blade 2','Blade 3')
```

Function:

```matlab
1  simFile_loc = [MatlabPath Sim_name_folder '\'];
2
3  calllib('QBladeDLL','setLibraryPath',DllPath)
4  calllib('QBladeDLL','createInstance',1,24)
5  simName = 'NREL5MW_DIPC.sim';
6  calllib('QBladeDLL','loadSimDefinition',[simFile_loc simName])
7  calllib('QBladeDLL','initializeSimulation')
8
9  simTime = 1000; %in timestep, actual time is timestep*#timesteps
10 valuestr = 'Pitch Angle Blade 1 [deg]';
11 valuestr2 = 'Pitch Angle Blade 2 [deg]';
12 valuestr3 = 'Pitch Angle Blade 3 [deg]';
13
14 for i_for2 = 1:1:simTime
15
16     calllib('QBladeDLL','advanceTurbineSimulation')
17     calllib('QBladeDLL','advanceController_at_num',[0 0 0 0 0],0)
18
19     Pitch1 = calllib('QBladeDLL','getCustomData_at_num',valuestr, 0, ...
           0) ;
20     Pitch2 = calllib('QBladeDLL','getCustomData_at_num',valuestr2, ...
           0, 0);
21     Pitch3 = calllib('QBladeDLL','getCustomData_at_num',valuestr3, ...
           0, 0);
22
23     PitchAngles(i_for2,:) = [Pitch1 Pitch2 Pitch3] ;
24 end
25
26 calllib('QBladeDLL','closeInstance')
```

D.4.5. TWO TURBINE SIMULATION

This example will show how to interact with two turbines in the same simulation. For this example, example D.4.2 has been expanded with a second turbine. This second turbine is placed 376 metres downstream (3 rotor diameters). This first wind turbine is set up to use a free-vortex wake to model the aerodynamics. Different to example D.4.2, using the free vortex model generates a wake behind the first turbine that will interact with the second turbine. This second turbine runs a BEM code. Both turbines are controlled using the $K\omega^2$ controller implementation from example D.4.2. Once the wake comes starts to interact with the second turbine it lowers the effective wind speed. The $K\omega^2$ will lower the torque when the wind speed decreases.

NOTE: This example only works with QBlade Enterprise Edition (i.e. QBlade-EE).

D

```matlab
1  if libisloaded('QBladeDLL')
2      unloadlibrary 'QBladeDLL'
3  end;
4
5  addpath('..\..\');
6
7  %this is setup using relative path and depends on the location of ...
       this file, if there are issues use absolute path to these files
8  loadlibrary('../../QBladeEE_2.0.5.2.dll',
9  '../QBladeDLLFunctions.h','alias','QBladeDLL')
10
11 m = libfunctions('QBladeDLL') ;
12
13 if isempty(m)
14     fprintf('Error')
15 end
16
17 %this is setup using relative path and depends on the location of ...
       this file, if there are issues use absolute path to these files
18 calllib('QBladeDLL','setLibraryPath','../../QBladeEE_2.0.5.2.dll')
19
20 calllib('QBladeDLL','createInstance',1,24)
21
22 %this is setup using relative path and depends on the location of ...
       this file, if there are issues use absolute path to these files
23 projectFile = '../../Source/NREL5MW_TwoTurbines.qpr';
24
25 calllib('QBladeDLL','loadProject',projectFile)
26 calllib('QBladeDLL','initializeSimulation')
27
28 simTime = 1400; %in timestep, actual time is timestep*#timesteps
29 valuestr = 'Rotational Speed [rpm]';
30 valuestr2 = 'Gen. HSS Torque [Nm]';
31 % valuestr2 = 'Gen. Power (w.o. losses) [kW]';
32 f = waitbar(0,'Initializing Simulation') ;
33
34 K = 2.24;
35 N = 97;
36 for i = 1:1:simTime
37     calllib('QBladeDLL','advanceTurbineSimulation')
38     omega_WT1 = calllib('QBladeDLL','getCustomData_at_num',valuestr, ...
```

```
              0, 0) ;
39      genTorqueQB_WT1 = ...
             calllib('QBladeDLL','getCustomData_at_num',valuestr2, 0, 0) ;
40      genTorqueQB_store_WT1(i,:) = genTorqueQB_WT1;
41
42      omega_g_WT1 = omega_WT1*N;
43      genTorque_WT1 = K.*(omega_g_WT1*(2*pi/60))^2;
44      genTorque_store_WT1(i,:) = genTorque_WT1 ;
45      V_hub_WT1(i,:) = calllib('QBladeDLL','getWindspeed', -20, 0, ...
             87.6, [0 0 0]);
46
47      calllib('QBladeDLL','setControlVars_at_num',[genTorque_WT1 0 0 0 ...
             0],0)
48
49      omega_WT2 = calllib('QBladeDLL','getCustomData_at_num',valuestr, ...
             0, 1) ;
50      genTorqueQB_WT2 = ...
             calllib('QBladeDLL','getCustomData_at_num',valuestr2, 0, 1) ;
51      genTorqueQB_store_WT2(i,:) = genTorqueQB_WT2;
52
53      omega_g_WT2 = omega_WT2*N;
54      genTorque_WT2 = K.*(omega_g_WT2*(2*pi/60))^2;
55      genTorque_store_WT2(i,:) = genTorque_WT2 ;
56      V_hub_WT2(i,:) = calllib('QBladeDLL','getWindspeed', 350, 0, ...
             87.6, [0 0 0]);
57
58      calllib('QBladeDLL','setControlVars_at_num',[genTorque_WT2 0 0 0 ...
             0],1)
59      waitbar(i/simTime,f,'Simulation Running')
60  end
61  close(f)
62  % calllib('QBladeDLL','storeProject','Test.qpr')
63  calllib('QBladeDLL','closeInstance')
64
65  figure(1);
66  subplot(2,1,1)
67  plot(genTorqueQB_store_WT1,'LineWidth',1.5)
68  hold on
69  plot(genTorqueQB_store_WT2,'LineWidth',1.5)
70  grid on
71  legend('QB HSS Torque WT 1','QB HSS Torque WT 2','Location','southwest')
72  title('Generator Torque')
73
74  subplot(2,1,2)
75  plot(V_hub_WT1(:,1),'LineWidth',1.5)
76  hold on
77  plot(V_hub_WT2(:,1),'LineWidth',1.5)
78  grid on
79  legend('Wind Speed Turbine 1','Wind Speed Turbine ...
         2','Location','southwest')
80  title('Wind speed')
```

Figure D.3 shows the output of the two turbine example. The interaction between the two turbines starts after 1000 timesteps (roughly 50 seconds). The drop in generator torque is due to the drop in wind speed. As it settles to its new steady state, the small fluctuations in the generator torque that remain are a result of the free-vortex implementation
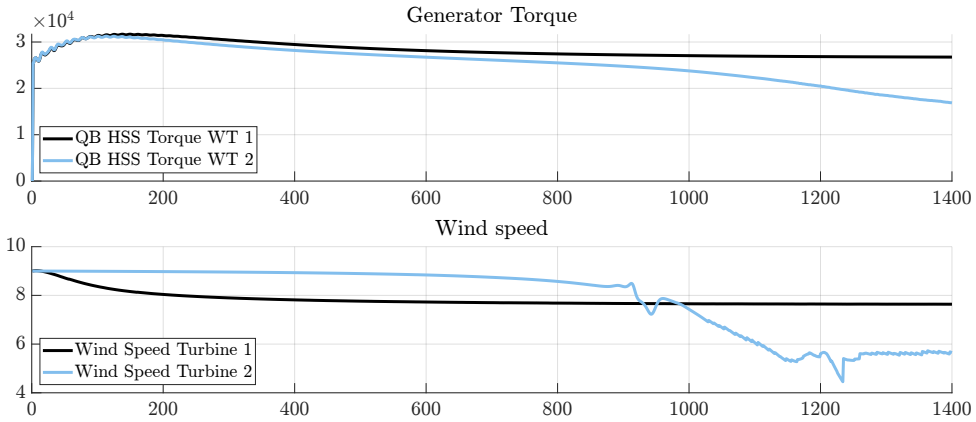
of the wake.

Figure D.3: Output of the example code running the $K\omega^2$ controllers for the two turbine simulation.

D.4.6. COMMON MISTAKES

- It is important to remember that in the function **get custom data**, the string should correspond to the label of the graphical data in the GUI and not to the header of the export simulation data.

- When running an n-turbines simulation, check which is the first turbine loaded in the dropdown menu in the simulation setup screen. Note that the order in the dropdown menu is alphabetical and not the order of adding the turbine.

- When QBlade receives an update, it is not uncommon for channel names to change. Whenever updating to a new version of QBlade, double-check the channel names within the GUI.

BIBLIOGRAPHY

[1] L. Brandetti and D. van den Berg, "QBlade 2.0.5.2 Matlab Tutorial", Tech. Rep., 2023. DOI: 10.4121/22134710.

[2] J. Jonkman, S. Butterfield, W. Musial, and G. Scott, "Definition of a 5-MW Reference Wind Turbine for Offshore System Development", Tech. Rep., 2009. DOI: NREL/TP-500-38060. [Online]. Available: https://www.nrel.gov/docs/fy09osti/38060.pdf.

[3] S. P. Mulders and J. W. van Wingerden, "Delft research controller: An open-source and community-driven wind turbine baseline controller", ser. Journal of Physics: Conference Series, vol. 1037, 2018. DOI: 10.1088/1742-6596/1037/3/032009. [Online]. Available: https://dx.doi.org/10.1088/1742-6596/1037/3/032009.

[4] S. P. Mulders, "Wind turbine control: Advances for load mitigations and hydraulic drivetrains", Ph.D. dissertation, 2020. DOI: 10.4233/uuid:521577f0-a361-4f92-94c5-02a3bc61ef44. [Online]. Available: https://doi.org/10.4233/uuid:521577f0-a361-4f92-94c5-02a3bc61ef44.

[5] N. R. E. Laboratory, "Rosco. version 1.0.0", Tech. Rep., 2020. [Online]. Available: https://github.com/NREL/rosco.

[6] S. P. Mulders, M. B. Zaaijer, R. Bos, and J. W. van Wingerden, "Wind turbine control: Open-source software for control education, standardization and compilation", in *Journal of Physics: Conference Series*, vol. 1452, 2020. DOI: 10.1088/1742-6596/1452/1/012010. [Online]. Available: https://iopscience-iop-org.tudelft.idm.oclc.org/article/10.1088/1742-6596/1452/1/012010.

[7] L. Brandetti, Y. Liu, S. P. Mulders, C. Simão Ferreira, S. Watson, and J. W. van Wingerden, "On the ill-conditioning of the combined wind speed estimator and tip-speed ratio tracking control scheme", ser. Journal of Physics: Conference Series, 2022. DOI: 10.1088/1742-6596/2265/3/032085. [Online]. Available: https://iopscience.iop.org/article/10.1088/1742-6596/2265/3/032085.

[8] W. Munters and J. Meyers, "Towards practical dynamic induction control of wind farms: Analysis of optimally controlled wind-farm boundary layers and sinusoidal induction control of first-row turbines", *Wind Energy Science*, vol. 3, pp. 409–425, 2018. DOI: 10.5194/wes-3-409-2018. [Online]. Available: https://wes.copernicus.org/articles/3/409/2018/.

[9] J. A. Frederik, B. M. Doekemeijer, S. P. Mulders, and J. W. van Wingerden, "The helix approach: Using dynamic individual pitch control to enhance wake mixing in wind farms", *Wind Energy*, vol. 23, no. 8, pp. 1739–1751, 2020. DOI: 10.1002/we.2513. [Online]. Available: https://doi.org/10.1002/we.2513.

E

QBLADE TURBINE MODEL

This section details the turbine model (Section 5.3) implementation in QBlade. Note that a rigorous validation procedure has been conducted, encompassing comparison with the AC model with B-L dynamic stall model [1] and referenced experimental data [2], [3]. However, validation results are not explicitly presented in this appendix due to scope constraints. To account for the flow curvature effect, a virtual airfoil geometry was computed for the NACA0021 blade geometry using the transformation technique based on the chord-to-radius ratio and available in QBlade [4]. Lift and drag polars for the blades and the struts are computed at a Reynolds number of 8.34×10^4 with $Ncrit = 7$ and free transition. The polars are then extrapolated with the Montgomerie method [5]. In order to enhance the accuracy of the aerodynamic estimation, the ATEFlap model [6] has been selected as a dynamic stall model with a boundary layer pressure lag time constant (T_f) of 5 and a peak pressure lag time constant (T_p) of 1.5. The main settings for the QBlade turbine model are summarised in Table E.1. The interested reader is referred to Marten et al. [7] for further explanations of the listed quantities.

Table E.1: QBlade turbine model settings.

Parameter	Value
Reynolds number	8.34×10^4
Blade discretisation	30 (sinusoidal)
Dynamic stall model	ATEFlap ($T_f = 5$, $T_p = 1.5$)
Wake integration type	EF (1st Order Euler Forward integration)
Full wake length	12 revolutions

BIBLIOGRAPHY

[1] J. Leishman and T. Beddoes, "A Semi-Empirical Model for Dynamic Stall", *Journal of the American Helicopter Society*, vol. 34, no. 3, pp. 3–17, 1989. DOI: 10.4050/JAHS.34.3.3. [Online]. Available: https://doi.org/10.4050/JAHS.34.3.3.

[2] B. LeBlanc and C. Simão Ferreira, "Estimation of blade loads for a variable pitch vertical axis wind turbine from particle image velocimetry", *Wind Energy*, pp. 1–20, 2021, ISSN: 10991824. DOI: 10.1002/we.2674. [Online]. Available: https://doi.org/10.1002/we.2674.

[3] B. LeBlanc and C. Simão Ferreira, "Estimation of blade loads for a variable pitch Vertical Axis Wind Turbine with strain gage measurements", *Wind Energy*, pp. 1–16, 2022, ISSN: 10991824. DOI: 10.1002/we.2713. [Online]. Available: https://doi.org/10.1002/we.2713.

[4] A. Bianchini, F. Balduzzi, J. M. Rainbird, J. Peiro, J. M. R. Graham, G. Ferrara, and L. Ferrari, "An Experimental and Numerical Assessment of Airfoil Polars for Use in Darrieus Wind Turbines—Part I: Flow Curvature Effects", *Journal of Engineering for Gas Turbines and Power*, vol. 138, no. 3, p. 032 602, Sep. 2015. DOI: 10.1115/1.4031269. [Online]. Available: https://doi.org/10.1115/1.4031269.

[5] B. Montgomerie, "Methods for Root Effects, Tip Effects and Extending the Angle of Attack Range to 6180, With Application to Aerodynamics for Blades on Wind Turbines and Propellers", Swedish Defence Research Agency, Tech. Rep., 2004. [Online]. Available: https://www.foi.se/rest-api/report/FOI-R--1305--SE.

[6] L. Bergami and M. Gauanaa, "ATEFlap Aerodynamic Model: A Dynamic Stall Model Including the Effects of Trailing Edge Flap Deflection", Technical University of Denmark, Tech. Rep., 2012. [Online]. Available: https://backend.orbit.dtu.dk/ws/portalfiles/portal/6599679/ris-r-1792.pdf.

[7] D. Marten, J. Saverin, R. Behrens de Luna, and S. Perez-Becker, "QBlade documentation", Tech. Rep., 2021. [Online]. Available: https://docs.qblade.org/.

LIST OF ABBREVIATIONS

AC Actuator Cylinder.

B-L Beddoes-Leishman.

BPM Brooks, Pope and Marcolini.

BVI Blade-Vortex Interaction.

BWES Blade-effective wind speed.

BWI Blade-Wake Interaction.

CART Controls Advanced Research Turbine.

CFL Courant-Friedrichs-Lewy.

ESC Extremum Seeking Control.

FWH Ffwocs Williams and Hawkings.

HAWT Horizontal-axis wind turbine.

LB-VLES Lattice-Boltzmann Very Large Eddy Simulations.

LBL-VS Laminar Boundary Layer - Vortex Shedding.

LCoE Levelised Cost of Energy.

MPC Model Predictive Control.

NREL National Renewable Energy Laboratory.

OASPL Overall Sound Pressure Level.

PA Psychoacoustic annoyance.

PI Proportional and integral.

PSD Power Spectral Density.

RWES Rotor-effective wind speed.

SPL Sound Pressure Level.

SQAT Sound Quality Analysis Toolbox.

SQM Sound Quality Metrics.

SS Separation-Stall.

T-I Turbulence - Interaction.

T-S Tollmien-Schlichting.

TBL-TE Turbulent Boundary Layer - Trailing Edge.

TEB-VS Trailing Edge Blunt - Vortex Shedding.

VAWT Vertical-axis wind turbine.

VR Variable resolution.

WSE-TSR Wind speed estimator - tip-speed ratio.

Curriculum Vitæ

Livia Brandetti

28-11-1994	Born in Rome, Italy

Education

2008–2013	Highschool Primo Levi Institute, Rome, Italy
2013–2016	Bachelor's degree in Energy Engineering La Sapienza University of Rome, Rome, Italy
2016–2018	Master's degree in Sustainable Energy Technology (Wind Energy) Delft University of Technology, Delft, The Netherlands
2018–2019	Wind Energy Researcher Delft University of Technology, Delft, The Netherlands
2019–2023	Doctoral degree in Aerospace Engineering Delft University of Technology, Delft, The Netherlands *Thesis title:* Design for urban vertical-axis wind turbines: balancing performance and noise *Promotors:* Prof. dr. ir. J. W. van Wingerden and Prof. dr. S. Watson *Copromotor:* Dr. ir. S. P. Mulders

LIST OF PUBLICATIONS

JOURNAL PAPERS

- **L. Brandetti**, S.P. Mulders, R. Merino-Martinez, S. Watson and J.W. van Wingerden, Multi-objective optimisation of vertical-axis wind turbine controllers: balancing aero-servo-elastic performance and noise. *Wind Energy Science Discussion*, under review, DOI:10.5194/wes-2023-154 (in this thesis)

- **L. Brandetti**, S.P. Mulders, Y. Liu, S. Watson and J.W. van Wingerden, Analysis and multi-objective optimisation of wind turbine torque control strategies. *Wind Energy Science*, 8, 2023, DOI:10.5194/wes-8-1553-2023 (in this thesis)

- **L. Brandetti**, F. Avallone, D. De Tavernier, B. LeBlanc, C. Ferreira and D. Casalino, Assessment through high-fidelity simulations of a low-fidelity noise prediction tool for a vertical-axis wind turbine. *Journal of Sound and Vibration*, 547, 2023, DOI:10.1016/j.jsv.2022.117486 (in this thesis)

PATENT

- S.P. Mulders, **L. Brandetti**, J.W. van Wingerden, F. Spagnolo, J. S. Thomsen, J. X. V. Neto, Controlling a wind turbine with a scaled power coefficient, 22205531.1

CONFERENCE PAPERS

- S. Shubham, F. Avallone, **L. Brandetti**, N. Wright, A. Ianakiev, Effect of struts and central tower on aerodynamics and aeroacoustics of vertical axis wind turbines using mid-fidelity and high-fidelity methods, in *American Institute of Aeronautics and Astronautics (AIAA) Science and Technology (SciTech) Forum and Exposition*, Orlando, FL, USA, 2024, DOI:10.2514/6.2024-1485.

- **L. Brandetti**, Y. Liu, A. K. Pamososuryo, S.P. Mulders, S. Watson and J.W. van Wingerden, Unscented Kalman filter-based blade-effective wind speed estimation for a vertical-axis wind turbine, in *22nd International Federation of Automatic Control (IFAC) World Congress*, Yokohama, Japan, 2023, DOI:10.1016/j.ifacol.2023.10.1033

- Y. Liu, **L. Brandetti** and S.P. Mulders, Sensor fault-tolerant control for wind turbines: an iterative learning method, in *22nd International Federation of Automatic Control (IFAC) World Congress*, Yokohama, Japan, 2023, DOI:10.1016/j.ifacol.2023.10.192

- S.P. Mulders, **L. Brandetti**, F. Spagnolo, Y. Liu, P.B. Christensen and J.W. van Wingerden, A learning algorithm to advanced wind turbine controllers for the calibration of internal model uncertainties: A wind speed measurement-free approach,

in *2023 American Control Conference (ACC)*, San Diego, California, USA, 2023, DOI:10.23919/ACC55779.2023.10156125

- **L. Brandetti**, Y. Liu, S.P. Mulders, C. Ferreira, S. Watson and J.W. van Wingerden, On the ill-conditioning of the combined wind speed estimator and tip-speed ratio tracking control scheme, in *Journal of Physics: Conference Series*, Delft, The Netherlands, vol 2265, 2022, DOI:10.1088/1742-6596/2265/3/032085 (in this thesis)

- **L. Brandetti**, D. De Tavernier, B. LeBlanc and C. Ferreira, Experimental test of variable loads on a vertical-axis wind turbine, in *Journal of Physics: Conference Series*, Delft, The Netherlands, vol 1618, 2020, DOI:10.1088/1742-6596/1618/3/032037

- P. F. Melani, F. Balduzzi, **L. Brandetti**, C. Ferreira and A. Bianchini, An experimental and numerical analysis of the dynamic variation of the angle of attack in a vertical-axis wind turbine, in *Journal of Physics: Conference Series*, Delft, The Netherlands, vol 1618, 2020, DOI:10.1088/1742-6596/1618/5/052064